MICROCHANNEL HEAT EXCHANGERS FOR INTEGRAL LIGHT WATER REACTORS

A Dissertation
Presented to
The Academic Faculty

by

Daniel Kromer

In Partial Fulfillment
of the Requirements for the Degree
Doctor of Philosophy in Nuclear Engineering
from the Woodruff School of Mechanical Engineering

Georgia Institute of Technology
August, 2019

MICROCHANNEL HEAT EXCHANGERS FOR INTEGRAL LIGHT WATER REACTORS

Approved by:

Dr. Srinivas Garimella, Advisor
G.W.W. School of Mechanical Engineering
Georgia Institute of Technology

Dr. Farzad Rahnema
G.W.W. School of Mechanical Engineering
Georgia Institute of Technology

Dr. Bojan Petrovic
G.W.W. School of Mechanical Engineering
Georgia Institute of Technology

Dr. Thomas Fuller
School of Chemical and Biomolecular Engineering
Georgia Institute of Technology

Dr. S. Mostafa Ghiaasiaan
G.W.W. School of Mechanical Engineering
Georgia Institute of Technology

Date Approved: April 29, 2019

To my mother, Elizabeth Ann Kromer

ACKNOWLEDGEMENTS

I would like to thank my advisor, Dr. Srinivas Garimella, for his guidance throughout my Ph.D. Every time I had doubts about my project, work, or ability, Dr. Garimella gave me the confidence I needed to proceed. Additionally, I would like to thank all the past and present members of the Sustainable Thermal Systems Lab. Their knowledge, support, and companionship has been invaluable during my time at Georgia Tech. Particularly, I would like to thank Alex Huning, who helped initiate the I^2S-LWR heat exchanger project along with the senior design teams in NRE 4232. I would also like to thank Dr. Bojan Petrovic for his work developing the I^2S-LWR concept and his unending energy and optimism in the project. In addition to agreeing to serve on my reading committee, Dr. Mostafa Ghiaasiaan has played an important role in my heat transfer education. His courses and books on single-phase convection and two-phase flow form the basis of much of my understanding of the subjects. I would also like to thank my girlfriend, Emily Pleadwell, who has essentially acted as my editor in the writing of this dissertation. Finally, I would like to thank the US Department of Energy's Nuclear Energy University Programs (NEUP) for their financial support of the Integral Inherently Safe Light Water Reactor (I^2S-LWR) project.

TABLE OF CONTENTS

LIST OF TABLES

LIST OF FIGURES

LIST OF SYMBOLS AND ABBREVIATIONS

Variables

a shorter rectangular length (m)

A area (m^2)

A_{cx} cross-sectional area (m^2)

A_r area ratio (-) [$A_r = nA_{cx,ch} / A_{cx,header}$]

b longer rectangular length (m)

Bd Bond number (-) [$\mathrm{Bd} = \Delta\rho g D_h^2 / \sigma$]

Bo boiling number (-) [$\mathrm{Bo} = q'' / \left(G i_{fg} \right)$]

Br Brinkman number (-) [$\mathrm{Br} = \left(\mu G^2 \right) / \left(\rho^2 q'' \right)$].

c_p heat capacity (J kg^{-1} K^{-1})

C_0 two-phase distribution coefficient (-) [Eq. (3.12)]

C_A Armand constant for void fraction (-) [Eq. (3.20)]

Ca capillary number (-) [$\mathrm{Ca} = \left(\mu_l G \right) / \left(\rho_l \sigma \right)$]

C_c contraction coefficient (-)

Co convection number (-) [$\mathrm{Co} = [(1-x)/x]^{0.8} (\rho_v / \rho_l)^{0.5}$]

D_o reference diameter (m) [Eq.(3.5)]

D_h hydraulic diameter (m) [$D_h = 4A_{cx} / p_{wall}$]

e_f specific flow exergy (J kg^{-1}) [$e_f = \left(h - h_0 \right) - T_0 \left(s - s_0 \right)$]

E two-phase convection enhancement factor (-)

$\dot{E}_d$ exergy destruction rate (W)

$\dot{E}_f$ total flow exergy (W) [$\dot{E}_f = e_f \dot{m}$]

f Darcy friction factor (-)

f_{Fanning} Fanning friction factor (-) [$f_{\text{Fanning}} = f / 4$]

fn function of [example: $\text{Nu} = \text{fn}\left(\text{Re}, \text{Pr}\right)$]

F Adams *et al.* (1998) microchannel enhancement factor (-)

F_{CHF} F-factor for non-uniform critical heat flux (-)

F_{dc} Shan and Siddiqui (2000) droplet contact enhancement factor (-)

F_{fl} fluid-surface parameter (-)

F_{PR} pressure correction factor (-)

Fr Froude number (-) [$\text{Fr} = G^2 / \left(\rho^2 g D_{\text{h}}\right)$]

g gravitational acceleration (m s^{-2}) [$g = 9.8$ m s^{-2}]

G mass flux (kg m^{-2} s^{-1})

Gz Graetz number (-) [$\text{Gz} = \text{Re}\,\text{Pr}\,D_{\text{h}} / l_{\text{ch}}$]

h heat transfer coefficient (W m^2 K^{-1})

h_{ch} channel height / radius of curvature (m)

i enthalpy (J kg^{-1})

i_{fg} enthalpy of vaporization (J kg^{-1})

I moment of inertia (m^3)

l length (m)

l_{fin} fin length (m)

l_{flat} flat length at channel bottom (m)

ID inner diameter (m)

P pressure (Pa)

P_{c} critical pressure (Pa)

P_r reduced pressure (-) [$P_r = P / P_c$]

p_{wall} wetted perimeter (m)

PDR Pitch-to-dimeter ratio (-) [$PDR = pitch / OD$]

Pr Prandtl number (-) [$\mathrm{Pr} = c_p \mu / k$]

k thermal conductivity (W m^{-1} K^{-1})

k_L pressure loss coefficient (-)

M molar mass (kg kmol^{-1})

M Maranzana number (-) [Eq. (3.7)]

m value used in fin efficiency calculation (m^{-1}) [Eq. (4.7)]

$\dot{m}$ mass flow rate (kg s^{-1})

n number of flow paths, number of segments, generic number (-)

$n_{ch,ps}$ number of channels per sheet (-)

n_{sheet} number for of sheets for each fluid per MCHX (-)

N_{con} confinement number (-) [$\mathrm{N}_{con} = \sqrt{\sigma / \left(g \Delta \rho D_h^2 \right)} = \mathrm{Bd}^{-1/2}$]

NTU number of transfer units (-)

Nu Nusselt number (-) [$\mathrm{Nu} = hD_h / k$]

OD outer dimeter (m)

$\dot{q}$ heat duty / heat transfer rate (W)

q'' heat flux (W m^{-2})

R thermal resistances (K W^{-1})

R'' thermal insulance (m^2 K W^{-1}) [$R'' = AR$]

Ra Rayleigh number (-)

Re Reynolds number (-) [$\mathrm{Re} = GD_h / \mu$]

S nucleate boiling suppression factor (-)

S_b bending stress (Pa)

S_m membrane stress (Pa)

S_t total stress (Pa)

Su Suratman number (-) [$\mathrm{Su} = \sigma\rho D_h / \mu^2$]

t thickness (m)

t_{fin} fin thickness (m)

t_{sheet} sheet thickness (m)

T temperature (°C)

T_s surface temperature (°C)

T_{wall} wall temperature (°C)

V velocity (m/s)

V_{gj} mean drift velocity (m s^{-1})

$\dot{w}$ rate of work transfer (w)

w_{ch} channel width (m) [$w_{ch} = 2h_{ch} + l_{flat}$]

We Weber number (-) [$\mathrm{We} = \left(G^2 D_h\right) / \left(\sigma\rho\right)$]

x quality (-)

x_a actual quality / non-equilibrium quality (-)

X Martinelli parameter (-) [Eq. (3.31)]

X_{tt} turbulent-turbulent Martinelli parameter (-)
[$X_{tt} = \left(\left(1-x\right)/x\right)^{0.9} \left(\rho_v / \rho_l\right)^{0.5} \left(\mu_l / \mu_v\right)^{0.1}$]

z axial channel length or length from channel inlet (m)

Greek symbols

α void fraction (-)

α_V coefficient of thermal expansion (K^{-1})

β volumetric quality (-) [Eq. (3.13)]

$\Delta\rho$ density difference (kg m^{-3}) [$\Delta\rho = \rho_l - \rho_v$]

ΔT_{lm} log mean temperature difference (°C)

ΔT_{sub} degree of subcooling at the boiling-loop inlet (°C)
[$\Delta T_{sub} = T_{sat}\left(P_{boil,in}\right) - T_{boil,in}$]

ΔT_{sup} degree of superheat between the hot-loop and boiling-loop inlets (°C)
[$\Delta T_{sup} = T_{hot,in} - T_{sat}\left(P_{boil,in}\right)$]

ε surface roughness (m)

ε_f effectiveness (-)

ε_m emissivity (-)

η_{fin} fin efficiency (-) [See Eq. (4.7)]

η_o overall surface efficiency (-) [For finned surface, See Eq. (4.7)]

η_p isentropic pump efficiency (-)

η_t isentropic turbine efficiency (-)

η_{th} thermal efficiency (-)

μ viscosity (kg m^{-1} s^{-1})

ν kinematic viscosity (m^2 s^{-1})

ρ density (kg m^{-3})

σ surface tension (N m^{-1})

σ_{sb} Stephan-Boltzmann constant (5.670×10^{-8} W m^{-2} K^{-4})

τ_{wall} wall shear stress (Pa)

φ two-phase multiplier (-)

Abbreviations

2FM	two-fluid model
AD	average deviation (%) [Eq. (3.16)]
AAD	absolute average deviation (%) [Eq. (3.15)]
B&W	Babcock and Wilcox
BS	boiling-side
BWR	boiling water reactor
CFWH	closed feedwater heater
CS	cold-side
CVCS	chemical volume control system
DBA	design basis accident
DFM	drift flux model
DHRS	decay heat removal system
ECCS	emergency core cooling system
EES	Engineering Equation Solver
HEM	homogenous equilibrium model
HP	high pressure
HS	hot-side
HX	heat exchanger
IP	intermediate pressure
I^2S-LWR	Integral Inherently Safe Light Water Reactor
IRIS	International Reactor Innovative and Secure
LOCA	loss of coolant accident
LP	low pressure
LWR	light water reactor
MCHX	microchannel heat exchanger

OFWH	Open feedwater heater
PCCS	passive containment cooling system
PCM	photo-chemical machining
PRCCS	passive reactor cavity cooling system
PWR	pressurized water reactor
RCS	reactor cooling system (primary coolant loop)
RH	reheater
RPM	rotations per minute
RPV	reactor pressure vessel
SMR	small-to-medium reactor
STSL	Sustainable Thermal Systems Laboratory
SS	stainless steel
TBHX	tube-bundle heat exchanger
VFD	variable frequency drive

Subscripts

0	property of the surroundings (exergy analysis)
a	acceleration
amb	ambient
avg	average
boil	boiling fluid or secondary coolant (liquid-boiling MCHX)
bottom	bottom half of channel or bottom resistance path
c	circular cross-section
ch	channel
cold	cold fluid or secondary coolant (liquid-liquid MCHX)
de	dryout completion

di	dryout initiation
e	electric (Megawatts electric MW_e)
f	fluid (liquid, vapor, or two-phase mixture)
fin	fin property
foul	fouling
fr	frictional
FC	forced convection
g	gravitational
Gn	Gnielinski (1976) correlation
header	header property
hot	hot fluid or primary coolant
HEM	homogenous equilibrium model
in	inlet
inactive	inactive length at both end of test section
l	liquid – value calculated as if only liquid were present [example: $\mathrm{Re}_l = G(1-x)D_h/\mu_l$]
la	larger cross-sectional area
lo	liquid only – value calculated as if entire two-phase mixture were in the liquid phase [example: $\mathrm{Re}_{lo} = GD_h/\mu_l$]
parallel	parallel resistance path
pipe	pipe property
m	minor loss
nu	non-uniform heat flux
NB	nucleate boiling
NC	natural convection
out	outlet

pool	pool boiling
rad	radiation
sat	saturated property
seg	control-volume segment
sm	smaller cross-sectional area
th	thermal (megawatts thermal, MW_{th})
top	top half of channel or top resistance path
total	total or total surface area
tp	two-phase
tt	liquid turbulent – vapor turbulent
tv	liquid turbulent – vapor viscous
TS	test section
u	uniform heat flux
vv	liquid viscous – vapor viscous
vt	liquid viscous – vapor turbulent
v	vapor – value calculated as if only vapor were present [example: $\mathrm{Re}_v = GxD_h/\mu_v$]
vo	vapor only – value calculated as if entire two-phase mixture were in the vapor phase [example: $\mathrm{Re}_{vo} = GD_h/\mu_v$]
wall	wall or sheet material between channels

SUMMARY

The Integral Inherently Safe Light Water Reactor (I^2S-LWR) is a large (2850 MW_{th}) pressurized water reactor that includes primary-to-secondary coolant heat exchangers located in the downcomer of the reactor pressure vessel. This integral configuration, which is often reserved for lower power reactors, eliminates the possibility of large line-break accidents, reduces primary coolant inventory, and does not require large external steam generators. A microchannel heat exchanger (MCHX) configuration is selected to meet the limited volume and high heat duty requirements of this design. The steady-state thermal-hydraulic performance of a liquid-liquid and liquid-boiling (steam generating) MCHX are modeled using empirical correlations from the literature and the designs are optimized to meet the I^2S-LWR requirements. A test facility and a representative MCHX test section were constructed to validate the assumptions and modeling techniques used in the I^2S-LWR MCHX design. Experimental heat duty and pressure drop are compared with model predictions. In addition, Nusselt numbers, friction factors, and other parameters are extracted from the data and compared with correlations from the literature when possible.

CHAPTER 1. INTRODUCTION

This chapter provides background on the current state of nuclear power plant design, the Integral Inherently Safe Light Water Reactor (I^2S-LWR), steam generator design, and microchannel heat exchangers (MCHXs). It also describes the objectives and motivations of this investigation. Finally, an outline of this dissertation is included at the end.

1.1 Current State of Nuclear Energy and Reactor Design

In 2017, 20% of electricity in the United States was generated using nuclear energy, representing roughly 54% of the carbon-free electricity generation (EIA, 2018a). With dire predictions about the impact of burning fossil fuel from the United Nations Intergovernmental Panel on Climate Change (IPCC, 2018), the role of nuclear energy as a steady carbon-free power source is more critical than ever. However, Haratyk (2017) found that 18 of the 102 Gigawatts of installed U.S. nuclear capacity are in danger of early retirement in the next two years because of the growth of negative demand and competition from cheap natural gas. He also found that 58 Gigawatts of capacity may become unprofitable in the coming years. The U.S. Energy Information Administration estimates the levelized cost of advanced nuclear plants entering service in 2022 to be \$99.1 MWh^{-1} as compared to \$57.3 MWh^{-1} for natural gas combined cycle plants (EIA, 2018b). Therefore, retiring nuclear plants will likely be replaced with natural gas combined cycles due to economic conditions. Haratyk (2017) estimates the replacement of 20 Gigawatts of nuclear capacity with combined cycle plants would result in an increase in carbon emissions from the power sector by 3.2-3.7%. The recent construction of four

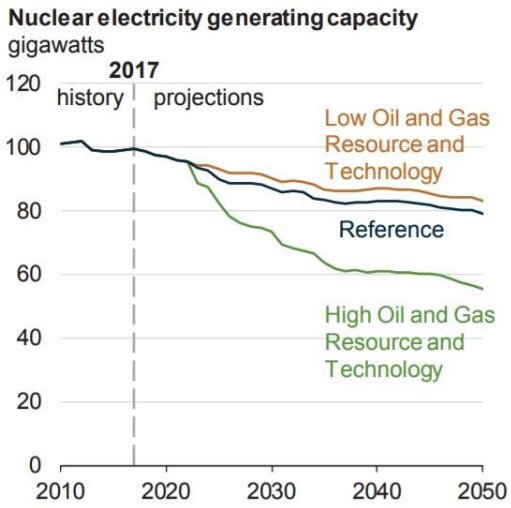

Figure 1.1 Projected U.S. nuclear electrical generation capacity (EIA, 2018a)

Westinghouse AP1000 pressurized water reactors (PWRs), the first new U.S. reactor construction projects in more than twenty years, has been plagued with cost overruns and delays, despite the AP1000 being advertised as a simplified design with fewer pumps, valves, instrumentation, and piping than earlier third-generation PWRs. These resulted in the bankruptcy of Westinghouse in March of 2017 and the abandonment of two of the partially constructed AP1000 projects at the Virgil C. Summer Nuclear Station in July of the same year. In September of 2018, stakeholders in the remaining two AP1000 projects at the Alvin W. Vogtle Nuclear Station voted to continue construction even though the project was five years behind schedule and thirteen billion dollars over budget. These trends are captured in the Energy Information Agency outlook for U.S. nuclear capacity shown in Figure 1.1.

Additionally, the failure of backup cooling systems and subsequent meltdowns of three boiling water reactors (BWRs) following a 2011 tsunami in Fukushima, Japan has raised questions about the safety of nuclear plants and undermined public confidence.

These events showed that scenarios outside of strict design-basis accident (DBAs) must be considered if similar disasters are to be avoided. Design-basis accidents are scenarios that nuclear plants are designed to withstand without the loss of systems, structures, and components necessary to ensure public health and safety (U.S. NRC, 2018). Therefore, future nuclear plant designs must not only be cheaper and simpler to construct, but must also be robust enough to survive extraordinary and unexpected situations. Fourth-generation nuclear plants offer innovative coolant/moderator combinations, improved fuel lifecycles, higher electrical generation efficiency, increased safety, and potentially cheaper/simpler designs (Behar, 2014). However, these plants are generally still in the design phase and face technical and regulatory hurdles before they can be considered as viable, carbon-free, base-load power options. As a result, there is still considerable interest in improved light water reactors, beyond current generation III+ designs. Such designs leverage existing technical and regulatory expertise with light water reactor technology while challenging the paradigms that have led to the expense and safety concerns of present reactors.

The reexamination of reactor design requires a short review of existing systems. The reactor coolant system (RCS, or primary coolant loop) of a Westinghouse AP1000 is representative of many loop-type PWR designs and is shown in Figure 1.2. The reactor pressure vessel (RPV) contains the core and nuclear fuel, which transfers heat to the primary coolant. The coolant then flows through the hot-leg piping into two large, external steam generators. Here, the primary coolant exchanges heat with lower-temperature, lower-pressure water known as the secondary coolant. The secondary coolant exits the steam generator as saturated steam and is the working fluid in a Rankine power cycle. The

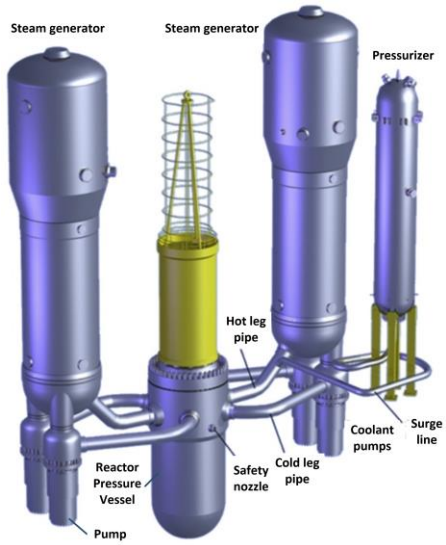

Figure 1.2: AP1000 reactor cooling system (Namgung and Giang, 2016)

primary coolant is then pumped back into the RPV through four cold-leg pipes to repeat the process. The pressurizer, attached to one of the two hot-leg pipes, controls the pressure of the RCS and ensures the coolant remains subcooled as it is heated in the core. To accomplish this, the primary coolant in the pressurizer is heated to saturated conditions and steam occupies the top portion of the vessel. The pressure in the RCS can then be increased or decreased by heating or cooling the fluid in the pressurizer, respectively. The steam in the pressurizer also provides a surge volume for the subcooled primary coolant in the RCS to expand as reactor power and temperature increase.

There are several important characteristics of this loop-type PWR design that lead to high costs and safety concerns. First, the large and unique pressure vessels (RPV, steam generators, and pressurizer) require expensive forging. Only five manufacturers worldwide have forges capable of making these large components for the AP1000 (World Nuclear Association, 2018b), none of which have facilities located in North America. Secondly, if any section of the RCS is punctured or ruptures, the high-pressure primary coolant will

escape and flash to steam. Without sufficient water in the RCS to cool the core, the fuel can overheat, leading to a hydrogen gas explosion or meltdown. A large line-break loss-of-coolant-accident (LOCA) is a DBA in which a hot-leg or cold-leg between the RPV and steam generator is severed. The Emergency Core Cooling System (ECCS), which includes cooling water injection systems, is sized based on these LOCA scenarios to provide water to cool the fuel and limit the increase in fuel cladding temperature. This prevents metal-water reactions which result in the oxidation of fuel cladding and generation of hydrogen gas. In the event of a LOCA, the reactor containment building, simply referred to as the containment, prevents the escape of the expanding coolant and serves as the final barrier in preventing the release of radiation to the public. PWR containments are made of steel or steel-lined reinforced concrete and form a cylindrical or hemispherical vessel. The containment encloses the entire RCS and parts of the emergency systems such as the ECCS. The size of the containment is dictated by the maximum pressure that would be observed during a LOCA, which is dependent on the primary coolant inventory of the RCS. A typical PWR containment building is designed to contain a pressure of 4.46 bar and has an inside diameter of 37.8 m, height of 62.5 m, and an internal free volume of approximately 56,000 m^2 (Testa and Kunkle, 1984). The RCS, containment, and associated safety systems make up a significant portion of the nuclear island (portion of the plant that is specific to a nuclear power plant). Components and construction of the nuclear island constitute approximately 28% of the total cost of a nuclear power plant and are a driving factor in other costs such as project management and site development (World Nuclear Association, 2018a). In loop-type PWR designs, the control rod drive mechanisms (CRDMs) protrude above the RPV head in tubular housings that are extensions of the RPV. The failure of one of these

housings results in a large differential pressure that drives CRDM out of the RPV and associated control rods out of the core. This DBA is called a rod ejection accident, which causes a surge in reactor power and fuel temperature. After shutdown, decaying fission products in the fuel continue to produce heat, referred to as decay heat or residual heat. Earlier PWR and BWR designs relied on actively powered and controlled cooling systems to remove decay heat and prevent the core from overheating during emergency situations. In the event that electricity is not available (station blackout), backup generators are used to power these systems. However, the events at Fukushima, in which offsite electricity was not available and backup generators were flooded, showed the inherent flaw in such "active" systems. Generation III+ reactor designs, such as the AP1000, employ "passive" systems driven by gravity, gas pressure, and natural convection for emergency cooling.

1.2 Integral Pressurized Water Reactors

Integral PWR designs address these financial and safety concerns by placing the entire RCS inside the RPV (Reyes and Lorenzini, 2010; Petrovic *et al.*, 2012; Memmott *et al.*, 2017a). The elimination of the external steam generators and pressurizer reduces the number of large, expensive pressure vessels and decreases the primary coolant inventory. As a result, the containment, which houses the RCS and must contain expanding coolant in the event of a LOCA, can be substantially reduced in volume and economically constructed for higher pressure operation. In the case of a LOCA, the smaller volume results in quicker pressure equalization between the RCS and containment, reducing coolant loss from the RCS. Once equilibrium occurs, the higher pressure ensures that sufficient coolant remains in the liquid state to cover the core and provide cooling. A natural-circulation path can be established in which water is boiled in or on the RPV and

condensed on containment walls or an emergency heat exchanger, providing a passive means of decay heat removal. The smaller containment and nuclear island can be seismically isolated at less expense than loop-type PWR designs. Sections of the nuclear island can also be located below ground, reducing the risk from external threats such as an airplane collision. The primary coolant never leaves the RPV in the integral configuration. Instead, the secondary coolant is pumped into the RPV and internal steam generator. This eliminates the possibility of a large line-break LOCA, although smaller LOCAs can still occur. The removal of this accident scenario and the high-pressure containment design reduces requirements on emergency systems such as the ECCS, or allows them to be removed altogether. Finally, CRDMs can be located entirely inside the RPV above the core, eliminating the potential for a rod ejection accident. Therefore, integral PWR designs preclude some DBAs and allow for the development of simplified passive safety systems. The smaller size and elimination of components/systems also provides an economic incentive for such designs.

As previously discussed, the size of the RPV is limited by forging capabilities and therefore should not exceed the size of the current largest PWRs based on both economic and technical considerations. The 1400 MW_e European Pressurized Water Reactor (EPR-1400) represents one of the largest RPVs to date and is approximately 5 meters in diameter (Tanaka and Sato, 2011; Memmott *et al.*, 2017a). Thus, the primary engineering challenge of integral PWR designs is fitting the RCS and other components into the RPV. This includes the core, steam generators, pressurizer, and primary coolant pumps. The smaller coolant inventory allows the pressurizer volume to be reduced as less expansion volume is required during heat-up transients. Coolant pumps must be both compact and able to

operate under high temperatures and high external pressures. Alternatively, the primary coolant can be driven by natural convection in the RPV. However, the flow rate of coolant across the core is likely less than that of pump-driven designs, decreasing heat removal. The steam generators, each larger than the RPV in loop-type PWR designs, represent a unique challenge and are the subject of this investigation. In integral reactor designs, they are often located in the annulus between the core barrel and inside diameter of the RPV, known as the downcomer. Limited RPV volume generally results in a smaller core. The power density of the core can be increased to match the overall power of loop-type PWRs, although this results in higher fuel temperatures and decreased thermal margin (such as overpower to fuel melt). As a result of the decreased core size and limited heat exchanger capacity, integral PWR designs typically operate at a lower power than loop-type PWR designs (Petrovic, 2014).

An example of an integral PWR design is the 350 MW_e International Reactor Innovative and Safe (IRIS) (Petrovic *et al.*, 2012), shown in Figure 1.3. The primary coolant flows up through the core and core barrel. Eight axial spool pumps then drive the primary coolant through steam generators located in the downcomer. These pumps, which use high temperature bearing and winding materials, are located entirely in the RPV and only require small penetrations for power cables. The pressurizer is integrated into the head of the RPV. The spherical high-pressure containment of the IRIS design is capable of passive, long-term heat rejection in the event of a small/medium line-break LOCA. The small high-pressure containment also ensures that the core remains covered throughout accident transients and safety cooling water injection systems are not required. Drawbacks

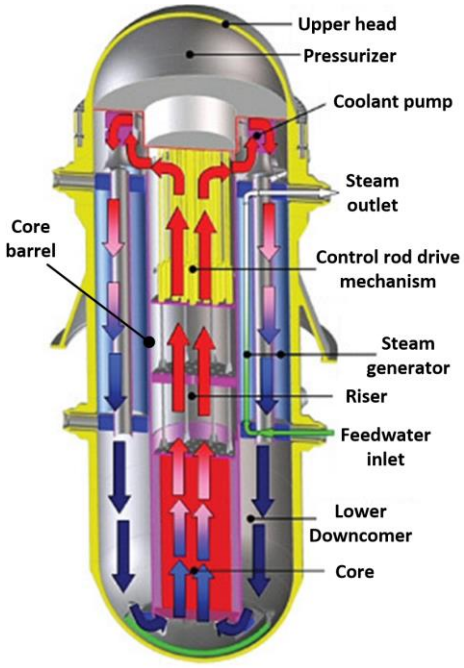

Figure 1.3 IRIS pressure vessel (Petrovic *et al.*, 2012)

of the design include a large RPV (6.21 m inner diameter) and decreased power compared to loop-type PWR designs.

The International Atomic Energy Agency defines small reactors as those producing less than 300 MW_e, and medium reactors as those producing less than 700 MW_e. These often take advantage of the improved safety and simplification of an integral design while also adopting a modular mass-production approach to reduce construction cost and time. Carelli *et al.* (2010) performed an economic analysis of small-to-medium reactors (SMRs) and made the following observations. The size and cost of SMRs open new markets for nuclear energy where the capacity and expense of large reactor projects are not practical. Additionally, many SMRs at a single nuclear plant could match the output of a larger reactor, creating a demand for a large number of units. Factory fabrications could then be employed to produce uniform modules and components, replacing expensive site fabrication and achieving economies-of-production. Finally, standardization and the

quantity of SMRs produced will allow best practices and cost reductions from learned-economies to develop quickly. However, these advantages must be weighed against economies of scale. Capital costs (i.e., the cost of initial construction) and operation/maintenance costs tend to decrease on a per unit electricity output basis as the size of a plant increases. Economies of scale may also result from the lower thermal efficiency of smaller plants and unique set-up costs such as licensing. These trends are reflected in the continued increase in the size and power of commercial LWR designs. The results of the analyses by Carelli *et al.* (2010) showed that SMRs and larger reactors were equivalent when competing in traditional nuclear markets. They did, however, note that a comparison on a consistent basis was difficult due to the innovative features of SMRs and that additional investigation was required.

Small reactors specifically designed for modular assembly-line production are referred to as small modular reactors. NuScale is developing a 60 MW_e small modular reactor designed to take advantage of this approach (Reyes and Lorenzini, 2010), shown in Figure 1.4. The primary coolant is driven by natural convection, eliminating the need for pumps. The primary coolant loop itself is similar to that of the IRIS design, with hot coolant from the core rising through the core barrel and being cooled by the steam generator in the downcomer. A small high-pressure containment (3.8 MPa) surrounds the RPV and the entire structure is located in a pool. In accident scenarios requiring decay heat removal in which the steam generators are not available, the primary coolant can be purposely vented to the containment, creating a natural-circulation heat-removal path between the core and pool. This innovative design essentially transforms a LOCA into a passive decay heat removal system. One should note that although the power is small, the NuScale RPV is

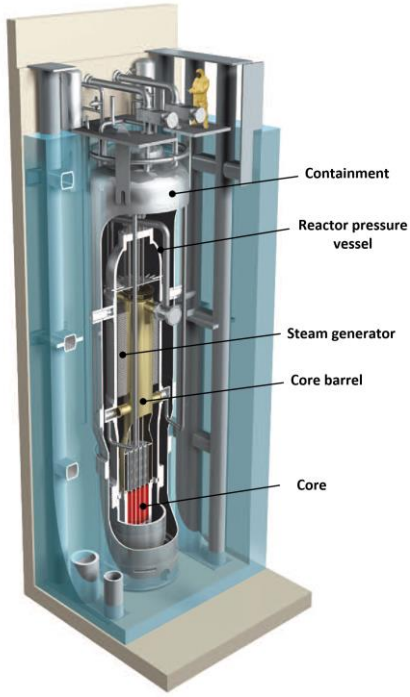

Figure 1.4: NuScale small modular reactor (Reyes and Lorenzini, 2010)

comparable to those of higher power PWRs. It stands 13.42 m tall and has a diameter of 2.74 m as compared to an AP1000 RPV with a height of 12 m and dimeter of 4.03 m. Each NuScale reactor also has an 18.3 m high, 4.6 m diameter containment pressure vessel and individual balance of plant components (turbine, condenser, generator, etc.). It would also require more than twenty of these reactors to match the 1250 MW_e of a single AP1000. Therefore, the NuScale design will need to achieve significant economies of production to compete with the economies of scale embraced by larger PWR designs.

1.3 Integral Inherently Safe Light Water Reactor

The Integral Inherently Safe Light Water Reactor (I^2S-LWR) is a design being developed by a team of international researchers led by Georgia Tech (Petrovic *et al.*, 2017b). The goal of the I^2S-LWR concept is to develop a large (~1000 MW_e) PWR with

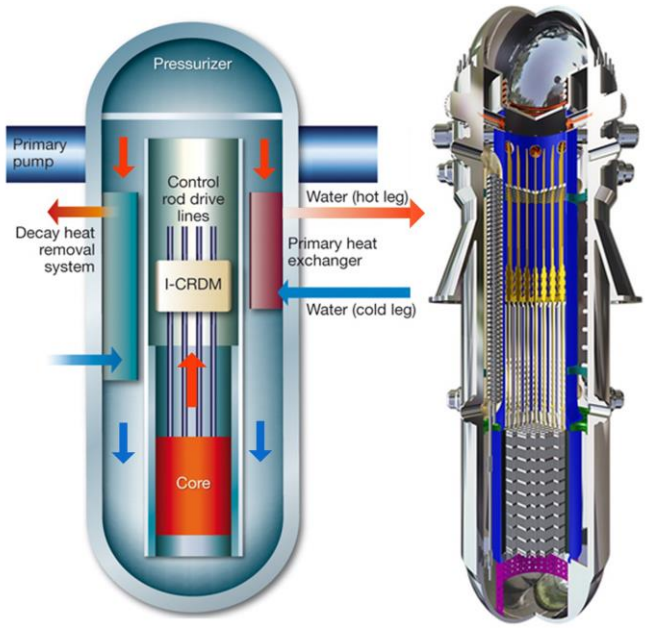

Figure 1.5: I^{2}S-LWR pressure vessel (Petrovic *et al.*, 2017a)

improved safety and economics beyond generation III+ designs. To accomplish this, the I^{2}S-LWR design takes advantage of an integral configuration while also maintaining economies of scale. This requires compact primary-to-secondary heat exchangers different from the steam generators in other large PWR designs. Figure 1.5 shows a schematic and model of the I^{2}S-LWR. The design includes an integral CRDM and a pressurizer integrated into the RPV head. The primary coolant flow path is again similar to that of the previously discussed IRIS design. Primary-to-secondary and decay heat removal heat exchangers share space in the downcomer. The primary-to-secondary heat exchangers employ a novel microchannel design discussed in more detail in the following chapter. The following two subsections discuss some of the other important aspects of the I^{2}S-LWR design. A more detailed explanation of these and other aspects of the design is given in the I^{2}S-LWR final report (Petrovic *et al.*, 2017a).

1.3.1 I^{2}S-LWR high power density core

The volumetric constraints of the integral design require a higher power density core to meet the power output goals of the I^2S-LWR design. By developing fuel materials with higher thermal conductivity, the power density of the core can be increased while still providing an acceptable thermal margin. Specific aspects of the thermal margin that were examined included overpowering to fuel melt, departure from nucleate boiling (DNB), and subchannel void fraction. Additionally, fuels with a higher density of uranium (heavy metal density), will allow the core to operate at a higher power without higher uranium enrichment requirements or increased refueling frequency. New cladding materials can also limit water-cladding oxidation reactions and generation of explosive hydrogen in accident scenarios. Therefore, stainless steel and silicon carbide (SiC) are being examined to replace traditional zirconium-based cladding, and uranium silicide (U_3Si_2) is being considered to replace uranium oxide (UO_2) fuels. To conserve space, the reactor coolant pumps are attached to the RPV with motors external to the vessel and hydraulic components inside. The casing around the seal-less centrifugal pumps then acts as the pressure boundary (Memmott *et al.*, 2017a). Typical PWR reactor pumps incorporate a flywheel to provide an extended coast down in a complete loss of flow accident (CLOFA). Weight and size limitations of mounting the coolant pumps to the RPV make this impossible in the I^2S-LWR design, resulting in a faster decrease in coolant flow rate through the core in CLOFA. Therefore, CLOFA and steady-state conditions were used to determine the thermal margin of the high power density core. It should be noted that a higher primary coolant core outlet temperature allows for higher plant thermal efficiency, but comes at the cost of decreased heat removal and thermal margin. Additionally, high coolant velocity can lead to flow-induced vibrations and increased cladding fretting wear.

Coolant velocities were therefore kept to values similar to those in existing reactors. With these considerations, core power and primary coolant conditions (i.e., temperatures, pressures, and flow rates) were determined in conjunction with the design of fuel assemblies.

1.3.2 I^2S-LWR containment and safety systems

I^2S-LWR safety systems are designed to provide indefinite passive cooling following DBAs using the atmosphere as the ultimate heat sink. Four decay heat removal system (DHRS) helical-coil heat exchangers are located in the downcomer of the RPV. These draw primary coolant into the coils at core height through natural circulation. Heat is removed from the primary coolant by high-pressure water from an intermediate loop on the shell side of the helical-coil heat exchangers. The intermediate loop, which is also driven by natural circulation, rejects heat to the air in a dedicated dry cooling tower. The DHRS consists of four independent trains and it has been shown that three of the four are capable of long-term decay heat removal following a station blackout (Wang *et al.*, 2015).

The I^2S-LWR cylindrical containment has a height of 40 m and diameter of 22 m and is designed for pressures up to 0.91 MPa (Wang *et al.*, 2018). It is both smaller and has a higher operating pressure than loop-type PWR designs and incorporates several passive safety systems. In the event of a LOCA, the pressure between the RPV and containment is quickly equalized because of the higher pressure containment and an automated depressurization system. Water is then fed into the RPV from elevated and pressurized tanks, ensuring that the core remains covered throughout the accident transient. The escaping steam is condensed by a heat exchanger located at the top of the containment

as part of the passive containment cooling systems (PCCS). The condensed coolant collects in the reactor cavity around the RPV. Emergency valves allow the accumulating condensate to be fed into the RPV by gravity. Condensate in the reactor cavity is cooled by a heat exchanger, which is part of the passive reactor cavity cooling system (PRCCS). Both the PCCS and PRCCS operate in a manner similar to the DHR, with a passive intermediate loop rejecting heat to the atmosphere in a dry cooling tower. The three systems (PCCS, PRCCS, and DHRS) allow for the indefinite removal of decay heat from the reactor following a LOCA.

1.4 Microchannel Heat Exchanger Background

Microchannel heat exchangers (MCHXs) can be manufactured by bonding metal sheets with small hydraulic diameter channels etched into their surfaces. Small, semi-circular channels and other features are created using a photo-chemical etching technique. Alternating sheets, carrying the two fluids, are then diffusion bonded to create a high-strength heat exchanger with a large surface-area-to-component volume ratio. The small hydraulic diameters of the channels result in high heat transfer coefficients and a large number of channels per sheet. This allows for large surface areas and heat duties in relatively small volumes, ideal for the requirements of the I^2S-LWR design. Additionally, small channel dimensions and relatively thick surrounding sheet material allow MCHXs to operate at high pressures. Le Pierres *et al.* (2011) suggest treating MCHXs as rectangular plate-stayed pressure vessels and applying Section VIII Division I Mandatory Appendix XIII of the ASME Boiler and Pressure Vessel Code for their design. The sheet thickness and dimensions between channels, with the minimum wall material thermal resistance between fluids, can then be determined for the required application pressure. One

Figure 1.6 MCHX and shell-and-tube comparison (Bowdery, 2006)

commercial vendor of such heat exchangers, Heatric, has over 2700 MCHX units in operation across the world (Heatric, 2015). Their small sizes reduce installation and capital costs. Additionally, they are often used in offshore oil and gas platforms, where the compact size and weight is an economic advantage compared to larger, conventional heat exchangers. MCHX designs have also been shown to be robust in the presence of thermal stresses. Heatric claims that the MCHX designs have operated successfully for up to thirty years with multiple daily start-ups/shutdowns and temperature differences between fluids of up to 222°C (Bowdery, 2006). An MCHX design with an equivalent duty shell-and-tube heat exchanger is shown in Figure 1.6.

Li *et al.* (2009) identified supercritical CO_2 cycles and nuclear power as potential markets for MCHXs because of the high temperature and pressure ranges in which they can operate. They claim that 316 stainless steel (SS) is suitable for temperatures up to 550°C while Inconel® alloy 617 may be used in MCHXs with operating temperatures in excess of 900°C. MCHX designs have also been investigated for miniaturized thermal systems including the cooling of electric devices/processors (Phillips, 1988) and miniaturized absorption heat pumps (Determan and Garimella, 2012). An example of

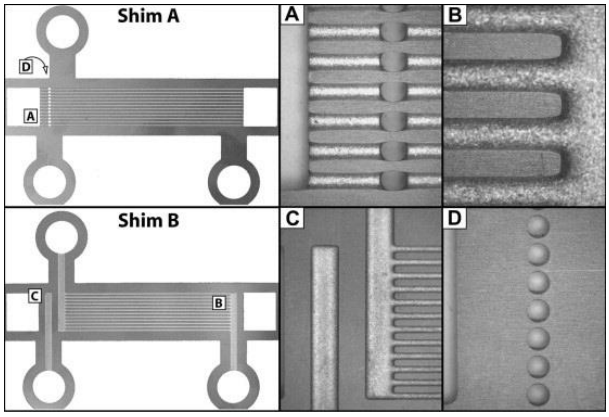

Figure 1.7: Monolithic microchannel heat pump sheet example (Determan and Garimella, 2012)

sheets/shims developed for a miniaturized absorption system by Determan and Garimella is shown in Figure 1.7.

1.5 Previous Steam Generators Designs

In many PWR designs, two to six large recirculating steam generators are often employed in which the secondary coolant is boiled on shell-side and primary coolant flows through internal U-tubes, allowing the primary coolant to enter and exit at the bottom of the vessel. These may be as high as 22.3 m tall, weigh as much as 790 short tons, and contain up to 8,523 U-tubes. At the top of the tube bundle, the secondary coolant has a quality (fraction of water in the vapor phase) between 0.10 and 0.40 (Steam, 2005). The low quality at the outlet results in an efficient nucleate boiling heat transfer regime over the entire length of the steam generator. The saturated liquid is recirculated along the side of the steam generator and is mixed with the incoming feedwater (secondary coolant). Internal moisture separators at the top of the vessel are then used to ensure high-quality saturated steam for power generation. The secondary coolant inventory in recirculating

steam generators has significant thermal mass to continue to provide cooling if feedwater flow stops.

Once-through steam generator designs have dimensions similar to those of recirculating steam generators and use a counterflow tube bundle design. The primary coolant enters the top of the vessel on the tube side and exits at the bottom. Secondary coolant makes a single pass on the shell side and exits as a superheated vapor, eliminating the need for moisture separators. There are no baffles on the shell side of the heat exchanger. Heat transfer on the secondary side is governed by several regimes including liquid convection (in the integrated economizer design), nucleate boiling, film boiling/post-dryout, and vapor convection (Steam, 2005). The degree of superheating is limited by the temperature of the primary coolant and approximately 40% of the tube length is required for the less-efficient post-dryout and superheated vapor regimes.

Tubular once-through steam generator designs have been proposed for several integral PWR designs. The IRIS design proposed eight helical-coil steam generators situated in the downcomer (Cioncolini *et al.*, 2003). Other designs include the safe integral reactor with twelve tube bundle heat exchangers without baffles on the shell side (Kuridan and Beynon, 1997), and the NuScale small modular reactor in which steam generator coils are wrapped around the central core barrel in the downcomer (Williams *et al.*, 2014). These tubular steam generator designs have generally been developed for small reactors with lower power than the I^2S-LWR and require a large number of relatively thick tubes. Therefore, the MCHX design was selected based on the simplicity of fabrication and advantages in both strength and power density. However, the design and performance of a tube bundle heat exchanger for the I^2S-LWR design is discussed in Appendix A.

1.6 Research Objectives

The primary objective of this investigation is to design and validate a primary-to-secondary heat exchanger for the proposed I^2S-LWR, which must meet several unique design constraints. Two MCHX solutions have been identified. The first is a liquid-liquid design, in which both primary and secondary coolants remain subcooled in the MCHX. This design is coupled with a flash Rankine cycle, which generates saturated steam from the secondary coolant. The second is a liquid-boiling design in which the MCHX acts as a steam generator and produces saturated or superheated vapor secondary coolant that may be utilized in a conventional nuclear Rankine cycle. Models for the two MCHX designs are developed to determine their feasibility in meeting the design requirements. Secondary coolant conditions from these models are utilized with thermodynamic balance-of-plant models to determine the thermal efficiency of the plant, and thus, the practicality of the design. Modeling techniques and experimental results of this investigation may also be used to guide MCHX designs for a variety of other applications.

The experimental component of the investigation is used to assess the thermal-hydraulic model of the MCHX. A liquid-liquid test facility and MCHX test section with channel dimensions similar to those in the I^2S-LWR design was fabricated. While the test facility could not simulate the extreme temperatures and pressures of the reactor, fluid conditions were tested over a wide range of Reynolds numbers, including the conditions similar to the I^2S-MCHX design. The modeling approach applied to the I^2S-LWR MCHX design was also applied to the representative test section, and results were compared with the measured performance. The average Nusselt number and friction factor in the heat exchanger channels were also calculated from a specific subset of experiments and

compared with the predictions of correlations used in the model. The test facility was then modified so that liquid-boiling tests could be conducted. Temperature and pressure limits of the test facility make it impossible to match all I^2S-LWR MCHX dimensionless numbers that govern two-phase flow and boiling heat transfer. However, the dimensionless parameters based on fluid properties and geometry were matched well, and experimental results helped determine the accuracy of the overall model. Tests designed to investigate subcooled boiling, saturated boiling, and dryout heat transfer regimes were also performed to provide further insight into the boiling process.

1.7 Organization of Thesis

The remainder of this thesis is organized as follows:

- Chapter 2 discusses the layout and requirements of the I^2S-LWR MCHX design. An explanation of the two MCHX designs, liquid-liquid and liquid-boiling, is also included.
- Chapter 3 reviews heat transfer and pressure drop correlations for two-phase and single-phase internal flows. Special emphasis is placed on microchannels and the different heat transfer regimes encountered over the length of a once-through steam generator. Additionally, modeling techniques for nuclear steam generators are reviewed and specific issues such as fouling, flow instabilities, and maldistribution are addressed.
- Chapter 4 discusses the modeling and performance of the liquid-liquid MCHX design. Parametric studies and the optimization process used to arrive at the finalized design are discussed.

- Chapter 5 describes the experimental facility, test section, and analysis used to validate the liquid-liquid MCHX design technique. Comparisons between the model predictions and experimental results for heat duty and pressure drop are presented. The Nusselt number and friction factor are also deduced from a subset of the data and compared with the predictions of the correlations.
- Chapter 6 discusses the modeling and performance of the liquid-boiling MCHX design (steam generator). This chapter also includes the design of an accompanying nuclear Rankine cycle.
- Chapter 7 describes the modified experimental facility and analysis used to validate liquid-boiling MCHX design techniques. Comparisons between the model predictions and experimental results for heat duty and pressure drop are discussed. Additionally, specific tests were performed to investigate specific regimes including subcooled boiling, saturated boiling, and dryout.
- Chapter 8 includes conclusions and key results of this investigation. Finally, some recommendations for future work and potential concerns in the development of the MCHX design for the I^2S-LWR are presented.
- Appendix A discusses an alternative tube-bundle heat exchanger design for the I^2S-LWR. The performance of this heat exchanger is compared with that of the liquid-liquid and liquid-boiling MCHX.
- Appendix B contains a discussion about boundary conditions for the liquid-boiling MCHX model. A brief cost estimate of MCHX blocks, and a comparison with a conventional steam generators is also included.
- Appendix C includes selected sample calculations.

CHAPTER 2. I^{2}S-LWR PRIMARY-TO-SECONDARY MICROCHANNEL HEAT EXCHANGER

This chapter describes the design requirements and layout of the I^{2}S-LWR MCHX design. It also discusses two alternative power generation schemes and designs for the MCHX. Additionally, an alternative tubular design, used for comparison, is discussed.

2.1 I^{2}S-LWR Primary-to-Secondary Heat Exchanger Requirements

High-level design goals for the I^{2}S-LWR are presented in Petrovic *et al.* (2017b) and establish the drivers for the primary-to-secondary heat exchanger requirements. These include limiting the RPV to dimensions of the largest PWRs, generating electrical power in excess of 910 MW_e, and the passive removal of decay heat through dedicated DHRS heat exchangers. Core thermal margin and integral primary coolant pump characteristics were used to determine primary coolant conditions and core power as discussed in Section 1.3.1. A list of primary-to-secondary heat exchanger design requirements is provided below:

1. Size/Volume:

The heat exchangers must fit in the downcomer region between the OD of the core barrel (300 cm) and the ID of the RPV (490 cm) with a maximum height of seven meters. The MCHXs also shares the downcomer with four helical-coil DHRS heat exchangers. A cross-section of the I^{2}S-LWR RPV with relevant dimensions is shown in Figure 2.1.

2. Heat duty:

The heat exchangers must remove 2850 MW_{th} with primary coolant entering at 330°C, 16.3 MPa, and a flow rate of 15,498 kg s^{-1}.

3. Plant thermal efficiency:

A 32% thermal efficiency (generating > 910 MW_e) was determined to be the minimum for the I^2S-LWR design to be economically competitive with existing nuclear plants. The secondary coolant is the working fluid in the plant Rankine cycle. Therefore, secondary coolant conditions exiting the MCHXs must yield efficient power generation (i.e., a high secondary coolant outlet temperature and pressure is required).

4. Pressure drop:

Eight centrifugal pumps, situated above the MCHXs inside the RPV, provide the driving force for the primary coolant. Pump design and sizing indicates that primary coolant frictional pressure drop across the MCHX should not exceed 500 kPa. Secondary coolant pumps are located outside the RPV and are not under the same design constraints, but required power constitutes a parasitic loss on net electricity production.

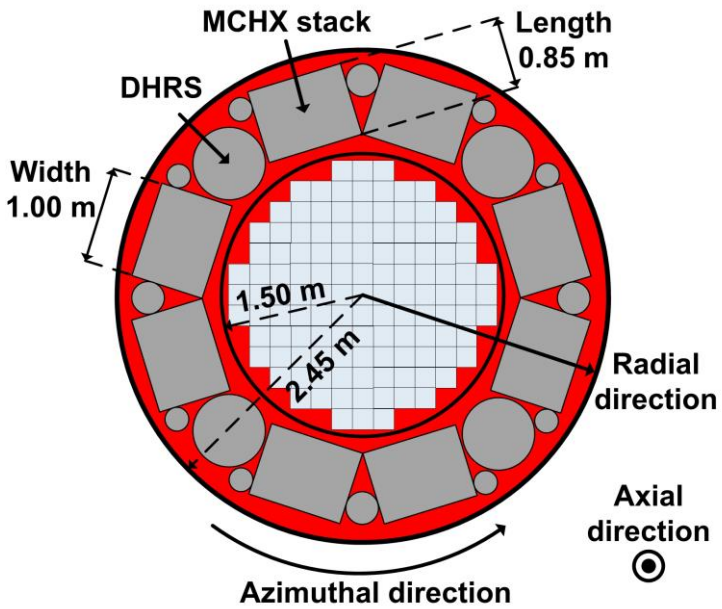

Figure 2.1: I^2S-LWR RPV cross-section

5. Mechanical integrity:

The heat exchanger must be designed such that the complete loss of pressure of either coolant stream will not result in a mechanical failure. This pressure vessel requirement sets a lower bound for channel dimensions and thicknesses between coolant streams.

2.2 I²S-LWR Microchannel Heat Exchanger Geometry and Layout

A photo-chemical etching technique (sometimes called photo-chemical machining or PCM) is used to create features in stainless steel sheets that make up the MCHX. In this technique, a photoresist film and mask are applied to the sheets. The photoresist film is activated by UV light, creating a barrier that resists the etchant. Film underneath opaque sections of the mask is not activated, leaving the surface underneath unprotected. An acidic solution of ferric chloride is then used to dissolve the exposed sheet and inactivated film, creating the desired features. Following the etching process, the activated photoresist film is removed, leaving the original surface. Channels produced in this process have semi-circular cross-sections and have widths at least twice that of the depth or channel height (Nageswara and Deepak, 2007). An approximate cross-section of channels in a MCHX created with this process is shown in Figure 2.2.

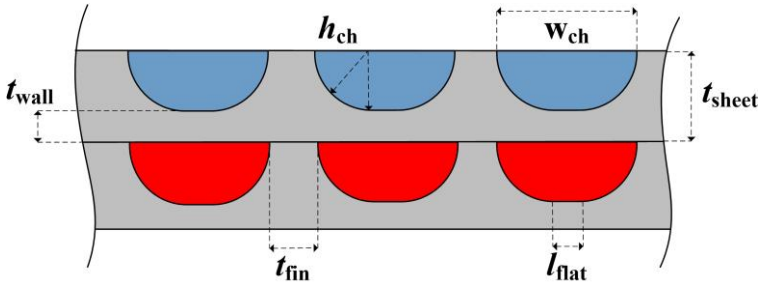

Figure 2.2: MCHX channel cross-section

Individual MCHX blocks consist of a series of microchannel etched sheets, alternating between primary and secondary coolant sheets that direct the two fluids in a counterflow orientation as shown in Figure 2.3 and Figure 2.4. The 316 stainless sheets are designed such that the primary coolant enters and exits in the radial direction, while the secondary coolant enters and exits in the azimuthal direction on the sides of the sheets. The radial, axial, and azimuthal directions are shown in Figure 2.1. Primary coolant channels span the full radial length of the sheet. The secondary coolant sheets contain triangular headers that redirect the coolant ninety degrees into channels counterflow to those in the primary coolant sheets. Another triangular header at the far end of the channel redirects the secondary coolant flow ninety degrees to the side opposite that of the entrance location.

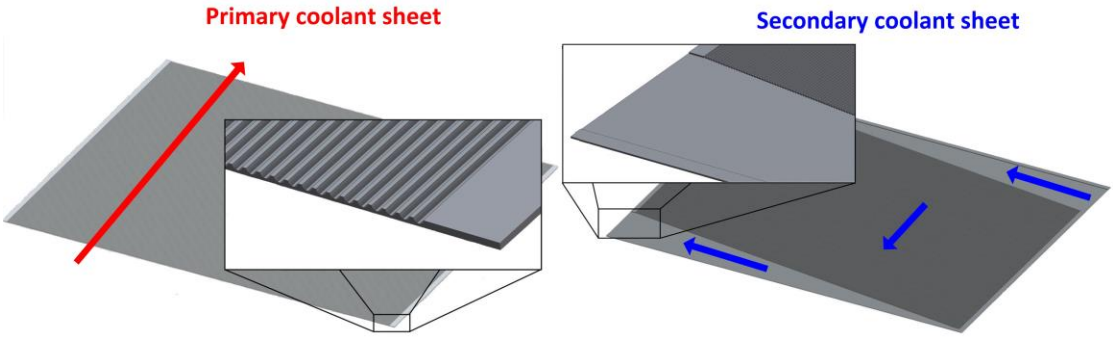

Figure 2.3: Primary and secondary coolant sheets

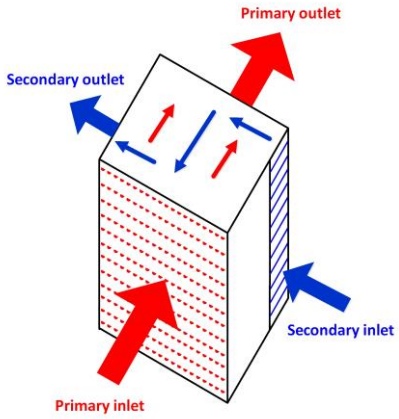

Figure 2.4: MCHX coolant flow path

The triangular headers on the secondary sheets result in channels that are shorter than those on the primary coolant sheets. The span in which the two streams are in counterflow is referred to as the active channel length. A set of these sheets are joined in a high-temperature, high-pressure diffusion bonding process. Heatric has reported diffusion bonding MCHX blocks (stacks of sheets) with the following dimensions: 1.5 m (width) × 0.65 m (length) × 0.60 m (height) (Le Pierres *et al.*, 2011). Using these dimensions as a template, the height of the I^2S-MCHX block was kept at 0.6 m (axial direction). The sheet thickness dictates the number of sheets per MCHX block. The width (azimuthal direction) and length (radial direction) of the design that could realistically fit into the downcomer are 1.0 m × 0.85 m, respectively. A cross-flow design could also be considered, in which the secondary coolant channels are perpendicular to those in the primary coolant sheet. Secondary coolant channels would span the full azimuthal width of the sheet, again allowing the secondary coolant to enter and exit in the azimuthal direction. This configuration would eliminate the triangular headers on the secondary coolant sheets and have the advantage of lowering the secondary coolant pressure drop (the header regions have a high frictional pressure gradient) and reduce the potential of maldistribution in the secondary sheets. However, the cross-flow orientation would result in unfavorable and two-dimensional temperatures profiles within the MCHX, increasing the exergy destruction rate in the heat exchanger.

MCHX blocks are stacked in eight azimuthal positions in the downcomer. The MCHX stacks, associated headers, and the DHRS heat exchangers are distributed around the core as shown in Figure 2.1. Eleven individual MCHX blocks are placed on top of each other to create a 6.6 m high stack. This height (< 7 m) allows the stack to be located

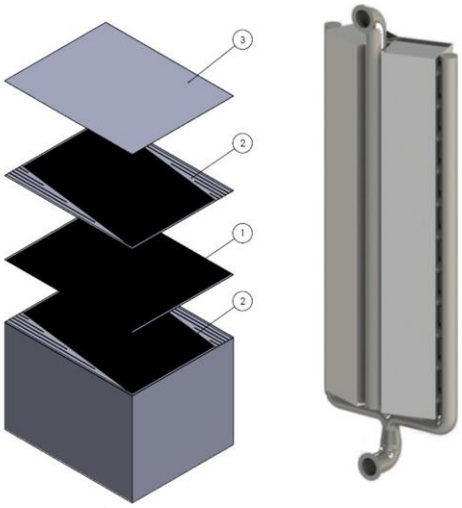

Figure 2.5: I^{2}S-LWR MCHX and MCHX stack

sufficiently above the core to avoid neutron activation of ^{59}Co in the stainless steel (Matijević *et al.*, 2017). Activation would make the removal of the MCHXs for maintenance or replacement difficult because of the high energy gamma decay of ^{60}Co. Penetrations of the RPV for secondary coolant can also be kept above the height of the core, allowing coolant to continue to cover the core in the unlikely event of a primary coolant leak through one of these penetrations. Each stack has its own primary coolant headers, and adjacent stacks share common secondary coolant headers. An example of an MCHX block and an MCHX stack pair are shown in Figure 2.5.

The flow of the primary and secondary coolant through the MCHX stack is shown in Figure 2.6. The primary coolant enters the rectangular inlet header at the top of the stack and travels down the height of the heat exchanger stack in the axial direction. It is then directed ninety degrees into the channels where it flows in the radial direction and is cooled. After exiting the channels, the primary coolant is directed ninety degrees downward through the outlet header and out the bottom of the stack. To minimize downcomer volume committed to primary coolant headers, the MCHX blocks are fixed at a slight angle (1.7°).

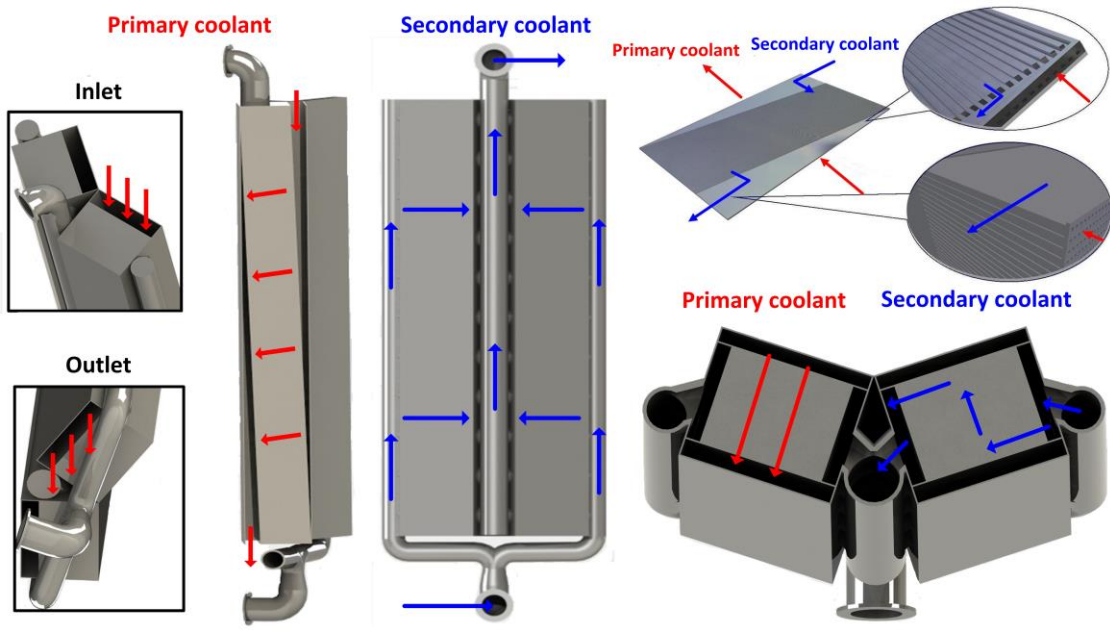

Figure 2.6: MCHX stack coolant flow paths

The primary inlet header narrows radially, traveling down the height of the stack in the axial direction, while the outlet header becomes longer. This also helps to ensure an even flow distribution into the heat exchangers and maintains a constant radial length of the stack. The secondary coolant enters the RPV through four penetrations below and between pairs of MCHX stacks. The header splits and supplies the secondary coolant on the outside of the two MCHX stacks. The coolant exits the inlet headers and collects in small plenums on the outside of the heat exchangers before entering the secondary sheets, as previously described. The secondary coolant then collects in a plenum on the inside of the MCHX stack before entering the outlet header. The outlet headers are situated between MCHX stacks and collect the secondary coolant from the stacks on both sides. The outlet headers carry the secondary coolant out of the RPV through four penetrations above and between the heat exchanger stack pairs. The secondary coolant inlet and outlet headers are mechanically attached to the RPV so that they can be easily removed for maintenance, inspection, and possible replacement.

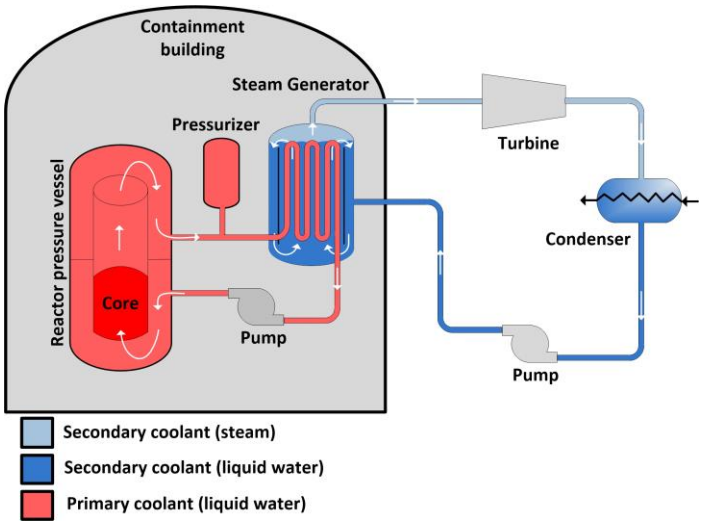

Figure 2.7: Simplified PWR primary and secondary coolant loops

2.3 MCHX Designs and Power Generation Schemes

In conventional PWR designs, the primary coolant exchanges heat with the secondary coolant in large external steam generators. Subcooled secondary coolant (feedwater) enters the steam generator and exits as saturated steam (recirculating steam generator) or superheated steam (once-through steam generator). The steam is then used to generate electricity using a Rankine power cycle. A simplified sketch of the primary and secondary coolant loops in a loop-type PWR is shown in Figure 2.7.

Two concepts have been proposed for the power conversion system in the I^2S-LWR. The first is a flash Rankine cycle that does not require steam generation in the MCHX as proposed by Memmott *et al.* (2017b). This design eliminates the complexity and uncertainty associated with microchannel flow boiling including increased maldistribution, flow instabilities, and bubble confinement (Kandlikar, 2002). The potential of increased fouling build-up and dryout associated with a flow boiling design are also of concern. The flash Rankine cycle operates in a manner similar to that of conventional PWR Rankine

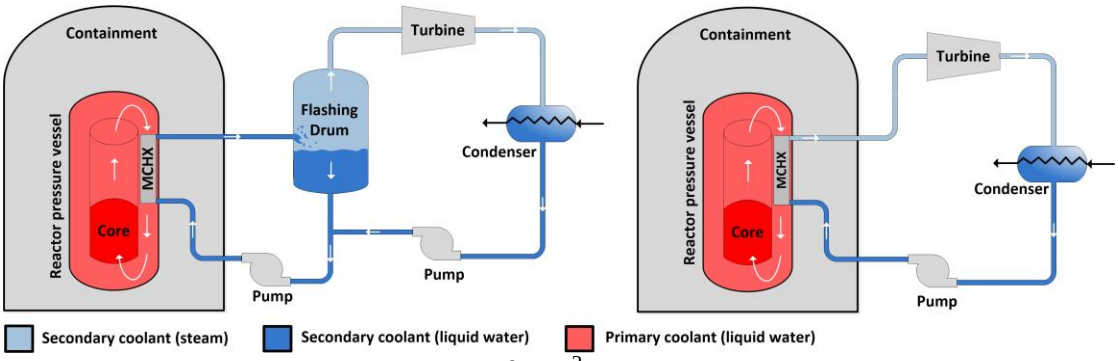

Figure 2.8: Simplified I^{2}S-LWR power cycles

cycles, except that saturated steam is produced in a flashing drum instead of a steam generator. The secondary coolant is heated in the MCHX under high-pressure, subcooled conditions before entering a flashing drum where the pressure is reduced, producing saturated steam and saturated liquid water. The MCHX design accompanying this scheme is referred to as the liquid-liquid design because primary and secondary coolant remain as subcooled liquids over the length of the heat exchanger. Despite the concerns listed above, a second design using the MCHXs as a once-through steam generator offers several advantages over the liquid-liquid, flash Rankine cycle concept. The most obvious is the avoidance of the capital cost associated with flash drums. Additionally, the large heat of vaporization of water results in reduced secondary coolant flow rate through the MCHX for a given reactor power. This reduces the capital cost and parasitic power losses of the large secondary coolant pumps required in the flash Rankine cycle. Finally, this design provides superheated steam at temperatures and pressures higher than those generated in the flashing drum, resulting in increased thermal efficiency of the power cycle. This final point can also be thought of as avoiding the exergy destruction generated in the flashing process. This MCHX design is referred to as liquid-boiling because of the boiling secondary coolant. A simplified schematic of the two power generation schemes is shown in Figure 2.8.

2.4 Alternative Tube-Bundle Heat Exchanger Design

An alternative design utilizing a tube-bundle heat exchanger (TBHX) was also investigated, as shown in Figure 2.9 without the accompanying shell. The primary coolant flows axially down the length of the tubes on the shell side while the secondary coolant on the inside of the tubes flows upward in a counterflow orientation. Circular headers at either end of the tube array distribute and collect the secondary coolant. The TBHXs are located in the same eight rectangular locations in the downcomer as the MCHX stacks, shown in Figure 2.1. The flow paths of the two coolants are shown in Figure 2.10. There are no baffles on the primary coolant shell sides to limit pressure drop. Instead, the thermal resistance of both fluids is minimized by the small diameter of tubes, the small pitch between tubes, and highly turbulent conditions. The small tubes and tight square pitch also result in a large surface-area-to-volume ratio, further increasing heat transfer. Spacer grids are located throughout the length of the tubes to reduce flow-induced vibrations and provide structural support. The shells of the eight TBHXs occupy the same rectangular cross-sectional areas in the downcomer as the MCHX stacks shown in Figure 2.1 The TBHX design has the advantage of using conventional nuclear technology, being similar to existing once-through steam generators. It is therefore subject to less regulatory scrutiny and uncertainty than the MCHX design. However, the larger number of small welds connecting the tubes and headers may prove difficult to fabricate. To meet the heat transfer requirement, tubes substantially smaller than other once-through nuclear steam generators designs are required. Additionally, this tubular design would be subject to the same flow-induced-vibration fretting and stress-corrosion cracking issues observed in current PWR steam generators (Steam, 2005). They would therefore be subject to the inspection and

plugging campaigns required for each tube in existing steam generator designs. This may prove difficult as each of the eight TBHX would need to be removed from the RPV and require thousands of individual inspections. Finally, the TBHX design has less heat transfer area and a higher overall thermal resistance than the MCHX design. As a result, a larger temperature difference is necessary to remove the required 2850 MW_{th} from the primary coolant. This is accomplished through lower secondary coolant temperatures, which decrease the thermal efficiency of the plant power cycle. Detailed analysis of the TBHX design is shown in Appendix A.

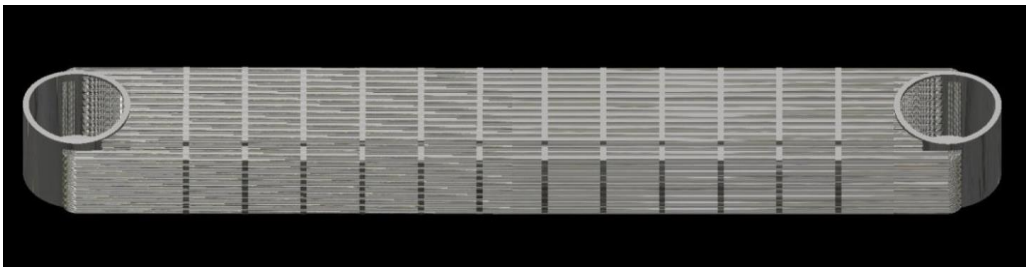

Figure 2.9: Tube-bundle heat exchanger CAD image

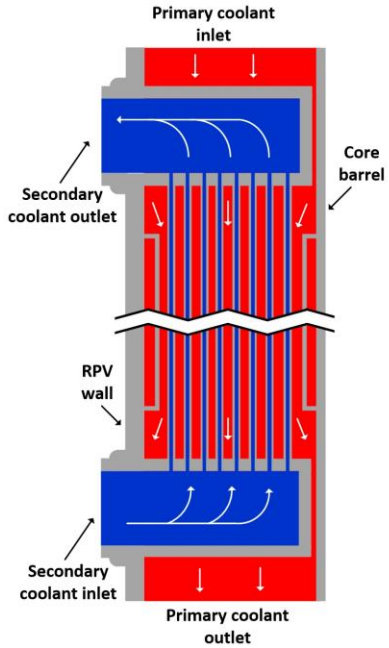

Figure 2.10: Tube-bundle heat exchanger schematic

CHAPTER 3. BACKGROUND AND LITERATURE REVIEW

This chapter provides background on both single-phase and boiling microchannels flows. It also discusses modeling techniques and reviews the literature on once-through steam generator design. Other issues such as fouling, flow instabilities, and maldistribution are also addressed.

3.1 Single-Phase Microchannel Background

The steady-state one-dimensional conservation equations are used to describe flow in channels in heat exchanger design. These are shown in Eq. (3.1) for a single-phase channel of constant cross-section and flow rate. The terms on the right-hand side of the momentum equation represent acceleration, gravity, and viscous forces, from right to left. The terms on the right-hand side of the energy equation represent kinetic energy, gravitational energy, and heat transfer.

$$\begin{aligned} &\text{Continuity:} \quad \frac{\partial G}{\partial z} = 0 \\ &\text{Momentum:} \quad \frac{\partial P}{\partial z} = -G^2 \frac{d}{dz}\left[\frac{1}{\rho}\right] - \rho g \sin\theta - \frac{p_{\text{wall}} \tau_{\text{wall}}}{A_{\text{cx}}} \\ &\text{Energy:} \quad G\frac{\partial i}{\partial z} = -\frac{G^3}{2}\frac{d}{dz}\left[\frac{1}{\rho^2}\right] - Gg\sin\theta + \frac{p_{\text{wall}} q''_{\text{wall}}}{A_{\text{cx}}} \end{aligned} \tag{3.1}$$

These equations can be further simplified into algebraic equations by integrating over a length, Δz, and assuming constant fluid properties. The algebraic conservation equations for a horizontal channel when kinetic energy is ignored are shown in Eq. (3.2). The heat transfer rate, $\dot{q}$, is the heat flux at the wall, q'', integrated over the surface area,

$p_{\text{wall}}\Delta z$. The frictional pressure drop, ΔP_{fr}, is the result of integrating the viscous term in the momentum equation. To solve these equations, closure relationships for the heat transfer rate and frictional pressure drop are required. The local heat flux can be determined based Newton's law of cooling: $q'' = h\left(T_{\text{wall}} - T\right)$. Where h is the heat transfer coefficient and T the mean fluid temperature of the fluid. In steady-state heat exchanger modeling, a thermal resistance network (a function of the geometry and the heat transfer coefficient of both fluids) and the log mean temperature difference, are used to determine the heat transfer rate: $\dot{q} = \Delta T_{\text{lm}} / R = UA\Delta T_{\text{lm}}$. The frictional pressure drop can be expressed in terms of the Darcy friction factor, f, as shown in Eq. (3.3). Correlations for the Nusselt number, $\text{Nu} = hD_{\text{h}} / k$, and friction factor have been used extensively to predict the heat transfer coefficient and frictional pressure drop in conventional macroscale channels. For most liquids, the fluid properties, the heat transfer coefficient, and the friction factor do not vary significantly over the length of the channel. As a result, only a single control volume length is required to accurately model the channel: $\Delta z = l_{\text{ch}}$.

$$\begin{aligned} &\text{Continuity:} \quad \dot{m}_{z+\Delta z} = \dot{m}_z = \dot{m} \\ &\text{Momentum:} \quad P_{z+\Delta z} = P_z - \Delta P_{\text{fr}} \\ &\text{Energy:} \quad \dot{m}i_{z+\Delta z} = \dot{m}i_z + \dot{q} \end{aligned} \tag{3.2}$$

$$\Delta P_{\text{fr}} = f\,\frac{G^2}{2\rho}\,\frac{\Delta z}{D_{\text{h}}} \tag{3.3}$$

For the dimensions and fluid conditions under consideration in this investigation, Nusselt number correlations developed for macrochannels should be valid. However, for turbulent microchannel heat transfer, Sobhan and Garimella (2001) found that most of the available microchannel correlations in the literature predicted Nusselt numbers higher than

those predicted by the macrochannel Dittus and Boelter (1930) correlation. One such correlation, developed by Adams *et al.* (1998), proposed a modification to the widely used Gnielinski (1976) correlation, Eq. (3.4). Eq. (3.5) shows the modification developed by Adams *et al.* (1998). The largest diameter for which a deviation from macroscale correlations was observed was D_0 = 1.167 mm, which is used as a reference diameter in Eq. (3.5).

$$\mathrm{Nu}_{\mathrm{Gn}} = \frac{(f/8)(\mathrm{Re}-1000)\mathrm{Pr}}{1+12.7(f/8)\left(\mathrm{Pr}^{2/3}-1\right)} \tag{3.4}$$

$$f = \left(1.82\log(\mathrm{Re})-1.64\right)^{-2}$$

$$F = 7.6\times10^{-5}\,\mathrm{Re}\left[1-\left(D/D_0\right)^2\right] \tag{3.5}$$

$$\mathrm{Nu} = \mathrm{Nu}_{\mathrm{Gn}}\left(1+F\right)$$

However, some researchers have reported decreased heat transfer in microchannels/minichannels. Wang and Peng (1994) investigated rectangular channels with 311 μm < D_h < 747 μm using water and methanol in the turbulent regime. They proposed a modification to the correlation developed by Colburn (1933), by changing the leading coefficient significantly, from 0.023 to 0.00805, as shown in Eq. (3.6).

$$\mathrm{Nu} = 0.00805\,\mathrm{Re}^{4/5}\,\mathrm{Pr}^{1/3} \tag{3.6}$$

Ghiaasiaan (2018) noted that the differences between microchannel and macrochannel Nusselt number correlations were typically within a factor of two. He also alluded to potential causes for these deviations, including surface roughness and manufacturing imperfections, electro-kinetic surface forces, dissolved gasses, suspended particles, and fouling. Rosa *et al.* (2009) discussed several scaling effects that may influence microchannel heat transfer. These effects result from the assumptions used to develop

macrochannels correlation that may no longer be valid for microchannel flows. These include neglecting viscous heating, conjugate heat transfer (such as axial conduction in the material and fluid), fully developed flow, constant fluid properties, and the applicability of continuum mechanics. They suggested criteria for when these scaling effects may have significant influence. The dimensionless Maranzana number, M shown in Eq. (3.7), represents the ratio between axial conduction in material walls and convection heat transfer from the wall (Maranzana *et al.*, 2004). $A_{\text{cx,wall}}$ is the cross-sectional area of the heat exchanger, $p_{\text{wall}} \times l_{\text{ch}}$ is the wetted area, and k_{wall} and k_{f} are the thermal conductivities of the wall material and fluid, respectively. For values of M less than 0.01, conjugate heat transfer in the wall material can be safely ignored. Otherwise, complex heat flow patterns may result, requiring three-dimensional numerical simulations to ensure accuracy.

$$\mathrm{M} = \frac{k_{\text{wall}}}{k_{\text{f}}} \frac{A_{\text{cx,wall}}}{p_{\text{wall}} l_{\text{ch}}} \frac{1}{\mathrm{Re}\,\mathrm{Pr}} \tag{3.7}$$

Morini (2006) suggests using Eq. (3.8) as a criterion for when viscous dissipation can be ignored. For Brinkman numbers satisfying the inequality, the temperature rise resulting from viscous dissipation will be less than 5% of that resulting from wall heat flux. Correlations developed from experimental data or a temperature profile with negligible viscous heating may not be accurate for microchannels that do not satisfying this inequality.

$$\mathrm{Br} = \frac{\mu G^2}{\rho^2 q''} \quad < \quad \frac{0.05 D_{\text{h}}^2}{2 A_{\text{cx}} f\,\mathrm{Re}} \tag{3.8}$$

Heat transfer enhancement due to developing flow at the inlet is another consideration. Morini (2006) stated that laminar flow entrance effects can be ignored for Graetz numbers

(Gz) less than ten. Slip flow and temperature-jump at the wall (a breakdown of continuity and the no-slip boundary condition) result when the mean free path of particles, λ, becomes comparable to the characteristic length of the system. This is unlikely in liquid channels, but will start to become significant for gas flow with a Knudsen number, $\mathrm{Kn} = \lambda / D_h$, greater than 10^{-3} (Gad-El-Hak, 2006). Large temperature changes over the length of the channel affect fluid properties, particularly viscosity, which influence both heat transfer and fluid dynamics. Property changes can be accurately accounted for by segmenting the channel length in discrete control volumes and using local properties. However, this technique cannot be employed to experimentally measure the Nusselt number/heat transfer coefficient if only channel inlet and outlet conditions are known. If scaling effects are not significant, Rosa *et al.* (2009) suggests using macrochannel Nusselt number correlations such as the Hausen (1943) correlation for developing laminar flow and the Gnielinski (1976) correlation for fully-developed turbulent flow. However, they also noted that there were discrepancies in single and multi-channel experiments and that such correlations may not be as accurate for multichannel heat exchanger design due to maldistribution (non-uniform channel flow rates).

Much of the literature focuses on circular or rectangular channel cross-sections. However, channels resulting from the photo-chemical etching process used in the construction of MCHXs yield a semi-circular cross section. Adams *et al.* (1999) investigated turbulent heat transfer in an irregularly shaped, non-circular channel with D_h = 1.13 mm. They found that the Gnielinski (1976) correlation accurately predicted the Nusselt number of the irregularly shaped channel.

Steinke and Kandlikar (2005) collected over 200 data sets from friction factor experiments spanning hydraulic diameters from D_h = 1 μm to 1200 μm and included both laminar and turbulent regimes. They found the departure from macrochannel correlations to be primarily due to experimental errors such as neglecting channel inlet and outlet pressure losses, neglecting developing flow in short test sections, and large experimental uncertainties. They also found that studies that accurately accounted for these effects reported results consistent with macroscale phenomena. Webb (2003) compared several microchannel pressure drop studies using single and multichannel experimental test sections. He found that many of the investigators using single channel test sections found friction factors consistent with macroscale correlations. However, data collected using multichannel test sections showed both increased and decreased microchannel frictions factors. He associated this discrepancy in multichannel data to maldistribution between channels as the result of poor header design and manufacturing imperfections resulting in differing channel dimensions.

3.2 Two-Phase Flow and Flow Boiling Background

Many different flow regimes exist in two-phase flows and transitions are less straight forward than single-phase flows, which is only dependent on the relative magnitudes of viscous and inertial forces. However, just as in single-phase flows, the presence of different flow regimes can have significant impact on transport processes such as heat transfer and the frictional pressure gradient. Maps of conditions where different flow regimes occur have been developed, although the applicability of such flow regime maps is dependent on fluid properties, channel orientation, heat transfer conditions, and channel dimensions used to develop the map. A brief overview of the important flow

regimes likely to occur in once-through steam generator channels is presented here. Bubbly flow occurs at low quality and is characterized by dispersed vapor bubbles in the bulk liquid. As the quality increases, the bubbles coalesce into larger bullet-shaped bubbles occupying much of the channel cross-section. These are separated by liquid slugs, giving the name to this regime, slug flow. As the quality and mixture velocity further increases, the size of the liquid slugs decreases and the individual bubbles break down. Gas and liquid mix irregularly in the center of the channel with no obvious interfacial shape. This churn flow regime also typically has a thick liquid film on the walls. Annular flow is established at even higher qualities. Here the vapor flows at high velocity through the core of the channel with a slower moving liquid film on the channel walls. Small liquid droplets may also be entrained in the vapor core. Following the evaporation of the liquid film, the channel in occupied by only vapor and entrained liquid droplets in the mist flow regime. If the gravitational forces are significant and the channel is not vertically oriented, stratified flow may also occur, in which vapor flows at the top of the channel and the dense liquid flows along the bottom.

The homogeneous equilibrium model (HEM) is the simplest two-phase flow model and allows the flow to be treated as a single fluid, simplifying calculations. This model assumes that the two phases are perfectly mixed throughout the channel cross-section, travel at the same velocity, and are in thermodynamic equilibrium. However, in certain flow regimes, such as annular or stratified flow, there may be a large velocity difference or slip velocity between the two phases. The two phases can also be treated individually using separate mass, momentum, and energy conservation equations in a two-fluid model (2FM). These equations can be solved relatively easily at steady-state and when assuming one-

dimensional ensemble (time) averaged values. However, this involves assumptions about the transport properties between phases which can be highly dependent on the flow regime. The conservation equation for both phases in the 2FM can be summed to give the mixture conservation equations. Eq. (3.9) shows the steady-state, one-dimensional, 2FM mixture conservation equations assuming a constant channel cross-section (Ghiaasiaan, 2017). The three terms on the right-hand sides of the momentum and energy equations represent the same values as in the single-phase conservation equations, Eq. (3.1). The momentum equation is also sometimes expressed as the sum of the acceleration, gravitational, and frictional pressure drops, as shown in Eq. (3.10). If the two phases are in thermodynamic equilibrium, only the mixture energy conservation equation is required to apply the 2FM. However, a second momentum conservation equation for either of the two phases is required, in addition to the mixture momentum equation. This can be replaced by a closure relation for the void fraction, α, allowing only the mixture conservation equations to be considered in the 2FM. As with the single-phase conservation equations, the transient, multidimensional 2FM conservation equations form a set of partial differential equations which are difficult to solve, often requiring computational fluid dynamics software. However, many steady-state two-phase problems such as boiler tubes and in-tube condensation can be addressed using the one-dimensional ordinary differential equations in Eq. (3.9).

Continuity: $\frac{\partial G}{\partial z}=0$

Momentum: $\frac{\partial P}{\partial z}=-G^2\frac{d}{dz}\left[\frac{x^2}{\alpha\rho_{\mathrm{v}}}+\frac{(1-x)^2}{(1-\alpha)\rho_{\mathrm{l}}}\right]-\left[(1-\alpha)\rho_{\mathrm{l}}+\alpha\rho_{\mathrm{v}}\right]g\sin\theta-\frac{p_{\mathrm{wall}}\tau_{\mathrm{wall}}}{A_{\mathrm{cx}}}$

Energy: $G\frac{\partial i}{\partial z}=-\frac{G^3}{2}\frac{d}{dz}\left[\frac{x^3}{\alpha^2\rho_{\mathrm{v}}^2}+\frac{(1-x)^3}{(1-\alpha)^2\rho_{\mathrm{l}}^2}\right]-Gg\sin\theta+\frac{p_{\mathrm{wall}}q''_{\mathrm{wall}}}{A_{\mathrm{cx}}}$

(3.9)

$$\left(-\frac{\partial P}{\partial z}\right)=\left(-\frac{\partial P}{\partial z}\right)_{\mathrm{a}}+\left(-\frac{\partial P}{\partial z}\right)_{\mathrm{g}}+\left(-\frac{\partial P}{\partial z}\right)_{\mathrm{fr}} \tag{3.10}$$

These can be further simplified into algebraic equations by again integrating over some length, Δz. Eq. (3.11) shows algebraic 2FM mixture conservation equations for a horizontal tube when changes in kinetic energy are ignored. Again, closure relations for the heat transfer rate and frictional pressure drop are required. Additionally, the void fraction is required to determine the acceleration pressure drop. Unlike single-phase flows, the two-phase heat transfer coefficient and frictional pressure gradient change significantly over the length of a heated channel, being a function of the quality and pressure. Therefore, small control volumes (small Δz) are required to describe a boiling channel.

Continuity: $\dot{m}_{\mathrm{z+\Delta z}}=\dot{m}_{\mathrm{z}}=\dot{m}$

Momentum: $P_{\mathrm{z+\Delta z}}=P_{\mathrm{z}}-\Delta P_{\mathrm{fr}}-G^2\left(\left[\frac{x^2}{\alpha\rho_{\mathrm{v}}}+\frac{(1-x)^2}{(1-\alpha)\rho_{\mathrm{l}}}\right]_{\mathrm{z+\Delta z}}-\left[\frac{x^2}{\alpha\rho_{\mathrm{v}}}+\frac{(1-x)^2}{(1-\alpha)\rho_{\mathrm{l}}}\right]_{\mathrm{z}}\right)$ (3.11)

Energy: $\dot{m}i_{\mathrm{z+\Delta z}}=\dot{m}i_{\mathrm{z}}+\dot{q}$

Diffusion models, such as the drift flux model (DFM), address the two phases separately, but substitute one of the momentum equations with a relationship for the slip velocity between of the two phases. The DFM is also often used as a means of developing void-quality relations for one-dimensional flows, as shown in Eq. (3.12). This is

accomplished using two parameters: C_0, the two-phase distribution coefficient, which is a measure of the overall slip, and V_{gj}, the mean drift velocity, which represents the effect of local slip velocities. Eq. (3.13) shows the equation for the HEM void fraction which is equal to the volumetric quality, β. When C_0 is set to 1 and V_{gj} to zero, the HEM definition of void fraction is recovered from the DFM relation.

$$\alpha_{DFM} = \frac{x}{C_0\left[x + \frac{\rho_v}{\rho_l}(1-x)\right] + \frac{\rho_v V_{gj}}{G}} \tag{3.12}$$

$$\alpha_{HEM} = \beta = \frac{1}{1 + \left(\frac{1-x}{x}\right)\left(\frac{\rho_v}{\rho_l}\right)} \tag{3.13}$$

Because of the complex nature of two-phase flows, empirical correlations for heat transfer, frictional pressure drop, and void fraction are often developed. Many of these correlations are a function of dimensionless numbers such as the Reynolds number. These quantities can be defined as if the entire flow were a single phase or as if one of the two phases were removed and the other fully occupied the channel. Dimensionless numbers with the subscript lo (liquid-only) or vo (vapor-only) are calculated assuming the entire flow rate were in the liquid or vapor state at saturation. Similarly, dimensionless numbers with the subscript l (liquid) or v (vapor) are calculated using the quality and assuming only one of the two phases is present in the channel. Equation (3.14) shows the difference between liquid (l) and liquid only (lo) Reynolds numbers.

$$\mathrm{Re}_l = \frac{G(1-x)D}{\mu_l} \quad \mathrm{Re}_{lo} = \frac{GD}{\mu_l} \tag{3.14}$$

Discussion of two-phase correlations often involves comparing predicted and experimental values. The absolute average deviation (AAD), sometimes called the mean average deviation, is often used for this purpose and is shown in Eq. (3.15). The average deviation (AD) is also sometimes used, shown in Eq. (3.16). A model or correlation with a high degree of scatter compared to experimental values may have a small AD, resulting from equal positive and negative errors, while the AAD would be significantly larger. In cases where the correlation constantly overpredicts or underpredicts experimental data, the magnitude of the AD will be similar that of the AAD.

$$\mathrm{AAD} = \frac{1}{n}\sum_{i=1}^{n}\left|\frac{\text{Predicted - Measured}}{\text{Measured}}\right| \times 100\% \tag{3.15}$$

$$\mathrm{AD} = \frac{1}{n}\sum_{i=1}^{n}\frac{\text{Predicted - Measured}}{\text{Measured}} \times 100\% \tag{3.16}$$

Table 3.1 contains representative properties and dimensionless numbers for the secondary coolant in the liquid-boiling MCHX design and boiling water in MCHX experiments that are discussed in Chapter 7. A hydraulic dimeter of D_h = 0.862 mm was assumed for the channels. The limitations of the test facility dictated that boiling experiments cannot be run at the temperature and pressure of the I^{2}S-LWR MCHX design. However, many of the properties and dimensionless numbers that govern two-phase flow are in good agreement. Notable property exceptions are the vapor density, ρ_v, the reduced pressure P_r, and to a lesser extent the surface tension, σ. Differences in these properties result in differences in some dimensionless numbers such as the convection number, Co. The fluid conditions and dimensionless numbers listed in Table 3.1 are used throughout this chapter to compare different correlations. It should be noted that a constant heat flux was assumed for these comparisons; although the heat flux will likely vary significantly

Table 3.1: Representative I^{2}S-LWR and MCHX test section conditions

Property	G (kg m^{-2} s^{-1})	q'' (kW m^{-2})	T_{sat} (°C)	P_{sat} (kPa)	P_r (-)	k_l (W m^{-1}K^{-1})	k_v (W m^{-1}K^{-1})	μ_l (kg m^{-1}s^{-1})	μ_v (kg m^{-1}s^{-1})	ρ_l (kg m^{-3})	ρ_v (kg m^{-3})	σ (N m^{-1})	i_{fg} (kJ kg^{-1})
MCHX test section	200	250	150	475.7	0.02156	0.6683	3.154×10^{-2}	1.825×10^{-4}	1.399×10^{-5}	917.1	2.545	0.05496	2114
I^{2}S-LWR MCHX	200	250	285	6911	0.3132	0.5611	5.976×10^{-2}	9.162×10^{-5}	1.892×10^{-5}	741.5	36.02	0.01782	1511
Non-dimensional numbers	**Bd (-)**	**Bd$^{1/2}$ (-)**	**Bo (-)**	**Co (-) [x=0.5]**	**N_{con} (-)**	**Fr_{lo} (-)**	**Pr_l (-)**	**Pr_v (-)**	**Re_{lo} (-)**	**Re_{vo} (-)**	**We_{lo} (-)**	**X_{tt} (-) [x=0.5]**	**$Re_{lo}Bd^{1/2}$ (-)**
MCHX test section	0.1367	0.3697	5.913×10^{-4}	0.05353	2.705	5.63	1.178	1.02	944.6	1.232×10^{4}	0.7715	0.06935	349.2
I^{2}S-LWR MCHX	0.2556	0.5056	8.275×10^{-4}	0.2239	1.978	9.416	0.8778	1.604	1772	8579	2.457	0.2627	895.7

along the channel length in a boiling heat exchanger and is itself a function of the heat transfer coefficient.

3.2.1 Microchannel two-phase flows

In the previous section, it was shown that correlations developed for macrochannel phenomena were likely applicable for the proposed channel sizes in the study. However, the complex nature of two-phase flow results in significant changes within the microchannel range. These include changes in flow regimes and transitions, nucleate boiling bubble confinement, and the relative magnitude of different forces governing two-phase flow and heat transfer. One such difference is that buoyancy effects (gravitational forces) are negligible in comparison to inertial, surface tension, and viscous effects. As a result, stratified flow does not occur. The Bond number, Eq. (3.17), is used to compare the magnitude of gravitation and surface tension forces. The relation $\sqrt{\mathrm{Bd}} \le 0.3$ can used as a criterion for defining microchannels for which buoyancy effects are negligible and stratified flow will not occur (Suo and Griffith, 1964).

$$\mathrm{Bd} = \frac{\Delta\rho g D_h^2}{\sigma} \tag{3.17}$$

Another influential effect is that of bubble confinement. In microchannel boiling, bubbles can form on walls and grow to sizes comparable to that of the channel diameter before departing. As a result, boiling in a microchannel may not experience a bubbly flow regime. This effect is not observed in macrochannels, where bubbles that depart the wall are many orders of magnitude smaller in diameters than the channels. Harirchian and Garimella (2010) developed a threshold below which confinement effects were observed, as shown in Eq. (3.18), and observed an increase in heat transfer for confined flows at lower quality. They attributed this phenomenon to the presence of convective boiling in the thin liquid films around the confined bubbles, which is not present in nucleate-boiling dominated non-confined flows. The expansion of confined bubbles may also cause the transition to annular flow at lower quality, increasing heat transfer for channels in which convective boiling is the most efficient means of heat transfer (Ong and Thome, 2011a; Ong and Thome, 2011b). The film between the wall and bubble may become thin enough for partial dryout to occur, reducing heat transfer (Thome *et al.*, 2004). Kew and Cornwell (1997) compared several macroscale flow-boiling correlations with experimental data for small-diameter channels and found that they were not applicable for confinement numbers (N_{con}) greater than 0.5 and attributed this to partial channel dryout due to bubble confinement.

$$\mathrm{Bd}^{0.5}\mathrm{Re}_{lo} \leq 160 \tag{3.18}$$

$$N_{con} = \sqrt{\frac{\sigma}{g\Delta\rho D_h^2}} = \mathrm{Bd}^{-0.5} \tag{3.19}$$

Finally, applications and experiments with microchannels often involve many channels that share common inlet and outlet headers. An array of boiling channels is particularly susceptible to flow instabilities (including backflow and channel-to-channel flow oscillations) and maldistribution among channels. Thus, different trends may be observed

between single- and multi-channel experiments. Channels with individual flow control systems and an inlet orifice, in which known and stable inlet conditions occur, are said to have “hard inlet conditions”. Parallel channels sharing inlet and outlet headers are said to have “soft inlet conditions”. However, many investigators discussed in the following sections do not attempt to segregate hard and soft inlet condition data when developing microchannel boiling correlations.

3.2.2 Microchannel void fraction

Void-quality relationships in small channels exhibit trends different than those in larger channel. Triplett *et al.* (1999) measured the void fraction for air-water mixtures in 1.1 and 1.45 mm diameter tubes. They compared their data with correlations from the literature developed for conventional channels and found that the homogenous void fraction best fit the data. This observation was attributed to lower slip velocity in the small diameter channels as compared with that in larger channels. As a result of reduced buoyancy and large surface tension/viscous effects, local variation in velocity is expected to be small, leading to small mean drift velocities in the DFM, $V_{gj} \approx 0$. Under these conditions, the DFM reduces to a constant multiplied by the volumetric quality (or homogenous void fraction). Correlations of this type are referred to as Armand-type correlations because of the early work performed by Armand (1946) in which the constant C_A was found to equal 0.833.

$$\alpha = \frac{\beta}{C_0} = C_A \beta \tag{3.20}$$

Several authors have observed this linear relation between void fraction and volumetric quality. Zhao and Bi (2001) examined triangular channels with hydraulic diameters of 0.886 mm, 1.443 mm, and 2.886 mm using an air-water mixture. They fit their data to a DFM model with the mean drift velocity set to zero and found the distribution coefficient to be a function of phase densities as shown in Eq. (3.21). Zhang *et al.* (2010) developed an empirical correlation for the two-phase distribution parameter based on the confinement number, Eq. (3.22). The authors used a database of six different minichannel void-fraction experiments from several authors. The correlation had an AAD of 12.7% when compared with the database. It is worth noting that as the hydraulic diameter increases (and the confinement number decreases), C_0 approaches 1.2, leading to the Armand coefficient of 0.833.

$$C_0 = 1.2 - 0.2\sqrt{\rho_v / \rho_l} \tag{3.21}$$

$$C_0 = 1.2 + 0.380\exp\left(-1.39 / \mathrm{N_{con}}\right) \tag{3.22}$$

Figure 3.1 shows the void fraction predicted by several correlations over the full quality range using the representative properties for I^{2}S-LWR MCHX and MCHX test section listed in Table 3.1. The HEM, which assumes no interphase slip, results in the largest void fraction. It is also worth noting that Armand-type correlations do not result in a void fraction of one at a quality of one, which suggests they might not be applicable at higher quality. The low vapor density at MCHX test section conditions result in a rapid increase in void fraction at low quality as compared to I^{2}S-LWR MCHX conditions. Acceleration pressure drop is also calculated using each of the listed void fraction correlations in Figure 3.1. This value is calculated using an inlet quality of zero (and inlet

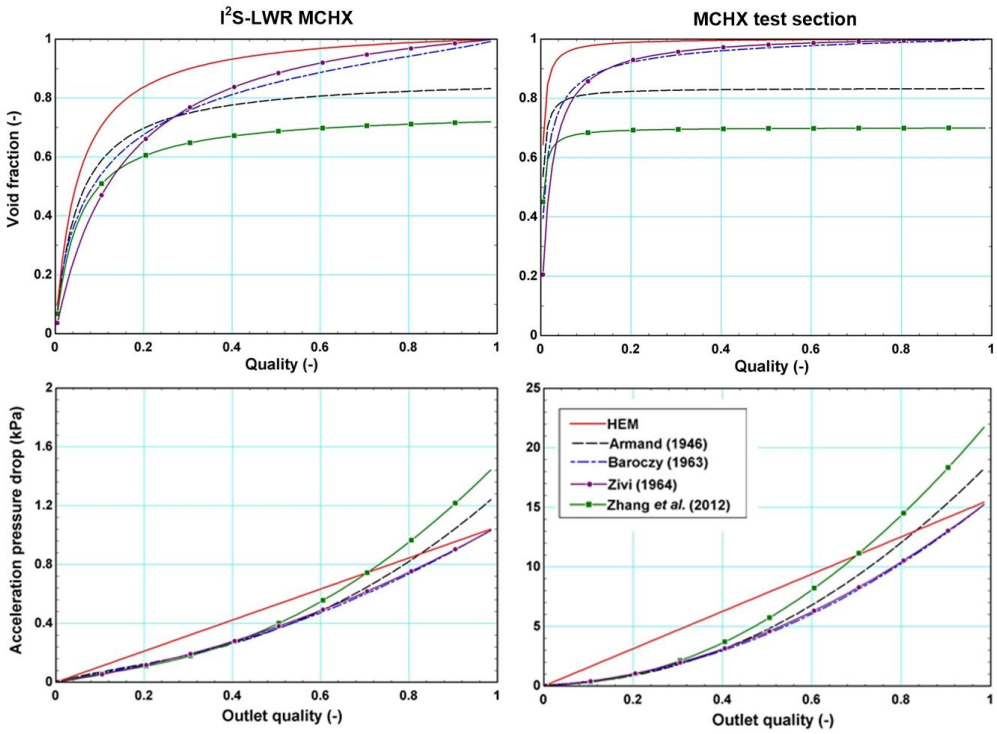

Figure 3.1: Representative void fractions and acceleration pressure drop

void fraction of zero), the listed outlet quality, and the corresponding void fraction correlation.

3.2.3 Two-phase frictional pressure drop

Using the homogeneous equilibrium model (HEM), one can construct a two-phase frictional pressure gradient correlation similar to that of a single-phase fluid, as shown in Eq. (3.23). The two-phase or homogeneous density is expressed according to Eq. (3.24).

$$\left(-\frac{\partial P}{\partial z}\right)_{\text{fr}} = f_{\text{tp}} \frac{G^2}{2\rho_{\text{tp}}} \frac{1}{D_{\text{h}}} \tag{3.23}$$

$$\rho_{\text{tp}} = \rho_{\text{HEM}} = \left(\frac{x}{\rho_{\text{v}}} + \frac{1-x}{\rho_{\text{l}}}\right)^{-1} \tag{3.24}$$

A friction factor correlation and a model for two-phase viscosity can then be used to calculate the two-phase Reynolds number and friction factor. Using Blasius's fanning friction factor correlation for turbulent flow over a plate, Eq. (3.25), and the McAdams *et al.* (1942) viscosity model, Eq. (3.26), a closed set of equations is formed. The two-phase Reynolds number is expressed as $\mathrm{Re}_{\mathrm{tp}} = GD_{\mathrm{h}} / \mu_{\mathrm{tp}}$.

$$f_{\mathrm{Fanning}} = 0.079\,\mathrm{Re}^{-0.25} \tag{3.25}$$

$$\mu_{\mathrm{tp}} = \left(\frac{x}{\mu_{\mathrm{v}}} + \frac{1-x}{\mu_{\mathrm{l}}} \right)^{-1} \tag{3.26}$$

Combining equation (3.23) through (3.26) and the definition of two-phase Reynolds number, the two-phase frictional pressure gradient can be expressed as the product of any single-phase pressure gradient (l, lo, v, vo) and a two-phase multiplier term as shown in Eq. (3.27). When using Blasius's correlation and the McAdams *et al.* (1942) two-phase viscosity model, the liquid only (lo) two-phase multiplier is shown in Eq. (3.28). Using different viscosity models and single-phase friction factor correlations, a variety of HEM two-phase multipliers can be generated.

$$\left(-\frac{\partial P}{\partial z}\right)_{\mathrm{fr}} = \phi_{\mathrm{lo}}^2 \left(-\frac{\partial P}{\partial z}\right)_{\mathrm{fr,lo}} = \phi_{\mathrm{l}}^2 \left(-\frac{\partial P}{\partial z}\right)_{\mathrm{fr,l}} = \phi_{\mathrm{vo}}^2 \left(-\frac{\partial P}{\partial z}\right)_{\mathrm{fr,vo}} = \phi_{\mathrm{v}}^2 \left(-\frac{\partial P}{\partial z}\right)_{\mathrm{fr,v}} \tag{3.27}$$

$$\phi_{\mathrm{lo}}^2 = \left[1 + x\left(\frac{\mu_{\mathrm{l}} - \mu_{\mathrm{v}}}{\mu_{\mathrm{v}}}\right)\right]^{-0.25} \left[1 + x\left(\frac{\rho_{\mathrm{l}}}{\rho_{\mathrm{v}}} - 1\right)\right] \tag{3.28}$$

Frictional pressure-drop equations derived from the HEM can be applied reasonably well to regimes where the two-phases are well dispersed, such as bubbly flow. However, in separated flows where there is a large slip velocity, such as annular or stratified flow, a more complicated model is required. Phenomenological models have been

developed but they are often flow regime dependent, leading to uncertainties in transitions (Ghiaasiaan, 2017). These can also be difficult to implement in design codes. Consequentially, a large number of studies have focused on the development and evaluation of empirical correlations. These models often take the form of functions for the two-phase multiplier.

One such widely used correlation was developed by Friedel (1979). The Friedel correlation for both horizontal flow and vertical upwards flow is shown in Eq. (3.29) and a second equation was developed for vertical downward flow. He suggests using Eq. (3.30) to calculate the friction factor for Re_{lo} or Re_{vo} greater than 1055.

$$\phi_{lo}^2 = (1-x)^2 + \frac{x^2 \rho_l f_{vo}}{\rho_v f_{lo}} + 3.24 x^{0.78} (1-x)^{0.24} \left(\frac{\rho_l}{\rho_v}\right)^{0.91} \left(\frac{\mu_v}{\mu_l}\right)^{0.19} \left(1-\frac{\mu_v}{\mu_l}\right)^{0.7} \mathrm{Fr}^{-00454} \mathrm{We}^{-0.035} \tag{3.29}$$

$$f = 4\left[1.7372 \ln\left(\frac{\mathrm{Re}}{1.964 \ln(\mathrm{Re}) - 3.8215}\right)\right]^{-2} \tag{3.30}$$

Chisholm (1967) developed a correlation using the method of Lockhart and Martinelli (1949) and the Martinelli parameter, shown in Eq. (3.31). The Martinelli parameter can be calculated by using an appropriate single-phase friction factor correlation and the liquid (l) and vapor (v) Reynolds numbers. The liquid (l) two-phase multiplier can be obtained using Eq. (3.32) and the constant from Table 3.2. The constant, *C*, is selected based on the combination of flow regimes determined by liquid (l) and vapor (v) Reynolds numbers. The transition from laminar (viscous) to turbulent is assumed to be 2000.

$$X^2 = \frac{\phi_l^2}{\phi_v^2} = \frac{\left(-\partial P / \partial z\right)_{fr,l}}{\left(-\partial P / \partial z\right)_{fr,v}} \tag{3.31}$$

$$\phi_l^2 = 1 + \frac{C}{X} + \frac{1}{X^2} \tag{3.32}$$

Table 3.2: Chisholm (1967) flow regime constants

Liquid Regime	Vapor Regime	*C*
viscous	viscous	5
turbulent	viscous	10
viscous	turbulent	12
turbulent	turbulent	20

Kim and Mudawar (2013d) performed an extensive study comparing experimental data from 16 different microchannel boiling pressure drop experiments to correlations from the literature. Their database included nine working fluids, mass fluxes from 33 to 2738 kg m^{-2} s^{-1}, and hydraulic diameters from 0.349 to 5.35 mm. It also included single and multichannel test sections and reduced pressure from 0.005 to 0.78. They used their database to assess the accuracy of 24 different two-phase frictional pressure-drop correlations. They found the correlation of Mishima and Hibiki (1996) to provide the best agreement with their database with an AAD of 27.6%. However, they noticed that the correlation was inconsistent, underpredicting experimental pressure gradients less than 10 kPa m^{-1} and overpredicting it above 10 kPa m^{-1}. They believed that in boiling flows, droplets would be entrained in the vapor core as slug and intermittent flows regimes transition to annular flow. They also cited recent high-speed videos showing that condensing flows do not have such entrainment. Consequentially, they treated adiabatic/condensing and boiling flows separately. This choice was supported by the differences in trends when comparing correlations to boiling and adiabatic/condensing datasets. In an earlier study of adiabatic/condensing microchannel flows, Kim and Mudawar (2013a) developed a pressure drop model using the method developed by Chisholm (1967). They chose the constant, *C*, to be a function of dimensionless numbers which relate inertial, viscous, and surface tensions forces because of their relevance in

microchannels. They chose the Reynolds number and Sutratman number as variables in their correlation, adding a modification based on Weber and boiling numbers to account for differences in boiling flows. This frictional boiling pressure drop correlation achieved an AAD of 17.2% when compared with the experimental database and consistently showed this level of accuracy in relevant subsets of the data. The correlation is summarized in the equations and table below (Kim and Mudawar, 2013d). Eq. (3.33) is used to calculate the liquid (l) and vapor (v) friction factors/pressure drops used determine the Martinelli parameter. The transition from laminar to turbulent is again assumed to be 2000 based on the liquid (l) and vapor (v) Reynolds numbers.

$$\begin{aligned} f &= 64\,\mathrm{Re}^{-1} && \text{for } \mathrm{Re} < 2000 \\ f &= 0.316\,\mathrm{Re}^{-0.25} && \text{for } 2000 \le \mathrm{Re} < 20000 \\ f &= 0.184\,\mathrm{Re}^{-0.2} && \text{for } \mathrm{Re} \ge 20000 \end{aligned} \tag{3.33}$$

$$\begin{aligned} C &= C_{\mathrm{nb}}\left(1 + 60\,\mathrm{We}_{\mathrm{lo}}^{0.32}\mathrm{Bo}^{0.78}\right) && \text{for } \mathrm{Re}_{\mathrm{l}} \ge 2000 \\ C &= C_{\mathrm{nb}}\left(1 + 530\,\mathrm{We}_{\mathrm{lo}}^{0.52}\mathrm{Bo}^{1.09}\right) && \text{for } \mathrm{Re}_{\mathrm{l}} < 2000 \end{aligned} \tag{3.34}$$

Table 3.3: Kim and Mudawar flow regime equations

Liquid Regime	**Vapor Regime**	C_{nb}
viscous	viscous	$0.39\,\mathrm{Re}_{\mathrm{lo}}^{0.03}\,\mathrm{Su}_{\mathrm{vo}}^{0.10}\left(\frac{\rho_{\mathrm{l}}}{\rho_{\mathrm{v}}}\right)^{0.35}$
turbulent	viscous	$8.7\times10^{-4}\,\mathrm{Re}_{\mathrm{lo}}^{0.17}\,\mathrm{Su}_{\mathrm{vo}}^{0.50}\left(\frac{\rho_{\mathrm{l}}}{\rho_{\mathrm{v}}}\right)^{0.14}$
viscous	turbulent	$0.0015\,\mathrm{Re}_{\mathrm{lo}}^{0.59}\,\mathrm{Su}_{\mathrm{vo}}^{0.19}\left(\frac{\rho_{\mathrm{l}}}{\rho_{\mathrm{v}}}\right)^{0.36}$
turbulent	turbulent	$8.7\times10^{-4}\,\mathrm{Re}_{\mathrm{lo}}^{0.17}\,\mathrm{Su}_{\mathrm{vo}}^{0.50}\left(\frac{\rho_{\mathrm{l}}}{\rho_{\mathrm{v}}}\right)^{0.14}$

Figure 3.2 shows seven different frictional pressure gradient correlations for the fluid conditions described in Table 3.1. It can be observed that there is an approximately ten-fold increase in the test section pressure gradient as compared to I^{2}S-LWR conditions. This is largely the result of the higher vapor velocity at lower pressure in the test section. For both sets of conditions, a jump in several of the correlations can be observed around a quality of 0.2 as the vapor (v) Reynolds number becomes turbulent. This effect was particularly prominent in the correlations of Lee and Lee (2001) and Chisholm (1967). Otherwise, the trends and magnitude of the correlations are generally in agreement. More information on the correlations is available in Table 3.4. Many of these correlations suggest specific correlations to determine the liquid (l), liquid-only (lo), vapor (v), and/or vapor only (vo) fraction factor/frictional pressure gradient. These suggestions are not listed in Table 3.4 but were carefully adhered to in using the correlations. When no suggested single-phase correlations were recommended, the Churchill (1977b) friction factor correlation, Eq. (4.6), was used.

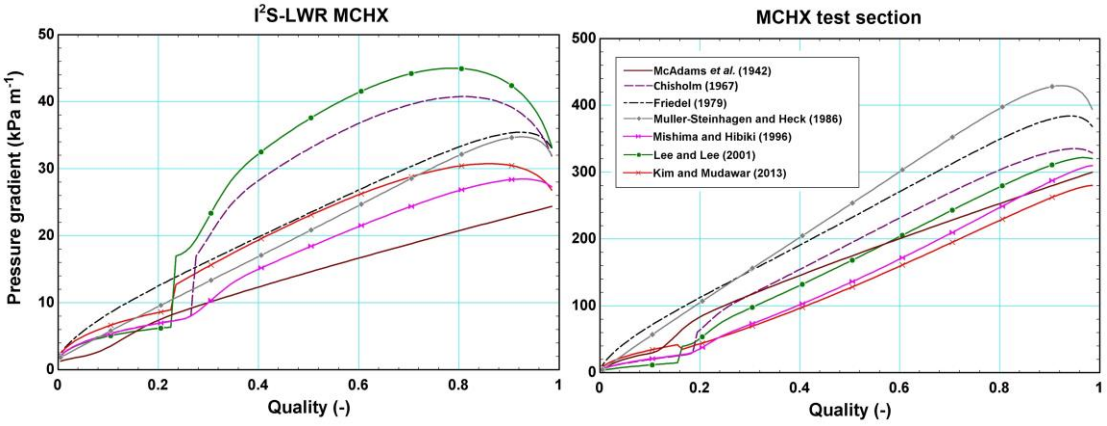

Figure 3.2: Representative frictional pressure gradients

Table 3.4: Two-phase frictional pressure gradient correlations

Author(s)	Equation
McAdams *et al.* (1942)	$\mu_{tp}=\left(\frac{x}{\mu_v}+\frac{1-x}{\mu_l}\right)^{-1}$ $\rho_{tp}=\left(\frac{x}{\rho_v}+\frac{1-x}{\rho_l}\right)^{-1}$ $\mathrm{Re}_{tp}=\frac{GD_h}{\mu_{tp}}$ $f_{tp}=\mathrm{fn}\left(\mathrm{Re}_{tp},\varepsilon/D_h\right)$ Churchill(1977b) $\left(\frac{\partial P}{\partial z}\right)_{fr}=-\frac{G^2}{2\rho_{tp}}\frac{f_{tp}}{D_h}$
Comments: HEM correlation	
Chisholm (1967)	$X^2=\left[\frac{(\partial P/\partial z)_l}{(\partial P/\partial z)_v}\right]$ $\phi_v^2=1+CX+X^2$ $\left(\frac{\partial P}{\partial z}\right)_{fr}=\phi_v^2\left(\frac{\partial P}{\partial z}\right)_v$ $C_{vv}=5,\ C_{tv}=10,\ C_{vt}=12,\ C_{tt}=20$ Viscous/turbulent based on Re_l and $\mathrm{Re}_v \le 2300$
Comments: Lockhart-Martinelli type correlation, D_h = 1.149 − 25.83 mm, Adiabatic, Fluids: Air-Water Air-Hydrocarbons Air-Oils, Developed from experimental database of Lockhart and Martinelli (1949)	
Friedel (1979)	$\rho_{tp}=\left(\frac{x}{\rho_V}+\frac{1-x}{\rho_L}\right)^{-1}$ $\mathrm{We}_{tp}=\frac{G^2D_h}{\rho_{tp}\sigma}$ $\mathrm{Fr}_{tp}=\frac{G^2}{gD_h\rho_{tp}^2}$ $A=(1-x)^2+x^2\frac{\rho_l f_{vo}}{\rho_v f_{lo}}$ $\phi_{lo}^2=A+3.24x^{0.78}(1-x)^{0.24}\left(\frac{\rho_l}{\rho_v}\right)^{0.91}\left(\frac{\mu_v}{\mu_l}\right)^{0.19}\left(1-\frac{\mu_v}{\mu_l}\right)^{0.7}\mathrm{Fr}_{tp}^{-0.0454}\mathrm{We}_{tp}^{-0.035}$ $\left(\frac{\partial P}{\partial z}\right)_{fr}=\phi_{lo}^2\left(\frac{\partial P}{\partial z}\right)_{lo}$
Comments: D_h > 4 mm, Fluids: Air-Water Air-Oils Argon-water R12, Developed from database compiled from several authors (25,000 data points)	
Müller-Steinhagen and Heck (1986)	$\left(\frac{\partial P}{\partial z}\right)_{fr}=\left[\left(\frac{\partial P}{\partial z}\right)_{lo}+2\left\{\left(\frac{\partial P}{\partial z}\right)_{vo}-\left(\frac{\partial P}{\partial z}\right)_{lo}\right\}x\right](1-x)^{1/3}+\left(\frac{\partial P}{\partial z}\right)_{vo}x^3$
Comments: D_h = 4 − 392 mm, Fluids: Air-Water Water Hydrocarbons Refrigerants, Developed from database compiled from several authors (9,313 data points)	
Mishima and Hibiki (1996)	$X^2=\left[\frac{(\partial P/\partial z)_l}{(\partial P/\partial z)_v}\right]$ $C=21\left[1-\exp(-0.333D_h)\right]$ D_h in mm $\phi_v^2=1+CX+X^2$ $\left(\frac{\partial P}{\partial z}\right)_{fr}=\phi_v^2\left(\frac{\partial P}{\partial z}\right)_v$
Comments: Lockhart-Martinelli type correlation, D_h = 1.05 - 4.06 mm, Adiabatic, Fluids: Air-Water R133-N_2 Ammonia, Developed from database compiled from six authors	

Table 3.5: Two-phase frictional pressure gradient correlations (continued)

Lee and Lee (2001)	$X^2 = \left[\frac{(\partial P/\partial z)_l}{(\partial P/\partial z)_v}\right]$ $\phi_l^2 = 1 + \frac{C}{X} + \frac{1}{X^2}$ $\psi = \frac{G(1-x)\mu_l}{\rho_l \sigma}$ $\lambda = \frac{\mu_l^2}{\rho_l \sigma D_h}$ $\left(\frac{\partial P}{\partial z}\right)_{fr} = \phi_l^2 \left(\frac{\partial P}{\partial z}\right)_l$ $C_{vv} = 6.833\times10^{-8}\lambda^{-1.317}\psi^{0.719}\mathrm{Re}_{lo}^{0.557}$, $C_{tv} = 3.627\mathrm{Re}_{lo}^{0.174}$, $C_{vt} = 6.185\times10^{-2}\mathrm{Re}_{lo}^{0.451}$, $C_{tt} = 0.048\mathrm{Re}_{lo}^{0.451}$ Viscous/turbulent based on Re_l and $\mathrm{Re}_v \leq 2000$
Comments: Lockhart-Martinelli type correlation, D_h = 0.78 − 6.67 mm (rectangular channels), Adiabatic, Fluids: Air-Water, Developed from a rectangular channels database compiled from six authors (305 data points)	
Kim and Mudawar (2013d)	$X^2 = \left[\frac{(\partial P/\partial z)_l}{(\partial P/\partial z)_v}\right]$ $\phi_l^2 = 1 + \frac{C}{X} + \frac{1}{X^2}$ $\left(\frac{\partial P}{\partial z}\right)_{fr} = \phi_l^2 \left(\frac{\partial P}{\partial z}\right)_l$ $C_{nb,vv} = 0.39\mathrm{Re}_{lo}^{0.03}\mathrm{Su}_v^{0.03}$, $C_{nb,tv} = 3.627\mathrm{Re}_{lo}^{0.174}$, $C_{nb,vt} = 6.185\times10^{-2}\mathrm{Re}_{lo}^{0.451}$, $C_{nb,tt} = 0.048\mathrm{Re}_{lo}^{0.451}$ Viscous/turbulent based on Re_l and $\mathrm{Re}_v \leq 2000$ IF $\mathrm{Re}_l < 2000 \rightarrow$ $C = C_{nb}\left(1 + 60\mathrm{We}_{lo}^{0.32}\mathrm{Bo}^{0.78}\right)$ ELSE $\rightarrow$ $C = C_{nb}\left(1 + 530\mathrm{We}_{lo}^{0.52}\mathrm{Bo}^{1.09}\right)$
Comments: Lockhart-Martinelli type correlation, D_h = 0.349 − 5.35 mm, x = 0 - 1, G =33 − 2738 kg m^{-2} s^{-1}, Fluids: Refrigerants Ammonia Water CO_2, Developed from database compiled from 16 authors (2,379 data points)	

3.2.4 Boiling heat transfer regimes

Five distinct heat transfer regimes are observed on the secondary coolant side of a once-through steam generator. Listed in order of increasing quality and in the direction of fluid flow, they include: liquid convection, subcooled boiling, saturated boiling, post-dryout, and vapor convection. Upon entering the channel, heat transfer is governed by forced liquid convection. If the heat flux in the channel is sufficiently high, fluid near the wall will eventually become superheated to the point that nucleation will occur while the bulk fluid temperature is less than the saturation temperature. This is referred to as the onset of nucleate boiling (ONB) and marks the start of subcooled boiling. As the fluid temperature continues to increase, the onset of significant void (OSV) is reached and bubbles begin to accumulate in the stream. As the mean temperature approaches the saturation temperature, nucleate boiling becomes the dominant heat transfer mechanism (fully developed subcooled boiling) and the heat transfer coefficient increases. Saturated flow boiling heat transfer, occurring when the mean fluid temperature reaches the saturation temperature, is a combination of nucleate boiling and forced convection boiling (also called convective boiling). At low quality, nucleate boiling is dominant. As quality increases, churn and annular flow is established. Heat transfer is then dominated by evaporation at the liquid-vapor interface of the thin liquid film on channel walls. The efficient cooling of the liquid film limits superheating near the wall, suppressing nucleate boiling. The magnitude of these competing mechanisms determines whether the heat transfer coefficient will increase or decrease with quality. In once-through steam generator designs with larger channels, nucleate boiling is sometimes assumed to dominate heat transfer over the entire saturated boiling length. As the vapor quality increases along the

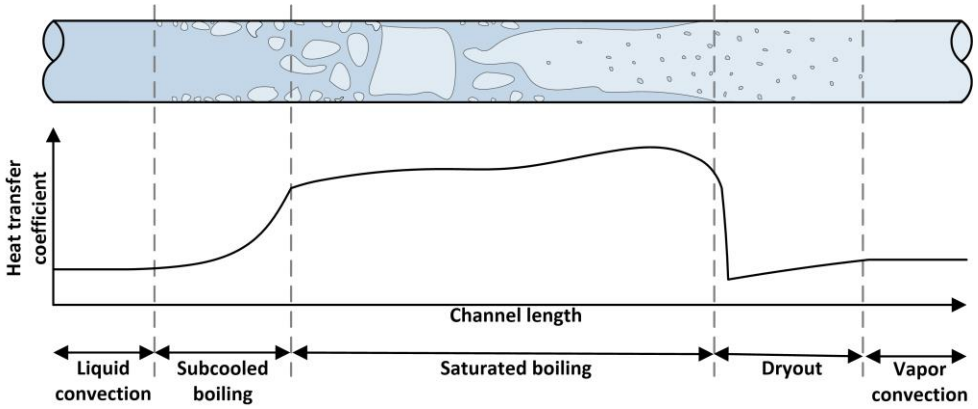

Figure 3.3: Boiling channel heat transfer regimes

length of the channel, the annular film thins and liquid is entrained in the vapor as small, dispersed droplets. Dryout incipience (di) marks the start of a decrease in heat transfer as dry regions of the wall are exposed and mist flow is established. Heat transfer between the tube and two-phase mixture is then largely governed by convection between the wall and vapor. Once the entrained droplets completely evaporate, heat transfer in the remainder of the channel is governed by forced vapor convection. Figure 3.3 shows a representative steam generator channel and the relative magnitude of the heat transfer coefficient in the five heat transfer regimes.

3.2.5 Saturated boiling heat transfer

As stated earlier, saturated flow boiling heat transfer is a combination of nucleate boiling and forced convection. After surveying correlations in the literature developed for flow boiling, Ghiaasiaan (2017) noted three common methods of accounting for these competing effects. The first type follows a method developed by Chen (1966) in which a linear combination of nucleate boiling and convective heat transfer coefficients is used to establish the boiling heat transfer coefficient, $h = h_{\mathrm{NB}} + h_{\mathrm{FC}}$. A second type of correlation uses an asymptotic sum of the two separately calculated heat transfer coefficients in which

the larger of the two makes a more significant contribution. These correlations follow the form: $h^{N} = h_{NB}^{N} + h_{FC}^{N}$. This same method, discussed by Churchill and Usagi (1972), is used by Churchill in his friction factor and Nusselt number correlations (Churchill, 1977a, b) for single-phase flow in the laminar, transition, and turbulent regimes. A third type uses different methods to calculate the heat transfer coefficient depending on the flow regime. These can account for fundamental differences in heat transfer mechanism. For example, in horizontal flow, either stratified or annular flow may take place at similar qualities. In the annular flow regime, heat transfer is dominated by forced convection and nucleate boiling is suppressed. In stratified flow, nucleate boiling in the bottom of the channel may be the most important factor. However, this type of correlation has the added complexity of requiring an accurate flow regime map. Correlations developed for pool boiling are often employed to determine the nucleate boiling contribution to the heat transfer coefficient. These correlations generally have a large uncertainty, especially when not accounting for fluid-surface effects. Additionally, the influence of bulk fluid motion on nucleate boiling is not explicitly captured. Empirical forced convection correlations have been developed based on a method similar to the two-phase multiplier concept used in two-phase frictional pressure drop correlations. Eq. (3.35) shows the correlation developed by Dengler and Addoms (1956) in which the liquid (1) heat transfer coefficient is multiplied by a two-phase convection enhancement factor. Analytical models for convective heat transfer in thin liquid films have been developed, although these are more commonly used to describe annular condensation. Several important examples of flow boiling heat transfer correlations are discussed below.

$$\frac{h_{\mathrm{FC}}}{h_{\mathrm{l}}} = 3.5 X_{\mathrm{tt}}^{-1/2}$$
$$X_{\mathrm{tt}} = \left(\frac{\rho_{\mathrm{v}}}{\rho_{\mathrm{l}}}\right)^{0.5} \left(\frac{\mu_{\mathrm{l}}}{\mu_{\mathrm{v}}}\right)^{0.1} \left(\frac{1-x}{x}\right)^{0.9} \tag{3.35}$$

Bennett and Chen (1980) updated the widely used Chen (1966) correlation, which sums the forced convection and nucleate boiling heat transfer coefficients. The forced convection contribution is calculated using the Dittus and Boelter (1930) correlation multiplied by a two-phase enhancement factor, *E*, shown in Eq. (3.37). The enhancement factor was derived using the Reynolds analogy from the two-phase and liquid (l) pressure gradients, while also accounting for differences in the rates of momentum and temperature diffusion (i.e., $\mathrm{Pr} \neq 1$).

$$h_{\mathrm{FC}} = 0.023 \mathrm{Re}_{\mathrm{l}}^{0.8} \mathrm{Pr}_{\mathrm{l}}^{0.4} \frac{k_{\mathrm{l}}}{D_{\mathrm{h}}} E \tag{3.36}$$

$$E = \left(\frac{\mathrm{Pr}_{\mathrm{l}}+1}{2}\right)^{0.444} \left(1 + \frac{1}{X_{\mathrm{tt}}^{0.5}}\right)^{1.78} \tag{3.37}$$

The nucleate boiling contribution was modified from the pool boiling work of Forster and Zuber (1955), shown below in Eq. (3.38), where $\Delta T_{\mathrm{sat}} = T_{\mathrm{wall}} - T_{\mathrm{sat}}(P)$ and $\Delta P_{\mathrm{sat}} = P_{\mathrm{sat}}(T_{\mathrm{wall}}) - P$. A suppression factor, S, is used to account for the reduction of nucleate boiling. Forced convection heat transfer decreases superheat near the wall, required for nucleate boiling. This phenomenon is modeled by the decrease of the suppression factor as the liquid (l) Reynolds number and convection enhancement increase.

$$h_{\mathrm{NB}} = 0.00122 \frac{k_{\mathrm{l}}^{0.79} c_{\mathrm{p,l}}^{0.45} \rho_{\mathrm{l}}^{0.49}}{\sigma^{0.5} \mu_{\mathrm{l}}^{0.29} i_{\mathrm{fg}}^{0.24} \rho_{\mathrm{v}}^{0.24}} \Delta T_{\mathrm{sat}}^{0.24} \Delta P_{\mathrm{sat}}^{0.75} S \tag{3.38}$$

$$S = 0.9622 - 0.5822 \tan^{-1}\left(\frac{\mathrm{Re}_\mathrm{l} E}{6.18 \times 10^4} \right) \tag{3.39}$$

Liu and Winterton (1991) developed a widely cited correlation using an enhancement factor for forced convection and a suppression factor for nucleate boiling. They cited the overprediction of the Chen (1966) correlation at high quality and underprediction at lower qualities, raising questions about the validity of the additive approach. By using an asymptotic method, Eq. (3.40), the contribution of nucleate boiling would be further reduced at high qualities as the convective contribution became larger by comparison.

$$h^2 = \left(E_2 E h_\mathrm{lo} \right)^2 + \left(S_2 S h_\mathrm{NB} \right)^2 \tag{3.40}$$

The Dittus and Boelter (1930) correlation is again used as a basis for forced convection. However, they use the liquid-only (lo) Reynolds number, considering the entire flow rate to be in the liquid phase.

$$h_\mathrm{lo} = 0.023 \mathrm{Re}_\mathrm{lo}^{0.8} \mathrm{Pr}_\mathrm{l}^{0.4} \frac{k_\mathrm{l}}{D_\mathrm{h}} \tag{3.41}$$

$$E_1 = \left[1 + x \mathrm{Pr}_\mathrm{l} \left(\frac{\rho_\mathrm{l}}{\rho_\mathrm{v}} - 1 \right) \right]^{0.35} \tag{3.42}$$

The Cooper (1984) correlation, Eq. (3.43), is used to determine the nucleate boiling heat transfer coefficient. Cooper showed that the reduced pressure could accurately account for the influence of fluid properties on nucleate boiling, simplifying correlations. Therefore, his correlation is only a function of the reduced pressure, $P_\mathrm{r} = P / P_\mathrm{c}$, molecular mass, *M*, and wall heat flux.

$$h_{NB} = 55 P_r^{0.12} \left(-\log_{10} P_r\right)^{-0.55} M^{-0.5} q^{"2/3} \tag{3.43}$$

$$S_1 = \left(1 + 0.055 E^{0.1} \mathrm{Re}_{lo}^{0.16}\right)^{-1} \tag{3.44}$$

They also include a second set of suppression/enhancement factors based on the liquid-only (lo) Froude number: $\mathrm{Fr}_{lo} = G^2 / \left(\rho_l^2 \, g \, D_h\right)$. The Froude number provides a dimensionless comparison of inertial forces over gravitational forces. It can be used as a threshold for the occurrence of stratified flow. In this capacity, it serves as a simplistic flow regime map, stratified or not stratified, in this and other correlations. For vertical tubes, and for horizontal tubes with Fr > 0.05, E_2 = 1 and F_2 = 1. Otherwise, Eq. (3.45) is used for horizontal tubes in stratified flow.

$$\begin{aligned} E_2 &= \mathrm{Fr}_{lo}^{(0.1-2\mathrm{Fr}_{lo})} \\ S_2 &= \mathrm{Fr}_{lo}^{0.5} \end{aligned} \tag{3.45}$$

Bertsch *et al.* (2008) compared 25 different flow boiling heat transfer correlations developed for both macrochannels and microchannels against a database assembled from ten independent microchannel studies. The database included eight different fluids, hydraulic diameters ranging from 0.16 to 2.01 mm, mass fluxes from 20 to 3000 kg m^{-2} s^{-1}, qualities from 0 to 1, and heat fluxes from 0.4 to 115 kW m^{-2}. Single and parallel channels experiments were also included. They noted that correlations developed for microchannels fared no better than those developed for macrochannels, which they attributed partially to the small data sets used in the development of some correlations. They also concluded that the Cooper (1984) correlation, developed for pool boiling, showed the lowest AAD from the experimental database. A second pool boiling correlation, Gorenflo (1993), was also accurate in predicting experimental results. While

somewhat surprising, the authors noted that several other investigators have drawn similar conclusions about the importance of nucleate boiling in microchannel flows. Indeed, it seems odd that a correlation developed for pool boiling would accurately describe nucleate boiling in a microchannel, which may be influenced by bubble confinement and inertial/shear forces from the bulk fluid motion. Additionally, the suppression of nucleate boiling at high quality is ignored. However, the Cooper (1984) correlation had an AAD of 36.1% and only predicted 48.1% of the data within ±30%. The authors also observed that the Cooper (1984) correlation underpredicted heat transfer at low vapor qualities and slightly overpredicted it at higher qualities.

One such nucleate boiling dominated microchannel correlation was developed by Haynes and Fletcher (2003), who tested refrigerants in a circular tubes with diameters of 0.92 and 1.95 mm, mass fluxes from 110 to 1840 kg m^{-2} s^{-1}, heat fluxes from 11 to 170 kW m^{-2}, and qualities from -0.35 (subcooled) to 1. They found that both subcooled and saturated flow boiling could be represented by the linear combination of liquid-only (lo) and nucleate boiling heat transfer coefficients, as shown in Eq. (3.46). The nucleate boiling term is multiplied by $\Delta T_{\text{sat}} = T_{\text{wall}} - T_{\text{sat}}$ and divided by $\Delta T_{\text{wall}} = T_{\text{wall}} - T$, making the correlation applicable for subcooled boiling as well. In saturated flow boiling, it can safely be assumed that the mean temperature of the fluid is equal to the saturation temperature. The liquid-only (lo) heat transfer coefficient is calculated using the Gnielinski (1976) correlation for Re_{lo} great than 2300.

$$h = h_{\text{lo}} + h_{\text{NB}} \frac{\Delta T_{\text{sat}}}{\Delta T_{\text{wall}}} \tag{3.46}$$

The Gorenflo (1993) pool boiling correlation is used to determine the nucleate boiling heat transfer coefficient. In calculating the nucleate boiling heat transfer coefficient, the authors chose to use the heat flux from nucleate boiling while ignoring the contribution from forced convection, as shown in Eq. (3.49). The Gorenflo (1993) correlation uses a reference wall heat flux, $q_0^{''}$ = 20 kW m^{-2}, surface roughness, ε_0 = 0.4 μm, and heat transfer coefficient, $h_{\mathrm{NB},0}$ = 5.6 kW m^{-2} K^{-1} (for water). The pressure correction factor, F_{PR}, and coefficient, *n*, have been correlated for water as a function of reduced pressure and are shown in Eq. (3.48). It should be noted that quality plays no role in the correlation.

$$\frac{h_{\mathrm{NB}}}{h_{\mathrm{NB},0}} = F_{\mathrm{PR}} \left(\frac{q_{\mathrm{NB}}^{''}}{q_0^{''}} \right)^n \left(\frac{\varepsilon}{\varepsilon_0} \right)^{0.133} \tag{3.47}$$

$$F_{\mathrm{PR}} = 1.73 P_{\mathrm{r}}^{0.27} + \left(6.1 + \frac{0.68}{1 - P_{\mathrm{r}}} \right) P_{\mathrm{r}}^{0.27} \tag{3.48}$$

$$n = 0.9 - 0.3 P_{\mathrm{r}}^{0.15}$$

$$q''_{\mathrm{NB}} = q'' - q''_{\mathrm{FC}} = q'' - h_{\mathrm{lo}} \left(T_{\mathrm{wall}} - T \right) \tag{3.49}$$

After expanding their microchannel database, Bertsch *et al.* (2009) proposed a Chen-type heat transfer correlation. The Cooper (1984) correlation was chosen to calculate the nucleate boiling heat transfer coefficient. Based on the observation of several authors that bubble suppression was not dependent on channel size, a linear suppression term based on quality was selected with the form: $S = 1 - x$. The forced convection term was developed based on vapor-only (vo) and liquid-only (lo) heat transfer coefficients as shown in Eq. (3.50). The Hausen (1943) correlation for developing laminar flow, Eq. (3.51), was selected for both the liquid and vapor heat transfer coefficients. They concluded that the enhancement factor should decrease with the confinement number, especially in the higher quality annular flow regime. They used a polynomial to capture the effect of quality on

forced convection enhancement. The resulting correlation is shown in Eq. (3.52), is able to predict over 60% of heat transfer coefficients in the database within ±30%, and has an AAD of 28%.

$$h_{FC} = h_{lo}\left(1-x\right) + h_{vo}x \tag{3.50}$$

$$h_{lo} = \left(3.66 + \frac{0.0668\dfrac{D_h}{l_{ch}}\mathrm{Re}_{lo}\,\mathrm{Pr}_l}{1+0.04\left(\dfrac{D_h}{l_{ch}}\mathrm{Re}_{lo}\,\mathrm{Pr}_l\right)} \right)\frac{k}{D_h} \tag{3.51}$$

$$h = h_{NB}\left(1-x\right) + h_{FC}\left[1+80\left(x^2-x^6\right)\exp\left(-0.6\mathrm{N}_{con}\right)\right] \tag{3.52}$$

Figure 3.4 shows nine different boiling heat transfer coefficient correlations for the fluid conditions described in Table 3.1. At higher reduced pressure, nucleate boiling is more efficient as a result of an increase in possible nucleation sites and shorter waiting times before bubbles can grow following a departure (McGillis *et al.*, 1991). This trend is easily observed in the Cooper (1984) correlation, Eq. (3.43). Additionally, the vapor has higher density at higher pressure, resulting in less acceleration as the quality increases and decreasing the effect of two-phase forced convection. Therefore, nucleate boiling tends to be the dominant heat transfer mechanism at higher pressure while convective heat transfer

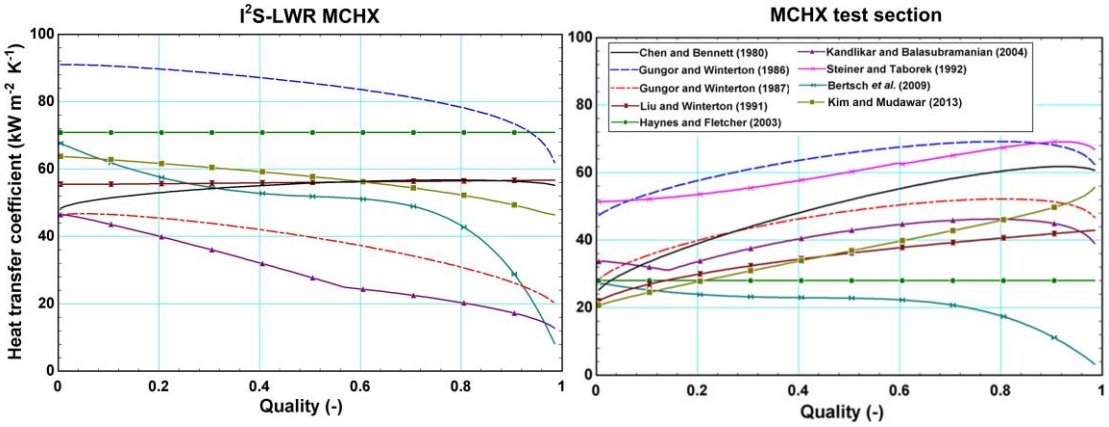

Figure 3.4: Representative saturated boiling heat transfer coefficients

exerts a greater influence at lower pressure. These trends can be observed at the different pressures of the I^2S-LWR and test section conditions. Overall, the heat transfer coefficients decrease with quality for the I^2S-LWR conditions in which nucleate boiling appears to be the more effective mode of heat transfer. As the quality increases, nucleate boiling is suppressed, causing a decrease in heat transfer. The opposite trend can be observed for lower pressure test section conditions where forced convection is more effective. At these conditions, suppression of nucleate boiling is more than offset by the increase in forced convection heat transfer as the quality increases. It can also be observed that there are differences in the magnitudes of the heat transfer coefficients over the quality range for both sets of conditions. More information on the different correlations is available in Table 3.5.

Table 3.5: Boiling heat transfer coefficient correlations

Author(s)	Equation
Bennett and Chen (1980)	$E = \left(\frac{\mathrm{Pr_l}+1}{2}\right)^{0.444}\left(1+X_{\mathrm{tt}}^{-0.5}\right)^{1.78} \qquad S = 0.9622 - 0.5866\tan^{-1}\left(\frac{\mathrm{Re_l}E^{1.25}}{6.18\times10^4}\right)$ $h_{\mathrm{NB}} = 0.00122\frac{k_{\mathrm{l}}^{0.79}c_{\mathrm{p,l}}^{0.45}\rho_{\mathrm{l}}^{0.49}}{\sigma^{0.5}\mu_{\mathrm{l}}^{0.29}h_{\mathrm{vap}}^{0.24}\rho_{\mathrm{v}}^{0.24}}\Delta T_{\mathrm{sat}}^{0.24}\Delta P_{\mathrm{sat}}^{0.75}S \qquad h_{\mathrm{FC}} = 0.023\mathrm{Re_l}^{0.8}\mathrm{Pr_l}^{0.4}\left(k_{\mathrm{l}}/D_{\mathrm{h}}\right)E \qquad h = h_{\mathrm{FC}} + h_{\mathrm{NB}}$
Comments: Chen type correlation, x = 0.01 − 0.71, q'' = 6 − 2,400 kW m^{-2}, Fluids: Water Ethylene-glycol	
Gungor and Winterton (1986)	$h_{\mathrm{NB}} = 55P_{\mathrm{r}}^{0.12}\left[-\log_{10}\left(P_{\mathrm{r}}\right)\right]^{-0.55}M^{-0.5}q''^{2/3} \qquad h_{\mathrm{l}} = 0.023\mathrm{Re_l}^{0.8}\mathrm{Pr_l}^{0.4}\left(k_{\mathrm{l}}/D_{\mathrm{h}}\right)$ $E_1 = 1 + 24000\mathrm{Bo}^{1.16} + 1.37\left(1/X_{\mathrm{tt}}\right)^{0.86} \qquad S_1 = \left(1+1.15\times10^{-6}E_1^2\mathrm{Re_l}^{1.17}\right)^{-1}$ IF $\mathrm{Fr_{lo}} < 0.05 \rightarrow \quad \mathrm{E_2} = \mathrm{Fr_{lo}}^{(0.1-2\mathrm{Fr_{lo}})} \quad S_2 = \mathrm{Fr_{lo}}^{1/2} \qquad$ ELSE $\rightarrow \quad E_2 = 1 \quad S_2 = 1$ $h = h_{\mathrm{l}}E_1E_2 + h_{\mathrm{NB}}S_1S_2$
Comments: Chen type correlation, D_{h} = 2.95 − 32 mm, x = 0 - 1, q'' = 1.1 − 2,280 kW m^{-2}, G = 67 − 61518 kg m^{-2} s^{-1}, Fluids: Water Refrigerants Hydrocarbons, Developed from database compiled from 30 sources (4,202 data points)	
Gungor and Winterton (1987)	$h_{\mathrm{l}} = 0.023\mathrm{Re_l}^{0.8}\mathrm{Pr_l}^{0.4}\left(k_{\mathrm{l}}/D_{\mathrm{h}}\right) \qquad$ IF $\mathrm{Fr_{lo}} < 0.05 \rightarrow \quad \mathrm{E_2} = \mathrm{Fr_{lo}}^{(0.1-2\mathrm{Fr_{LO}})} \qquad$ ELSE $\rightarrow \quad \mathrm{E_2} = 1$ $h = h_{\mathrm{l}}\left(1+3000\mathrm{Bo}^{0.86}+1.12\left(\frac{x}{1-x}\right)^{0.75}\left(\frac{\rho_{\mathrm{l}}}{\rho_{\mathrm{v}}}\right)^{0.41}\right)E_2$
Comments: D_{h} = 2.95 − 32 mm, x = 0 - 1, q'' = 1.1 − 2,280 kW m^{-2}, G = 67 − 61518 kg m^{-2} s^{-1}, Fluids: Water Refrigerants Hydrocarbons, Developed from database compiled from 30 sources (4,202 data points)	
Liu and Winterton (1991)	$h_{\mathrm{NB}} = 55P_{\mathrm{r}}^{0.12}\left[-\log_{10}\left(P_{\mathrm{r}}\right)\right]^{-0.55}M^{-0.5}q''^{2/3} \qquad h_{\mathrm{lo}} = 0.023Re_{\mathrm{lo}}^{0.8}\mathrm{Pr_l}^{0.4}\left(k_{\mathrm{l}}/D_{\mathrm{h}}\right)$ $E_1 = \left(1+x\mathrm{Pr_l}\left[\left(\frac{\rho_{\mathrm{l}}}{\rho_{\mathrm{v}}}\right)-1\right]\right)^{0.35} \qquad S_1 = \left(1+0.55E^{0.1}\mathrm{Re_{lo}}^{0.16}\right)^{-1}$ IF $\mathrm{Fr_{lo}} < 0.05 \rightarrow \quad \mathrm{E_2} = \mathrm{Fr_{lo}}^{(0.1-2\mathrm{Fr_{lo}})} \quad S_2 = \mathrm{Fr_{lo}}^{1/2} \qquad$ ELSE $\rightarrow \quad \mathrm{E_2} = 1 \quad S_2 = 1$ $h = \left[\left(h_{\mathrm{lo}}E_1E_2\right)^2 + \left(h_{\mathrm{NB}}S_1S_2\right)^2\right]^{1/2}$

Table 3.5: Boiling heat transfer coefficient correlations (continued)

Comments: Asymptotic correlation, D_h = 2.95 – 32 mm, x = 0 – 1, q'' = 1.1 – 2,280 kW m^{-2}, G = 67 – 61518 kg m^{-2} s^{-1}, Fluids: Water Refrigerants Hydrocarbons, Developed from a database compiled from 30 sources (4,202 data points)	
Steiner and Taborek (1992)	IF $\mathrm{Re_{lo}} > 2300$ (Turbulent) $\rightarrow$ $f_{lo} = \left(1.58\ln\left(\mathrm{Re_{lo}}\right) - 3.28\right)^{-2}$ $h_{lo} = \dfrac{\left(\mathrm{Re_{lo}} - 1000\right)\mathrm{Pr_l}\left(f_{lo}/2\right)}{1 + 12.7\left[\left(f_{lo}/2\right)^{1/2}\left(\mathrm{Pr_l}^{2/3} - 1\right)\right]}\dfrac{k_l}{D_h}$ ELSE (Laminar) $\rightarrow$ $h_{lo} = \mathrm{fn}(\mathrm{Re_{lo}}, \mathrm{Pr_l}, \varepsilon/D_h)\left(k_l/D_h\right)$ (Churchill 1977a) (Same procedure to calucate h_{vo}) IF x < 0.6 $\rightarrow$ $E = \left[\left(1-x\right)^{1.5} + 1.9x^{0.6}\left(\rho_l/\rho_v\right)^{0.35}\right]^{1.1}$ ELSE $\rightarrow$ $E = \left\{\left[\left(1-x\right)^{1.5} + 1.9x^{0.6}\left(\rho_l/\rho_v\right)^{0.35}\right]^{-2..2} + \left[\left(h_{vo}/h_{lo}\right)x^{0.01}\left(1+8\left(1-x\right)^{0.7}\right)\left(\rho_l/\rho_v\right)^{0.67}\right]^{-2}\right\}^{-0.5}$ $F_{NB} = F_{PR}\left(\dfrac{q''}{q''_{NB,0}}\right)^{n}\left(\dfrac{D_h}{D_0}\right)^{-0.4}\left(\dfrac{\varepsilon}{\varepsilon_0}\right)^{-0.133}F\left(M\right)$ $F_{PR} = 2.816P_r^{0.45} + \left(3.4 + \dfrac{1.7}{1-P_r^7}\right)P_r^{3.7}$ $n = 0.8 - 0.1\exp(1.75P_r)$ $F\left(M\right) = 0.377 + 0.199\ln(M) + 2.8427\times10^{-5}M^2$ $h_{NB,0} = 25800$ W m^{-2} K^{-1} $q''_{NB,0} = 150000$ W m^{-2} $D_0 = 0.01$ m $\varepsilon_0 = 1.0\times10^{-6}$m $h = \left[\left(h_{FC}E\right)^3 + \left(h_{NB,0}F_{NB}\right)^3\right]^{1/3}$
Comments: Asymptotic correlation, D_h = 1 – 32 mm, x = 0.0 – 1.00, q'' = 0.8 – 4,600 kW m^{-2}, G = 3.9 – 4,850 kg m^{-2} s^{-1}, Fluids: Water Hydrocarbons Refrigerants Cryogenics, Developed from a large experimental database compiled at the University of Karlsruhe	
Haynes and Fletcher (2003)	IF $\mathrm{Re_{lo}} > 2300$ (Turbulent) $\rightarrow$ $f_{lo} = \left(1.58\ln\left(Re_{lo}\right) - 3.28\right)^{-2}$ $h_{lo} = \dfrac{\left(\mathrm{Re_{lo}} - 1000\right)\mathrm{Pr_l}\left(f_{lo}/2\right)}{1 + 12.7\left[\left(f_{lo}/2\right)^{1/2}\left(\mathrm{Pr_l}^{2/3} - 1\right)\right]}\dfrac{k_l}{D_h}$ ELSE (Laminar) $\rightarrow$ $h_{lo} = \left(4.36 + \dfrac{0.0273}{z_{ch}^{\ *} + 0.0233{l_{ch}}^{*1/3}}\right)\dfrac{k_l}{D_h}$ $z_{ch}^{\ *} = \left(z_{ch}/D_h\right)/\left(\mathrm{Re_{lo}Pr_l}\right)$ $l_{ch}^{\ *} = \left(l_{ch}/D_h\right)/\left(\mathrm{Re_{lo}Pr_l}\right)$ $F_{PR} = 1.73P_r^{0.27} + \left(6.1 + \dfrac{0.68}{1-P_r}\right)P_r^2$ $n = 0.9 - 0.3P_r^{0.15}$ $q''_{FC} = h_{lo}\left(T_{wall} - T\right)$ $q''_{NB} = q'' - q''_{FC}$ $h_{NB} = h_0F_{PR}\left(q''_{NB}/q''_0\right)^n\left(\varepsilon/\varepsilon_0\right)^{0.133}$ $h_0 = 5600$ W m^{-2} K^{-1} $\varepsilon_0 = 0.4\times10^{-6}$m $q''_0 = 20000$ W m^{-2} $h = h_{FC} + h_{NB}$

Table 3.5: Boiling heat transfer coefficient correlations (continued)

Comments: Single-phase liquid and nucleate boiling correlation, D_h = 0.92 – 1.95 mm, x = 0.0 – 1.00, q'' = 11 – 170 kW m^{-2}, G = 110 – 1840 kg m^{-2} s^{-1}, Fluids: Refrigerants	
Kandlikar and Balasubramanian (2004)	IF $\mathrm{Re_{lo}} > 3000$ (Turbulent) $\rightarrow$ $f_{lo} = \left(1.58\ln\left(\mathrm{Re_{lo}}\right) - 3.28\right)^{-2}$ $h_{lo} = \dfrac{\left(\mathrm{Re_{lo}} - 1000\right)\mathrm{Pr_L}\left(f_{lo}/2\right)}{1 + 12.7\left[\left(f_{lo}/2\right)^{1/2}\left(\mathrm{Pr_l}^{2/3} - 1\right)\right]}\dfrac{k_l}{D_h}$ IF $\mathrm{Re_{lo}} < 1600$ (Laminar) $\rightarrow$ $h_{lo} = 4.364\left(k_l / D_h\right)$ ELSE (Transition) $\rightarrow h_{lo}$ = Linear interpolation between laminar and turbulent IF $\mathrm{Fr_{lo}} \le 0.04$) $\rightarrow$ $f_2\left(\mathrm{Fr_{lo}}\right) = \left(25\mathrm{Fr_{lo}}\right)^{0.3}$ ELSE $\rightarrow$ $f_2\left(\mathrm{Fr_{lo}}\right) = 1$ $h_{NBD} = h_{lo}\left(0.6683\mathrm{Co}^{-0.2}\left(1-x\right)^{0.8} f_2\left(\mathrm{Fr_{lo}}\right) + 1058.0\left(1-x\right)^{0.8}\mathrm{Bo}^{0.7}\right)$ $h_{CBD} = h_{lo}\left(1.136\mathrm{Co}^{-0.9}\left(1-x\right)^{0.8} f_2\left(\mathrm{Fr_{lo}}\right) + 667.2\left(1-x\right)^{0.8}\mathrm{Bo}^{0.7}\right)$ $h = \max\left(h_{CBD}, h_{NBD}\right)$
Comments: D_h = 0.19 – 2.92 mm, x = 0 – 0.98, q'' = 5 – 91 kW m^{-2}, G = 50 – 570 kg m^{-2} s^{-1}, Fluids: Water Refrigerants, Developed from database compiled from four authors	
Bertsch *et al.* (2009)	$h_{lo} = \left(3.66 + \dfrac{0.0668\left(D_h/l_{ch}\right)\mathrm{Re_{lo}Pr_l}}{1 + 0.04\left[\left(D_h/l_{ch}\right)\mathrm{Re_{lo}Pr_l}\right]^{2/3}}\right)\dfrac{k_l}{D_h}$ $h_{vo} = \left(3.66 + \dfrac{0.0668\left(D_h/l_{ch}\right)\mathrm{Re_{vo}Pr_v}}{1 + 0.04\left[\left(D_h/l_{ch}\right)\mathrm{Re_{vo}Pr_v}\right]^{2/3}}\right)\dfrac{k_v}{D_h}$ $h_{FC} = h_{vo}x + h_{lo}\left(1-x\right)$ $h_{NB} = 55P_r^{0.12}\left[-\log_{10}\left(P_r\right)\right]^{-0.55} M^{-0.5} q''^{2/3}$ $E = 1 + 80\left(x^2 - x^6\right)\exp\left(-0.6N_{con}\right)$ $S = 1 - x$ $h = h_{FC}E + h_{NB}S$
Comments: Chen type correlation, D_h = 0.16 – 2.92 mm, x = 0 – 1, q'' = 4 – 1150 kW m^{-2}, G = 50 – 570 kg m^{-2} s^{-1}, Fluids: Water Refrigerants N_2, Developed from database compiled from 14 authors (3899 data points)	
Kim and Mudawar (2013c)	$h_l = 0.023\mathrm{Re_l}^{0.8}\mathrm{Pr_l}^{0.4}\left(k_l/D_h\right)$ $h_{FC} = \left(5.2\mathrm{Bo}^{0.08}\mathrm{We_{lo}}^{-0.54} + 3.5\left(1/X_{tt}\right)^{0.94}\left(\rho_v/\rho_l\right)^{0.25}\right)h_l$ $h_{NB} = \left(2345\mathrm{Bo}^{0.7}P_r^{0.38}\left(1-x\right)^{-0.51}\right)h_l$ $h = \left(h_{FC}^2 + h_{NB}^2\right)^{1/2}$
Comments: Asymptotic correlation, D_h = 0.19 – 6.5 mm, x = 0 – 1, G = 19 – 1608 kg m^{-2} s^{-1}, Fluids: Water Refrigerants CO_2, Developed from database compiled from 37 authors (10,850 data points)	

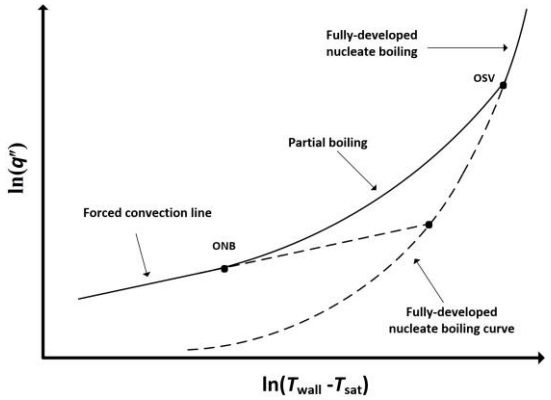

Figure 3.5: Boiling curve in the subcooled boiling region

3.2.6 Subcooled boiling

Subcooled boiling heat transfer occurs following the onset of nucleate boiling (ONB) and until the mean fluid temperature reaches saturation. After ONB, heat transfer is governed by both liquid forced convection and partial nucleate boiling. Following the onset of significant void (OSV), nucleate boiling becomes the dominant mode of heat transfer. Figure 3.5 shows the boiling curve in the subcooled boiling region (Ghiaasiaan, 2017).

Rohsenow and Bergles (1964) developed a mechanistic model for the mechanical stability of bubbles at the ONB. They then developed a curve fit for their model resulting in Eq. (3.53), in which P is the pressure in bar. This correlation provides a relationship between wall temperature and heat flux at the ONB. For heat exchangers considered in the present study, the ONB occurs shortly after the wall temperature exceeds the saturation temperature (< 1°C).

$$\left(T_{\text{wall}} - T_{\text{sat}}\right)_{\text{ONB}} = 0.556\left(\frac{q''}{1082P^{1.156}}\right)^{n} \qquad (3.53)$$
$$n = 0.463P^{0.0234}$$

Many correlations have been developed for fully developed subcooled boiling. One such microchannel correlation was developed by Kandlikar (1998) and is shown in Eq. (3.54) . The single-phase convective heat transfer coefficient, h_{lo}, is calculated using the Gnielinski (1976) correlation for $2{,}000 \leq \mathrm{Re}_{lo} \leq 10^4$ and $0.5 \leq \mathrm{Pr}_l \leq 2{,}000$. F_{fl} is a fluid-surface parameter derived from experimental data and is equal to 1 for water.

$$q'' = h\left(T_{wall} - T\right) = \left[1058\left(G\, i_{fg}\right)^{-0.7} F_{fl} h_{lo} \left(T_{wall} - T_{sat}\right)\right]^{3.33} \tag{3.54}$$

Correlations are also available in the literature for heat transfer in the partial boiling regime. These correlations often involve contributions from convective and fully-developed nucleate boiling heat transfer. Rohsenow and Bergles (1964) proposed an asymptotic method using the calculated convective heat flux, $q''_{FC} = h_{lo}(T_{wall} - T)$, and the calculated fully developed nucleate boiling heat flux, $q''_{NB} = \mathrm{fn}(T_{wall} - T_{sat})$. The correlation is shown in Eq. (3.55) and is also a function of the fully developed subcooled boiling heat flux at the ONB, $q''_{NB,ONB}$. However, when the ONB occurs at $T_{wall} \approx T_{sat}$, the subcooled boiling heat flux at ONB is approximately zero. The previously discussed correlation developed by Haynes and Fletcher (2003) was developed using data from the ONB through the saturated flow boiling regime and uses a simple linear combination of convective and nucleate boiling heat transfer coefficients. This correlation allows one to use a single correlation between the ONB through saturated flow boiling. The saturate boiling correlations of Gungor and Winterton (1986) and Liu and Winterton (1991), shown in Table 3.5, can also be used in the subcooled boing regime according to Eq. (3.56) and Eq. (3.57).

$$q'' = h\left(T_{\text{wall}} - T\right) = q''_{\text{FC}}\left(1 + \left[\frac{q''_{\text{NB}}}{q''_{\text{FC}}}\left(1 - \frac{q''_{\text{NB,ONB}}}{q''_{\text{NB}}}\right)\right]^2\right)^{1/2} \tag{3.55}$$

$$q'' = h\left(T_{\text{wall}} - T\right) = S_2 S_1 h_{\text{NB}}\left(T_{\text{wall}} - T_{\text{sat}}\right) + E_2 E_1 h_{\text{l}}\left(T_{\text{wall}} - T\right) \tag{3.56}$$

$$q'' = h\left(T_{\text{wall}} - T\right) = \sqrt{\left[S_2 S_1 h_{\text{NB}}\left(T_{\text{wall}} - T_{\text{sat}}\right)\right]^2 + \left[E_2 E_1 h_{\text{lo}}\left(T_{\text{wall}} - T\right)\right]^2} \tag{3.57}$$

The onset of significant void (OSV) marks the point when bubbles leave nucleation sites and accumulate in the stream. Before the OSV, the pressure drop is not significantly different than that of the single-phase liquid. After the OSV, a two-phase pressure drop correlation can be applied using the non-equilibrium quality, x_{a}. The OSV can also be used to delineate partial boiling and fully developed subcooled boiling. Saha and Zuber (1974) developed a widely used correlation for the OSV, shown in Eq. (3.58). They identified a hydrodynamically and thermally controlled OSV and developed a correlation for each.

$$\begin{array}{lll} \text{For } \text{Re}_{\text{lo}}\,\text{Pr}_{\text{l}} > 70{,}000 & \text{(Hydrodynamically controlled)} & x_{\text{OSV}} = -154\,\text{Bo} \\ \text{For } \text{Re}_{\text{lo}}\,\text{Pr}_{\text{l}} < 70{,}000 & \text{(Thermally controlled)} & x_{\text{OSV}} = -0.0022\,\text{Bo}\,\text{Re}_{\text{lo}}\,\text{Pr}_{\text{l}} \end{array} \tag{3.58}$$

Fluid conditions in the heat exchangers in this study have relatively small boiling numbers (Bo) and are generally within the thermally controlled region. Under these conditions, the Saha and Zuber correlation predicts the OSV near saturation, $x_{\text{OSV}} \approx 0$. In cases when the OSV occurs at a significant degree of subcooling, the actual quality can be calculated using the correlation of Ahmad (1970), shown in Eq. (3.59).

$$x_{\text{a}} = \frac{x - x_{\text{OSV}}\exp\left(x / x_{\text{OSV}} - 1\right)}{1 - x_{\text{OSV}}\exp\left(x / x_{\text{OSV}} - 1\right)} \tag{3.59}$$

Figure 3.6 shows six subcooled boiling heat transfer correlations over a range of subcooled temperatures for a heat flux of 100 kW m^{-2} and the fluid conditions listed in Table 3.1. The single-phase liquid Churchill (1977a) heat transfer coefficient is also shown for

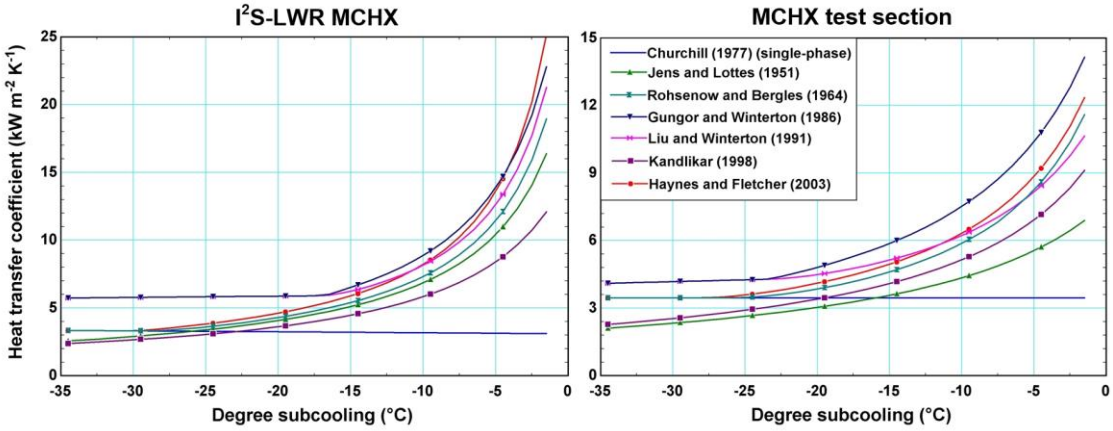

Figure 3.6: Representative subcooled boiling heat transfer coefficients

comparison. The Jens and Lottes (1951) and Kandlikar (1998) correlations are both for fully developed subcooled boiling and therefore have values lower than the single-phase correlation at high degrees of subcooling. All of the correlations show that the heat transfer coefficient rapidly increases as the fluid approaches saturation. At I^2S-LWR conditions, the nucleate boiling contribution is expected to be larger due to the higher reduced pressure. Therefore, there is a larger increase in the heat transfer coefficient as the fluid approaches saturation as compared to the lower pressure test section conditions.

3.2.7 Dryout and post-dryout heat transfer

Critical heat flux (CHF) describes a state of decreased heat transfer efficiency as a result of limited liquid contact with the wall. Critical heat flux conditions (CHFC) describe the situation/properties at which CHF first occurs. In the case of a heated channel in which fluid properties change along the length, CHFC manifest as a sharp increase in local wall temperature for a prescribed heat flux or as a decrease in local heat flux for a constant wall temperature. In a heat exchanger in which neither of these boundary conditions apply, both, an increase in wall temperature, and a decrease in local heat flux, occur. CHF in a heated

channel is the result of two different phenomena: departure from nucleate boiling (DNB) and dryout. DNB is the result of the build-up of vapor near the wall during nucleate boiling. Heat transfer then takes place through vapor by conduction, convection and/or radiation. DNB can result from several different mechanisms, including the coalescence of bubbles near the wall or the formation of a vapor blanket. Dryout-type CHF results from the breakdown of the liquid film at higher quality during annular flow due to evaporation. In most heat exchanger designs, DNB is unlikely because of the relatively low heat fluxes and wall temperatures bound by the hot-side fluid temperature. However, dryout occurs in once-through steam generators as vapor quality approaches one.

In the design of once-through steam generators, identifying where dryout incipience occurs (CHFC) is critical. The length of the heat exchanger required to heat the secondary coolant from dryout incipience to a superheated state may be significant, especially if dryout occurs at a low quality. Predicting dryout at quality lower than it actually occurs will result in a design with excess channel length, problematic if size or cost is limited. Conversely, a predicted dryout quality higher than the actual value will result in an undersized heat exchanger and a two-phase outlet condition. Three types of empirical correlations for CHFC have been developed to capture the complex nature of this phenomenon (Ghiaasiaan, 2017).

1. Local-condition correlations:

These correlations use only local conditions to determine CHFC. Additionally, correlations for the dryout incipience quality have been developed and take the form shown in Eq. (3.60). The heat flux or quality predicted by these correlations can be compared with the local conditions to determine if CHFCs have occurred. It is worth noting that CHFC may not be strictly a function of local conditions and may also be dependent on upstream

conditions. Local correlations for dryout quality are used in this investigation because of their ease of implementation in design codes and the recent development of such correlations for microchannels.

$$\begin{aligned} q''_{\mathrm{CHF}} &= \mathrm{fn}\left(G, D_{\mathrm{h}}, P, x, \text{fluid properites}\right) \\ x_{\mathrm{di}} &= \mathrm{fn}\left(G, D_{\mathrm{h}}, P, q'', \text{fluid properites}\right) \end{aligned} \tag{3.60}$$

2. Inlet-condition correlations:

These correlations are dependent on channel inlet conditions and the heated channel length, *z*, and take the form shown in Eq. (3.61). They are generally developed using channels with a constant heat flux. In the case of a constant channel heat flux, inlet conditions can be used to calculate the length from the inlet where CHFC occur. However, in cases where the heat flux varies over the channel length, such as a heat exchanger, the use of such correlations is complex. Several authors have suggested an overall power hypothesis as an estimate for non-uniform heat flux CHFC (Collier and Thome, 1994; Hewitt *et al.*, 1994). They claim that total heat input for CHFC to occur is equal in both uniformly and non-uniformly heated channels. Therefore CHFC will occur at the same quality in both cases. Others have suggested the use of an "F-factor", Eq. (3.62), which relates the critical heat flux for uniformly heated channels (u) to the critical local heat flux of non-uniformly heat channels (nu) (Weisman and Ying, 1985).

$$q''_{\mathrm{CHF}} = \mathrm{fn}\left(G, D_{\mathrm{h}}, P, i_{\mathrm{in}}, z, \text{ fluid properites}\right) \tag{3.61}$$

$$F_{\mathrm{CHF}} = \frac{\left(q''_{\mathrm{CHF}}\right)_{\mathrm{u}}}{\left(q''_{\mathrm{CHF}}\right)_{\mathrm{nu}}} \tag{3.62}$$

3. Global-condition correlations:

These correlations are often based on an observed relationship between the quality at CHFCs and the boiling length, *z*, as shown in Eq. (3.63). These correlations have proved successful for predicting dryout-type CHFCs for complex geometries (such as BWR rod bundles) with non-uniform power distributions and inherently account for upstream effects (Ghiaasiaan, 2017).

$$x_{\mathrm{CHF}} = \mathrm{fn}\left(G, D_h, P, z, ...\right) \tag{3.63}$$

Kim and Mudawar (2013b) compiled a large database of experiments in which dryout occurred from 26 sources for mini/microchannels with hydraulic diameters from 0.51 to 6.0 mm. The database includes 664 data points for water and 333 data points from twelve other fluids. They compared nine correlations for dryout quality based on local conditions developed for small channels with the database and found the quality predicted by Mastrullo *et al.* (2012) to be the most accurate. The Mastrullo *et al.* (2012) correlation, shown in Eq. (3.64), had an AAD of 24.1% when compared with the entire database, and 20.9% when compared with the experimental data points for water, despite being developed from a dataset of R410A and carbon dioxide in 6 mm channels. Kim and Mudawar (2013b) also developed their own correlation, shown in Eq. (3.65). The correlation had an AAD of 17.1% when compared with the database, and 11.2% for water. They also found that 94.7% of data points for water fell within ±30% of the predictions. They noted that dryout incipience, x_{di}, and dryout completion, x_{de}, occurred at practically the same quality for water and attributed this observation to the high heat of vaporization of water. Their database included both horizontal and vertical tube orientations. In larger channels, dryout incipience is expected to occur earlier due to gravitation forces decreasing liquid film thickness at the top of the channel. However,

in microchannels, gravitational force exerts a smaller influence and the two orientations can be assumed to be equivalent. Table 3.6 shows the predicted dryout quality using the two correlations discussed above for the representative conditions in Table 3.1.

$$x_{\mathrm{di}} = 1 - 20.82 q''^{0.273} G^{1.231} D_{\mathrm{h}}^{0.252} \frac{\mu_{\mathrm{l}}}{i_{\mathrm{fg}}^{0.273} \left(\rho_{\mathrm{l}} \sigma\right)^{1.252}} P_{\mathrm{r}}^{-0.721} \tag{3.64}$$

q'' in $(\mathrm{W\,m^{-2}})$, G in $(\mathrm{kg\,m^{-2}\,s^{-1}})$, D_{h} in (m)

$$x_{\mathrm{di}} = 1.4 \mathrm{We}_{\mathrm{lo}}^{0.03} P_{\mathrm{r}}^{0.08} - 15.0 \mathrm{Bo}^{0.15} \mathrm{Ca}^{0.35} \left(\frac{\rho_{\mathrm{v}}}{\rho_{\mathrm{l}}} \right)^{0.06} \tag{3.65}$$

Table 3.6: Predicted dryout quality

Correlation	I²S-LWR MCHX	MCHX test section
Mastrullo *et al.* (2012)	0.988	0.967
Kim and Mudawar (2013b)	0.880	0.735

Post-dryout heat transfer, also referred to as liquid-deficient heat transfer, results after the breakdown of the annular film and the entrainment of the remaining liquid in the vapor as small dispersed droplets. Heat transfer between the channel and two-phase mixture is then largely governed by convection between the wall and vapor. Droplet impingement on the wall (rewetting) and radiation between the wall and droplets can also contribute. However, in heat exchangers, radiative heat transfer is usually negligible because of the relatively small temperature difference between the wall and fluid. Thermodynamic non-equilibrium is also possible in this regime. Heat transfer between the vapor and wall can be more effective than heat transfer between the vapor and entrained droplets. This results in a mean vapor temperature higher than the saturation temperature, further reducing heat transfer. As a result, the post-CHF heat transfer can be less than that predicated by single- phase vapor correlations using the saturation temperature.

Dougall and Rohsenow (1963) proposed a simple and widely cited correlation, shown in Eq. (3.66). They assumed equilibrium conditions and only accounted for vapor convection with the wall by using the Dittus and Boelter (1930) correlation for turbulent flow. The Reynolds number was modified to account for the velocity of the two-phase mixture.

$$h = 0.023\left(\frac{GD_{\mathrm{h}}}{\mu_{\mathrm{v}}}\left[x + \frac{\rho_{\mathrm{v}}}{\rho_{\mathrm{l}}}(1-x)\right]\right)^{0.8} \mathrm{Pr}_{\mathrm{v}}^{0.4}\,\frac{k_{\mathrm{v}}}{D_{\mathrm{h}}} \tag{3.66}$$

Shah and Siddiqui (2000) compiled a database of 546 data points (including 232 for water) for liquid deficient heat transfer in vertical tubes. Their data set included nine fluids, inner diameters from 1.09 to 24.3 mm, mass fluxes from 3.7 to 5,176 kg m^{-2} s^{-1}, heat fluxes from 0.6 to 1,921 kW m^{-2}, and CHF quality from -1.4 to 0.96. They used their database to develop a correlation for the heat transfer coefficient and non-equilibrium quality. Non-equilibrium quality is calculated based on a graphical method and has the functional form $x_{\mathrm{a}} = \mathrm{fn}(x, x_{\mathrm{CHF}}, \mathrm{Bo}, \mathrm{Fr}_{\mathrm{lo}})$. The non-equilibrium quality and mean fluid enthalpy are used to calculate the vapor temperature, T_{a}, which governs heat transfer: $q'' = h(T_{\mathrm{wall}} - T_{\mathrm{a}})$. A vapor forced convention heat transfer coefficient is calculated using Eq. (3.67) based on the vapor (v) Reynolds number as calculated in Eq. (3.68). Liquid droplet contact with the wall is accounted for through the use of an enhancement factor shown in Eq. (3.69). The overall heat transfer coefficient, based on the non-equilibrium temperature, is then calculated by multiplying the forced convection heat transfer coefficient by the enhancement factor: $h = F_{\mathrm{dc}} h_{\mathrm{FC}}$. The data points collected by them were from controlled (and generally constant) heat flux experiments in which the wall temperatures and fluid pressure were measured. The non-equilibrium vapor temperature, T_{a}, was unknown and therefore the experimental and predicted heat transfer coefficients were defined based on the saturation temperature for the

purpose of comparison: $h = q'' / \left(T_{\text{wall}} - T_{\text{sat}} \right)$. Using this definition, the correlation has an AAD of 13.5% when compared with data for water, and 16.6% for the other fluids. Finally, it should be noted that liquid deficient heat transfer correlations generally do not distinguish between post-dryout and post-DNB CHFCs. To ensure conditions are in the liquid-deficient heat transfer regime, post CHFC data have been limited to those with wall temperatures in excess of the Leidenfrost/minimum film boiling temperature by multiple authors (Groeneveld and Delorme, 1976; Chen *et al.*, 1979; Shah and Siddiqui, 2000). This prevents the inclusion of data from the post-DNB heat transfer regime known as transition boiling, in which partial surface wetting occurs. Such large jumps in wall temperature will typically not occur in post-dryout conditions in once-through steam generators. Thus, the applicability of these correlations in this investigation, partially those involving a non-equilibrium quality/temperature, is uncertain.

$$\begin{aligned} h_{\text{FC}} &= 0.023\,\text{Re}_{\text{v}}^{0.8}\,\text{Pr}_{\text{v}}^{0.4}\,\frac{k_{\text{v}}}{D_{\text{h}}} \qquad \text{For } \text{Re}_{\text{v}} < 10^4 \\ h_{\text{FC}} &= 0.00834\,\text{Re}_{\text{v}}^{0.8774}\,\text{Pr}_{\text{v}}^{0.6112}\,\frac{k_{\text{v}}}{D_{\text{h}}} \quad \text{For } \text{Re}_{\text{v}} > 10^4 \end{aligned} \tag{3.67}$$

$$\text{Re}_{\text{v}} = \frac{G D_{\text{h}} x_{\text{a}}}{\mu_{\text{v}} \alpha_{\text{HEM}}} \tag{3.68}$$

$$\begin{aligned} F_{\text{dc}} &= 2.64 P_{\text{r}} - 1.11 \quad \text{For } P_{\text{r}} > 0.80 \\ F_{\text{dc}} &= 1 \qquad\qquad\quad \text{For } P_{\text{r}} < 0.80 \end{aligned} \tag{3.69}$$

Figure 3.7 shows three post-CHF heat transfer correlations for a heat flux of 100 kW m^{-2} and the fluid conditions listed in Table 3.1. Dryout was assumed to occur at a quality of 0.80 and the heat transfer coefficient is defined based on the saturation temperature for the non-equilibrium Shah and Siddiqui (2000) correlation. This results in a decreasing heat transfer coefficient as the non-equilibrium vapor temperature increases with increasing

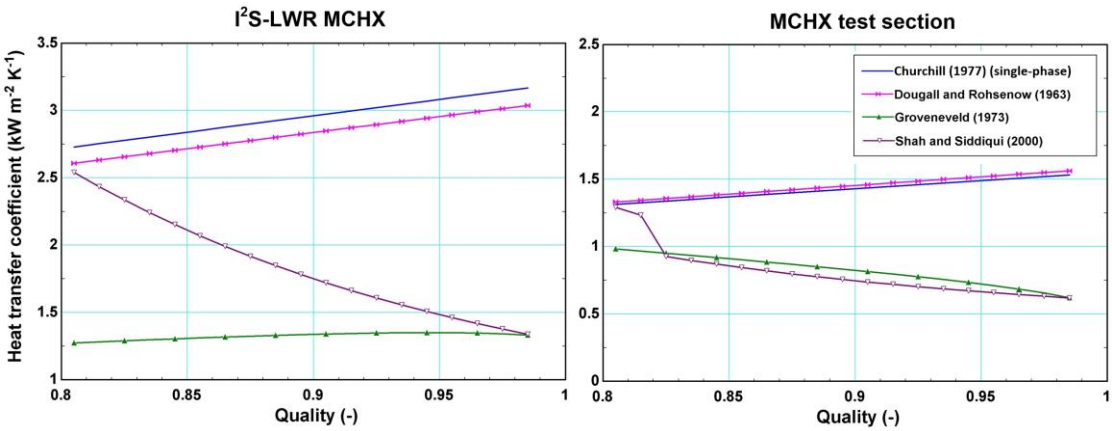

Figure 3.7: Representative dryout heat transfer coefficients

quality. The single-phase vapor (v) heat transfer coefficient from the Churchill (1977a) correlation is also included for reference. Compared to the saturated boiling heat transfer coefficients in Table 3.5, there is an order of magnitude decrease at similar quality.

3.3 Once-Through Steam Generators

Kuridan and Beynon (1997) discussed the design of tube-bundle once-through steam generators for the Safe Integral Reactor (SIR), shown in Figure 3.8, which are similar to those proposed as the alternative TBHX design for the I^{2}S-LWR steam generators. Each of the twelve steam generators has a heat duty of 83 MW (1000 MW_{th} total power) and contains

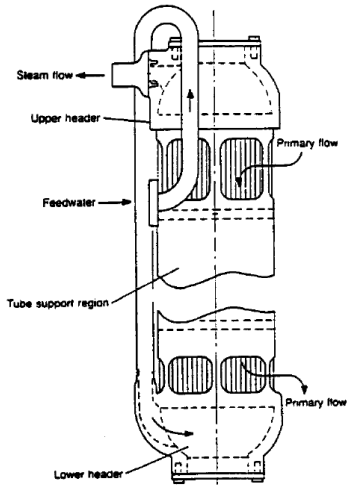

Figure 3.8: SIR tube-bundle steam generator (Kuridan and Beynon, 1997)

2728 Inconel® 690 tubes with an ID of 9.7 mm and OD of 12.7 mm. They only included three heat transfer regimes on the secondary-coolant side: subcooled liquid convection, saturated nucleate boiling, and post-dryout (liquid deficient). The steam generator was segmented along the tube length into a fixed number of equal heat duty, one-dimensional, steady-state control volumes for each of the three heat transfer regimes. This required an iterative process, because the dryout incipience quality was determined using local conditions, including the heat flux, which could not be determined in advance. They assumed an equal flow distribution in all tubes (no maldistribution) and the length of each control volume was then determined based on the specified heat duty. The length required for each heat transfer regime was then calculated by summing the lengths of the control volumes. Momentum conservation equations for both the primary and secondary coolants were ignored and no information on the pressure drop was given. The dryout quality was calculated using a correlation attributed to Macbeth and is shown in Eq. (3.70). Subcooled liquid convection heat transfer coefficients for both the primary and secondary coolant were calculated using the Dittus and Boelter (1930) correlation and the nucleate boiling heat transfer coefficient was calculated using the correlation of Thom *et al.* (1965). They believed that non-equilibrium conditions would result after dryout because of the lower velocity and lower pressure as compared to typical once-through LWR steam generator conditions. They therefore chose to compare two different non-equilibrium post-dryout heat transfer correlations developed by Groeneveld and Delorme (1976) and Chen *et al.* (1979). The lengths of the three different heat transfer regimes when using the two post-dryout correlations are shown in Table 3.7. The post-dryout length, which includes superheated vapor convection, represented the majority of the steam generator but the quality at which dryout incipience occurred was not reported. Additionally, no other correlations for

dryout quality or CHFC were examined. This study indicates that post-dryout heat transfer may represent a significant fraction of once-through steam generator length. It is also worth noting that the resistance network did not include a fouling resistance for either the primary or secondary coolant.

$$x_{\mathrm{di}} = 1 - \frac{q''}{0.15 i_{\mathrm{fg}} D_{\mathrm{h}}^{-0.1} G^{0.51}} \tag{3.70}$$

Table 3.7: SIR steam generator lengths

Post-dryout correlation	Length (m)			
	Subcooled	Nucleate	Post-dryout	Total
Groenveld and Delorme (1976)	0.935	2.847	6.900	10.68
Chen *et al.* (1976)	0.934	2.835	6.085	9.85

Cioncolini *et al.* (2003) discussed the design of helical coil steam generators for the IRIS design. Each of the eight steam generators has a heaty duty of 125 MW and contains 655 Inconel® 690 tubes with an ID of 13.24 mm and OD of 17.24 mm. The tubes containing the secondary coolant had an average uncoiled length of 32 meters. They used the system level code RELAP5 (Reactor Excursion and Leak Analysis Program) to conduct a steady-state analysis on a single representative tube. This program solves the one-dimensional 2FM conservation equations for a series of control volumes and includes two-phase correlations and flow regime maps. They chose to use the built-in correlations for straight horizontal tubes to describe the secondary coolant in the coils and correlations for liquid cross-flow through a tube bank to describe the primary coolant on the outside of the coils. They also examined two control volume discretization schemes for the secondary coolant, one with equal volumes/length, and one with increasing volumes based on local fluid velocity (increasing as the water boils). No difference in results were observed with the two schemes. Figure 3.9

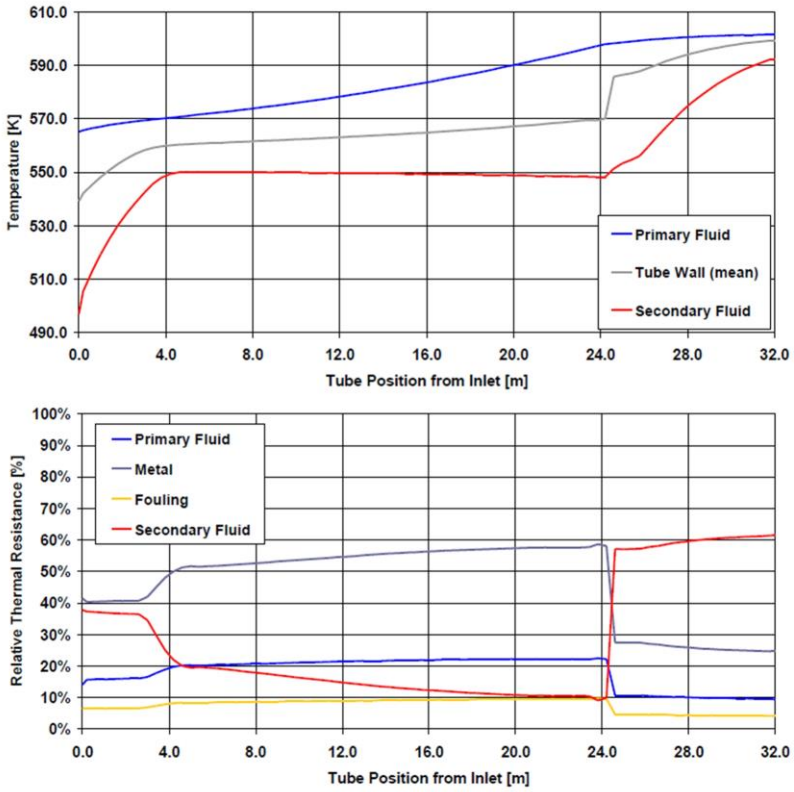

Figure 3.9: IRIS steam generator temperature and resistance profiles (Cioncolini *et al.*, 2003)

shows the temperature profile and relative thermal resistance along the length of the helical coil steam generator. No specific lengths for the different heat transfer regimes were given, but the relative locations of the regimes are evident based on the relative thermal resistances. Starting at the secondary coolant inlet, z = 0 m, the resistance of the secondary coolant is relatively high and comparable to that of the primary coolant as both are in the liquid convection heat transfer regime. As the secondary coolant temperature approaches saturation, the subcooled nucleate boiling heat transfer begins to contribute, decreasing the secondary coolant resistance. The large heat transfer coefficient during the saturated boiling regime results in a low relative secondary coolant resistance, between 10% and 20% of the total thermal resistance. In this heat transfer regime, the thermal resistance of the metal tube is the dominant resistance because of the relatively larger tube thickness. A 2 mm tube thickness is

required by the ASME boiler and pressure vessel code based on the external pressure on the tubes by the primary coolant (Luzzi and Di Marcello, 2011b). Dryout appears to occur approximately 24 meters from the inlet and is marked by a sharp increase in the secondary thermal resistance. In the remaining eight meters of coil, the secondary coolant is in the liquid-deficient and vapor convection heat transfer regimes and the temperature again increases. Dryout appears to occur near a quality of 1 in this analysis and the post-dryout/vapor convection length represents approximately a quarter of the heat exchanger length. Assumptions about the fouling resistance were not discussed by the authors, but it is worth noting that the relative fouling resistance is between 5% and 10% across the length of the heat exchanger. They also tested the transient capabilities of RELAP to detect flow instabilities. They constructed a system of two parallel steam generator channels sharing an inlet and outlet header. The channels were gradually heated and allowed to reach steady-state. Channel flow rates oscillated out of phase but this behavior was suppressed by including an orifice at the inlet of each channel. No flow rate oscillations occurred when the orifice pressure drop represented roughly twenty percent for the total pressure drop.

3.4 Fouling

Fouling or scaling is a well-studied phenomenon in boilers and steam generators because it not only retards heat transfer, but also contributes to the corrosion of heat transfer surfaces. In steam generators, it generally results from the deposition of dissolved ions (sometimes referred to as water hardness) and metal oxide particulate (from corrosion and oxidation in the system). It is particularly problematic in once-through steam generators where dissolved substances and contaminants are concentrated as the secondary coolant is converted to steam. Fortunately, fouling and corrosion can be limited through the carful control of water

chemistry. This includes the removal of particulate matter and dissolved ions, pH control, and limiting oxidation potential in the system. On the primary side of a PWR, the chemical and volume control system (CVCS) provides deaerated and demineralized water to the RCS using a feed and bleed approach to control the water level in the pressurizer, control water chemistry, remove fission gases, and provide seal water for the RCS pumps. Boric acid (used for chemical shim control) and lithium hydroxide are used by the CVCS to manage the pH and reactivity in the core. Hydrogen or hydrazine is also added to scavenge oxygen and limit oxidation reactions. The secondary coolant is treated in a bed of ion-exchange resin beads to remove dissolved ions and filter out suspended solids in a process known as condensate polishing. Oxygen in the secondary loop is removed through air ejection from the condenser and thermal deaeration in open feedwater heaters. Finally chemicals such as sodium phosphate, volatile amines (e.g., ammonia), and hydrazine are used to control the pH and scavenge oxygen in the secondary coolant (Steam, 2005). Chemical acid cleaning of the secondary side during shutdown has also been used to remove fouling build-up.

Fouling could be a significant issue for the I^2S-LWR MCHX. Thin walls between channels and high convective heat transfer coefficients may lead to fouling representing an appreciable fraction of the total thermal resistance. While expected fouling resistances for common fluids and operating conditions in macroscale heat exchangers are well documented, specific data on microchannel fouling under reactor cooling water conditions do not exist. To estimate the fouling resistance for design purposes, studies from the literature for both nuclear steam generators and microchannel heat exchangers were reviewed.

Schwarz (2001) analyzed data from Siemens recirculating steam generators with 22 mm OD tubes operating for up to 27 years. He noted that the inside of the tubes (primary

coolant side) did not have any significant fouling build-up, and therefore focused on the outer secondary coolant boiling side. Fouling on the outside of the tubes was mainly due to corrosion products such as iron oxides and iron hydroxides. He first examined data from plants initially using a phosphate-based treatment before switching to a hydrazine H-AVT (high pH through all volatile treatment) process. He observed that the fouling resistance was less than $\Delta R''_{foul} = 0.5 \times 10^{-5}$ m^2 K W^{-1} over a ten-year period with the H-AVT treatment, as compared to approximately $\Delta R''_{foul} = 2.0 \times 10^{-5}$ m^2 K W^{-1} over the same time period with the phosphate treatment. He also noted that the Siemens chemical cleaning process was extremely effective in removing iron oxide deposits. Among the plants using the H-AVT since commissioning, no appreciable fouling resistance was observed over the first 15 years of operation. Turner *et al.* (2000) collected steam generator tubes from pressurized heavy water reactors and experimentally measured the thermal resistance of fouled and cleaned tubes. For primary-side experiments, liquid water flowed through the inside of tube samples and a resistance heater provided a known heat flux to the outside of the sample. They found primary-side fouling thicknesses from 3 μm to 90 μm comprised of porous magnetite (an iron oxide compound) with an average thermal conductivity of $k_{foul} = 1.3 \pm 0.2$ W m^{-1} K^{-1}. Secondary-side experiments were performed with a heater on the inside of the tube samples and two-phase water with an inlet quality of 0.06 on the outside. They identified two types of fouling build-up on the secondary-side using a scanning electron microscope: dense and relatively thin deposits, less than 15 μm with $k_{foul} = 0.57$ W m^{-1} K^{-1}, as well as more porous and thicker deposits, up to 40 μm with $k_{foul} = 0.89$ W m^{-1} K^{-1}. However, when the test was modified to use liquid water on the outside of the tube samples (secondary-side) they found the thermal conductivities of both types of fouling materials to be similar to that of the primary-side,

indicating that the state of water in the fouling material pores may be significant. They also observed that for relatively thin fouling deposits, the presence of the fouling layer decreased thermal resistance. This was attributed to increased surface roughness as compared to the clean tubes, increasing heat transfer. The thermal conductivity of the fouling layer was therefore calculated using Eq. (3.71) with $R''_{\text{roughness}}$ equal to -4×10^{-6} m^2 K W^{-1} for the primary-side and -5×10^{-6} m^2 K W^{-1} for the secondary-side.

$$R''_{\text{foul}} = \frac{t_{\text{foul}}}{k_{\text{foul}}} + R''_{\text{roughness}} \tag{3.71}$$

Benzinger *et al.* (2007) performed a crystallization fouling study on rectangular microchannels with D_h = 178 μm using an aqueous solution of $Ca(NO_3)_2/NaHCO_3$ in the laminar flow regime (Re = 110). For several channel surfaces, including stainless steel, they consistently found the fouling resistance to asymptotically approach approximately $\Delta R''_{\text{foul}}$ = 1.0×10^{-4} m^2 K W^{-1}. Perry and Kandlikar (2008) studied particulate deposition fouling in rectangular adiabatic channels with D_h = 225 μm using 4 μm silica particles. The particles combined into approximately 24 μm clumps which did not accumulate in the channels, even at low flow rates (Re = 17). They attributed this finding primarily to a lift force on the particulate proportional to the sheer stress at the wall and particle size. However, significant particle deposition was found in lower velocity header regions. Furthermore, the introduction of fibrous material resulted in the collection of particulate at the channel inlets, resulting in a significant increase in pressure drop.

Based on the above discussion, fouling build-up in the I^{2}S-LWR MCHX design should be minimal. Dissolved ions and iron oxide particulate in both primary and secondary coolant inventories will be controlled as previously discussed. Furthermore, particle deposition will

be limited by the turbulent, high velocity flow in MCHX channels. If significant fouling occurs, chemical cleaning of MCHXs can be conducted during regularly scheduled refueling outages.

3.5 Boiling Flow Instabilities

Thus far, the discussion of boiling channels and steam generator design has focused on steady-state analysis. However, unanticipated transient phenomena, referred to as flow instabilities, have been observed in many types of boiling systems. Instabilities can degrade performance or produce unintended operating conditions. They may also lead to damage of heat exchange surfaces due to thermal fatigue from thermal cycling or transient burn-out. While mathematical descriptions of flow instabilities are available, this section focuses on the identification of possible phenomena, conditions in which they might occur, and possible remedies. Examples of flow instabilities in this section are discussed for channels with a constant heat input, although it is worth noting that flow rate oscillations will influence heat transfer in heat exchangers, further complicating the analysis.

1. Ledinegg instability:

This phenomenon results in the transition of an unstable steady-state operating condition to a stable steady-state condition and is also referred to as flow excursion. A simple example of the Ledinegg instability can be shown using a channel with a constant heat input downstream of a centrifugal pump (Ghiaasiaan, 2017). Figure 3.10 shows the ΔP-$\dot{m}$ curve for the heated channel (demand curve) and pump (supply curve) as well as a simple sketch of the system. Possible operating points are located at the intersection of the two curves, points A, B, and C. The S-shape of the demand curve is explained by the constant heat input

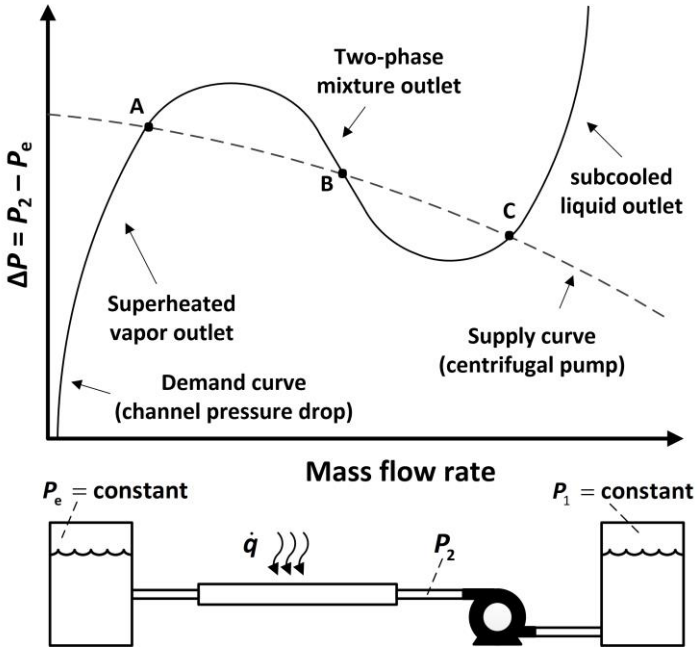

Figure 3.10: Ledinegg instability example

conditions. At low flow rates, all of the liquid is vaporized, and the channel pressure drop increases with mass flow rate. Further increases in mass flow rate result in a two-phase mixture at the outlet of the heated channel. Less of the liquid is boiled, and the velocity and pressure drop in the channel decreases. At higher flow rates, the outlet will remain a liquid and the pressure drop will again increase with the flow rate. At points A and B, small perturbations in the mass flow rate result in the re-establishment of the intial operating point. For example, if the system were operating at point A and experienced a small decrease in mass flow rate through the channel, the pressure drop thought the channel would also decrease. The pump would then supply a higher flow rate, returning the system to point A. However, if the same perturbation occurred while operating at point B, the pressure drop through the channel would increase, causing the pump to supply a lower flow, and pushing the system further toward point A. Likewise, a small increase in flow rate while operting at point B will result in the system moving to point C. Eq. (3.72) provides the stability criteria

for the Ledinegg instability and shows that the phenomenon occures in regions where the demand curve is steeper than the supply curve. As a result, this instability only occurs when fluid exits a heated channel as a two-phase mixture, where the slope of the demand curve is negitive. Postive displament pumps (which would be represented as vertical lines ΔP-$\dot{m}$ curve) are insenstive to pressure drop and can be use to provide stable two-phase outlet conditions. Alternatively, a large pressure drop element between the centrifugal pump and boilling channel will increase the slope of the demand curve, promoting stability.

$$\left(\frac{\partial \Delta P}{\partial \dot{m}}\right)_{\text{supply}} < \left(\frac{\partial \Delta P}{\partial \dot{m}}\right)_{\text{demand}} \tag{3.72}$$

2. Pressure drop oscillations:

Also called severe pressure drop oscillations, pressure drop oscillations result in flow rate oscillations. They can occur when a compressible volume (such as a surge tank, accumulator, flexible piping, or vapor bubble) is located upstream of a heated channel. Oscillations occur as a result of continued filling and discharge of the compressible region. An example of a system in which the pressure drop oscillation is likely is shown in Figure 3.11 and is similar to the example presented by Kakac and Bon (2008). In this example, a positive displacement pump is used, providing a constant flow rate into the surge tank. While the system is operating at point O, a small perturbation causes an increase in the surge tank pressure, P_2. This causes the flow rate leaving the tank to decrease (moving right on the demand curve), while the flow rate entering the tank remains constant, filling the tank and further increasing the pressure, P_2. This feedback mechanism continues to fill the tank and increase pressure until point B is reached. Here the increased pressure results in a sudden, large increase in channel flow rate. At operating point C, the flow rate exiting the surge tank

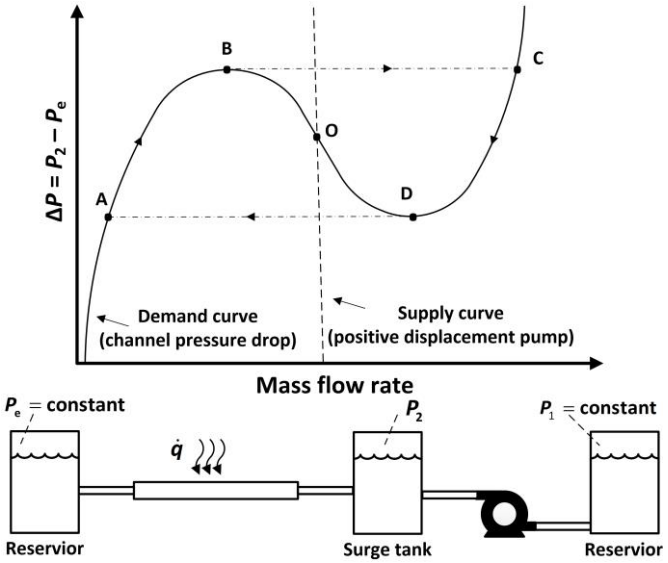

Figure 3.11: Pressure drop oscillations example

is greater than that entering from the pump, causing P_2 and the flow rate through the channel to decrease. The pressure in the surge tank continues to fall until point D is reached, where there is a sudden decrease in flow rate. At point A, the flow rate into the tank is again greater than that leaving, causing P_2 to increase. The pressure in the tank increases until point B is reached and the cycle repeats. Like the Ledinegg instability, pressure drop oscillations only occur when fluid exits the heated channel as a two-phase mixture, where the slope of the demand curve is negative. This instability can be eliminated by removing the compressible region. A large pressure drop element between the compressible volume and channel will cause the demand curve to monotonically increase with flow rate, eliminating the negatively sloped region in the ΔP-$\dot{m}$ curve.

3. Density wave oscillations:

This phenomenon occurs due to feedback delays between phase change, flow rate, and pressure drop. The effects of pressure changes propagate at the speed of sound while perturbations in two-phase mixture density, quality, enthalpy, etc., take longer to influence

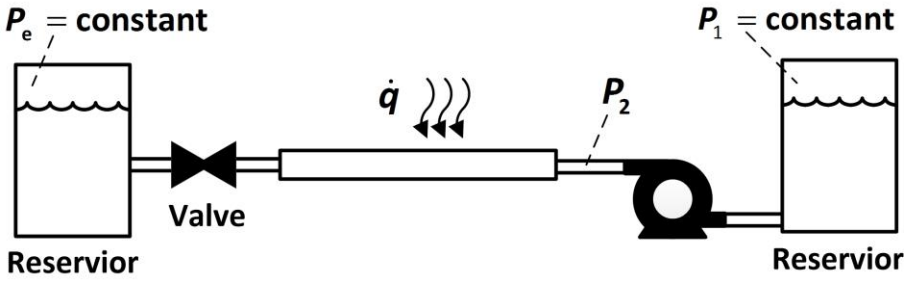

Figure 3.12: Density wave oscillation example

the system, proportional to the fluid velocity. A simple example, similar to that presented by Kakac and Bon (2008), helps to explain the concept. Figure 3.12 shows a system containing a heated channel, centrifugal pump, and a valve at the channel exit. To initiate the phenomenon, a perturbation occurs, which increases pressure drop across the valve. The pressure at the channel inlet, P_2, increases almost instantaneously, decreasing the flow rate through the pump. In a single-phase liquid system, the flow rate through the valve would instantaneously decrease, decreasing the pressure drop and stabilizing the system. However, for a boiling channel, the decrease in pressure drop through the valve is delayed, due to the time required for the changes in inlet conditions to influence the flow rate and properties at the outlet. This feedback delay between the valve pressure drop and flow rate can create a sustained oscillation. Transient modeling using the two-phase conservation equations is required to determine the frequency, amplitude, and propagation/dampening of the oscillations. While a valve at the exit of the channel is used in this example, changes in two-phase pressure drop along the length of the boiling channel can cause density wave oscillations. In the case of a single heated channel, a positive displacement pump can provide constant flow rate, decoupling the flow rate from the pressure drop and eliminating the instability. Additionally, pressure drop elements at the inlet of the channel provide an immediate feedback, stabilizing the system, while those at the outlet have the opposite effect.

4. Parallel channel instabilities:

Flow instabilities in parallel channels are different than those in single channels due to complicated channel-to-channel interactions in shared headers. Parallel channel instabilities may result in non-uniform steady-state flow rates (maldistribution) or out-of-phase oscillating flow rates among channels. Initiation may occur while operating in the negative slope region on ΔP-$\dot{m}$ demand curve. The Ledinegg instability causes an increase in the flow rates of some channels while others decrease. For a given pressure difference between header, multiple steady state flow rates are possible, as shown in Figure 3.10. This may result in a stable steady-state with significant maldistribution between channels. However, the transition can also trigger out-of-phase density wave oscillations (Xia *et al.*, 2012). Parallel channel instabilities may also result from the rapid expansion of confined nucleation bubbles in narrow microchannels (Qu and Mudawar, 2004). This can cause backflow and, in some cases, expel liquid and vapor back into the inlet header. The addition of a large pressure-drop element at the entrance to each channel can help combat this effect by maintaining a large pressure gradient between the growing bubble and inlet header (Mukherjee and Kandlikar, 2005). This also increases the slope of the demand curve and reduces feedback delay, making individual channels more stable against Ledinegg and density wave instabilities.

3.6 Maldistribution

In MCHXs designs, multiple parallel channels are connected by a single inlet and outlet header. A common assumption in such designs is that the mass flow rate entering and exiting the headers is distributed equally among parallel channels. However, poor header design may cause significant differences in channel flow rates, referred to as maldistribution. This can

result from pressure losses or gains in the inlet and outlet headers, causing different pressure boundary conditions between the inlets and outlets of channels. Parallel flow instabilities and manufacturing imperfections can also contribute to maldistribution. Finally, parallel channel arrays with two-phase inlet conditions, such as a compact condenser, are particularly prone to maldistributions. Differences in properties of the liquid and vapor, forces such as gravitational and inertial, and flow regime all play a role in flow distribution. However, for the MCHX steam generator considered here, the secondary coolant enters as a subcooled liquid.

Bajura and Jones (1976) performed an analytical and experimental investigation of air-flow in a parallel tube array. Their investigation included parallel and reverse header designs with tubes containing an adjustable orifice as shown in Figure 3.13. They observed that in the inlet header, deceleration due to branching increased the static pressure in the direction of flow while friction decreased the pressure. In the outlet header, acceleration from incoming channels and friction both decreased the static pressure in the direction of fluid flow. In Bajura and Jones' work, the frictional pressure drop was small compared to the acceleration and deceleration pressure changes, causing the static pressure to increase in the inlet header in the direction of flow. A simplified pressure versus channel number graph is shown in Figure 3.13 to illustrate this effect. The channel flow rate is proportional to the differential pressure across a given channel and it was observed that the reverse header configuration provided a more uniform differential pressure. However, the authors noted that the parallel header arrangement would likely provide a better distribution for a denser, more viscous fluid in which friction would cause a decreasing pressure gradient in the inlet header. The authors varied the sizes of the orifices in channels and found the distribution to improve when the orifice/channel pressure drop increased. They also varied the number of channels which affected the ratio of

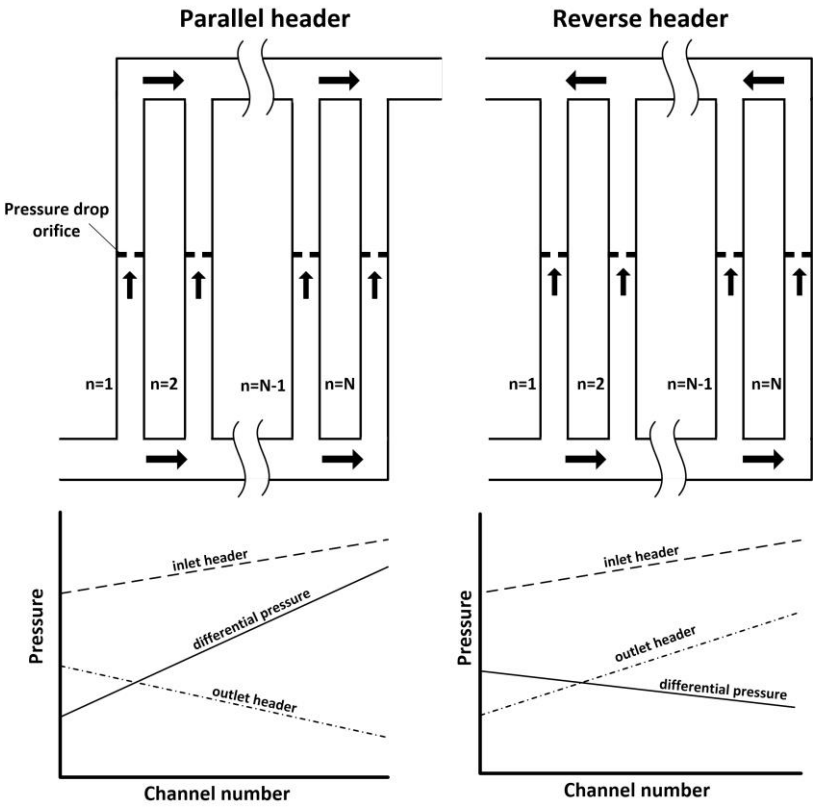

Figure 3.13: Representation of Bajura and Jones (1976) maldistribution experiment

channel cross-sectional area to header cross-sectional area: $A_r = nA_{cx,ch} / A_{cx,header}$. They found a smaller area ratio to improve distribution. It should be noted that in both of these cases, the distribution improved when channel pressure drop was increased relative to header pressure changes.

Webb (2003) investigated the effects of maldistribution on parallel single-phase microchannels using numerical simulation and suggested that discrepancies between single and multichannel microchannel pressure drop experiments were due to gross maldistribution, primarily from poor header design. He identified three common microchannel header arrangements in the literature, shown in Figure 3.14. The normal header design was shown to preferentially distribute fluid into central channels while those at the ends of the header were

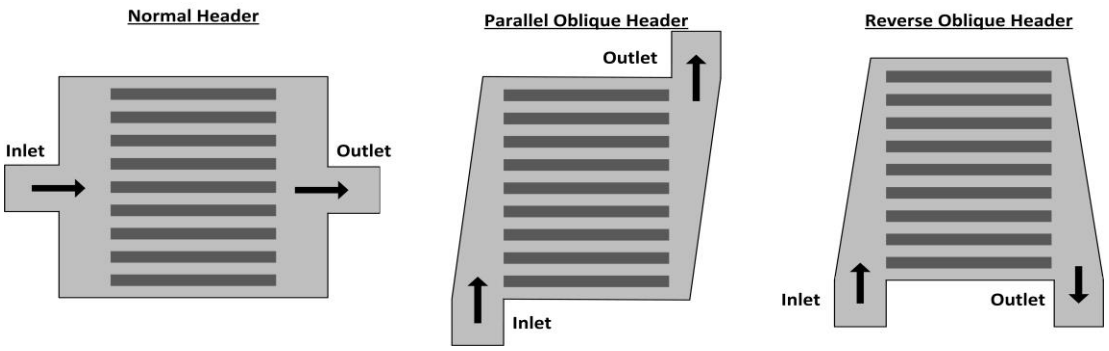

Figure 3.14: Common microchannel header arrangements

starved due to inlet jet effects. Webb also suggested using triangular headers, referred to as oblique parallel and oblique reverse, to limit the effects of acceleration and deceleration and provide a more uniform pressure in the inlet and outlet headers. Additionally, a positive pressure gradient in the inlet header resulting from deceleration may cause flow separation and recirculation zones, an effect that limits flow into nearby channels (Kumaran *et al.*, 2013). Webb (2003) also showed that manufacturing tolerances may play a significant part in microchannel maldistribution. For a circular laminar channel with constant pressure boundary conditions, he stated that $\dot{m} \propto D^4$. Thus, a 20 μm and 18 μm channel with the same inlet and outlet header pressures would have a 45% difference in flow rates.

Tuo and Hrnjak (2013) investigated the performance of an air-coupled microchannel evaporator using R134a. They used an upstream flashing tank to ensure that only liquid refrigerant would enter the evaporator test section. An infrared camera was used to measure the surface temperature of each channel and determine the relative locations where liquid convection, saturated boiling, and post-dryout/vapor convection occur. Image processing was then used to estimate flow distribution in the different channels. They used this data to develop a simple pressure drop/flow distribution model as shown in Figure 3.15. The pressure drop of each unique flow path from the inlet to the outlet of the evaporator is calculated by adding the

frictional and acceleration/deceleration pressure changes along the path as shown in Eq. (3.73) . Header pressure changes are calculated using the flow rates of all paths passing through the segment. The flow rate through each path and total pressure drop can then be iteratively calculated by requiring each of the flow paths to have an equal pressure drop. This model predicted approximately 92% of experimental pressure drop data within ±20%. Additionally, predicted wall temperatures using this flow distribution method closely follow those observed in experiments. They also noted that between 43% and 72% of the predicted pressure drop occurred in the outlet header due to the high velocity vapor state. They then used their model to determine the influence of the outlet header diameter, channel diameter, and channel length on flow distribution. In all three cases, the distribution improved when the ratio of channel-to-header pressure drop increased. Specifically, the distribution improved with increasing outlet header diameter, increasing channel length, and decreasing channel diameter.

$$\Delta P^{i} = \sum_{1}^{i} \Delta P_{idh}^{i} + \Delta P_{con}^{i} + \Delta P_{tube}^{i} + \Delta P_{exp}^{i} + \sum_{i}^{N} \Delta P_{odh}^{i} \tag{3.73}$$

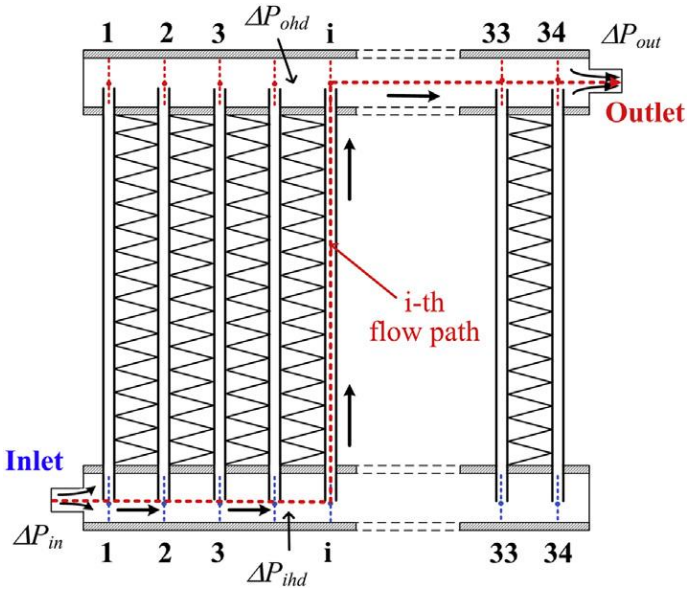

Figure 3.15: Flow path pressure drop model (Tuo and Hrnjak, 2013)

3.7 Summary

The literature discussed in this chapter provides a framework for modeling the liquid-liquid and liquid-boiling I^2S-LWR MCHX designs. Heat transfer and pressure drop correlations are required to solve the energy and momentum conservation equations. Correlations developed from larger channels can likely be used for liquid flows in microchannels, provided that scaling effects are not significant. Two-phase flow and flow boiling in microchannels is different from that in larger channels due to bubble confinement and the relative magnitudes of different forces in small diameter channels. There is significant disagreement among the heat transfer and pressure drop correlations discussed above, causing uncertainty in the performance of the liquid-boiling I^2S-MCHX. Furthermore, it is not clear whether microchannel or macrochannel correlations should be used for the conditions in the I^2S-LWR MCHX. Therefore, experiments were conducted to determine the most accurate correlations in the different heat transfer regimes encountered along the length of the liquid-boiling MCHX. Flow instabilities and maldistribution may negatively impact the performance of the I^2S-LWR MCHX or the MCHX test section. The design heuristic discussed above can be used to avoid these phenomena. Furthermore, the flow path method, discussed by Tuo and Hrnjak (2013), provides a relatively simple means of modeling both the pressure drop and flow distribution through an array of parallel microchannels with common headers. An estimate of the fouling resistance is required to accurately model the performance of the I^2S-LWR MCHX. A best estimate was therefore determined based on the available literature on steam generators and microchannel experiments.

CHAPTER 4. LIQUID-LIQUID MCHX DESIGN

This chapter discusses the design, modeling, and optimization of the I^2S-LWR liquid-liquid MCHX. This design is coupled with a flash Rankine cycle for power generation which is also discussed. In this chapter and the following chapter on liquid-liquid experiments, the primary coolant and secondary coolants are sometimes referred to as the hot coolant and cold coolant, respectively. Average values reported for dimensionless numbers or other parameters are evaluated at the average fluid properties in the channels.

4.1 Assumptions

Several simplifying assumptions were used in the design of the liquid-liquid MCHX. Additionally, unknown quantities required best estimates for design purposes. A list of these assumptions is presented below.

1. Uniform flow distribution:

A uniform flow distribution among all primary and secondary channels was assumed for heat transfer calculations (no maldistribution). A parallel flow path analysis was used to determine the pressure drop through the MCHX. This method also provides a coarse estimate of the flow distribution and showed little maldistribution. A more detailed analysis was deemed beyond the scope of the I^2S-LWR MCHX design. However, header geometry can be further studied in more detail in subsequent efforts to ensure a uniform distribution.

2. One-dimensional heat transfer:

Heat transfer was assumed to be one-dimensional, allowing for the use of a thermal resistance network. Fluid conduction in the direction of flow (referred to as axial conduction)

is negligible for $\mathrm{Pe} = \mathrm{Re}\,\mathrm{Pr} \gg 1$. A Maranzana number, Eq. (3.7), of less than 0.01 is a threshold when multi-dimensional conjugate heat transfer in the wall material can be ignored. The above criteria for neglecting multi-dimensional heat transfer were easily satisfied by this design: $\mathrm{Pe}_{\mathrm{hot,avg}} = 18408$, $\mathrm{M}_{\mathrm{hot,avg}} = 1.23 \times 10^{-6}$.

3. Fully-developed flow*:*

Fully-developed flow was assumed over the entire channel length. For turbulent conditions, hydrodynamic and thermal entrance lengths are approximately $10 \times D_h$ for $\mathrm{Pr} \approx 1$ (Ghiaasiaan, 2018). Bowdery, 2006. With an active channel length of 0.55 m and $D_h = 0.812$ mm, the entrance length of this design represents less than 2% of the total channel length. This is a conservative assumption due to the higher heat transfer coefficients in the developing region.

4. Macroscale correlations:

Correlations developed for larger macrochannels were used in the liquid-liquid MCHX design process. Continuum mechanics apply for the liquid microchannel conditions in this study. Eq. (3.8) suggests that viscous heating may have a small influence on the channel heat transfer coefficient, since $\mathrm{Br}_{\mathrm{hot,avg}} = 5.91 \times 10^{-5}$ and the right hand side equal to 3.66×10^{-5}.

5. Neglect header heat transfer:

Heat transfer was conservatively assumed to occur only in the active channel region, in which the two fluids are in counterflow. Heat transfer from primary coolant channels to secondary coolant in the triangular headers in adjacent sheets was ignored. Additionally, heat transfer from secondary coolant headers in the downcomer was also ignored.

6. Fouling resistance:

Based on the discussion in Section 3.4, a fouling build-up of 10 μm with a thermal conductivity of k_{foul} = 1.3 W m^{-1} K^{-1} was assumed on both primary and secondary surfaces (R''_{foul} = 7.7 × 10^{-6} m^2 K W^{-1}).

7. Surface roughness:

A root mean squared surface roughness of 2 μm was assumed for both primary and secondary surfaces based on the etching data of Nageswara and Deepak (2007). A similar roughness was measured in sheets etched for the test section in the investigation.

4.2 Liquid-Liquid MCHX Design

A liquid-liquid MCHX design that meets the requirements outlined in Section 2.1 was developed through the modeling and optimization efforts outlined in this chapter. Important dimensions of the design are presented in Figure 4.1. The total radial length of the MCHX stack, 0.85 m, and azimuthal width, 1.0 m, were dictated by the size of the downcomer. The radial length includes the active channel length as well as lengths required for primary inlet/outlet headers and triangular headers in the secondary coolant sheets. The azimuthal width is divided between the width of MCHX blocks and secondary plenums on the sides of the stack. The volume of the MCHX can be thought of as being split between fluid distribution and heat transfer regions. This presents a tradeoff as reducing pressure drop and increasing heat transfer both require additional volume. Figure 4.2 shows channel and sheet dimensions of the design. The channel dimensions, in reference to one another, were based on etching data of Nageswara and Deepak (2007) and conversations with Advanced Metal Etching, Inc. The overall channel sizes and values for the dimensions discussed above were determined

through parametric analyses. Sheet and fin thickness were dictated by pressure vessel requirements to ensure the mechanical stability of the MCHX.

Parameter	Value
MCHX stack radial length	0.85 m
MCHX block radial length	0.65 m
Primary coolant header radial length	0.20 m
Secondary coolant radial length	0.10 m
Active channel length, l_{ch}	0.55 m
MCHX stack azimuthal width	1.00 m
MCHX block azimuthal width	0.80 m
Secondary coolant plenum azimuthal width	0.20 m
MCHX block axial height	0.60 m
Channels per sheet	445
Sheets per MCHX block (primary and secondary)	530

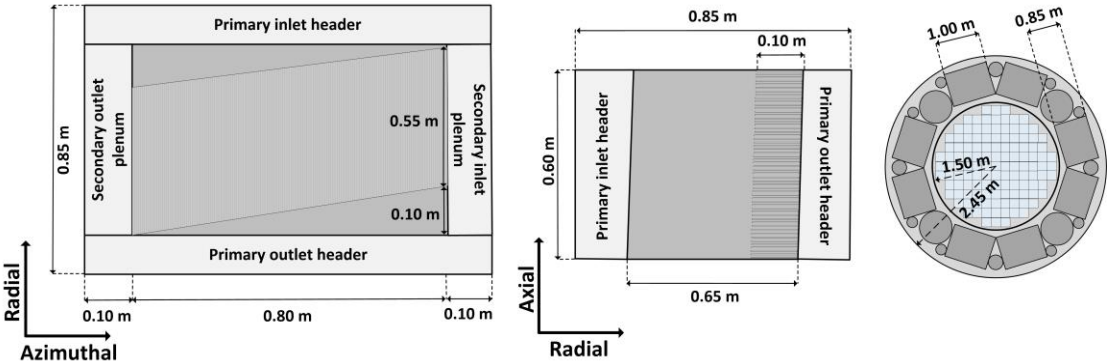

Figure 4.1: Liquid-liquid MCHX dimensions

Dimension	Symbol	Value
Channel height	h_{ch}	0.635 mm
Sheet thickness	t_{sheet}	1.130 mm
Wall thickness	t_{wall}	0.495 mm
Fin thickness	t_{fin}	0.400 mm
Flat length	l_{flat}	0.127 mm
Channel width	w_{ch}	1.397 mm
Hydraulic diameter	D_h	0.812 mm

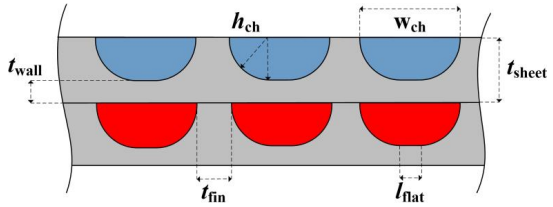

Figure 4.2: Liquid-liquid MCHX channel dimensions

Table 4.1 shows important fluid properties of a single liquid-liquid MCHX block and values for all 88 MCHX blocks in parentheses. The core power as well as the overall primary coolant flow rate and temperatures were determined through core safety analysis, as discussed in Section 1.3.1. After selecting the MCHX stack dimensions, secondary coolant conditions were optimized to meet thermal efficiency requirements of the flash Rankine cycle, resulting in a thermal cycle efficiency of 34.58%. Both primary and secondary channels had similar mass fluxes and were in the turbulent flow regime, resulting in high heat transfer coefficients.

Table 4.1: Liquid-liquid MCHX operating parameters

Parameter	**Primary coolant**	**Secondary coolant**
$\dot{q}$(MW)	32.39 (2,850)	
A (m^2)	228.2 (20,064) [for each coolant]	
$\dot{m}$ (kg s^{-1})	176.1 (15,498)	147.9 (13,016)
G (kg m^{-2} s^{-1})	2092	1757
T_{in} (°C)	330.0	279.3
T_{out} (°C)	298.8	318.2
P_{in} (MPa)	16.30	12.88
P_{out} (MPa)	15.86	11.76
ΔP_{total} (kPa)	433.8	1,117
ΔP_{fr} (kPa)	472.9	1,115
Re_{avg} (-)	20,642	16,411
h_{avg} (kW m^{-2} K^{-1})	38.82	32.18
f_{avg} (-)	0.0308	0.0319

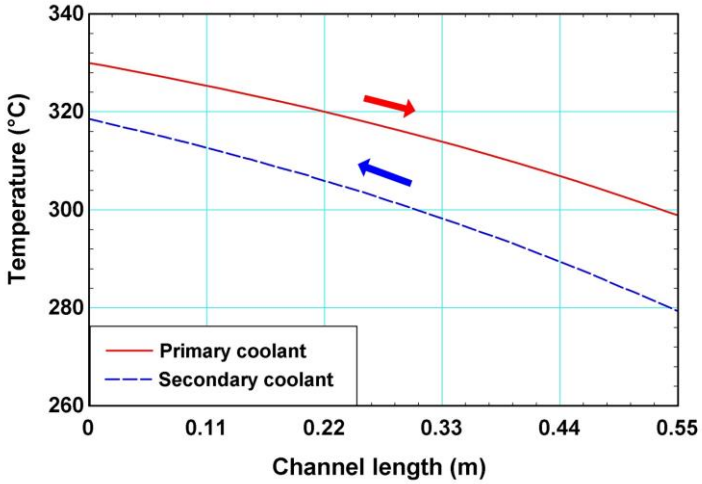

Figure 4.3: Liquid-liquid MCHX temperature profile

The temperature profiles of the two fluids over the MCHX channel length are shown in Figure 4.3.

Stainless steel 316 was selected for the construction of the MCHXs because of its strong corrosion resistance properties and successful use within the RPV of long running reactors. It has also be used extensively by Heatric, a manufacturer of industrial MCHXs, and is a recommended material for nuclear microchannel steam generators (Li *et al.*, 2009). Inconel® alloys have been used extensively in nuclear steam generators to prevent chloride-induced stress corrosion cracking that had been observed in earlier stainless steel tube designs (Harrod *et al.*, 2001). Inconel® has a very similar thermal conductivity and maximum allowable stress compared with 316 stainless steel (at temperatures of interest) and has been used in MCHXs (Li *et al.*, 2009). It could therefore be used instead of stainless steel with little impact on the design of the I^2S-LWR MCHX. For example, Inconel® 690 has a thermal conductivity of 17.3 W m^{-1} K^{-1} at 300°C, compared with 17.9 W m^{-1} K^{-1} for 316 stainless steel.

4.3 Analysis Platform

Calculations and analyses in this investigation were performed using the Engineering Equation Solver (EES) platform (Klein, 2017). EES is an equation solving program that contains built-in functions for thermodynamic and transport properties. Large systems of non-linear algebraic equations can be solved using Newton's method and a blocking technique designed to speed calculation. Thermodynamic water property functions were developed according to the International Association of Properties of Water and Steam (IAPWS) Formulation 1955 for the Thermodynamic Properties of Ordinary Water Substance for General and Scientific Use (Wagner and Pruß, 2002). Viscosity, surface tension, and thermal

conductivity functions for water were also developed according to IAPWS publications (Kestin *et al.,* 1984; Huber *et al.,* 2012). Thermal conductivity functions for 316 and 304 stainless steel were developed according to the data of Ho and Chu (1977). EES can also perform numerical uncertainly analyses for calculated parameters assuming that uncertainties in independent parameters are random and uncorrelated.

4.4 Heat Transfer Model

Heat transfer calculation were performed by segmenting the active channel length of the MCHX into twenty control volumes ($l_{seg} = l_{ch} / 20 = 0.0275\,\text{m}$). This method accounts for changes in fluid properties along the length of the heat exchanger. A grid independence study was performed and no significant changes in the heat duty were observed when the number of control volumes was increased beyond twenty. EES property routines were used to determine fluid and material properties. Fluid properties were evaluated at the average temperature and pressure of the fluid in the control volume segment. The thermal conductivity of 316 SS was evaluated at the average of the two average fluid temperatures in the segment. The one-dimensional single-phase control volume integrated conservations equations, shown in Eq. (3.2), were applied to both coolant channels. The segment heat duty and outlet enthalpies/temperatures were determined by simultaneously solving the energy conservation equations for both coolant channels and the UA-ΔT_{lm} equation, as shown in Eq. (4.1). The counterflow log mean temperature difference, ΔT_{lm}, is defined according to Eq. (4.2). The fluid momentum equations were simultaneously solved with energy balance equations to determine coolant outlet pressures, required to determine fluid outlet temperatures: $T = T(P, i)$. In the counterflow orientation, states at the outlet of a control volume become

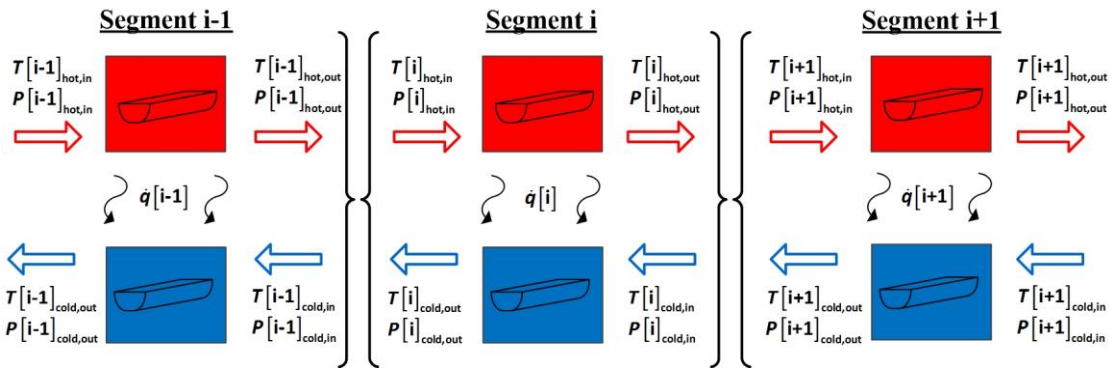

Figure 4.4: Channel segmentation method

the inlet states for neighboring control volume, as shown in Figure 4.4, resulting in a large system of equations. Inlet conditions for the MCHX were specified at opposite ends of the counterflow heat exchanger, and the system of equations was solved using the EES iterative solver.

$$\dot{q}_{\text{seg}} = \dot{m}_{\text{hot}}\left(i_{\text{hot,in}} - i_{\text{hot,out}}\right) = \dot{m}_{\text{cold}}\left(i_{\text{cold,out}} - i_{\text{cold,in}}\right) = UA_{\text{seg}}\Delta T_{\text{lm}} \tag{4.1}$$

$$\Delta T_{\text{lm}} = \frac{\left(T_{\text{hot,in}} - T_{\text{cold,out}}\right) - \left(T_{\text{hot,out}} - T_{\text{cold,in}}\right)}{\ln\left[\dfrac{\left(T_{\text{hot,in}} - T_{\text{cold,out}}\right)}{\left(T_{\text{hot,out}} - T_{\text{cold,in}}\right)}\right]} \tag{4.2}$$

The thermal resistance and *UA* of each segment were calculated using a one-dimensional resistance network consisting of two parallel heat transfer pathways, as shown in Figure 4.5. The upper path represents heat transfer from the top half of a primary coolant (hot) channel to the bottom half of a secondary coolant (cold) channel. The bottom path represents the heat transfer between the bottom half of a primary channel and top half of a secondary channel. Both paths consider resistances due to convection in both coolants, fouling on both coolant channel walls, and the 316 SS wall between the primary and secondary coolant channels. The regions between channels were treated as fins and the three resistances were calculated according to Eq. (4.3), where η_o is the overall finned surface efficiency. The

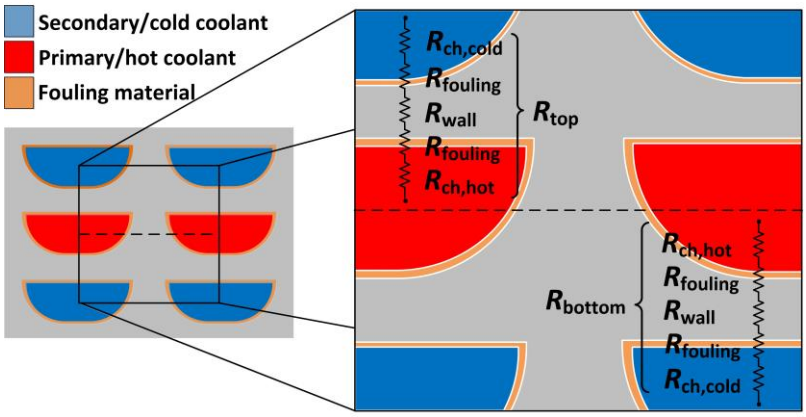

Figure 4.5: MCHX resistance network

resistance network represents one full primary and secondary coolant channel and is representative of all pairs of channels because of the uniform flow distribution assumption. Therefore, the total segment thermal resistance of one MCHX block was calculated by accounting for the total number of channels per sheet, $n_{ch,ps}$, and pairs of sheets per MCHX block, n_{sheet}, as shown in Eq. (4.4). Fin efficiencies were approximately 75% to 78% and the overall finned surface efficiencies were between 92% and 94% for both coolants.

$$R_{ch} = \frac{1}{\eta_o h A_{ch}} \quad R_{wall} = \frac{t_{wall}}{k_{wall} A_{wall}} \quad R_{fouling} = \frac{t_{foul}}{k_{foul} \eta_o A_{ch}} \tag{4.3}$$

$$R_{parrellel} = \frac{R_{top} R_{bottom}}{R_{top} + R_{bottom}} \quad R_{seg} = \frac{R_{parrellel}}{n_{ch,ps} n_{sheet}} \quad UA_{seg} = \frac{1}{R_{seg}} \tag{4.4}$$

The heat transfer coefficient for both coolant streams was determined using the Churchill (1977a) Nusselt number correlation. This correlation, developed from macrochannel data, spans the laminar, transition, and turbulent flow regimes by utilizing an asymptotic averaging technique to account for the different behavior in the three regimes and is shown in Eq. (4.5). Churchill (1977b) also developed a correlation for the Darcy friction factor, which is applicable in the three regimes using a similar asymptotic approach, shown in Eq. (4.6). These correlations are particularly useful when the flow rate and flow regime

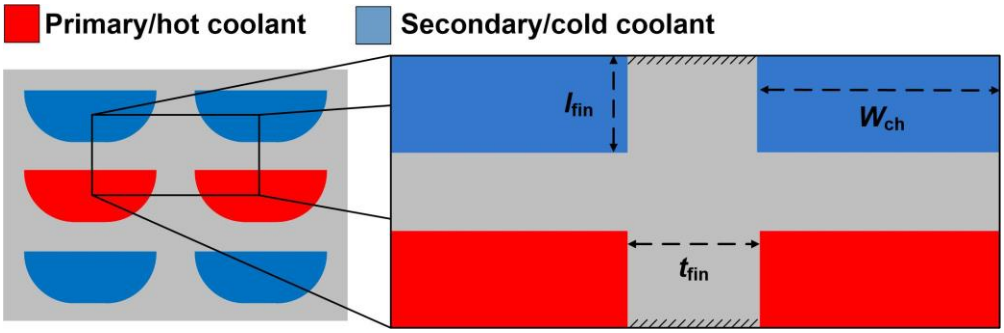

Figure 4.6: MCHX fin approximation

may vary during the design process. Both primary and secondary conditions in the liquid-liquid MCHX design are fully turbulent.

$$\mathrm{Nu}^{10} = 4.364^{10} + \left[\frac{\exp\left(\frac{2200-\mathrm{Re}}{365}\right)}{4.364^2} + \left(6.3 + \frac{0.079\left(f/8\right)^{0.5}\mathrm{Re}\,\mathrm{Pr}}{\left(1+\mathrm{Pr}^{0.8}\right)^{5/6}} \right)^{-2} \right]^{-5} \tag{4.5}$$

$$f = 8\left[\left(\frac{8}{\mathrm{Re}}\right)^{12} + \left(\left\{ 2.457 \ln\left(\left[\left(\frac{7}{\mathrm{Re}}\right)^{0.9} + 0.27\frac{\varepsilon}{D_h} \right]^{-1} \right) \right\}^{16} + \left\{ \frac{37530}{\mathrm{Re}} \right\}^{16} \right)^{-1.5} \right]^{\frac{1}{12}} \tag{4.6}$$

The regions between channels on the same sheet were treated as adiabatically tipped fins, as shown in Figure 4.6. They were assumed to be rectangular, with a uniform cross-sectional area of thickness, t_{fin}, and height, l_{fin} (equal to half of the channel height, $h_{ch}/2$). The overall surface efficiency was calculated using Eq. (4.7) (Incropera *et al.*, 2007), which assumes the channel length is significantly longer than the thickness of the fin. Once the overall surface efficiency was determined, the actual surface areas of the half channels were used to calculate the convective resistance in Eq. (4.3).

$$m = \left(\frac{2h}{k_{fin} t_{fin}} \right)^{1/2} \qquad \eta_{fin} = \frac{\tanh\left(m l_{fin}\right)}{m l_{fin}} \qquad \eta_o = 1 - \frac{A_{fin}}{A_{total}} (1 - \eta_{fin}) \tag{4.7}$$

The total heat duty of an MCHX block was determined by summing the heat duty in each segment. For the geometry and inlet fluid conditions specified in Section 4.2, this model predicted a heat duty of 32.39 kW per MCHX block or 2850 MW_{th} for all 88 MCHX blocks.

4.5 Pressure Drop and Flow Distribution Model

A parallel flow path model, similar to that presented by Tuo and Hrnjak (2013), was used to determine the pressure drop and flow distribution for the primary and secondary coolants. The primary coolant was modeled by dividing the heat exchanger stack and headers vertically into eleven segments, one for each MCHX block in the stack. Each flow path starts at the top of the inlet header, passes through a single MCHX block, and ends at the exit of the outlet header as shown in Figure 4.7. Therefore, there are a decreasing number of flow paths moving down the heat exchanger stack, while the number in the outlet header increases. The

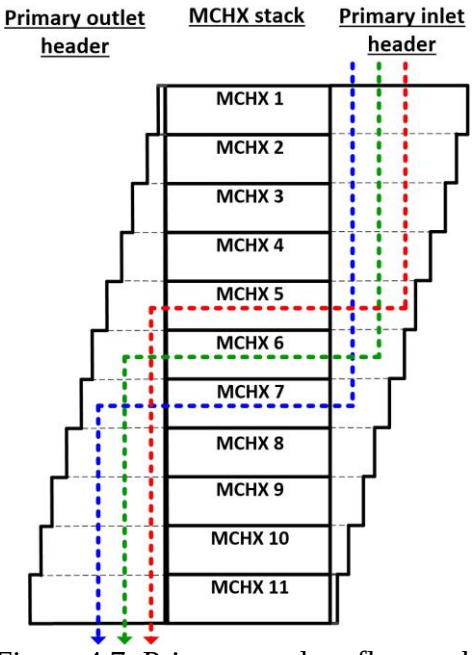

Figure 4.7: Primary coolant flow paths

tapered inlet and outlet headers were treated as rectangular ducts of the average cross-sectional area within the segment. Header segment pressure losses were calculated using the average cross-sectional area and the flow rate from all paths passing through the segment. As a result, all flow paths passing through a header segment have the same pressure change, and the pressure along the header length can be calculated. Because all flow paths start and end in the same locations and at the same pressures, they must all have the same total pressure drop. The mass flow rates of each path and the total pressure drop were iteratively solved using EES by imposing this requirement.

Flow paths represent fluid streamlines along which pressure changes can be calculated through the use of a mechanical energy balance for incompressible flow, as show in Eq. (4.8) . This includes reversible pressure changes due to acceleration/deceleration and changes in height, as well as irreversible pressure losses from friction and flow obstructions (minor losses). The sum of pressure losses along a flow path is shown in Eq. (4.9). Required friction factor and loss coefficient are shown in Table 4.2. For minor losses associated with expansions and contractions, the larger of the two velocities, either before or after the flow disturbance, is used in Eq. (4.8). Each pressure loss identified in Eq. (4.9) had a different value for each flow path. For example, the pressure loss from the 90° bend into channels is dependent upon the velocity in the header segment where the flow path turns into the heat exchanger. Therefore, the loss is larger in a higher velocity segment. Additionally, flow paths that cover longer distances in the inlet or outlet header will have a higher header frictional pressure losses compared to flow paths that cover shorter lengths. In typical microchannel applications, velocities in the channels are higher than those in the headers, which leads to inlet contraction

Table 4.2: Primary coolant frictional and minor pressure losses

Pressure loss	Equation	Reference
Inlet	$k_L = 0.50$	Cengel and Cimbala (2006)
Inlet header (rectangular header)	$f = \left[1.0875 - 0.1125(2b/2a)\right] f_c$ $f_c = 4\left[1.7372 \ln\left(\frac{\mathrm{Re}}{1.9464\ln(\mathrm{Re}) - 3.8215}\right)\right]^{-2}$ b = larger rectangular length (m) a = shorter rectangular length (m)	Techo *et al.* (1965)
90° bend into channel	$k_L = 1.20$	Cengel and Cimbala (2006)
Sudden expansion	$k_L = \left(1 - \frac{A_{sm}}{A_{la}}\right)^2$ sm = smaller cross-sectional area (header) la = larger cross-sectional area (channel)	Ghiaasiaan (2017)
Channel	See Eq. (4.6)	Churchill (1977b)
Sudden contraction	$C_c = 1 - \frac{1 - A_{sm}/A_{la}}{2.08(1 - A_{sm}/A_{la}) + 0.5371}$ $k_L = \left(\frac{1}{C_c} - 1\right)^2$ sm = smaller cross-sectional area (header) la = larger cross-sectional area (channel)	Ghiaasiaan (2017)
90° bend into header	$k_L = 1.2$	Cengel and Cimbala (2006)
Outlet header (rectangular header)	listed above	Techo *et al.* (1965)
Outlet	$k_L = 1.10$	Cengel and Cimbala (2006)

and outlet expansion pressure losses. Here, header velocities were greater than those in the microchannels, and the trend was reversed. The cross-sectional area occupied by the flow path in headers, required for expansion and constriction losses, was calculated using the header velocity and conservation of mass: $A_{cx,header} = \left(\dot{m}_{flow\ path}\right) / \left(\rho V_{header}\right)$. Fluid properties in the inlet and the outlet header were evaluated at the inlet and outlet temperatures identified in Table

4.1, respectively. Fluid properties required for channel pressure drop calculations were evaluated at the average of the inlet and outlet temperatures.

$$\Delta P = P_{in} - P_{out} = \underbrace{\frac{\rho}{2}\left(V_{out}^2 - V_{in}^2\right)}_{\substack{\text{dynamic pressure/} \\ \text{acceleration}}} + \underbrace{\rho g\left(z_{out} - z_{in}\right)}_{\text{gravity}} - \underbrace{f\left(\frac{\rho V^2}{2}\right)\frac{l}{D_h}}_{\text{friction}} - \sum \underbrace{k_L\left(\frac{\rho V^2}{2}\right)}_{\text{minor losses}} \tag{4.8}$$

$$\Delta P^i = \Delta P_{inlet} + \sum_{1}^{i} \Delta P_{header,in}^i + \Delta P_{90,in}^i + \Delta P_{exp}^i + \Delta P_{ch}^i + \Delta P_{con}^i + \Delta P_{90,out}^i + \sum_{i}^{N} \Delta P_{header,out}^i + \Delta P_{outlet} \tag{4.9}$$

This method predicted a frictional pressure drop of 472.9 kPa and total pressure drop of 433.8 kPa for the final design conditions specified in Section 4.2. Gravity resulted in a significant increase in pressure as the coolant flowed down the MCHX stack. Pressure changes due to acceleration/deceleration in headers had a negligible effect. This was a result of the changing cross-sectional areas of the inlet/outlet headers, which created a nearly constant velocity along the axial height. Table 4.3 shows the irreversible pressure losses averaged over the eleven flow paths. Pressure drop in the channels accounted for less than 20% of the total, with the major portion of the pressure drop occurring due to minor losses in the high velocity inlet and outlet headers. The flow path model also estimates the flow rate through each MCHX block in the stack and allows the pressure in the two headers to be calculated. Figure 4.8 shows the flow distribution in each MCHX block as well as the inlet and outlet header pressures. The pressure in the headers stayed relatively constant as frictional pressure losses in the headers were offset by pressure gains from gravity. As a result, the differential pressure and flow rate across each heat exchanger was also relatively constant. MCHX blocks in the center of the stack received flow rates slightly higher than those at the top and bottom due to smaller cross-sections at the bottom of the inlet header and top of the

outlet header. This led to a higher friction factor, smaller hydraulic diameter, and consequentially a higher frictional pressure drop for a given flow rate. Despite this, all eleven units had flow rates within ±3% of the evenly distributed flowrate of 176.1 kg s^{-1}, helping to validate the even distribution assumption used in the heat transfer model. The pressure drop in parallel channels should typically be larger than header pressure changes to ensure an even flow distribution, as discussed in Section 3.6. Here the tapered headers result in a uniform

Table 4.3: Average primary coolant flow path pressure losses

Pressure loss	**Avg. velocity (m s^{-1})**	**Avg. ΔP (kPa)**
Inlet	14.8	35.8
Inlet header	15.4	11.6
90° bend into channel	15.4	93.6
Sudden expansion into channel	15.4	78.3
Channel losses	3.00	77.7
Sudden contraction into header	13.7	21.7
90° bend into header	13.7	80.8
Outlet header	13.7	10.1
Outlet	13.3	63.3

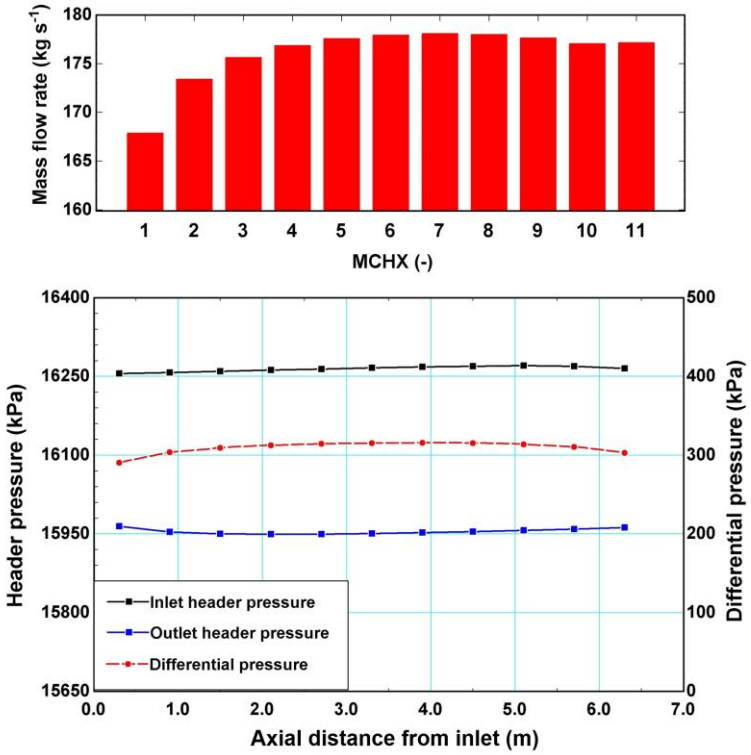

Figure 4.8: Primary coolant flow distribution

differential pressure across all MCHX blocks in the stack. By further increasing the cross-sectional area of the primary coolant header, the pressure changes in the header can be reduced relative to the channel pressure drop, ensuring an even distribution. However, increasing the header volume comes at the cost of heat transfer area, as discussed in Section 4.7.

The secondary coolant pressure drop was also modeled using a parallel flow path method. An equal flow rate into each sheet in the MCHX stack was assumed. Secondary coolant sheets were split into ten equal length segments in the azimuthal direction, each with a flow path from inlet to outlet header, as shown in Figure 4.9. Frictional losses in the flat inlet and outlet headers were calculated with the turbulent friction factor correlation developed by Dean (1978), shown in Eq. (4.10). Pressure losses along the flow path were calculated as described previously using Eqs. (4.8) and (4.9). Flow rates and total pressure drop were again solved iteratively by requiring an equal pressure drop for all paths.

$$f = \frac{0.3472}{\mathrm{Re}^{0.25}} \tag{4.10}$$

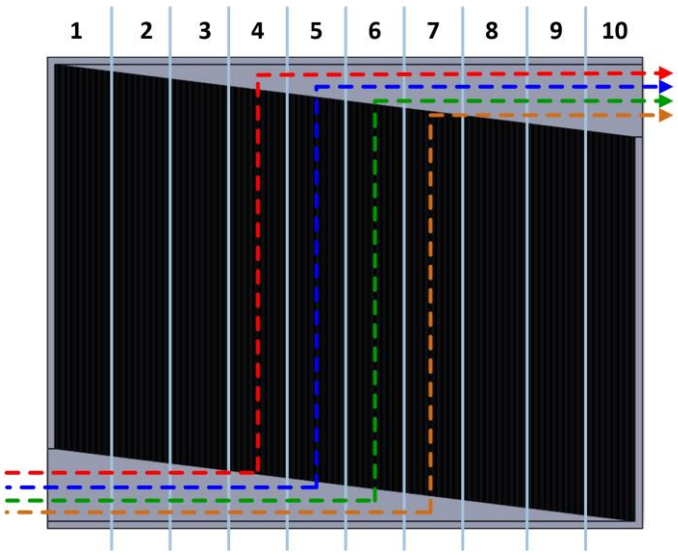

Figure 4.9: Secondary coolant flow paths

This method predicted a total secondary pressure drop of 1115 kPa and frictional pressure drop of 1117 kPa. No gravitational pressure changes were included, and acceleration/deceleration in headers again had a negligible effect due to relatively constant velocity in the headers. The average pressure losses over the ten flow paths are presented in Table 4.4. The frictional pressure drop in the headers was significantly higher than that of the

Table 4.4: Average secondary coolant flow path pressure losses

Pressure loss	**Avg. velocity (m s^{-1})**	**Avg. ΔP (kPa)**
Header inlet	11.5	25.3
Inlet header frictional losses	12.2	373
90° bend into channel	12.2	68.2
Sudden expansion into channel	12.2	57.6
Channel frictional losses	2.43	46.2
Sudden contraction into header	13.4	19.9
90° bend into header	13.4	72.7
Outlet header frictional losses	13.4	381
Header outlet	13.0	70.6

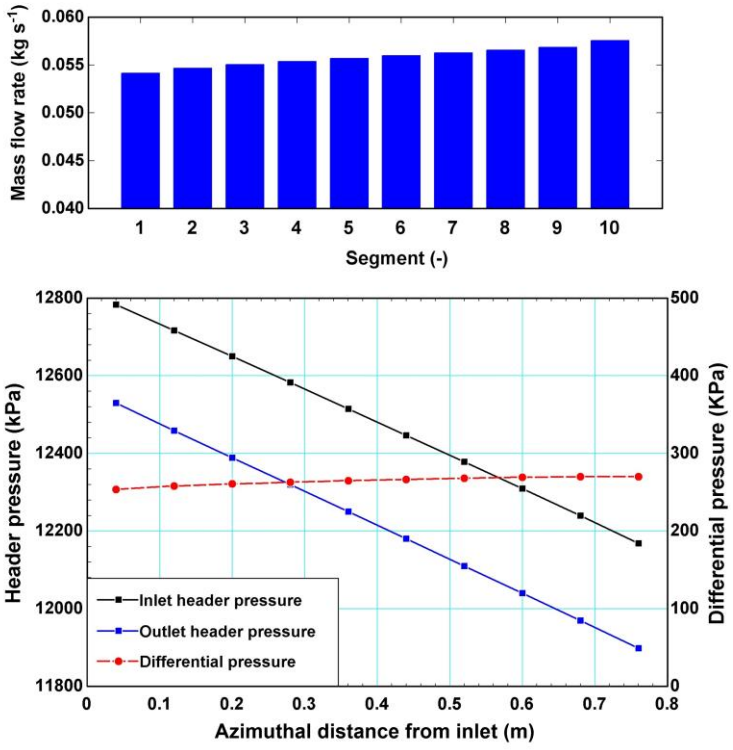

Figure 4.10: Secondary coolant distribution

primary coolant because of the smaller hydraulic diameter of the flat triangular headers. As a result, there was a larger decrease in pressure along the lengths of the headers as shown in Figure 4.10. However, the parallel oblique (triangular) header design led to a symmetric pressure drop in both headers and a nearly constant differential pressure over the header length. Non-uniformity in channel pressure drop and flow rate was the result of higher temperature and lower density in the outlet header, which led to a higher velocity and pressure drop when compared to the inlet header. Consequently, flow paths with shorter outlet header lengths (higher number segments) had a larger flow rate. Still, flow rates in all paths were within ±3% of the evenly distributed value of 0.05582 kg s^{-1}.

4.6 Mechanical Integrity

Under normal operating conditions, the primary coolant has an inlet pressure of 16.3 MPa, while the secondary coolant inlet pressure is 12.9 MPa. In accident scenarios, one coolant pressure may be dramatically reduced. The complete loss of pressure in the secondary coolant, a differential pressure of 16.3 MPa, was used as the design basis for mechanical integrity. In addition, the differential design pressure was multiplied by a safety factor of 1.5, resulting in a differential design pressure of 24.45 MPa. It should be noted that both primary and secondary coolant channels have the same dimensions and therefore have the same pressure limits.

Le Pierres *et al.* (2011) suggested treating MCHX channels as a rectangular plate stayed pressure vessel. The channels were assumed to be rectangular and walls between channels were treated as stay plates as shown in Figure 4.11. Section VIII Division I Mandatory Appendix XIII of the ASME boiler and pressure vessel code (ASME, 2019)

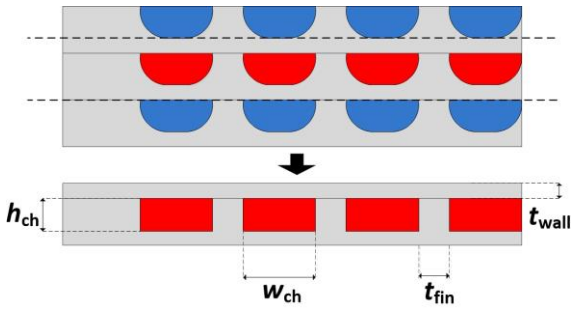

Figure 4.11: MCHX pressure vessel approximation

Table 4.5: Channel membrane and bending stresses

Fin	**Wall**
$S_m = \frac{Pw_{ch}}{t_{fin}}$	$S_m = \frac{Ph_{ch}}{2t_{wall}}$
$S_b = 0$ Pa	$S_b = \frac{Pw_{ch}^2 t_{wall}}{24I} \quad I = \frac{t_{wall}^3}{12}$

requires the membrane stress, S_m, to remain below $S \times E$, where S is the maximum allowable stress of the material and E is the joint efficiency. The total stress, sum of the membrane stress and bending stress, S_b, must remain below 1.5 ($S \times E$). $E = 0.7$ is an accepted joint efficiency for diffusion bonding and the maximum allowable stress of 316 SS at 400°C is 111 MPa (Li *et al.*, 2009). Table 4.5 contains the equations for the bending and membrane stress on both the fins and walls. Using the above requirements, the equations in Table 4.5, and a safety factor adjusted pressure of 24.45 MPa, the minimum wall thickness and fin thicknesses of channels was determined for the channel width and height.

The total wall stress is the limiting stress for the channel dimensions in Figure 4.2. Stated another way, for a channel height of 0.635 mm and width of 1.397 mm, the minimum sheet thickness that meets the BPVC total wall stress requirements is 1.130 mm ($t_{wall} = 0.495$ mm). Wall membrane stress, fin membrane, and fin total stress are not at the BPVC limits given these dimensions.

4.7 Geometric Optimization

The outer dimensions of the MCHX stack were set by the available downcomer volume. Thus, dimensions of the channels, sheets, and headers were varied to meet design requirements. While all dimensions discussed in Section 4.2 were investigated, the channel size and the radial length of the primary coolant header had the greatest impact on performance.

When the influence of the channel size was investigated, the channel height, h_{ch}, was varied and the other dimensions in Figure 4.2 were adjusted proportionately. BPVC thickness requirements were also satisfied. Figure 4.12 shows the result of a parametric study in which inlet conditions, header dimensions, and active channel length were held constant at the final design values. As the size of the channels was reduced, the heat transfer increased as a result of several factors. Smaller channels allowed for a larger number of channels per sheet and sheets per heat exchanger, thereby increasing heat transfer surface area per unit volume. Smaller wall thicknesses sufficed to satisfy structural strength requirements for smaller channels, decreasing the conductive resistance. Finally, the smaller channels also yielded

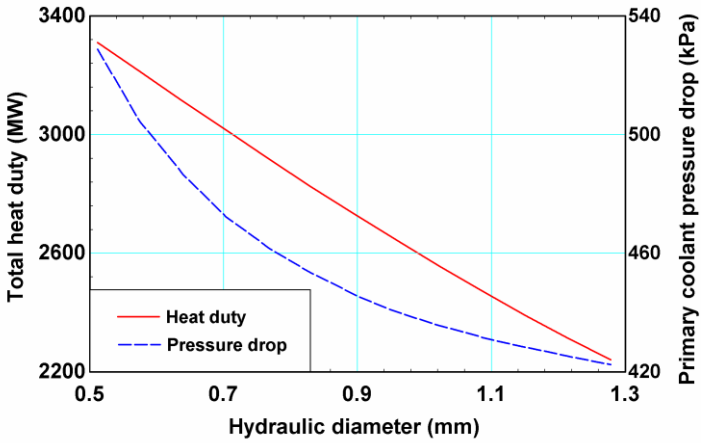

Figure 4.12: Influence of channel size

higher convective heat transfer coefficients. Due to the increasing number of channels, the mass flux remained relatively constant as the size of the channels was decreased. As a result, the Reynolds number decreased linearly with the hydraulic diameter. The turbulent Nusselt number also decreased, proportional to approximately $Re^{0.8}$, in accord with the Dittus and Boelter (1930) correlation. However the heat transfer coefficient increases linearly as the hydraulic diameter decreases for a given Nusselt number. Therefore, there was a modest increase in the heat transfer coefficient as the size of the channel was decreased, approximately proportional to $D_h^{-0.2}$. Increased heat transfer for small channels was weighed against the increased pressure drop. For a fixed friction factor and mass flux, the frictional pressure drop increases as the channel size decreases, proportional to D_h^{-1}. The friction factor also increases as the channel size decreases as a result of decreasing Reynolds number, further increasing the frictional pressure drop. However, much of the pressure drop through the MCHX stacks occurred in header regions and the overall pressure drop was not significantly influenced by the channel size. Smaller channels may also increase the potential for clogging/plugging of the channels. To account for this concern, a relatively large hydraulic dimeter of 0.812 mm was selected. If clogging/plugging was not a significant concern, a design with smaller channels could be employed with a shorter active channel length and more radial length available for primary and secondary coolant headers, decreasing the frictional pressure drops. Due to that fact that heat transfer performance increased with decreasing channel size, the minimum hydraulic diameter was used for both primary and secondary coolant channels.

The effect of small deviations in channel dimensions was also investigated. The channel height was increased by 10% (h_{ch} = 0.699 mm, D_h = 0.890 mm) while the number of

channels per sheet ($n_{ch,ps}$), flat length (l_{flat}), and sheet thickness (t_{sheet}) was held constant, resulting in a thinner fin (t_{fin} = 0.273 mm). The fluid inlet conditions and other dimensions of the MCHX where fixed at the final design values reported in Section 4.2. The heat duty decreased by 17 MW or 0.60%. Similarly, a 10% decrease in the channel height (h_{ch} = 0.572 mm, D_h = 0.734 mm, t_{fin} = 0.572 mm) resulted in an increase in the heat duty of 10 MW or 0.35%. The changes in the heat duty were small due to offsetting heat transfer effects. Smaller channels resulted in decreased surface area but also in increased mass flux and led to larger heat transfer coefficients. The pressure drop did not change significantly because much of the pressure drop is due to high velocity flow in the headers. The primary coolant pressure drop increased by 44 kPa or 10.1% when the channel size was reduced, and decreased by 24 kPa or 5.5% when the channel size was increased.

Figure 4.13 shows the total heat duty and primary coolant pressure drop as a function of primary coolant header radial length. The total radial length of the MCHX stack was fixed at 0.85 m, while the radial length of the secondary coolant headers was held constant at 0.10 m. The remaining 0.75 m was split between the active channel length and primary header length. Channel geometry and fluid inlet conditions were also held constant at final design

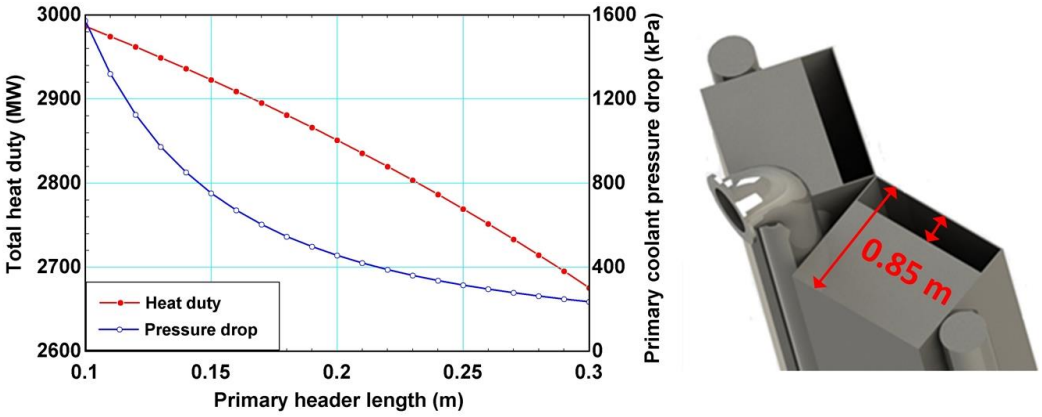

Figure 4.13: Influence of primary header length

values. As length of the header increases, the primary coolant pressure drop decreases due to an increased flow area and lower fluid velocity. However, the increased header length comes at the cost of less active channel length and presents a tradeoff between primary coolant pressure drop and heat duty. Decreasing the header length below 0.2 m results in a large increase in pressure drop as minor and frictional losses in the header regions rise proportional to the velocity squared.

4.8 Flash Rankine Cycle

The flash Rankine cycle concept is similar to a conventional Rankine cycle, except that steam is generated in a flashing drum instead of a boiler or steam generator (Memmott *et al.*, 2017a; Memmott *et al.*, 2017b). In the I^2S-LWR flash Rankine cycle design, secondary coolant is heated in the liquid-liquid MCHX at high pressure before it enters a flashing drum where the pressure is reduced; this produces saturated steam and saturated liquid water. The saturated liquid is then recycled back into the MCHX, while the steam is utilized for electrical power production. The expansion of saturated steam in a turbine to the condenser pressure would result in high moisture content at the turbine outlet (low quality). High moisture content can lead to turbine blade erosion and decreased efficiency, and should therefore be kept to less than 15% ($x = 0.85$) (Steam, 2005). Hence, external moisture separators between high and lower pressure turbines or turbines designed to remove moisture are required. Reheaters are also utilized in the design to heat turbine exhaust with higher temperature streams from other parts of the cycle, further reducing moisture content. Similar techniques are used in operating nuclear Rankine cycles where steam produced in steam generators (PWR) or the reactor core (BWR) is typically at or near saturation. Feedwater heaters are used in Rankine power cycles to heat the working fluid from the condenser temperature to a temperature closer

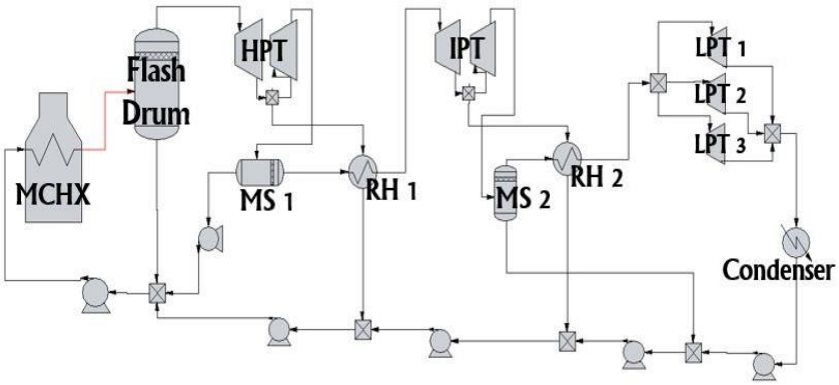

Figure 4.14: Flash Rankine cycle (Memmott *et al.*, 2017b)

to that of the heat source. This reduces irreversibility and improves cycle efficiency by increasing the average temperature of heat addition. In the flash Rankine cycle design, open feedwater heaters (OFWH) are used to heat the secondary coolant to temperatures closer to that of the primary coolant before it enters the MCHX. Existing nuclear plant Rankine cycle designs typically have between five and seven feedwater heaters (El-Wakil 1984, Steam 2005).

4.8.1 Flash Rankine cycle model

Memmott *et al.* (2017b) developed steady-state thermodynamic models for three designs for the I^2S-LWR flash Rankine cycle in ChemCAD and found the design shown in Figure 4.14 to be the most efficient. This design contains four OFWHs, three turbines, and two reheaters. The high and intermediate pressure turbines both have bleed streams that are diverted through a reheater before entering OFWHs. The high and intermediate pressure turbine exhaust streams are directed to an external moisture separator. The saturated steam from the moisture separators is superheated in reheaters while the saturated liquid and a small portion of steam are directed to OFWHs. Independent variables in their model included flash drum pressure, turbine outlet and bleed pressures, bleed stream flow rates diverted to the two

Table 4.6: Flash Rankine cycle assumptions

Assumption	Value
Condenser temperature / pressure	T = 42.9°C / P = 8600 Pa
Closest approach temperature (reheaters)	ΔT = 10°C
Isentropic turbine efficiency	η_t = 0.915
Isentropic pump efficiency	η_p = 0.85
Minimum turbine outlet quality	x = 0.88

reheaters, and the secondary coolant flow rate. Important assumptions that were used by Memmott *et al.* (2017b) to develop the model, including the condenser temperature and turbine efficiency, are shown in Table 4.6.

4.8.2 Flash Rankine cycle optimization

Primary coolant conditions were set by core safety analysis, as previously discussed. However, the secondary coolant flow rate and temperatures could be varied to maximize the thermal efficiency of the flash Rankine cycle. A range of potential coolant operating conditions meeting the overall heat duty requirement was calculated using the final design geometry and is shown Figure 4.15. The secondary coolant outlet pressure was chosen at a value that corresponds to the saturation pressure of water 5°C above the outlet temperature,

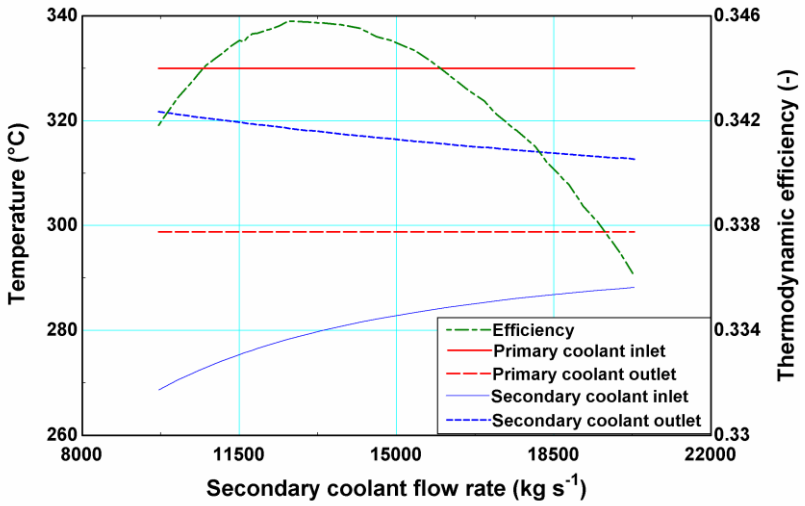

Figure 4.15: Secondary coolant flow rate optimization

which ensures single-phase operation without unnecessary load on secondary pumps. The figure shows that as the secondary coolant flow rate increases, the secondary coolant inlet temperature rises, while the outlet temperature falls. The inlet temperature rises because a higher coolant flow rate leads to a higher secondary coolant heat transfer coefficient, which in turn leads to a lower temperature difference requirement between the primary and secondary coolant to transfer the same heat duty. The decrease in the outlet temperature with increasing coolant flow rate is due to the increased thermal capacity rate of the coolant, which incurs a lower temperature rise for the same heat duty. Memmott *et al.* (2017b) performed an optimization of independent variables in their model to determine the maximum thermal efficiency of the flash Rankine cycle at each of the potential operating conditions. The thermal efficiency is shown in Figure 4.15, and a peak thermal efficiency of 34.58% was found to occur at a secondary coolant flow rate of 13,016 kg s^{-1}.

4.9 Impact of Fouling Assumptions

A fouling build-up of 10 μm with thermal conductivity of k_{foul} = 1.3 W m^{-1} K^{-1} on both the primary and secondary coolant channels was used as a design basis. Figure 4.16 shows

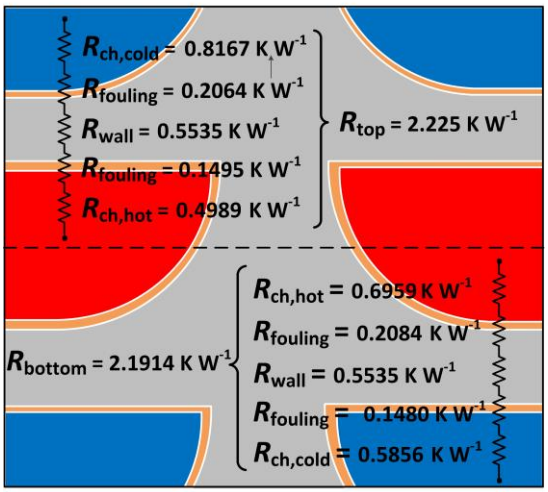

Figure 4.16: Representative resistances network

the parallel resistance network representing a primary and secondary coolant channel at segment ten of the twenty-segment model (l_{seg} = 0.0275 m). The fouling resistance represents almost 16% of the top and bottom resistances. The parallel resistance, shown in in Eq. (4.4), is reduced from 1.1022 K W^{-1} to 0.9259 W^{-1} when fouling is ignored. Thus the fouling resistance has a moderate impact on performance.

The amount and resistance of fouling material that may accumulate in the MCHX remains a relative unknown. Therefore, a parametric study on the impact of fouling thicknesses was performed. Figure 4.17 shows the total heat duty and secondary coolant outlet temperature for fouling thicknesses ranging from 0 to 40 μm (on both coolant channels). Fluid inlet conditions and the heat exchanger geometry were fixed at the final design values outlined in Section 4.2. The total heat duty decreased by approximately 15% over the entire range, indicating that fouling beyond 10 μm does not radically influence performance. If evidence of increased fouling becomes available, the I^2S-LWR heat exchanger design requirements can be met with modifications to the geometry or secondary coolant operating conditions.

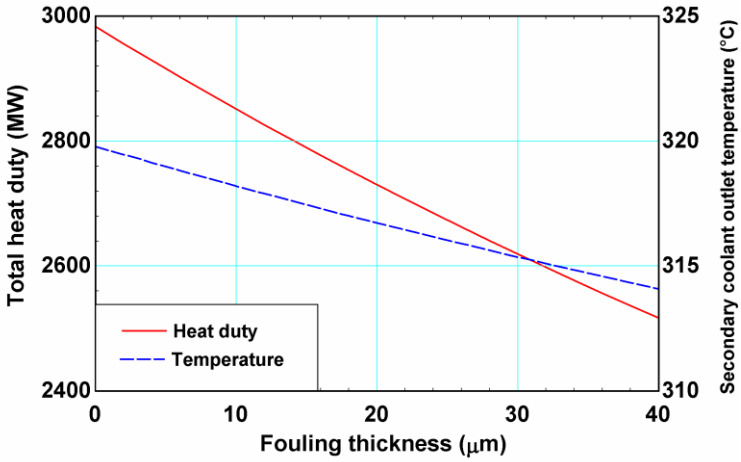

Figure 4.17: Influence of fouling material

CHAPTER 5. LIQUID-LIQUID EXPERIMENTS

An experimental investigation to validate the accuracy of the liquid-liquid MCHX model discussed in the previous chapter was conducted. Tests were conducted on a representative scaled MCHX test section under non-dimensional conditions similar to those in which the I^2S-LWR MCHX would operate. Measured values of the heat duty and pressure drop were compared with model predictions. Additionally, the average measured Nusselt number and friction factors were deduced from the data and compared with those predicted by the correlations used in the design. While the I^2S-LWR MCHX channels are in the turbulent flow regime, experiments were also conducted in the laminar, transition, and turbulent regimes.

5.1 MCHX Test Section

An MCHX test section was constructed from twenty photo-chemically etched 304L SS sheets, alternating between hot- and cold-fluid sheets. Sheets carrying the hot fluid have inlet and outlet headers connected by thirty straight channels. The cold-fluid sheets contain triangular (parallel oblique) headers etched into the sheet at both ends of the channels. The headers direct the fluid into thirty channels, counterflow to those of the hot sheets, replicating the I^2S-LWR MCHX configuration. The cold sheet channel length is 201 mm (active length) as compared to 273 mm in the hot sheets. The test section contains headers larger than the I^2S-LWR design, relative to the number of channels, to minimize the pressure drop in headers and help ensure an even flow distribution. Top and bottom cover plates were cut from 12.7 mm (0.5 in) and 6.35 mm (0.25 in) thick 304L SS plates, respectively, using a high-pressure water jet at the Georgia Tech Research Institute (GTRI) machine shop. A 12.7 mm inch thick

top plate was selected so that inlet piping (25.4 mm *OD*, 21.16 mm *ID*) could be welded onto the plate without damaging or deforming the channels in the sheets below. The sheets and cover plates were diffusion bonded to yield the test section. Guide pins inserted into two small holes at either end of the sheets and cover plates ensured dimensional stability during the bonding process. The sheets were photo-chemically etched by Advanced Metal Etching Inc. (AME) of Ligonier, Indiana. Diffusion bonding and the welding of headers were performed by Vacuum Process Engineering Inc. (VPEI) of Sacramento, California. A schematic of the two sheet designs and a CAD rendering of the test section are provided in Figure 5.1. Images of etched sheets and the final MCHX test section assembly are shown in Figure 5.2.

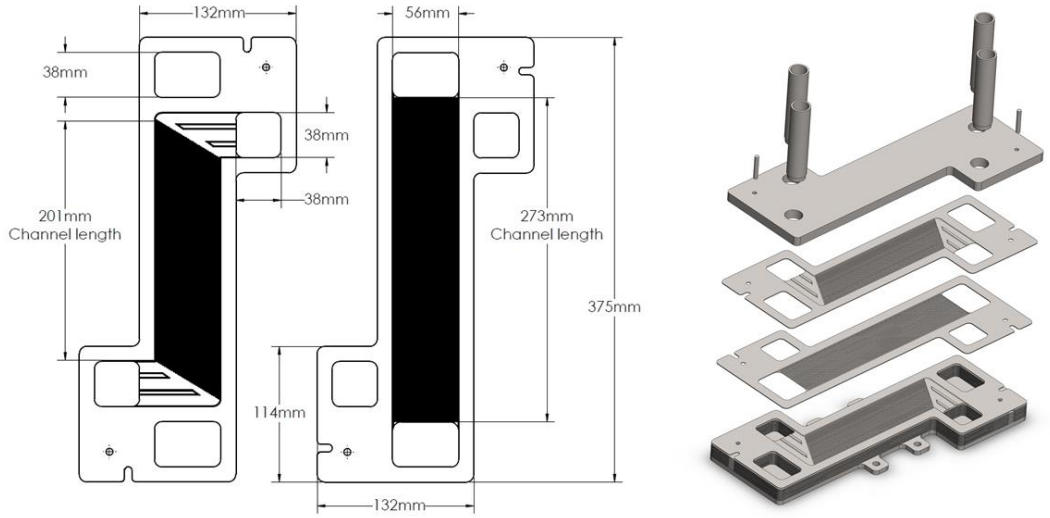

Figure 5.1: MCHX test section design

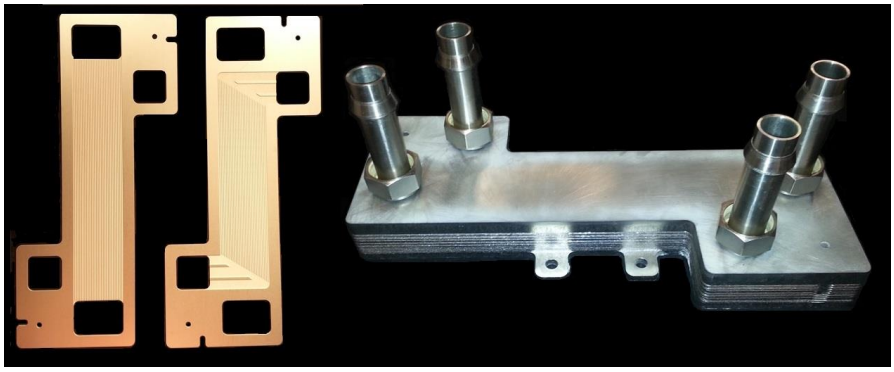

Figure 5.2: MCHX test section and microchannel sheets

Several measurement techniques were used to determine important channel and sheet dimensions. Channel width and fin thickness were measured using an Aven Tools CMOS 26100-240 camera attached to a Carton SPZT50 Trinocular Microscope. The dimensions were measured in reference to Meyer Gage Company rods of known diameter (ASNI B89.1.5-1998) using TSView image processing software, as shown in Figure 5.3. Three channel widths and two fin thicknesses were measured on ten different sheets (five hot sheets and five cold sheets).

The sheet thickness and channel height were measured using a Mitutoyo ID-S112T digital depth gage, as shown in Figure 5.4. The sheet thickness and the thickness at the center

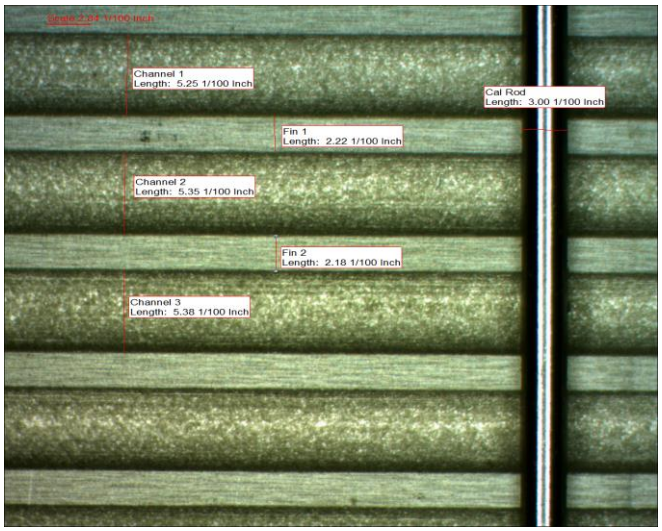

Figure 5.3: Channel width and fin thickness measurement technique

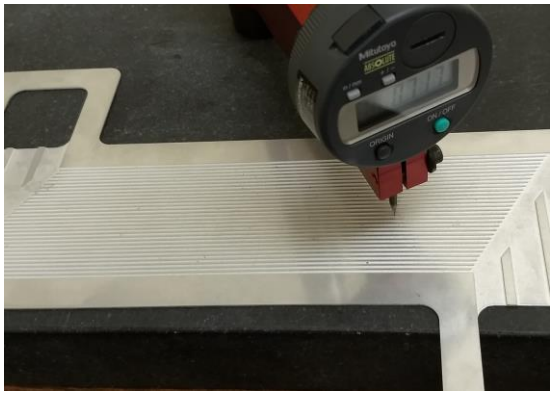

Figure 5.4: Sheet thickness and channel depth measurement technique

of a channel were measured in four locations per sheet. Thickness measurements at the center of channels were subtracted from the average thickness of the sheet to determine the channel height. This process was again repeated for five hot sheet and five cold sheets.

Channel dimensions for the test section were similar to those used in the I^2S-LWR liquid-liquid MCHX design listed in Figure 4.2. Two sets of sheets were fabricated by AME with the measured dimensions and standard deviations shown in Figure 5.5. The first set of sheets had wider channels and smaller fins than specified. This resulted in a hydraulic diameter of 0.8608 mm as compared to the desired value of 0.8049 mm. The first set was used for the construction of the MCHX test section due to time constraints. A second set was fabricated to demonstrate that the selected channel dimensions could be etched into the sheets. The width in the second set was closer to specifications, but the channel depth was slightly shallower, resulting in a hydraulic dimeter of 0.7304 mm. The manufacturer, AME, believed that given additional iterations, the specified dimensions could be met. In both sets of sheets, the standard deviation of measured dimensions were relatively low, indicating a high degree of control over the channel dimensions.

Dimension	Symbol	Specification (mm)	Set One (mm)	Set Two (mm)
Channel height	h_{ch}	0.6350 (0.025 in)	0.6140 ± 0.0200	0.5394 ± 0.0292
Sheet thickness	t_{sheet}	1.0160 (0.040 in)	1.0835 ± 0.0041	1.0388 ± 0.0076
Fin thickness	t_{fin}	0.5080 (0.020 in)	0.2337 ± 0.0221	0.5660 ± 0.0217
Channel width	w_{ch}	1.3716 (0.54 in)	1.7031 ± 0.0268	1.3622 ± 0.0371

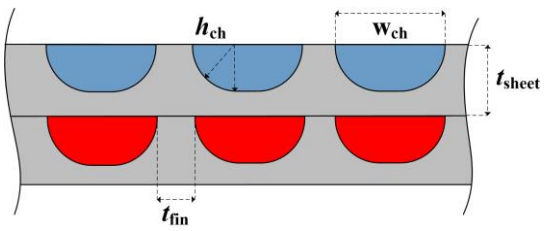

Figure 5.5: Test sections channel measurements

Additional measurements were taken on a single cold sheet from the second set using a ContourGT 3D optical microscope. Four surface roughness measurements were taken in 24 mm by 17 mm areas of the triangular header regions. These showed an average root mean square surface roughness of 1.00 μm, less than the assumed value of 2 μm for the I^2S-LWR MCHX design. A two-dimensional profile of all thirty channels and twenty-nine fin regions of the sheet was also collected. Analysis of the profile showed an average channel height of h_{ch} = 0.507 mm, channel width of w_{ch} = 1.295 mm, and fin thickness of t_{fin} = 0.577 mm. These measurements were consistent with the values reported for the second sheet set in Figure 5.5.

5.2 Liquid-Liquid Test Facility

5.2.1 Sustainable Thermal Systems Laboratory facilities

The Sustainable Thermal Systems Laboratory (STSL) contains several infrastructure facilities used in this experimental investigation. Saturated steam up to 1825 kPa and 208°C is provided by a lab boiler, which acts as a heat source for the test facility. High- and low-pressure steam distribution headers are located throughout the STSL and pressure regulators allow the steam outlet pressure to be controlled. Condensate return headers with in-line steam traps are also located in the lab. The heat sink for the test facility is a 175 kW lab chiller that supplies a glycol-water solution at controlled temperatures between -10°C to 20°C. The chiller loop distribution and return headers are connected by a valve designed to maintain a set pressure differential pressure between the two headers. Therefore, the flow rate through any parallel path established for experiments is inversely proportional to the hydraulic resistance.

5.2.2 Test facility description

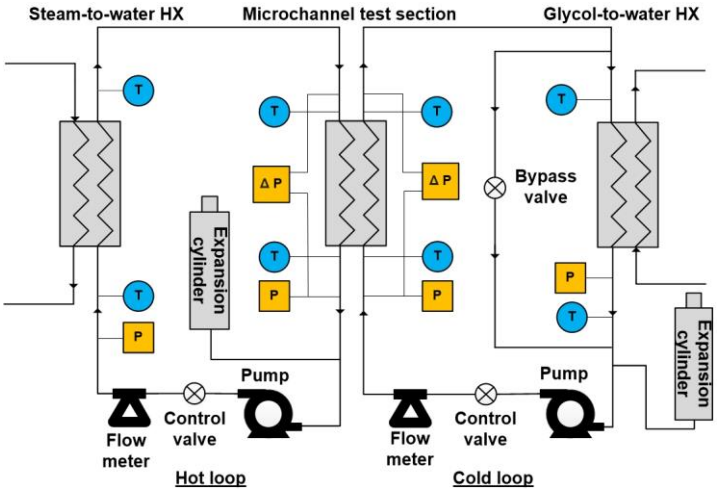

Figure 5.6: Liquid-liquid test facility schematic

The test facility consists of hot- and cold-liquid water loops coupled by the MCHX test section. A photograph and a schematic of the test facility are shown in Figure 5.7 and Figure 5.6, respectively. After the photograph was taken, piping and important components, such as the MCHX test section, were covered in insulation. This was done to both reduce heat loss to the surroundings, as well as to protect the experimenter from the high-temperature piping/components. The facility was designed for hot-side temperatures of up to

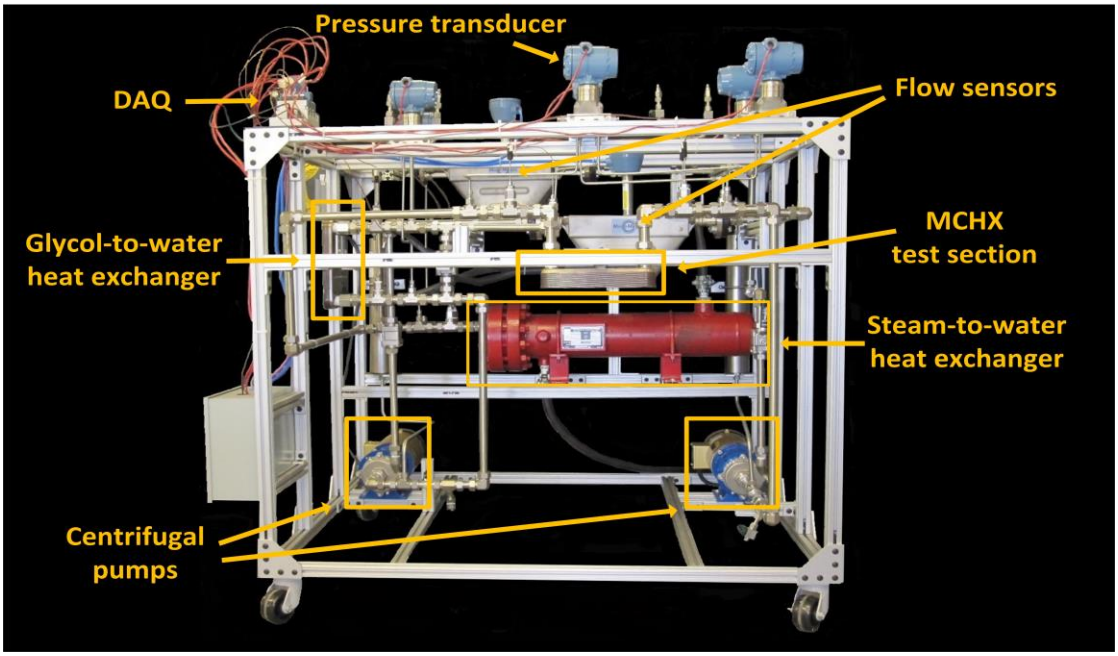

Figure 5.7: Liquid-liquid test facility

approximately 180°C and flow rates in both loops up to approximately one kg per second. Components in each loop are connected with 25.4 mm OD stainless steel tubing and an assortment of Swagelok fittings. This pipe diameter was selected to limit pressure drop between components and maximize fluid flow rates. An Armstrong shell-and-tube heat exchanger transfers heat from steam on the shell side to the hot-loop water on the tube side. The cold loop contains a GEA flat plate heat exchanger that is coupled to the lab chiller loop. A large temperature difference exists between the cold loop test conditions and the chiller loop temperature range. To control and limit the rate of heat transfer, a bypass around the glycol-to-water flat plate heat exchanger is included in the cold loop. The cold loop flow rate through the bypass is adjusted by opening or closing an in-line valve. The pumps on both loops are Liquiflo centrifugal pumps powered by 1.12 kW Baldor motors capable of suppling approximately 1.15 kg s^{-1} with a differential pressure of 165 kPa. The pumps are magnetically coupled to the motor, acting as a thermal break to limit heat transfer from the fluid to the motor. Magnetic couplings were also selected to eliminate leakage that may occur with mechanical couplings exposed to low-viscosity fluids, such as high-temperature water. Baldor variable frequency drives (VFDs) transform 120 Volt AC wall power to three-phase 240 Volt AC power to run the pump motors. Parker Hannifin piston-cylinder accumulators are installed on both loops to control the pressure and allow for fluid expansion. Liquid can flow into the bottom of these cylinders as the fluid in the loop expands, compressing gas above the piston. Both loops contain pressure relief valves designed to open at 3000 kPa. Table 5.1 provides model numbers and additional details about the components discussed above.

5.2.3 Data collection and instrumentation

Table 5.1: Liquid-liquid test facility equipment

Equipment	Manufacturer	Model number	Description/Other
Pumps (2)	Liquiflo	620FSEE020F08(320)	260°C max temperature
Motors (2)	Baldor	SuperE VEM3550	1.12 kW Three-phase AC 240V power
VFDs (2)	Baldor	VS1S11PS-0T	Input: Single-phase AC 120V, 20A max Output: Three-phase AC 240V, 5.8A max
Glycol-to-water heat exchanger	GEA Flat Plate	FP5X12L-10	10 plate 127 mm × 305 mm
Steam-to-water heat exchanger	Armstrong	WSE-4H-0602-400E-3-66SSSSS-18	4 pass 4 tube *ID* 17.8 mm l = 0.705 m
Piston-cylinder accumulators (2)	Parker Hannifin	A3NW116D1H	116 cm^3 displacement High temperature O-ring (177°C)

A summary of test facility instrumentation and associated measurement uncertainties is shown in Table 5.2. Data are acquired using a National Instruments modular compact data acquisition (DAQ) chassis. Several National Instruments modules are installed in the DAQ chassis to collect the various output signals from the instrumentation. Data are organized and exported into Microsoft Excel spreadsheets using National Instruments LabVIEW software. A graphic interface developed in LabVIEW displays instrument readings and trends in real time. Eight Omega J-type thermocouples are located at the inlets and outlets of the three heat exchangers. The voltage differentials generated by the thermocouples are collected using a NI-9213 thermocouple module, which contains built-in cold junction temperature compensation. Thermocouple signals were calibrated in LabVIEW at 10°C intervals between 40°C and 180°C using a NIST-calibrated thermocouple bath, to an uncertainty of ±0.25°C. The test facility contains four Rosemount pressure transducers, including at the exit of the test section on the hot loop and at the inlet to the test section on the cold loop. In addition, two Rosemount differential pressure transducers measure the differential pressure across the test section in both loops. The uncertainty in these pressure transducers is dictated by their

Table 5.2: Liquid-liquid test facility instrumentation

Instrument	Manufacturer	Model	Range (span)	Uncertainty and details
Pressure transducers (4)	Rosemount	3051S2CD4A2E12A1AM5	0 – 4000 kPa	± 0.035% of span (1400 Pa)
Differential pressure transducers (2)		Cold loop: 3051CD3A22A1AB4M6 Hot loop: 3051S2CD4A2E12A1AM5	0 – 200 kPa	± 0.035% of span (70 Pa)
Flow sensors (2)	Micro Motion	F100S129CVBAEZZZZ	0 – 1.4 kg s^{-1}	± 0.10% of measurement
Flow transmitters (2)		1500B3BABMEZZZ	-	-
Thermocouples (8)	Omega	JMQSS-125U-6	–40 – 750°C	± 0.25°C
DAQ chassis	National Instruments	NI cDAQ 9174	-	4 card slots
Thermocouple module		NI 9213	± 78.125 mV	16 channel
Current module (loop-powered)		NI 9208	± 20 mA	16 channel
Current module (single-ended measurement)		NI 9203	± 20 mA	8 channel
DC power supply	Sola	SDP 4-24-100LT	-	Input: 120V AC Output: 24V DC

measurement range, also called the span. The span can be adjusted, with a turndown ratio of ten to one, to limit the uncertainty in collected data. All six pressure transducers have a 4-20 mA current output signal connected to a NI 9208 current module. The NI 9208 module is connected to a Sola 24 V DC power supply that provides power for the transducers through the 4-20 mA signal loop (loop-power scheme). The flow rates in the two loops are measured using Micro Motion Coriolis flow sensors and transmitters. The flow transmitters are powered by the DC power supply and produce a separate 4-20 mA output signal loop. The output signal is captured with a NI 9203 current module using a single-ended current measurement in which the signal loops from the two transmitters share a common negative lead from the current module. The flow sensor uncertainty is proportional to the magnitude of the measurement.

5.3 Experimental Procedures

5.3.1 Test facility preparation

To leak check the facility, both loops are pressurized to 3000 kPa with compressed nitrogen. All connections and fittings are sprayed with soap solution to check for bubble formation, and loose fittings are tightened until bubble production ceases. After all fittings are checked, the loops are repressurized and left undisturbed for eighteen hours. If the loop pressures remains constant, they are deemed air-tight; otherwise the process is repeated.

To charge a loop with water, the expansion cylinders are first pressurized to the desired operating pressure of the loop, approximately 1800 kPa, using a compressed nitrogen cylinder. This ensures that the piston is at the bottom of the expansion cylinder, allowing for expansion volume and pressure control as the loop is heated and the water expands. Two charging ports with isolation valves are located at the highest point of the loop. A JB Industries DV-200 series vacuum pump is attached to one of the ports and a distilled water tank is attached to the other. The valve in-line with the vacuum pump is opened and the pump is started. The pressure in the loop is reduced to an absolute pressure of approximately 300 Pa, as measured by a Yellow Jacket 69075 SuperEvac vacuum gage. The isolation valve on the vacuum pump charging port is closed and the valve in-line with the distilled water tank charging port is then opened. Distilled water is drawn from the bottom of the tank until the loop reaches atmospheric pressure. The tank is then pressured to approximately 200 kPa absolute, ensuring the loop is filled and at positive gage pressure, limiting air inclusion. A single discharge port and isolation valve is located at the bottom of each loop. When discharging, water is first drained via gravity. Compressed air is then injected into the loop

through a charging port at the top of the loop to remove residual moisture and/or trapped water.

5.3.2 Start-up and shutdown

A list of steps to start the liquid-liquid test facility is provided below:

1) The expansion cylinders on both loops are pressurized to the desired operating pressure using compressed nitrogen. The high pressure prevents vaporization and cavitation that may occur as the loops are heated.

2) The chiller loop is started and set to the desired temperature using a Johnson Controls interface. After a steady flow rate and supply temperature are established in the chiller loop, valves connecting the glycol-to-water heat exchangers to the chiller loop distribution and return headers are opened. Starting the chiller loop first ensures that heat can be removed from the facility, eliminating the risk of the facility overheating/overpressurizing.

3) The cold-loop pump is started using the VFD, followed by the hot-loop pump. The flow rate in both loops is set to the desired experimental flow rate. However, the flow rate will change as the loops are heated due to changes in the fluid viscosity and pressure drop across components. Both loops are allowed to reach steady-state temperatures.

4) The pressure regulator on the steam distribution line is fully closed. Valves from the high pressure steam supply and condensate return headers are then opened. A rapid increase in loop temperature may damage components. Therefore, the pressure downstream of the regulator is slowly increased over the course of approximately ten minutes, allowing the facility to slowly heat to the desired temperature.

Shutdown of the test facility is completed by performing the steps listed above in reverse. First, the steam pressure is slowly reduced over a ten minute period to allow the facility to cool. The steam distribution and condensate return valves are then closed. After the two loops are cooled to steady-state temperatures, the hot-loop pump is stopped, followed by the cool-loop pump. The chiller loop distribution and return header valves are closed and the chiller loop is shut off. Finally, the compressed nitrogen in the two expansion cylinders is discharged.

5.3.3 Test facility control

The procedures to establish the desired conditions in the test facility are described below.

- Flow rate

The motor/pump speed (in RPM) is proportional to the three-phase frequency, and the flow rate supplied by the centrifugal pumps is, in turn, proportional to the pump speed. Therefore, the flow rate in each loop is controlled by changing the frequency of the three-phase power supplied by the VFDs. A valve downstream of the pump on each loop can also be adjusted. Opening the valve decreases the pressure drop through the loop and the differential pressure across the pump, thereby increasing the flow rate. Closing the valve has the opposite effect. The flow rate in the cold loop can also be controlled by changing the position of the bypass valve.

- Pressure

The pressure in each loop is controlled using the piston-cylinder accumulator connected to each loop upstream of the pumps. Compressed nitrogen on the top of the piston

compresses the water below the piston to an equal pressure. Using a simple manifold, nitrogen can be injected into each cylinder, increasing the pressure, or discharged from the cylinder, decreasing the pressure. The pressure of the entire loop is adjusted to arrive at the desired test-section inlet pressure.

- Hot-loop temperature

Temperature in the hot loop is a function of the heat added in the steam-to-water heat exchanger and rejected in the MCHX test section. The heat added from the steam-to-water heat exchanger is controlled by increasing or decreasing the steam pressure. A Joule-Thompson (constant enthalpy) expansion of saturated boiler steam to a lower pressure across the pressure regulator results in lower temperature superheated steam. The saturation temperature, at which most of the heat is transferred from the steam, also decreases at lower pressure, further decreasing heat transfer. Therefore, the steam pressure can be adjusted until the desired hot-loop test-section inlet temperature is achieved.

- Cold-loop temperature

Similarly, cold-loop temperatures are a function of the heat added from the MCHX test section and rejected in the glycol-to-water heat exchanger. The set point temperature supplied by the lab chiller can be adjusted, but the loop response is slow and other experiments conducted simultaneously in the lab may be affected by the temperature change. Instead, a control valve located between the glycol-to-water heat exchanger and chiller loop supply header is adjusted to change the glycol flow rate. Reducing the flow rate increases the convective thermal resistance and decreases the mean temperature difference across the heat exchanger, both reducing heat transfer. Increasing the glycol flow rate has the opposite effect. Additionally, the cold loop bypass flow around the glycol-to-water heat exchanger can be

adjusted to change the heat duty based on a similar logic. The bypass flow rate and glycol solution flow rate are both adjusted to achieve the desired cold-loop test-section inlet temperature.

5.4 Data Reduction and Test Section Model

Measurements were recorded over a thirty-second period at a rate of five Hertz and stored in LabVIEW. Trend graphs as well as running averages and standard deviations of the measurements were displayed in the LabVIEW interface. These values were observed to determine if the system had reached the desired steady-state test conditions. Data were then exported to a spreadsheet. The average values over the thirty-second recording period were used for analysis.

The fluid states at the inlets and outlets of the MCHX test section on both loops were evaluated from measured parameters using built-in EES property routines. Thermocouples at the inlet and outlet of the test section on both loops provided temperature measurements. The pressures at the inlet to the test section on the hot loop and outlet on the cold loop were measured by pressure transducers. Differential pressure transducer measurements across the test section yielded the remaining two pressures. The flow sensors and transmitters directly measured the mass flow rates of both loops.

5.4.1 Heat duty measurement

The heat duty of the test section was calculated using the enthalpy changes in the hot loop and the cold loop. This provided a redundant measurement of the heat duty. The specific enthalpy was evaluated using the EES enthalpy function with the measured temperature and

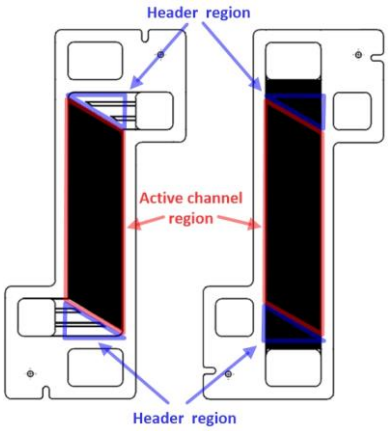

Figure 5.8: Header and active channel regions

pressure as inputs. The average of the two heat duties was used as the measured heat duty for each data point. Uncertainty in the measured heat duty was calculated using instrument uncertainties listed in Table 5.2 and the uncertainty analysis utilities in EES.

$$\begin{aligned} \dot{q}_{\text{hot}} &= \dot{m}_{\text{hot}} \left[i\left(T_{\text{hot,in}}, P_{\text{hot,in}}\right) - i\left(T_{\text{hot,out}}, P_{\text{hot,out}}\right) \right] \\ \dot{q}_{\text{cold}} &= \dot{m}_{\text{cold}} \left[i\left(T_{\text{cold,out}}, P_{\text{cold,out}}\right) - i\left(T_{\text{cold,in}}, P_{\text{cold,in}}\right) \right] \\ \dot{q}_{\text{TS}} &= \left(\dot{q}_{\text{hot}} + \dot{q}_{\text{cold}}\right) / 2 \end{aligned} \tag{5.1}$$

5.4.2 Heat transfer model prediction

Heat transfer in the test section was modeled using the same resistance network, correlations, and segmented approach as the liquid-liquid I^{2}S-LWR MCHX model discussed in Chapter 4. Ten control volume segments were used for the active channel length instead of twenty, due to the shorter length. Measured inlet temperatures, pressures, and flow rates were specified on opposite ends of the counterflow test section. The same assumptions were also made, with the two following exceptions. Fouling resistance was neglected in view of the new fabrication. Heat transfer between the triangular headers on the cold sheets and channels on the neighbouring hot sheets was included. These regions are shown in Figure 5.8. In the I^{2}S-

LWR MCHX design, heat transfer for these headers was conservatively ignored, but accounting for it in the test section provided better agreement with the measured heat duty.

Heat transfer from these header regions was modeled by including an additional segment at the beginning and end of the test section model. The two streams were treated as unmixed fluids in crossflow, for which Eq. (5.2) (Incropera *et al*., 2007) relates the effectiveness (ε_f) and number of transfer units (NTU). The resistance network is similar to the network used for the active channel region discussed in Section 4.4, except that the cold-sheet convective resistance did not include fins due to the absence of microchannel partition walls in the headers. For a flat channel with equal heat transfer on both surfaces and $10^4 < \text{Re} < 5\times10^5$, circular channel Nusselt number correlations can be applied without loss of accuracy when using the hydraulic diameter of the flat channel (Sparrow and Lin, 1963). Thus, the Churchill (1977a) correlation was used to determine the Nusselt number in the triangular headers. Due to the varying cross-section and flow rate in these regions, the Reynolds number was estimated using the average mass flux in each header. Using the effectiveness/NTU method, shown in Eqs. (5.3) and (5.4), the heat duties of the two header regions on both ends of the heat exchanger were calculated and incorporated into the segmented model. Here the "in" subscript refers to the inlet to the segment.

$$\varepsilon_f = 1 - \exp\left[\left(\frac{1}{C_r}\right) NTU^{0.22}\left\{\exp\left(-C_r\, NTU^{0.78}\right) - 1\right\}\right] \tag{5.2}$$

$$C_{hot} = c_{p,hot}\dot{m}_{hot} \quad C_{cold} = c_{p,cold}\dot{m}_{cold} \quad C_{min} = \max(C_{hot}, C_{cold}) \quad C_{max} = \min(C_{hot}, C_{cold}) \quad C_r = \frac{C_{min}}{C_{max}} \tag{5.3}$$

$$NTU = \frac{UA}{C_{min}} \quad \dot{q}_{max} = C_{min}\left(T_{hot,in} - T_{cold,in}\right) \quad \dot{q}_{header} = \dot{q}_{max}\varepsilon_f \tag{5.4}$$

5.4.3 Nusselt number measurement

The average measured Nusselt number in the active channel region was deduced for comparison with correlation predictions. To isolate the heat transfer in the active channel regions, the heat duty of the two header regions was subtracted from the average measured heat duty as shown in Eq. (5.5), where subscript "ch" refers to the active channel region. The inlet and outlet temperatures of the active channel region were calculated from the measured test section temperatures by accounting for heat transfer from the headers, as shown in Eq. (5.6). These temperatures were used to calculate the log mean temperature difference in the active channel region. Eq. (5.7) shows the calculation of the thermal resistances of the active channel region using the active channel heat duty and log mean temperature difference. The total resistance of the active channel region is a function of the average heat transfer coefficients in both the hot and cold sheet channels. The heat transfer coefficient for one of the two fluids, referred to as the coupling fluid, was estimated using the Churchill (1977a) Nusselt number correlation. The measured heat transfer coefficient of the other fluid could then be calculated from the parallel resistance network in Figure 4.5 using the EES iterative solver. Fouling was again ignored. The measured Nusselt number was calculated from the measured heat transfer coefficient using the fluid thermal conductivity and hydraulic diameter of the channels. Fluid properties were evaluated at the average temperature and pressure between the inlet and outlet of the test section. An uncertainty of ±25% was assigned to the Nusselt number predicted by the Churchill correlation used to calculate the convective resistance in the coupling fluid. The heat duties in the two header regions used to isolate the active channel heat transfer rate were also assigned an uncertainty of ±25%.

$$\dot{q}_{\text{ch}} = \dot{q}_{\text{TS}} - \dot{q}_{\text{header,1}} - \dot{q}_{\text{header,2}} \tag{5.5}$$

$$T_{\text{ch,hot,in}} = T_{\text{hot,in}} - \frac{\dot{q}_{\text{header,1}}}{c_{\text{p,hot}}\dot{m}_{\text{hot}}} \quad T_{\text{ch,hot,out}} = T_{\text{hot,out}} + \frac{\dot{q}_{\text{header,2}}}{c_{\text{p,hot}}\dot{m}_{\text{hot}}} \tag{5.6}$$

$$R_{\text{ch}} = \frac{1}{UA_{\text{ch}}} = \frac{\Delta T_{\text{lm,ch}}}{\dot{q}_{\text{ch}}} \tag{5.7}$$

5.4.4 Pressure drop model prediction

A pressure drop model for the hot side of the test section was developed in a manner similar to that of the I^{2}S-LWR design model. The heat exchanger was divided vertically, and the flow through each hot sheet was treated as an individual flow path (10 total). The flow paths start after the water expands into the heat exchanger header and ends when they contract into the outlet piping. The mass flow rate through each flow path/sheet was iteratively obtained by imposing an equal pressure drop through each path. Frictional pressure losses, acceleration/deceleration, expansions/contractions, and minor losses were calculated as described in Section 4.5 for the I^{2}S-LWR MCHX design model. Figure 5.9 shows the pressure losses accounted for in the model. Pressure losses in 0.15 m of 21.16 mm ID piping between the pressure taps and test facility were also included. The Churchill (1977b) correlation was used to calculate the friction factor and frictional pressure loss in the piping. Minor losses in

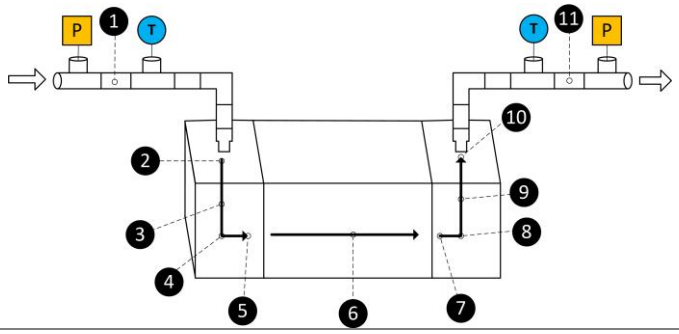

1	Pipe frictional and minor losses	7	Expansion out of channels
2	Expansion into header	8	90° bend out of channels
3	Inlet header friction	9	Outlet header friction
4	90° bend into channels	10	Contraction out of header
5	Contraction into channels	11	Pipe frictional and minor losses
6	Channel friction		

Figure 5.9: Hot-side pressure losses

the inlet and outlet piping each included a 90° bend (k_L = 0.85) and flow past two tee fittings (k_L = 0.20). Fluid properties were evaluated at the measured inlet temperature and pressure for loss before the channels (1 - 5) and at the measured outlet temperature and pressure for those after the channels (7 - 12). The averages of inlet and outlet measured temperatures and pressures were used to determine properties for the channel frictional pressure drop.

5.4.5 Friction factor measurement

To calculate the measured friction factor in the channel, the pressure drop in the channels was isolated from the other pressure losses between the two pressure transducer ports. The average pressure loss over the ten flow paths was calculated for each of the non-channel losses in Figure 5.9. These were subtracted from the measured differential pressure to isolate the frictional pressure drop in the channels. The channel friction factor was then calculated using Eq. (5.8). The flow was assumed to be fully developed and evenly distributed among all channels. The averages of inlet and outlet measured temperatures and pressures were used to evaluate fluid properties in the channel. In addition to the uncertainties in instrument measurements, an uncertainty of ±25% was assigned to the calculated pressure losses used to isolate the channel frictional pressure drop.

$$f = 2\rho\left(\frac{l_{ch}}{D_h}\right)\left(\frac{1}{G^2}\right)\Delta P_{fr} \tag{5.8}$$

5.5 Test Matrix

Four sets of liquid-liquid experiments were conducted on the MCHX test section. In the first set, flow rates in both loops were simultaneously increased between testing points. Data from this set of experiments were used to compare the measured test section heat duty

Table 5.3: Liquid-liquid experimental test matrix

Set	$\dot{m}_{hot}$ (kg s^{-1}) [≈ Re_{ch}]	$\dot{m}_{cold}$ (kg s^{-1}) [≈ Re_{ch}]	$T_{hot,in}$ (°C)	$T_{cold,in}$ (°C)	data points
1	0.1 – 0.90 [1540 – 15370]	0.1 – 0.78 [1370 – 13090]	140 – 170	110 – 140	45
2	0.03 – 0.90 [470 – 15580]	0.60 – 0.75 [6000 – 12500]	140 – 160	85 – 135	83
3	0.60 – 0.85 [9670 – 15850]	0.05 – 0.80 [680 – 12500]	140 – 160	85 – 135	75
4	0.03 – 0.90 [350 – 13740]	-	130	-	125

with model predictions. The second set of experiments was designed to measure the average Nusselt number in the hot loop channels with limited uncertainty. By maximizing the cold loop flow rate, the thermal resistance of the cold-side fluid was reduced, which in turn decreased the uncertainty in obtaining the hot channel heat transfer coefficients from the measured data.

A similar third set of tests was conducted with the high hot-loop flow rate maximized, so that the cold-side heat transfer coefficient and Nusselt number could be deduced with low uncertainty. In the fourth set, the hot fluid was maintained at a near-constant temperature, and measurements pertaining to the hot-side pressure drop were collected with no cold-loop flow. Table 5.3 shows the test matrix and range of fluid inlet temperatures. The test-section inlet pressure of both hot and cold fluids was kept between 1600 and 2000 kPa for all data points to ensure boiling did not occur.

5.6 Results and Discussion

While the design of the I^{2}S-LWR MCHX is based on turbulent heat transfer, the testing range in this study covered the lower Reynolds number laminar and transition regimes

as well. Data are separated by channel Reynolds number into approximate laminar, transition, and turbulent regimes for analysis. The following demarcations are used based on trends observed in the data: Re < 1600 Low-Re, 1600 ≤ Re ≤ 4000 Intermediate-Re, and Re > 4000 High-Re.

5.6.1 Heat duty and Nusselt number

Figure 5.10 shows the heat duties as measured by the hot- and cold-side enthalpy change for experimental datasets 1 – 3. The two heat duties have an AAD of 0.60% when the hot-side heat duty is treated as the measured value in Eq. (3.15). This confirms the accuracy of instrumentation measurement/data reduction techniques and that heat lost to the ambient is negligible. In the remainder of this chapter, the reported test-section heat duty is the average of the hot- and cold-loop heat duties.

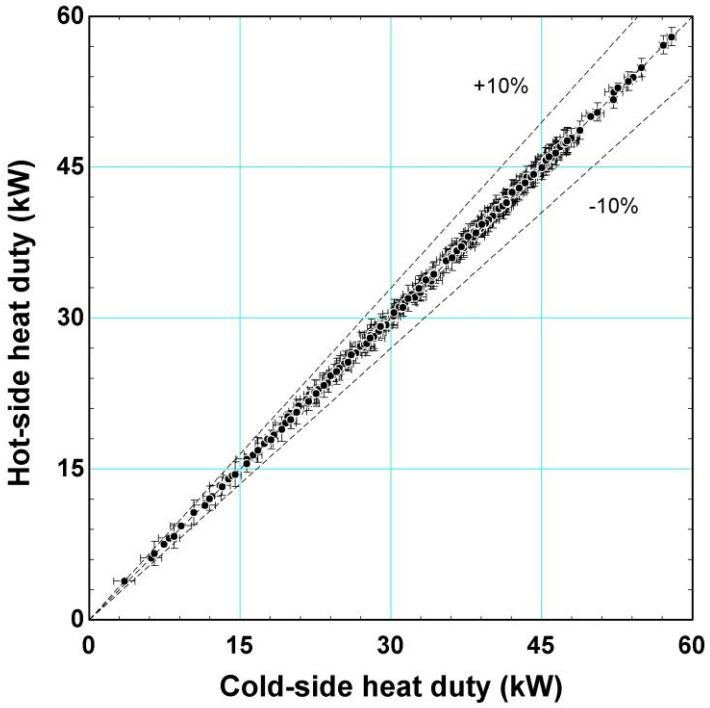

Figure 5.10: Hot-side and cold-side heat duty

A small subset of data from the first dataset was used in Figure 5.11. The left-hand graph shows the measured versus predicted heat duty of the test section when heat transfer from the header regions is ignored. The graph on the right shows the same values when header segments are added to either end of the model, as discussed in section 5.4.2. Neglecting header heat transfer in the model results in the underprediction of heat transfer by approximately 10%. Header heat transfer was ignored in the liquid-liquid I^2S-LWR MCHX design model. A similar increase in the heat duty would occur if heat transfer in these regions was accounted for. The header area is considered as providing a design margin, ensuring the operating conditions in Section 4.2 can be met. In the remainder of this chapter, heat transfer from header segments are included in model predictions.

Measured and model predicted heat duties are compared for experimental datasets 1 – 3 and are shown graphically in Figure 5.12. Data points are placed in the Intermediate-Re range if either fluid has a Reynolds number within the range specified above. Otherwise, if one of the Reynolds numbers is less than 1600, the data points are considered to be in the Low-Re range. The remaining 122 data points, for which both fluid Reynolds numbers are

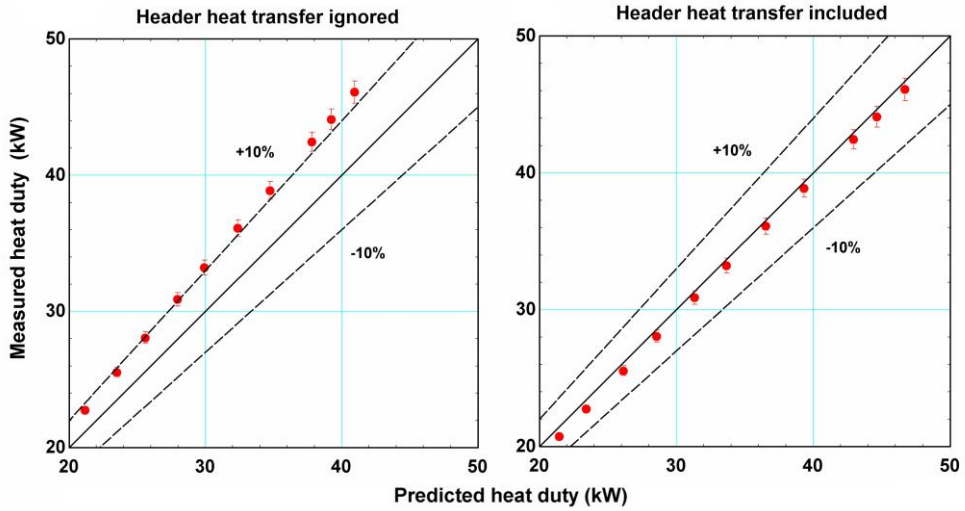

Figure 5.11: Influence of header heat transfer

greater than 4000, are placed in the High-Re range. The High-Re data have the best agreement between the measured and predicted heat duty, with an AAD of 1.28%. These data points are also the most representative of normal operating conditions for the I^2S-LWR MCHX, and this excellent agreement validates the modeling and assumptions used for the design. Intermediate-Re data show increased heat transfer compared with model predictions, with an AD of -7.96% and AAD of 8.30%. Data in which one or both of the fluids are in the Low-Re range agree well with the model predictions, with an AAD of 3.78%.

The second and third datasets are used to deduce the hot- and cold-side Nusselt numbers, respectively. Figure 5.13 shows measured hot-side Nusselt number versus Reynolds number for a subset of data from Set 2, while Figure 5.14 displays the measured cold-side Nusselt number for a subset of data from Set 3. In both figures, the Nusselt number begins to increase due to the onset of turbulence at a lower Reynolds number than predicted by the Churchill (1977a) correlation, consistent with the increased heat duty in the Intermediate-Re

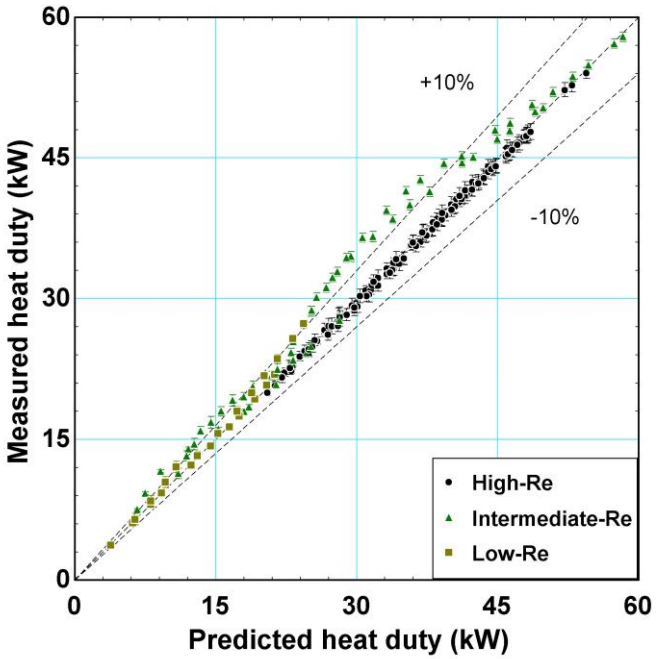

Figure 5.12: Measured versus predicted liquid-liquid heat duty

data in Figure 5.12. At higher and lower Reynolds numbers, the measured Nusselt numbers are significantly closer to the Churchill (1977a) predicted values. It can also be observed that uncertainty in the measured Nusselt number is significantly larger at higher Reynolds numbers. As the Reynolds number increases, the Nusselt number and heat transfer coefficient also increase, resulting in a lower measured convective resistance. The coupling fluid resistance, which was estimated using the Churchill (1977a) correlation and has large uncertainty, then accounts for a larger fraction of the total resistance. This leads to a larger uncertainty in the measured convective resistance and Nusselt number.

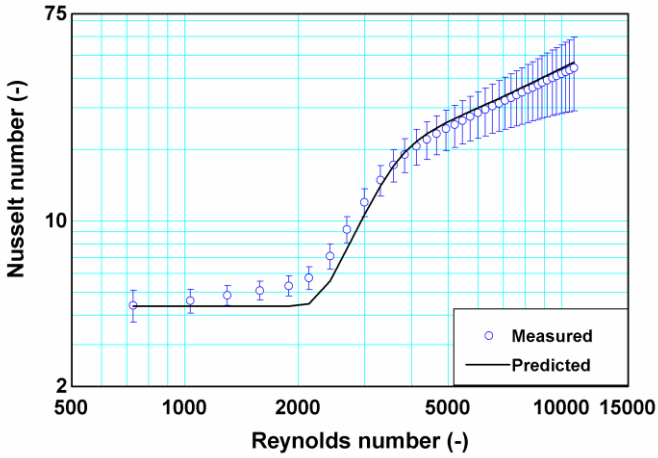

Figure 5.13: Cold-side Nusselt number versus Reynolds number

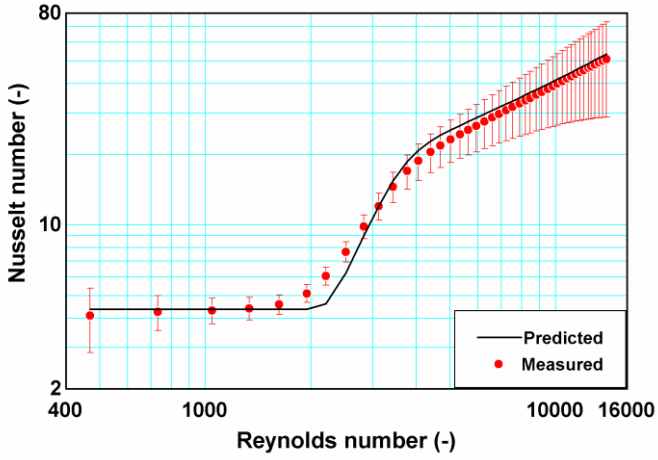

Figure 5.14: Hot-side Nusselt number versus Reynolds number

The measured and Churchill (1977a) correlation predicted Nusselt numbers from datasets 2 and 3 are shown in Figure 5.15. Data are classified as Low-Re, Intermediate-Re, and High-Re based on the Reynolds number of the fluid for which the Nusselt number was measured. It can be seen that Intermediate-Re data are consistently higher than predicted values, with an AD of -10.6% and AAD of 12.6%. Low-Re and High-Re data had an AAD of 5.48% and 4.37%, respectively. Despite the large uncertainty at larger Nusselt numbers, these results help further validate the use of circular-channel macroscale correlations for the I^2S-LWR MCHX design, particularly at Low-Re and High-Re conditions. In the intermediate-Re range, representing transition regime between laminar and turbulent flow, the Churchill (1977a) correlation provides an approximate, and consistently low, estimate of the Nusselt number. It should be noted that a Nusselt number of 4.364 was utilized by the Churchill (1977a) correlation for circular channels in fully-developed laminar flow with constant heat flux. Based on these results, it appears little error is introduced as a result of using this value for the semi-circular, varying heat flux channels in the MCHX test section. The assumptions

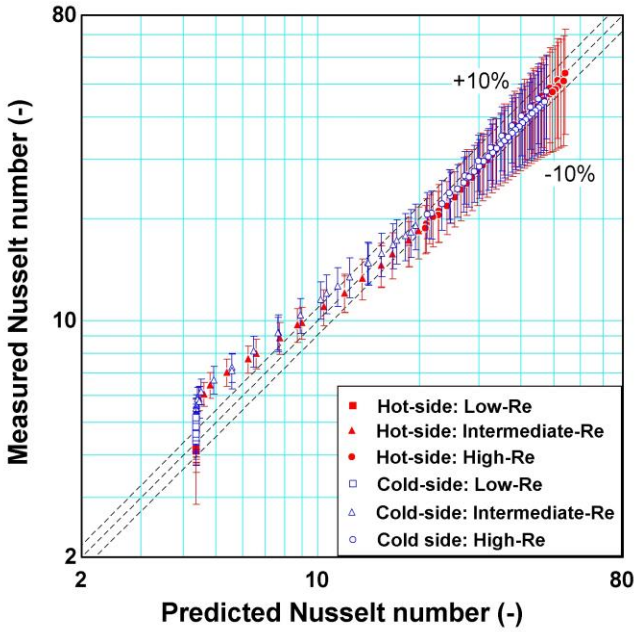

Figure 5.15: Measured versus predicted Nusselt number

of uniform flow distribution, one-dimensional heat transfer, and fully developed flow also appear to be validated by the accuracy of the heat transfer model and measured Nusselt number data.

5.6.2 Pressure drop and friction factor

Figure 5.16 shows the hot-side measured and predicted pressure drops data from experimental sets 1, 2, and 4. The measurement uncertainty, ±70 Pa, does not appear on the graph due to the small magnitude. The measured data closely follow model predictions but are generally higher than the predicted values. This trend is particularly prominent in the Low-Re region, where the AAD is 10.9% (AD -9.33%), and the Intermediate-Re region, where the AAD is 11.6% (AD -11.6%). High-Re data are in much better agreement with predicted values, with an AAD of 5.57% (AD -5.49%), although the measured values are generally larger than the model predictions. This small difference could be due to entrance/developing length effects, inaccuracies in minor pressure loss predictions, minor maldistribution, or

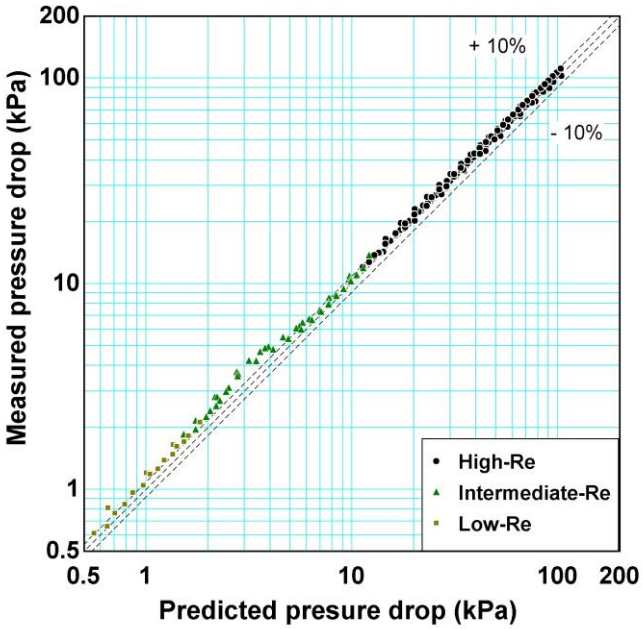

Figure 5.16: Measured versus predicted pressure drop

simply the shape of the semi-circular channel. The High-Re data, similar to I^2S-LWR MCHX conditions, closely follow the model predictions and help validate the pressure drop model described in Section 4.5. Unlike the I^2S-LWR design, the test section was specifically designed such that frictional losses in channels constitute a major portion of the total pressure drop, reducing the uncertainty of measured friction factors. Model results showed that the channel frictional pressure drop accounted for an average of 66.7% of the total pressure drop. Because of the low velocity conditions in the large cross-sectional area inlet and outlet headers, the pressure in the headers did not change significantly as liquid flowed into the sheets/channels. As a result, model predictions showed an even flow distribution, with the flow rates in individual sheets within ±1% of the evenly distributed value for all data points.

The Darcy friction factor, deduced from experimental sets 1, 2, and 4, is shown in Figure 5.17. The friction factor predicted by the Churchill (1977b) correlation is also shown. Because measured pressured drops are generally higher than model predictions, the measured friction factors have the same trend. The Low-Re region has an AAD of 14.0% (AD -12.1%),

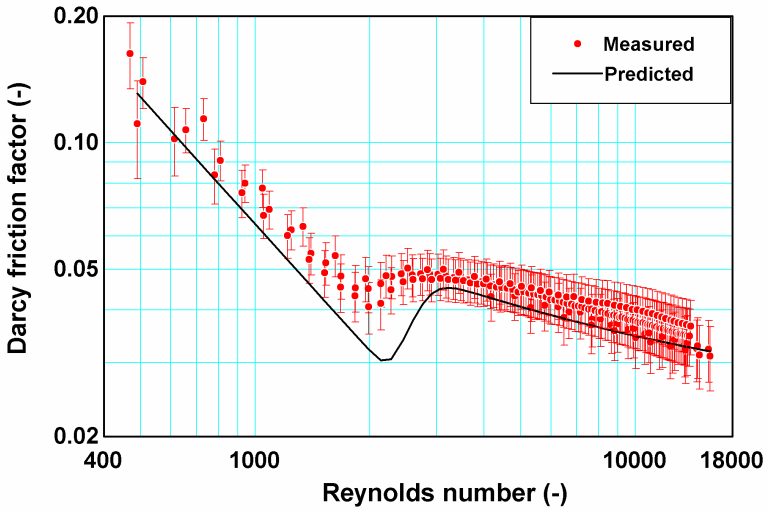

Figure 5.17: Friction factor versus Reynolds number

while the Intermediate-Re region has an AAD of 16.9% (AD -16.9%). The High-Re region data are again in better agreement with predictions, and have an AAD of 8.53%.

5.6.3 Summary of liquid-liquid results

A summary of the AD and AAD between predicted and measured data, and the number of data points are shown in Table 5.4. In addition to validating heat transfer and pressure drop models, results show that the Nusselt number and friction factor correlations developed for macroscale geometries can be accurately applied to non-circular microchannels, especially at the High-Re range under consideration for the I^2S-LWR MCHX. Furthermore, no appreciable effect of maldistribution, developing flow, or conjugate heat transfer were observed in the data. A conservative estimate of the I^2S-LWR MCHX performance was made by neglecting the heat transfer between secondary coolant headers in the sheets and neighboring primary coolant channels. Heat transfer in the header regions accounted for an average of 16.5% of the total heat duty. However, neglecting the header region caused the model to underpredict heat transfer by only approximately 10%, due to the larger temperature difference in the active channel region. This shows that heat transfer in the headers can in fact significantly impact the heat duty, providing some margin in meeting the I^2S-LWR MCHX design requirements. Including header heat transfer in the I^2S-LWR MCHX model would result in a decreased temperature difference between fluids for a given heat duty. The secondary coolant inlet and outlet temperatures could then be increased, improving the thermal efficiency and power output of the flash Rankine cycle. The average Reynolds number in the primary coolant channels of the I^2S-LWR MCHX design is 20,652, while the largest Reynolds number experimentally investigated is approximately 15,500. However, the

underlying momentum and heat transfer phenomena are expected to be the same across these Reynolds numbers.

Table 5.4: AD and AAD of liquid-liquid measured and predicted values

	Low-Re			**Intermediate-Re**			**High-Re**		
	#	**AD**	**AAD**	**#**	**AD**	**AAD**	**#**	**AD**	**AAD**
Heat duty	23	-3.06	3.78	58	-7.96	8.30	122	1.22	1.28
HS ΔP	21	-9.33	10.9	48	-11.6	11.6	158	-5.49	5.57
HS Nu	11	0.592	2.21	24	-7.91	11.5	48	4.78	4.79
CS Nu	12	-8.45	8.45	26	-13.1	13.7	37	3.64	3.83
HS & CS Nu	23	-4.13	5.46	50	-10.6	12.6	85	4.29	4.37
HS f	21	-12.1	14.0	48	-16.9	16.9	158	-8.39	8.53

CHAPTER 6. LIQUID-BOILING MCHX

This chapter discusses the design and modeling of the I^2S-LWR liquid-boiling MCHX and the coupling of the liquid-boiling MCHX with a Rankine cycle for power generation. Additionally, a comparison is made between the liquid-liquid and liquid-boiling MCHX designs based on the thermal efficiency of the accompanying power cycle. A simple exergy analysis is also performed to compare the two designs. The operating conditions and dimensions of the primary-coolant side of the liquid-boiling MCHX are the same as those in the liquid-liquid design. In this chapter and the following chapter on liquid-boiling experiments, the primary coolant and secondary coolant are sometimes referred to as the hot coolant and boiling coolant, respectively.

6.1 Assumptions

The same assumptions applied to the liquid-liquid MCHX design were also applied to the liquid-boiling design. Heat transfer was again ignored in the header regions and all heat transfer was assumed to occur in the active channel regions in which the primary and secondary coolant are in counterflow. A fouling build-up of 10 μm with thermal conductivity of $k_{foul} = 1.3$ W m^{-1} K^{-1} ($R''_{foul} = 7.7 \times 10^{-6}$ m^2 K W^{-1}) and a surface roughness of 2 μm were assumed on both the primary and secondary sides of the heat exchanger, consistent with the liquid-liquid design. In Section 4.1, it was shown that significant axial heat transfer in the fluid and conjugate, multi-dimensional heat transfer in the MCHX material was unlikely. This assumption was validated by the good agreement between the measured and predicted heat duty in liquid-liquid experiments. Therefore, heat transfer was again assumed to be one-

dimensional. A uniform flow distribution between all heat exchanger channels was assumed for heat transfer calculations. The parallel flow path model, discussed in Section 4.5, suggests an even distribution of the primary coolant along the height of the MCHX stack. The secondary coolant distribution is more complex in the liquid-boiling design because of the high-density subcooled-liquid state in the inlet header and the low-density superheated-vapor state in the outlet header. If not properly accounted for in the header design, this can result in a non-uniform pressures differential across the parallel channels, leading to maldistribution. This phenomenon is discussed in Section 6.4. Both fluids were assumed to be fully-developed upon entry into the active channel region. Channel flow rates were assumed to be steady with no boiling-related flow instabilities.

6.2 Liquid-Boiling MCHX Design

Primary coolant conditions are the same in both the liquid-liquid and liquid-boiling designs due to the I^2S-LWR primary-to-secondary heat exchanger design requirements, outlined in Section 2.1. Therefore, the same channel and primary-coolant header dimensions as the liquid-liquid design were used for the liquid-boiling MCHX. This ensured that primary-coolant pressure drop requirements were met and provided a means of directly comparing the two MCHX designs. Channel pressure vessel requirements, discussed in Section 4.6, were also met by these dimensions. Secondary coolant sheets were slightly modified to ensure an even flow distribution. The radial length occupied by the triangular (parallel oblique) headers on the secondary coolant sheet was increased from 0.1 m to 0.15 m, reducing the active channel length from 0.55 m to 0.50 m. The secondary-coolant inlet-header radial length is reduced by a wedge section, decreasing the radial length at the inlet of the sheet from 0.15 m to 0.035 m. This asymmetry in the sheet was introduced to increase the pressure drop in the

Parameter	Value
MCHX stack radial length	0.85 m
MCHX block radial length	0.65 m
Primary coolant header radial length	0.20 m
Secondary coolant header radial length	0.15 m
MCHX stack azimuthal width	1.00 m
MCHX block azimuthal width	0.80 m
Secondary coolant plenum azimuthal width	0.20 m
MCHX block axial height	0.60 m
Active channel length, l_{ch}	0.50 m
Channels per sheet	445
Sheets per MCHX block (primary and secondary)	530

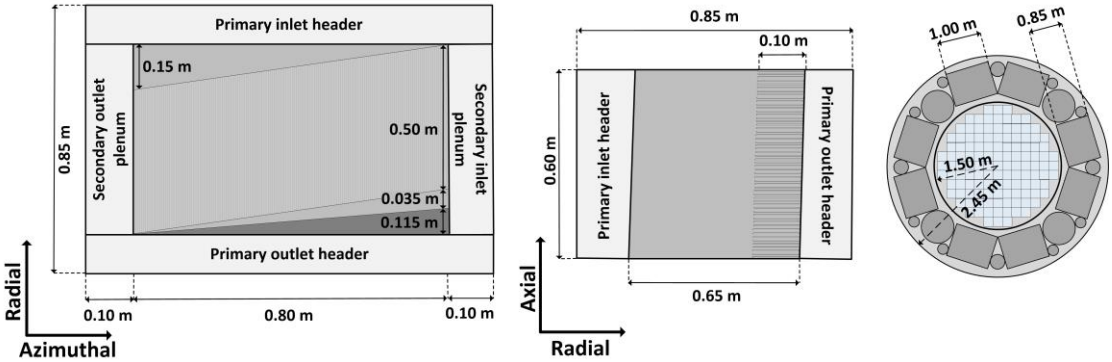

Figure 6.1: Liquid-boiling MCHX dimensions

inlet header and produce a uniform pressure differential between the inlet and outlet headers. Primary-coolant sheets were unchanged from the liquid-liquid MCHX design. A schematic of important dimensions of the liquid-boiling MCHX design is shown in Figure 6.1.

After the dimensions of the MCHX were selected, the secondary coolant conditions to meet heat transfer (2850 MW_{th}) and power generation requirements were determined. Table 6.1 shows important fluid properties for a single liquid-boiling MCHX block, and values for all 88 MCHX blocks are listed in parentheses. It should be noted that the secondary-coolant flow rate, 1711 kg s^{-1} is significantly lower than that for the liquid-liquid MCHX (13,016 kg s^{-1}). This is due to the high enthalpy of vaporization of water, allowing a relatively small flow rate to remove a relatively large amount of heat. Using these secondary-coolant conditions, the associated Rankine power cycle achieved a thermal efficiency of 39.0%. This represents

Table 6.1: Liquid-boiling MCHX operating parameters

Parameter	Primary coolant	Secondary coolant
$\dot{q}$ (MW)	32.39 (2850)	
A(m^2)	207.5 (18,260) [for each coolant]	
$\dot{m}$ (kg s^{-1})	176.1 (15,498)	19.44 (1711)
G (kg m^{-2} s^{-1})	2092	230.9
T_{in} (°C)	330.0	272.0
T_{out} (°C)	298.8	310.1
P_{in} (MPa)	16.30	7.666
P_{out} (MPa)	15.83	7.472
ΔP_{ch} (kPa)	77.70	9.486
ΔP_{total} (kPa)	433.8	193.8
h_{avg} (kW m^{-2} K^{-1})	39.50	46.82

a significant increase in the power generation of the I^2S-LWR when compared with the liquid-liquid MCHX. The liquid-boiling MCHX is able to achieve higher efficiency in part because it does not require a flashing drum, a major source of exergy destruction in the flash Rankine cycle utilized with the liquid-liquid design (discussed in Section 6.5).

Figure 6.2 shows the temperature profile over the active channel length of the liquid-boiling MCHX design. The locations of different heat transfer regimes are also displayed. Figure 6.3 shows the heat transfer coefficient for both coolants as well as the quality. Correlations and modeling techniques used to predicted MCHX performance are discussed in Section 6.3.1. The secondary-side wall temperature exceeds the saturation temperature shortly after entering the channel and an increase in the heat transfer coefficient occurs due to subcooled nucleate boiling. The secondary coolant reaches saturation 0.0625 m from the channel inlet. In Figure 3.4, it was shown that the saturated boiling heat transfer coefficient decreased with quality for the representative I^2S-LWR conditions as nucleate boiling is suppressed at higher quality. In liquid-boiling MCHX, the opposite trend can be observed (Figure 6.3), with the heat transfer coefficient increasing as the quality and distance from the inlet increases. The counterflow orientation causes a larger temperature difference and heat

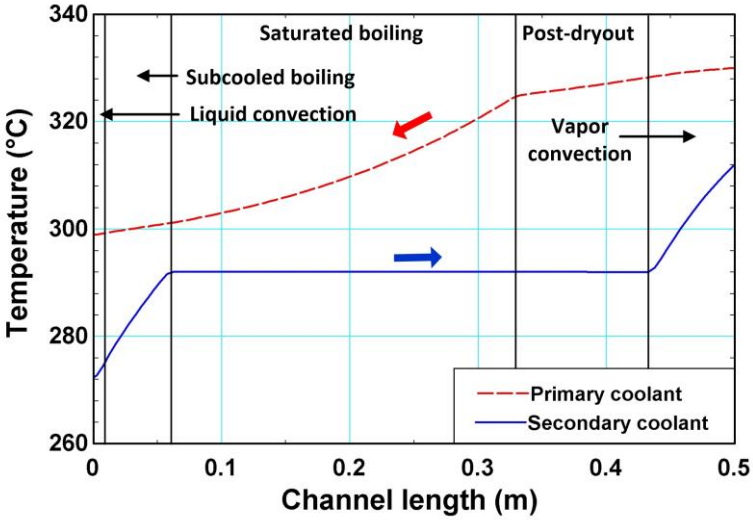

Figure 6.2: Liquid-boiling MCHX temperature profile

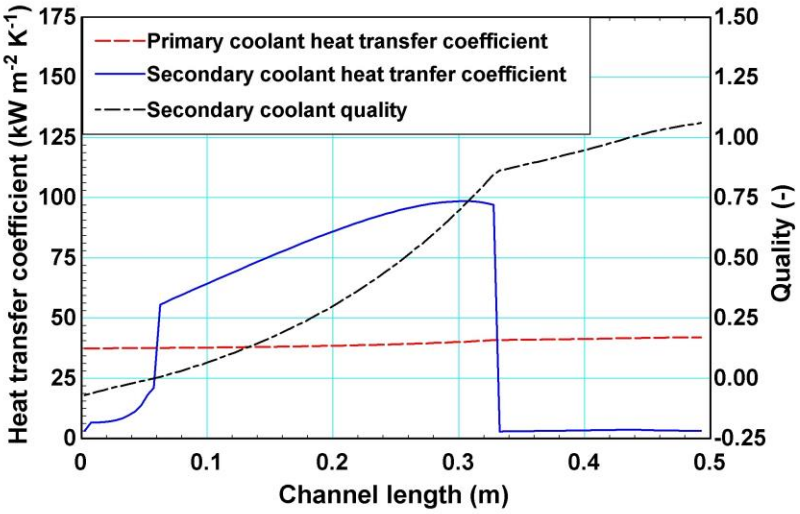

Figure 6.3: Liquid-boiling MCHX heat transfer coefficients and quality

flux closer to the primary coolant inlet. This increases nucleate boiling and causes the rise in heat transfer coefficient. Dryout occurs 0.3325 m from the inlet and at a quality of 0.86, marking a sharp drop in the transfer coefficient. At 0.4425 m from the inlet, the quality exceeds one and the fluid enters the vapor convection heat transfer regime.

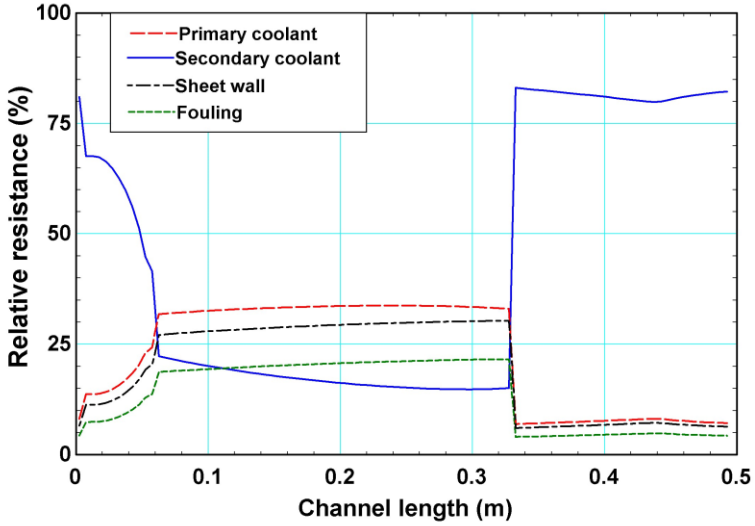

Figure 6.4: Liquid-boiling MCHX relative resistance

The relative thermal resistance along the channel length of the liquid-boiling MCHX is shown in Figure 6.4. The thermal resistance is dominated by the secondary coolant in most of the heat transfer regimes. At the inlet, the relative resistance of the secondary coolant is roughly 80%, but decreases as subcooled nucleate boiling occurs. During saturated boiling, the heat transfers coefficient increases significantly, decreasing the thermal resistance of the secondary coolant. In the post-dryout and vapor convective regimes, the secondary coolant again represents roughly 80% of the total thermal resistance. The thermal resistance of the stainless steel sheet, fouling build-up, and primary coolant stay relatively constant across the length of the heat exchanger and are much smaller than that of the secondary coolant, except in the saturated boiling region.

Figure 6.5 shows the pressure gradient of the two coolants across the active channel length of the MCHX as well as the secondary-coolant quality. The primary coolant pressure gradient is the result of friction and remained relatively constant across the channel length, increasing only slightly due to changes in fluid properties. The secondary-coolant pressure

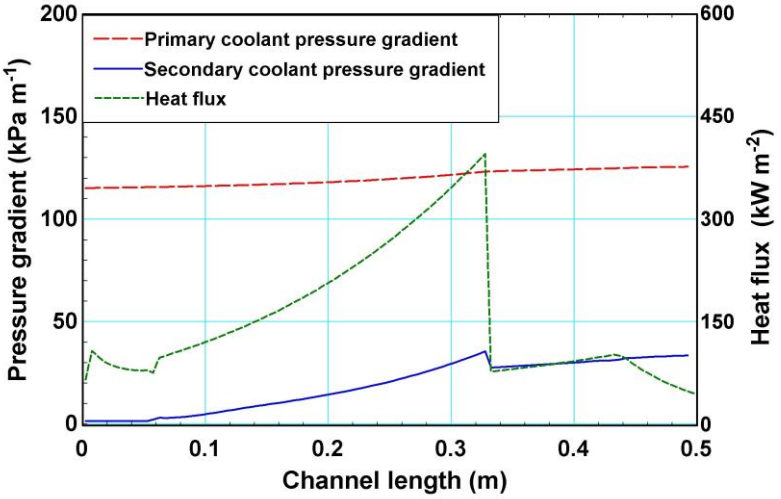

Figure 6.5: Liquid-boiling MCHX pressure gradients and heat flux

gradient remains constant in the liquid convection and subcooled boiling regimes. The onset of significant void (OSV) is not reached until the fluid is nearly at saturation. As a result, the pressure gradient remains small and was calculated as though the secondary coolant remained in a single-phase liquid state. In the saturated-boiling heat transfer regime, the pressure gradient increases along the length of the channel as the quality increases. In two-phase regimes (saturated boiling and post-dryout), the pressure gradient has a frictional and acceleration component. The frictional pressure gradient increases as the quality and velocity of the fluid increases (see Figure 3.2). The acceleration component of the pressure gradient is a function of the rate of vapor generation. The pressure gradient in the post-dryout regime is slightly lower than that of the saturated boiling regime due to a smaller contribution from acceleration, as a result of the low heat flux. The pressure gradient remains constant in the single-phase vapor convection regime. Due to the low mass flux of the secondary coolant, the pressure gradient of the secondary-coolant is significantly lower than that of the primary coolant. In the liquid-liquid MCHX (G = 1757 kg m^{-2} s^{-1}), the secondary coolant frictional pressure gradient is nearly constant over the length of the channel with an average value of

84 kPa m^{-1}. It is somewhat surprising that the secondary-coolant pressure gradient in the two-phase liquid-boiling MCHX is less than that in the single-phase liquid-liquid design. This is a result of the low mass flux (230.9 kg m^{-2} s^{-1}) and relatively high reduced pressure (~0.34) operating conditions of the liquid-boiling MCHX. At higher pressure, the vapor density is larger, resulting in lower velocity and decreased shear. This can be observed in Figure 3.2, in which the lower pressure test section conditions result in significantly larger frictional pressure gradients than the higher pressure I^2S-LWR conditions. Eq. (6.1) shows representative calculations of the secondary-coolant pressure gradient in the liquid-liquid and liquid-boiling MCHX at average channel conditions. The HEM is used to calculate the two-phase liquid-boiling pressure drop, and the McAdams *et al.* (1942) viscosity was used to calculate the two-phase Reynolds number (Re_{tp} = 5933). The friction factors are calculated using the correlation of Churchill (1977b). This straight forward calculation shows that increasing the vapor (and two-phase) density and decreasing the mass flux both result in lower pressure drop. The liquid-boiling two-phase pressure gradient calculated using the correlation of Chisholm (1967) at a quality of 0.5 is shown in Eq. (6.2). Similar trends can be observed with regard to effect mass flux and vapor density on the pressure gradient.

Liquid-boiling (x = 0.50): $$\left(\frac{\partial P}{\partial z}\right)_{fr} = \frac{G^2}{2\rho_{tp}}\frac{f_{tp}}{D_h} = \frac{\left(230.9\,\text{kg m}^{-2}\,\text{s}^{-1}\right)^2}{2\times 74.91\,\text{kg m}^{-3}}\frac{0.03918}{0.8116\times 10^{-3}\,\text{m}} = 17.18\ \text{kPa m}^{-1}$$

Liquid-liquid: $$\left(\frac{\partial P}{\partial z}\right)_{fr} = \frac{G^2}{2\rho}\frac{f}{D_h} = \frac{\left(1757\,\text{kg m}^{-2}\,\text{s}^{-1}\right)^2}{2\times 731.4\,\text{kg m}^{-3}}\frac{0.03195}{0.8116\times 10^{-3}\,\text{m}} = 84.43\ \text{kPa m}^{-1}$$

(6.1)

$$\mathrm{Re}_\mathrm{l} = 1047 \rightarrow \quad f_\mathrm{l} = 0.06112 \rightarrow \quad \left(\frac{\partial P}{\partial z}\right)_\mathrm{l} = \frac{\left[G(1-x)\right]^2}{2\rho_\mathrm{l}} \frac{f_\mathrm{l}}{D_\mathrm{h}} = 0.6865\ \mathrm{kPa\ m^{-1}}$$

$$\mathrm{Re}_\mathrm{v} = 4886 \rightarrow \quad f_\mathrm{v} = 0.04112 \rightarrow \quad \left(\frac{\partial P}{\partial z}\right)_\mathrm{v} = \frac{\left[Gx\right]^2}{2\rho_\mathrm{v}} \frac{f_\mathrm{v}}{D_\mathrm{h}} = 8.881\ \mathrm{kPa\ m^{-1}}$$

$$X = \left[\frac{\left(\partial P/\partial z\right)_\mathrm{l}}{\left(\partial P/\partial z\right)_\mathrm{v}}\right]^{1/2} = 0.2833 \quad \phi_\mathrm{l}^2 = 1 + \frac{12}{X} + \frac{1}{X^2} = 55.81 \quad \left(\frac{\partial P}{\partial z}\right)_\mathrm{fr} = \left(\frac{\partial P}{\partial z}\right)_\mathrm{l} \phi_\mathrm{l}^2 = 38.31\ \mathrm{kPa\ m^{-1}}$$

(6.2)

6.3 Heat Transfer Model

The liquid-boiling MCHX heat transfer model is similar to the liquid-liquid model discussed in Section 4.4 and was developed in EES. The active channel length of the liquid-boiling MCHX was segmented into one hundred control volumes ($l_{seg} = l_{ch} / 100 = 5$ mm). A larger number of segments were required for the liquid-boiling MCHX due to changes in the heat transfer coefficient and pressure gradient over the channel length. This is particularly prominent at transitions between heat transfer regimes, such as the transition from saturated boiling to post-dryout. A grid independence study showed no significant changes in the heat duty (< 0.1%) as a result of increasing the number of control-volume segments beyond one hundred. The integrated control-volume conservation equations were applied to both fluids in the segment, shown in Eq. (3.2) for a single-phase fluid, and Eq. (3.11) for a two-phase mixture. Segment fluid states and the heat duty were determined by solving the energy balance equations and the UA-ΔT_{lm} equation, as shown in Eq. (4.1). Simultaneously, the momentum conservation equations for both fluids were solved, allowing the outlet temperature to be evaluated from the pressure and specific enthalpy of the fluid: $T = T(P,i)$. The same thermal resistance network and fin assumptions as the liquid-liquid MCHX heat transfer model were used to determine the thermal resistance and UA of each segment. The heat transfer coefficient, frictional pressure gradient, and other correlations were evaluated using the

average enthalpy, pressure, and quality in the segment. The acceleration component of the two-phase momentum equation was evaluated using the void fraction and quality at the inlet and outlet of each segment.

6.3.1 Heat transfer regimes and correlations

Table 6.2 shows a summary of the transition criteria, heat transfer correlations, and pressure drop correlations used for the secondary-coolant in the liquid-boiling MCHX model. Of the correlations discussed in Chapter 3, the correlations in Table 6.2 were selected based on the data collected in liquid-boiling MCHX experiments These correlations resulted in the best agreement between model predicted and experimentally measured heat transfer and pressure drop (discussed in detail subsequently in Chapter 7). After the transition criteria were satisfied within a segment, the next heat transfer regime was implemented in the adjacent downstream segment. The secondary coolant enters the MCHX in the liquid convection heat transfer regime and the single-phase Churchill (1977a,b) correlations were used to determine the Nusselt number and friction factor. These correlations were also used for the primary coolant, which remains in the liquid convection regime over the entire channel length. The boiling-side wall temperature was calculated for each liquid convection segment. The transition to the subcooled boiling regime occurred in the downstream segment after the wall temperature exceeded the predicted wall temperature at the onset of nucleate boiling (ONB) condition of Bergles and Rohsenow (1964). The pressure drop in the subcooled boiling regime was calculated using the single-phase Churchill (1977b) friction factor correlation until the equilibrium quality exceeded the quality at OSV, as predicted by Saha and Zuber (1974) (a negative value). Following the OSV, the non-equilibrium quality, x_a, was calculated using the correlation of Ahmad (1970), shown in Eq. (3.59), and the pressure drop was then calculated

Table 6.2: Liquid-boiling model transition and correlation summary

Regime	Transition	Pressure drop	Heat transfer
Liquid convection	Inlet	Churchill (1977b)	Churchill (1977a)
Subcooled boiling	$T_{\text{wall}} > T_{\text{wall,ONB}}$ Bergles and Rohsenow (1964)		Gungor and Winterton (1986)
	$x_{\text{out}} > x_{\text{OSV}}$ Saha and Zuber (1974)	Friction: McAdams *et al.* (1942) Acceleration: Baroczy (1963)	
Saturated boiling	$x_{\text{out}} > 0$		Gungor and Winterton (1986)
Post-dryout	$x_{\text{out}} > x_{\text{di}}$ Kim and Mudawar (2013b)		Dougall and Rohsenow (1963)
Vapor convection	$x_{\text{out}} > 1$	Churchill (1977b)	Churchill (1977a)

for a two-phase mixture, using the non-equilibrium quality. The two-phase frictional pressure drop across the segments was calculated using the correlation of McAdams *et al.* (1942), while the acceleration pressure drop was calculated using the void fraction correlation of Baroczy (1963)**.** These two correlations were also used to calculate the pressure drop in saturated boiling and post-dryout two-phase heat transfer regimes. It is worth noting that the OSV was predicted to occur at approximately saturation conditions and the Churchill (1977b) friction factor correlation was therefore used to calculate the pressure drop in all subcooled boiling segments. The subcooled boiling heat transfer coefficient was calculated using the correlations of Gungor and Winterton (1986) (modified for subcooled boiling as suggested by the authors). Saturated boiling occurred after the equilibrium outlet quality of the neighboring upstream segment exceeded zero and the correlation of Gungor and Winterton (1986) was used to evaluate the segment heat transfer coefficient. The dryout incipience quality, x_{di}, was calculated in each saturated boiling segment using the correlation of Kim and Mudawar (2013b). The post-dryout heat transfer regime occurred after the outlet quality exceeded x_{di} in the upstream segment. The heat transfer coefficient in the post-dryout regime was calculated according to the correlation by Dougall and Rohsenow (1963). After the outlet quality exceeded one, the remaining downstream segments were in the vapor convection heat transfer

regime where the pressure drop and heat transfer coefficient were again calculated using the two single-phase Churchill (1977a,b) correlations.

6.3.2 Iterative solution method

An iterative solution method was required to simultaneously solve the energy, momentum, and UA-ΔT_{LM} equations within each segment. Inlet conditions occur at opposite ends of the MCHX, creating a large system of algebraic equations that must be solved simultaneously. The iterative EES solver was not capable of solving the large system of equations required in the liquid-boiling model, in part due the multiple secondary coolant heat transfer regimes that are dependent upon upstream conditions. Alternatively, inlet conditions for one coolant and the outlet conditions for the other coolant can be specified, defining one end the heat exchanger. In this method, conditions on one end of a segment are known and those on the other end are solved. This allows equations governing a single segment to be solved independently from neighboring segments. The solution for the entire heat exchanger can then be obtained by solving segments one at a time, starting from the end at which conditions are specified. However, this "side-to-side" method exacerbates underpredictions or overpredictions in the heat duty in boiling counterflow heat exchangers. The underprediction of the heat duty in a segment results in a smaller temperature difference in the next segment, further reducing the heat duty. The overprediction of the heat duty has the opposite effect, increasing the heat duty in the next segment. This phenomenon is discussed in more detail in Appendix B.2. Instead, an iterative solution method in which inlet conditions are specified on opposite sides of the heat exchanger was developed. In this "opposite-side" method, the program first updates only secondary (boiling-side) coolant properties and the heat duty in each segment. The primary (hot-side) coolant properties are then updated in the

direction of fluid flow based on the previously calculated segment heat duties. These two steps are repeated for several iterations until the solution converges. A description of steps in the opposite-side solution method used in this study is included below.

1. Initial values:

Initially, the hot-fluid inlet and outlet states of each segment are set to the heat exchanger hot-fluid inlet state. The hot-side heat transfer coefficient for each segment is calculated using average fluid properties within the segment. $T_{hot,in}$ and $P_{hot,in}$ in Figure 6.6 refer to the heat exchanger inlet temperature and pressure, respectively.

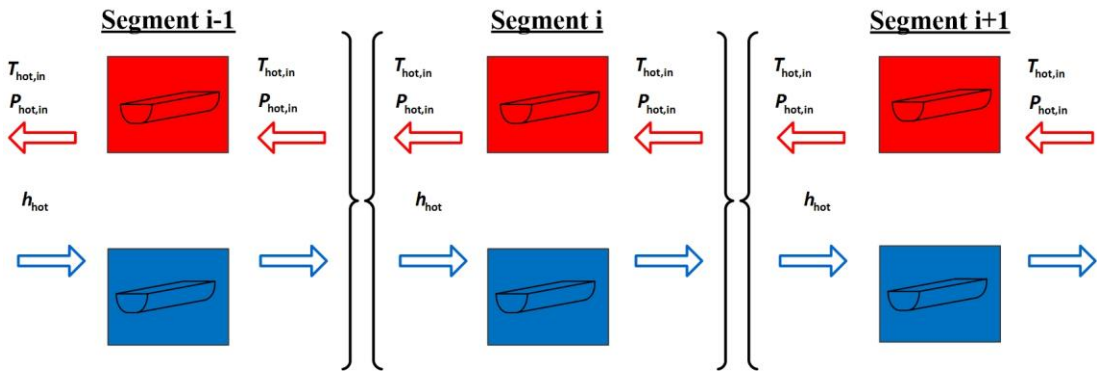

Figure 6.6: Opposite-side solution method: initial values

2. Boiling-fluid update:

The heat duty and boiling-fluid states are updated for each segment, leaving the hot-side properties unchanged. These calculations are performed for one segment at a time, starting at the boiling-side inlet. The outlet state of a segment then becomes the inlet state for the following downstream segment. The boiling-side outlet state, boiling-side heat transfer coefficient, and segment heat duty are determined iteratively using the hot-side temperatures and heat transfer coefficients from the previous step. Iterations are required to determine the average segment boiling-side properties, segment heat flux (required to evaluate boiling heat transfer correlations) and the boiling-side outlet temperature (required to determine the log-

mean temperature difference). The superscript on each variable in Figure 6.7 represents the number of times the variable has been updated, referred to as the overall iteration. The boiling-side enthalpy and pressure are passed between segments because the temperature and pressure are not sufficient to fix the state of a two-phase mixture. The [i] in Figure 6.7 refers to a property of segment "i", while the superscript refers to the number of times the values have been updated.

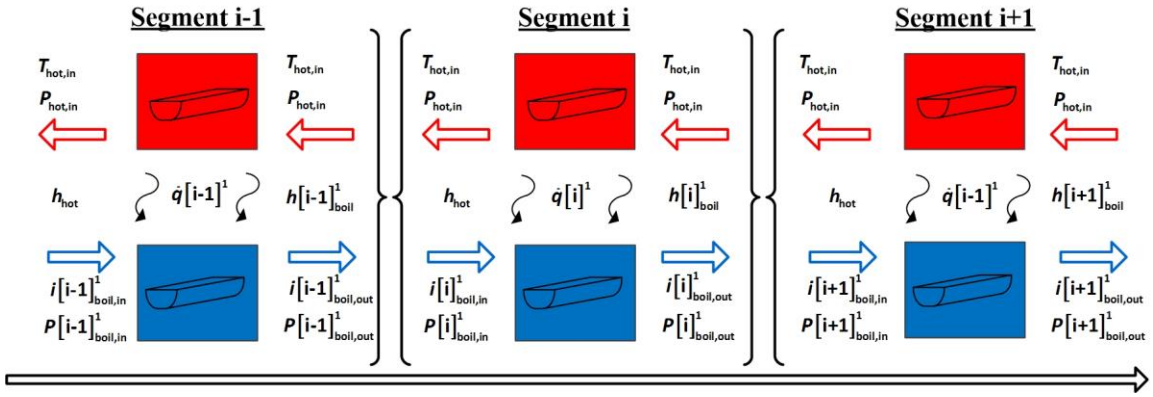

Figure 6.7: Opposite-side solution method: boiling-fluid update

3. Hot-fluid update:

The hot-side fluid states are updated for each segment using the heat duties calculated in the previous step, leaving the boiling-side properties unchanged. Updates are performed for one segment at a time in the direction of flow and segment outlet states become the inlet

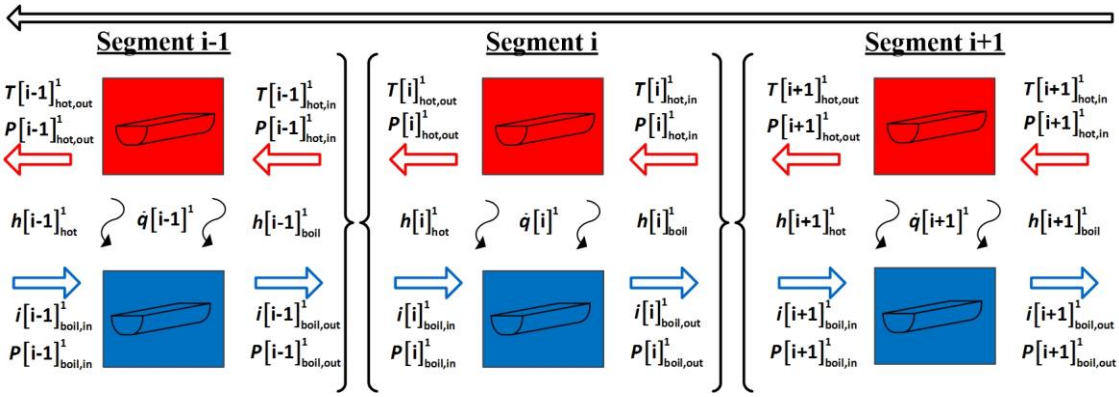

Figure 6.8: Opposite-side solution method: hot-fluid update

state for the following downstream segment. The heat transfer coefficient and frictional pressure drop are evaluated using average fluid properties within the segment.

4. Convergence:

A single boiling-side and hot-side update, steps two and three, form an overall iteration. The change in the heat duty of each segment and the change in the total heat duty from the previous overall iteration are calculated as shown in Eq. (6.3). Overall iterations continue until the change in the total heat duty is less than 0.05% and the change in the heat duty of each segment is less than 0.005% between iterations. Convergence typically occurs between eight and sixteen overall iterations. The superscript "j" in Figure 6.9 refers to the number of overall iterations in which the values have been updated.

$$\frac{\left|\dot{q}_{HX}^{j} - \dot{q}_{HX}^{j-1}\right|}{\dot{q}_{HX}^{j-1}} \times 100\% \tag{6.3}$$

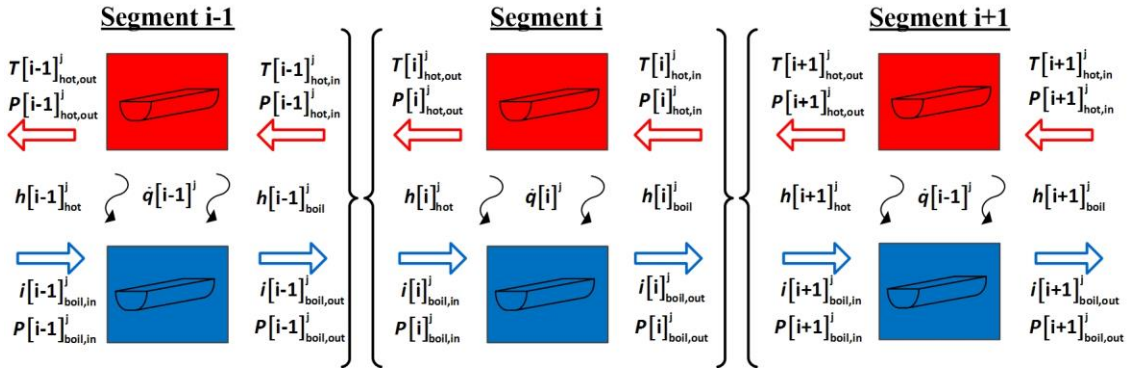

Figure 6.9: Opposite-side solution method: convergence

6.4 Pressure Drop and Flow Distribution Model

A parallel flow path model, described in Section 4.5, was applied to the secondary coolant sheets of the liquid-boiling MCHX design to determine the pressure drop and flow distribution. As in the liquid-liquid MCHX model, secondary-coolant sheets were split into

ten segments equal in length in the azimuthal direction (containing 44 or 45 channels). Each segment contains a flow path passing from the inlet header to the outlet header, as shown in Figure 4.9. A mechanical energy balance, shown in Eq. (4.8), was applied to the single-phase portion of flow paths along the inlet and outlet headers to determine the pressure change. To apply this equation, it was assumed that the steam in the outlet header was incompressible and had constant properties, evaluated using the secondary-coolant outlet conditions in Table 6.1. Additionally, this model is only valid if all flow paths result in superheated states at the outlet of channels. Otherwise, two-phase pressure drop and mixing would need to be considered in the outlet header.

Channel pressure drop was determined using the segmented heat transfer model described in Section 0. The primary and secondary coolant inlet temperatures and pressures were held constant at the values listed in Table 6.1 and the primary coolant mass flow rate was held constant at the evenly distributed value, $\dot{m}_{ch,hot} = 1.493$ g s^{-1}. This model was used to create a lookup table for secondary-coolant channel pressure drop for a given a channel mass flow rate. The frictional pressure drop in headers was calculated using the flat channel friction factor correlation of Dean (1978), shown in Eq. (4.10). Table 4.2 shows the minor losses and their associated loss coefficients along a flow path. The total pressure drop was calculated by summing the pressure changes along each flow path, as shown in Eq. (4.9). EES was utilized to iteratively calculate the mass flow rate of each flow path by requiring all flow paths to have the same total pressure drop.

The parallel flow model was first applied to a secondary sheet with equal inlet and outlet header dimensions. This symmetric sheet had the dimensions shown in Figure 6.1,

except that both inlet and outlet headers occupied the entire available area (the wedge section blocking part of the inlet header was removed). Figure 6.10 shows the resulting pressure in the headers and the flow distribution. The inlet header pressure drop was comparatively small because of the high-density, low-velocity subcooled liquid conditions. After vaporization, the low-density, high-velocity conditions in the outlet header lead to a significantly larger pressure drop. As a result, the flow paths traveling short lengths in the outlet header (the higher numbered paths) had significantly higher flow rates. The total pressure drop across the sheet was 79.68 kPa, and segments 8−10 had channel mass flow rates in which complete vaporization did not occur. As a result, two-phase conditions were present in the outlet header, which were not captured by this model. Still, it is clear that significant maldistribution would likely occur with this header configuration.

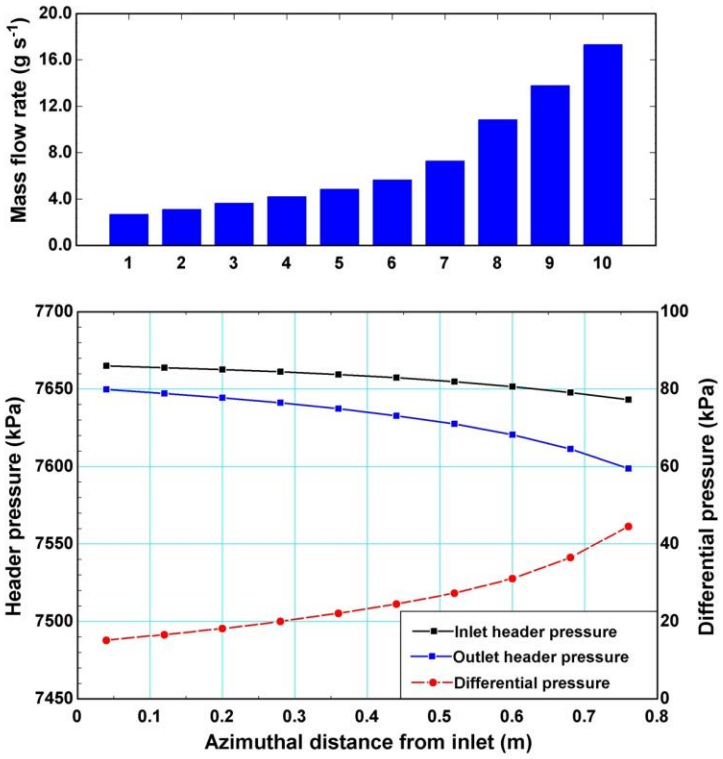

Figure 6.10: Symmetric sheet header pressure and flow distribution

By increasing the pressure drop in the inlet header, a more uniform pressure differential between channels was achieved. This was accomplished by adding a wedge section, shown in Figure 6.1, decreasing the radial length at the inlet to the header from 0.150 m to 0.035 m. The wedge section decreased the cross-sectional area of the inlet header by 76% along the length of the header, significantly increasing the velocity and frictional pressure gradient. Figure 6.11 shows the resulting pressure in the headers and flow

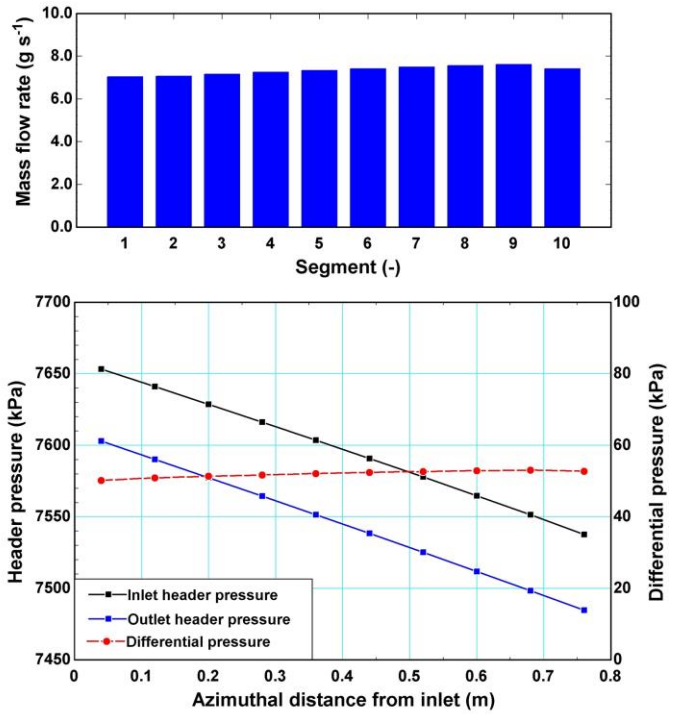

Figure 6.11: Asymmetric sheet header pressure and flow distribution

Table 6.3: Average flow-path frictional pressure losses

Pressure loss	**Avg. velocity (m s^{-1})**	**Avg. ΔP (kPa)**
Header inlet	4.30	3.55
Inlet header frictional losses	4.54	69.5
90° bend into channel	4.54	9.61
Sudden expansion into channel	4.54	6.98
Channel frictional losses	-	8.10
Sudden contraction into header	22.21	2.60
90° bend into header	22.21	10.54
Outlet header frictional losses	22.21	72.3
Header outlet	21.74	9.21

distribution in an asymmetric sheet. All flow paths were within ±5% of the evenly distributed value and resulted in superheated vapor states at the outlet of channels. Table 6.3 contains the average frictional pressure losses and associated velocities for the ten flow paths. As was the case for secondary coolant in the liquid-liquid design, the pressure drop in the high velocity header regions was the largest contributor to the overall pressure drop. The total pressure drop across the sheet was 193.8 kPa, significantly larger than in the symmetric sheet.

6.5 I^2S-LWR Rankine Cycle

A Rankine power cycle, similar to the proposed flash Rankine cycle in Section 4.8, was developed for the liquid-boiling MCHX. Because the secondary coolant exits the MCHX as superheated steam, the flashing drum was no longer required. A design similar to the flash Rankine cycle was selected to determine the impact of using the MCHX as a steam generator on the thermal efficiency of the I^2S-LWR plant. Otherwise, it would be unclear whether improvements in performance were attributable to the use of the liquid-boiling MCHX or the modified power cycle. A schematic of the cycle is shown in Figure 6.12. It should be noted that incremental improvements in the thermal efficiency are still possible by adding additional turbine bleed streams and feedwater heaters. Several pumps may also be removed by using closed feedwater heaters (CFWH) instead of open feedwater heaters (OFWH), with minimal effect on thermal efficiency. A high-temperature reheater (RH 2) and a closed feedwater heater (CFWH) were added to the flash Rankine cycle design. Utilizing superheated steam from the MCHX, the high-temperature reheater (RH 2) serves to further superheat the high-pressure turbine exhaust and decrease moisture in downstream turbines. This configuration is common in PWR Rankine cycles (Steam, 2005) and eliminates the need for a lower temperature reheater (RH 2 in the flash Rankine cycle, Figure 4.14). The CFWH, which

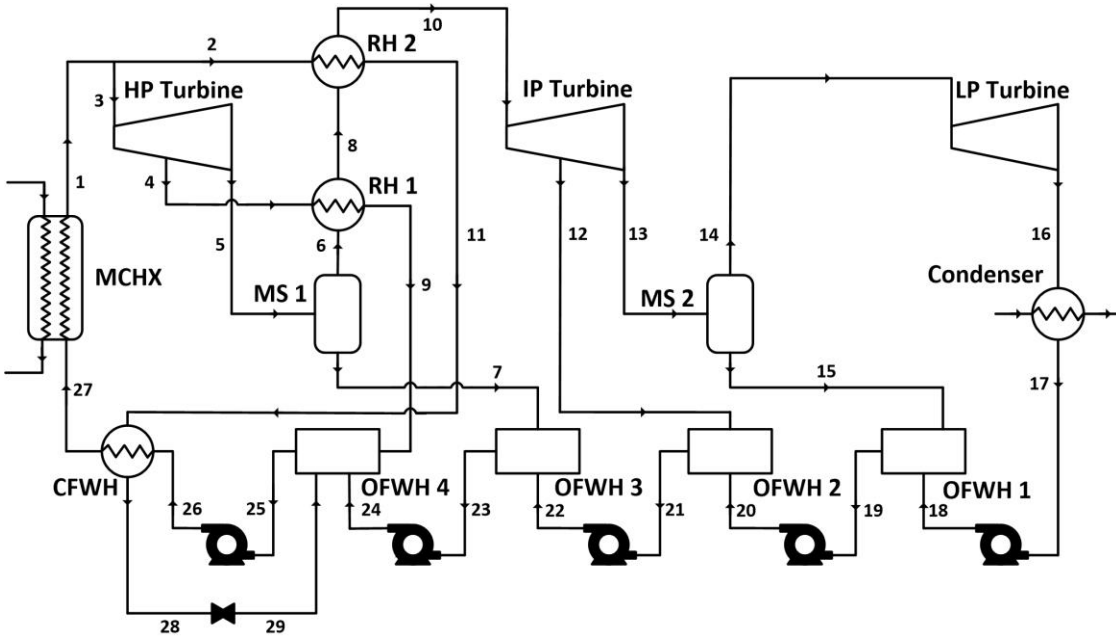

Figure 6.12: I^{2}S-LWR Rankine cycle

condenses the high-pressure steam from RH 2, allows the feedwater to be heated to temperatures above that of the high-pressure turbine bleed stream (state 4).

6.5.1 Rankine cycle model

A steady-state thermodynamic model of the Rankine cycle in Figure 6.12 was developed in EES. Thermodynamic water properties were evaluated using the built-in EES routines (Wagner and Pruß, 2002). Important assumptions (such as isentropic component efficiencies and the condenser temperature) used to develop the model were the same as those in the flash Rankine cycle and are listed in Table 4.6. All OFWH outlets (states 19, 21, 23, and 25) were assumed to be saturated liquids. Superheated steam exiting on the cold-side of the reheaters (state 8 and 10) were 10°C below the saturation temperature of steam on the hot side, consistent with the 10°C heat exchanger approach temperature assumption. These two requirements dictate the turbine bleed stream flow rates (state 4 and 12) as well as the enthalpy of the streams from the moisture separators to the OFWHs (states 7 and 15). The inlet and

outlet of the MCHX (states 1 and 27) were determined by the liquid-boiling MCHX model and were inputs to the EES cycle model. The flow rate of diverted high-pressure steam from the MCHX (state 2) was determined by requiring that the hot-side outlet of the CFWH (state 28) be in the saturated liquid state, and the cold-side outlet (state 27) be at the specified MCHX inlet state. Additionally, all piping and heat exchangers were assumed to have negligible pressure drop. The above requirements left four independent variables that could be varied to determine the maximum efficiency of the cycle: the outlet pressures and bleed stream pressures of the high and intermediate turbines (states 4, 5, 12, 13).

6.5.2 Secondary coolant conditions and Rankine cycle optimization

The lower the secondary-coolant pressure, the larger the difference between the primary coolant temperature and saturation temperature of the secondary coolant, increasing the heat duty of the liquid-boiling MCHX. However, a larger temperature difference also leads to a larger exergy destruction rate and a reduced thermal efficiency of the accompanying power cycle. Therefore, the MCHX should operate at the maximum possible pressure at which MCHXs can remove the required 2850 MW_{th}. Two additional constraints were placed on secondary-coolant conditions for the operation of the liquid-boiling MCHX and the accompanying Rankine cycle. First, the inlet to the MCHX (state 27) should be at least 20°C below the saturation temperature, ensuring that vapor generation does not occur before the secondary coolant enters MCHX channels. Further subcooling at the inlet would result in longer liquid convection and subcooled boiling lengths, both of which are less efficient than the saturated boiling heat transfer regime. Additionally, the secondary coolant should exit the MCHX (state 1) as a superheated vapor at least 20°C above the saturation temperature. This limits moisture in the high-pressure turbines as the coolant expands and ensures superheated

conditions in the secondary-coolant outlet header. However, heat transfer in the vapor convection regime is poor, and the secondary-coolant outlet temperature should therefore not exceed the above requirement in order to limit the length of this regime. For a given secondary-coolant inlet pressure, the above requirements dictate the inlet temperature ($T_{in} = T_{sat} - 20°C$) and outlet temperature ($T_{out} = T_{sat} + 20°C$). The approximate secondary-coolant mass flow rate can be calculated using Eq.(6.4). A range of potential secondary-coolant inlet conditions (T_{in}, P_{in}, and $\dot{m}_{boil}$) were calculated in this manner and were then used as inputs to the MCHX heat transfer model to determine the heat duty. The model predicted a heat duty of 2850 MW_{th} at a secondary-coolant inlet pressure of 7.666 MPa, representing the highest pressure at which the MCHXs can satisfy the above requirements.

$$\dot{m}_{boil} = \left(2850\ \text{MW}\right) / \left[i\left(T_{out}, P_{in}\right) - i\left(T_{in}, P_{in}\right) \right] \tag{6.4}$$

The secondary-coolant conditions, shown in Table 6.1, were then used as the inlet and outlet of the MCHX (states 1 and 27) in the Rankine cycle model. The four independent variables in the cycle model were then optimized to determine the maximum cycle efficiency. These included the intermediate system pressures at the outlet and bleed streams of the high and intermediate pressure turbine. EES contains several built-in optimization search methods. The Conjugate Direction method uses numeric derivatives to determine minimum or maximum values and was used here to determine the maximum thermal cycle efficiency. This resulted in an overall cycle efficiency of 39.03% and electrical power output of 1112.4 MW_e. A T-s diagram of the cycle is shown in Figure 6.13 and thermodynamic properties and the mass flow rate of each state are available in Appendix B.3. For comparison, the liquid-liquid MCHX design and accompanying Flash Rankine cycle had a thermal efficiency of 34.58

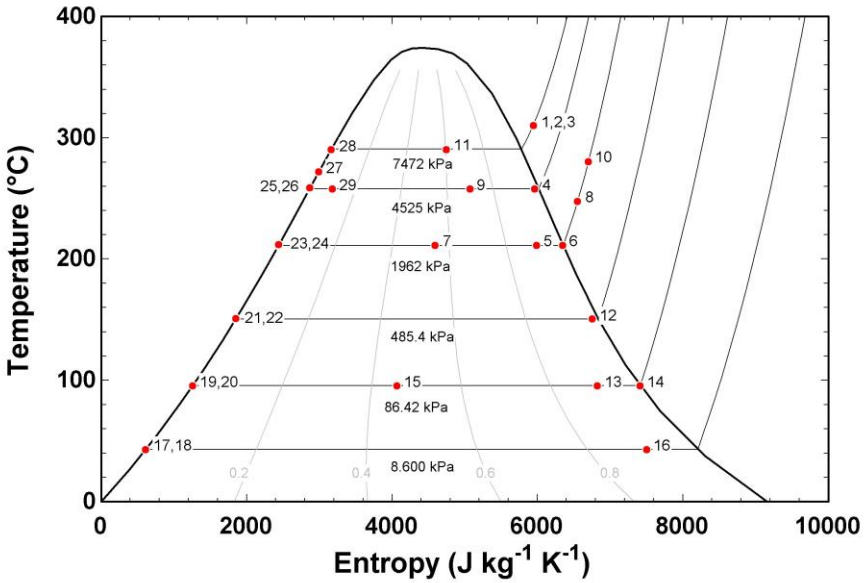

Figure 6.13: Rankine cycle T-s diagram

percent and produced 985.5 MW_e. In addition to the improved electric power, the liquid-boiling MCHX and accompanying Rankine cycle eliminate the need for flashing drums and large secondary coolant pumps.

6.5.3 Exergy analysis of the liquid-liquid and liquid-boiling MCHX designs

Exergy can be thought of as the maximum work that can be extracted as a system is brought into equilibrium with its surroundings. The flow exergy associated with a mass input into a control volume is defined as follows: $e_f = (i - i_0) - T_0 (s - s_0)$, where the subscript zero refers to properties evaluated at the temperature (T_0) and pressure (P_0) of the surroundings. Exergy analysis provides a means for determining amount of lost work (exergy destruction, $\dot{E}_d$) due to irreversibilities within the system. The temperature difference between fluid streams in heat exchangers is often a large source of exergy destruction in energy systems. In both the liquid-liquid and liquid-boiling MCHX designs the primary coolant conditions are the same, resulting in an equivalent exergy input into the two associated power cycles. The

liquid-liquid MCHX requires the use of a flashing drum to create steam, a significant source of exergy destruction. A simple comparison of the two MCHX designs was made by determining the exergy destruction rate in both the liquid-liquid and liquid-boiling MCHX designs as well as the flashing drum in the flash Rankine cycle. Eq. (6.5) shows the steady-state exergy balance for an open, adiabatic control volume with no work inputs and is used here to determine the exergy destruction rate. The temperature and pressure of the surroundings (environment) were assumed to be 30°C and 101.325 kPa (1 atm).

$$0 = \sum_{j}^{in} \dot{m}_j e_{f,j} - \sum_{j}^{out} \dot{m}_j e_{f,j} - \dot{E}_d \tag{6.5}$$

Figure 6.14 shows the exergy destruction rates and the flow exergy for the liquid-liquid and liquid-boiling MCHX designs. The difference between the inlet and outlet flow exergy of the primary coolant (states 1 and 2) shows that 1386 MW of work could be generated if no irreversibilities existed within the power cycles, resulting in a thermal efficiency of 48.63%. However, significant exergy destruction occurs within components, including the MCHX and flashing drum. The liquid-liquid MCHX design was slightly more efficient than the liquid-boiling MCHX, with exergy destruction rates of 56.1 MW and 69.62 MW, respectively. This difference can be explained by the temperature profiles in the two designs shown in Figure 4.3 and Figure 6.2. In the liquid-liquid design, the temperature of the secondary coolant increases while that of the primary coolant falls, leading to a consistent temperature difference between 10°C and 20°C. In the liquid-boiling design, a larger temperature difference exists between the two coolant streams because the secondary coolant temperature remains constant during the boiling process, leading to significant exergy destruction and irreversibility. However, the flashing drum had an exergy destruction rate of

	State (-)	Mass flow rate (kg s^{-1})	Temperature (°C)	Pressure (MPa)	Specific flow exergy (kJ kg^{-1}) [e_f]	Total flow exergy (MW) [$\dot{E}_f$]
1	subcooled liquid	15,498	330.0	16.30	453.0	7020
2	subcooled liquid	15,498	298.8	15.86	363.5	5634
3	subcooled liquid	13,016	279.3	12.88	314.9	4099
4	subcooled liquid	13,016	318.2	11.76	417.1	5429
5	saturated vapor	1,587	285.4	6.958	1,016	1613
6	saturated liquid	11,429	285.4	6.958	326.6	3732
7	subcooled liquid	1711	272.0	7.666	295.3	505.2
8	superheated vapor	1711	310.1	7.472	1065	1822

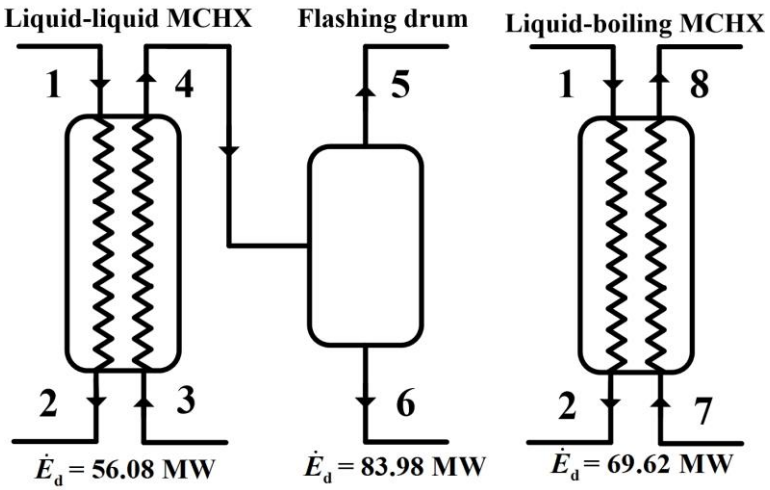

Figure 6.14: Exergy destruction analysis

84.0 MW. The liquid-liquid MCHX and flashing drum had a combined exergy destruction rate of 140 MW as compared with only 69.6 MW in the liquid-boiling design. This accounts for much of the difference in thermal efficiency between the two power cycles designs. Additionally, 119.5 MW was required to pump the secondary coolant (13,016 kg s^{-1}) from the flashing pressure (6.96 MPa) to conditions at the inlet of the MCHX (12.88 MPa) in the flash Rankine cycle. Significant exergy destruction is associated with the turbine inefficiency required to generate power for the pumps, as well as the inefficiencies of the pumps themselves. For comparison, only 14.8 MW of pumping power is required in the liquid-boiling Rankine power cycle. The capital cost of these high flow-rate, high differential-pressure pumps may also be significant.

6.6 Potential Design Concerns

The analysis in this chapter shows that the liquid-boiling MCHX design is capable of meeting design goals at stable, steady-state operation. However, several important assumptions used in the design process require further investigation before such a MCHX could be implemented in the I^2S-LWR. These were considered outside the scope of this investigation but are discussed briefly here. Recommendations for further investigation into these and other aspects of the design are discussed in Chapter 8.

6.6.1 Fouling

Fouling can be particularly problematic for once-through steam generators as dissolved ions and particulate matter are concentrated during the boiling process. However, once-through steam generators have been used successfully in existing PWR plants and fouling can be limited through careful control of feedwater chemistry. In this investigation, a fouling layer thickness of 10 μm with thermal conductivity of 1.3 W m^{-1} K^{-1} was assumed on both primary and secondary coolant heat transfer surfaces based on a brief review of the literature. The fouling layer thickness was increased to 40 μm to investigate the impact of

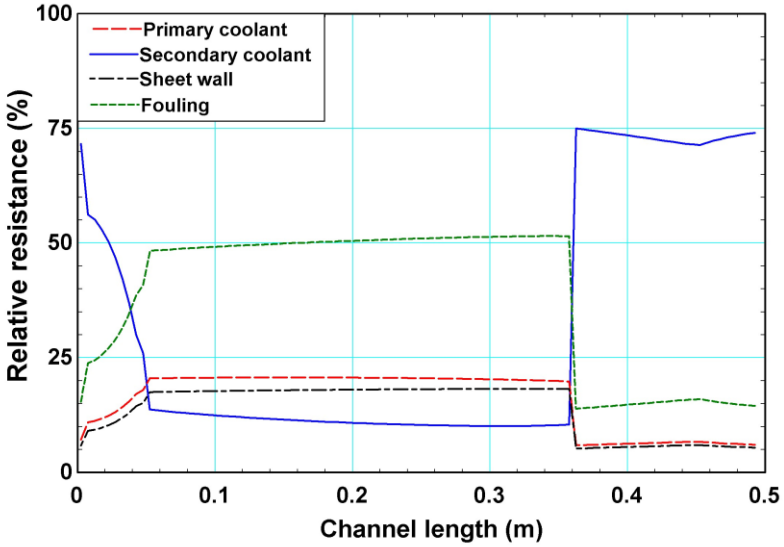

Figure 6.15: Increased fouling relative resistance

larger build-ups on MCHX performance. The geometry of the liquid-boiling MCHX was held constant at the values listed in Section 6.2 and new secondary inlet parameters were determined to achieve a heat duty of 2850 MW_{th}. This resulted in a secondary coolant inlet pressure to 6.870 MPa ($T_{boil,in}$ = 269.7°C, $\dot{m}_{boil}$ = 1965 kg s^{-1}) and a Rankine cycle thermal efficiency of 38.41%. 17.37 MW_e were lost when compared with the case of 10 μm of fouling build-up (η_{th} = 39.03%) used as the design basis. This shows that increased fouling can be accounted for with only minor losses in plant thermal efficiency. Figure 6.15 shows the relative thermal resistance along the length of the MCHX. The increased fouling resistance is significant in the saturated boiling regimes but the secondary coolant still dominates the resistance in the other regimes.

6.6.2 Channel blockage

Channel clogging or plugging may occur over the life of the MCHX or in an accident scenario. However, there is no information in the literature that could suggested the amount of blockage that might occur as the result of particulate matter in the primary or secondary coolant. The secondary coolant is filtered during the condensate polishing process and additional filtering can be performed before the coolant enters the MCHXs. Primary coolant is provided by CVCS and can be further filtered before entering the RPV. Regular maintenance of the MCHXs during refuelling outages may also provide the opportunity to remove any material clogging channels. Therefore, it was assumed in the design that plugged channels would be relatively rare. To estimate the impact of clogged channels, 20% of channels were removed from the MCHX sheets, increasing the mass flux in the remaining channels. Increased channel velocity led to an increase in the heat transfer coefficients of both

fluids also but decreased the heat transfer surface area. To meet heat duty requirements the secondary inlet pressure was reduced to 7.385 MPa ($T_{boil,in}$ = 268.0°C, $\dot{m}_{boil}$ = 1965 kg s^{-1}). Using these secondary coolant conditions, the Rankine cycle model achieved a thermal efficiency of 38.82%. This represents the loss of 5.99 MW_e when compared with the base case in which no channels were blocked. However, the blockage also results in an increase in the pressure drop across the channels. Although, it should be noted that a major portion of the pressure drop in both coolants occurred in the header regions. The primary-coolant channel pressure drop increased from 77.4 kPa to 118 kPa and the secondary-coolant channel pressure drop increased from 9.49 to 14.8 kPa. Thus, limited channel plugging does not represent a significant problem for the MCHX.

6.6.3 Maldistribution and flow instabilities

The uneven distribution of the secondary coolant in liquid-boiling MCHX channels will likely significantly degrade heat transfer performance. Maldistribution may cause premature dryout in channels with lower flow rates (decreasing the heat transfer) or produce two-phase outlet condition in high flow rate channels (carrying moisture downstream into the turbines). The flow path technique used in this study suggests that an even distribution can be achieved in both the liquid-liquid and liquid-boiling designs through the use of triangular (parallel oblique) headers. Approaches used to limit maldistribution, discussed in Section 3.6, suggest that the pressure change in the headers should be small compared to the pressure drop in parallel channels. However, this was not possible because of the size/volume requirements of fitting the MCHX stacks into the downcomer of the I^2S-LWR. Therefore, further

investigation into the flow distribution should be performed, particularly pertaining to secondary coolant in the liquid-boiling MCHX design.

The flow rate instabilities in boiling systems degrade heat transfer performance and lead to premature mechanical failure in some circumstances. Transient changes in channel flow rates may reduce heat transfer and lead to temporary or permeant maldistribution. No attempt to quantify the impact of the flow instabilities on the liquid-boiling MCHX design is made in this investigation and further study is therefore required. A discussion of boiling channel instabilities is presented in Section 3.5. In single channel systems, boiling instabilities can often be suppressed by decoupling the channel flow rate from the channel pressure drop and are often associated with two-phase outlet conditions. Pressure drop oscillations can be eliminated by removing any compressible volumes between the pump and boiling channel(s). Instabilities in parallel boiling channels are more complicated due to channel-to-channel interactions within shared headers. The literature suggests that parallel channel instabilities can be suppressed by including an orifice near the inlet of each channel. The secondary-coolant pressure drop of the liquid-boiling MCHX design is substantially lower than that of the liquid-liquid design and the additional pressure drop of an orifice would not significantly impact the design. Furthermore, an orifice would increase the percentage of the pressure drop occurring in the channels relative to the headers, potentially improving the flow distribution. However, the orifice may trap particulate matter that would otherwise pass through the channel.

CHAPTER 7. LIQUID-BOILING EXPERIMEMTNS

An experimental investigation to test the accuracy of the liquid-boiling MCHX model discussed in the previous chapter was conducted. Measured values of the heat duty and pressure drop were compared with the predictions of the model. Additionally, tests designed to isolate specific heat transfer regimes were conducted to assess the accuracy of correlations and transition criteria used in the model. Many aspects of the design and operation of the liquid-boiling test facility are similar to those of the liquid-liquid experiments discussed in Chapter 5.

7.1 Liquid-boiling Test Facility

Tests were conducted using the same MCHX test section used for liquid-liquid experiments, discussed in Section 5.1. In liquid-boiling experiments, the sheets with full-length channels carry the boiling water (simulating the secondary coolant), while hotter liquid water (simulating the primary coolant) flows through the sheets containing triangular headers on opposite ends of the channels. This configuration was selected to help ensure a uniform flow distribution on the boiling side and simplify heat transfer calculations in the header regions. Additionally, the test section is mounted with the inlet piping below the heat exchanger. This orientation was selected to help drain liquid from the test section that might otherwise accumulate in the outlet header.

7.1.1 Test facility design

The liquid-liquid test facility was substantially modified for boiling experiments. The liquid-boiling facility consists of three coupled, distilled water loops: the hot loop, boiling

loop, and cold loop. A photograph of the liquid-boiling facility is shown in Figure 7.1 (insulation was added around piping and important components after the photograph was taken.) A schematic of the facility is shown in Figure 7.2. All three loops contain relief valves designed to open at 3000 kPa to prevent over-pressurization. The hot loop is largely unchanged from the liquid-liquid facility and supplies high-pressure, subcooled water to the MCHX test section.

Liquid water in the boiling loop enters the MCHX test section and exits as a two-phase mixture. The two-phase mixture is condensed in a GAE flat plate heat exchanger, rejecting heat to the cold loop. A small Swagelok tank with a volume of one liter is located between the boiling-loop pump and condenser to ensure that sufficient liquid inventory is available for the pump. The flow rate of the boiling loop is substantially lower than that of the other two loops due to the large enthalpy of vaporization of water. Liquid sections of the boiling loop could therefore be constructed from 12.7 mm OD stainless steel tubing without significant pressure drop, as compared to the 25.4 mm OD tubing in the hot and cold loops. 25.4mm OD tubing connects the test section and condenser, where the fluid in the boiling loop is a two-phase mixture. Flow boiling systems, particularly those with two-phase outlet conditions, are subject to several possible instabilities discussed in Section 3.5. The Ledinegg instability can cause a large increase or decrease in the flow rate at a given centrifugal pump speed, making it impossible to obtain data at specific flow rates and/or two-phase outlet conditions. Density wave oscillations can cause dynamic variations in the flow rate, resulting from the delayed interaction of the pump and downstream pressure drop. These two instabilities can be eliminated with the use of a positive displacement pump. Therefore, a Liquiflo gear pump (a

Figure 7.1: Liquid-boiling test facility photograph

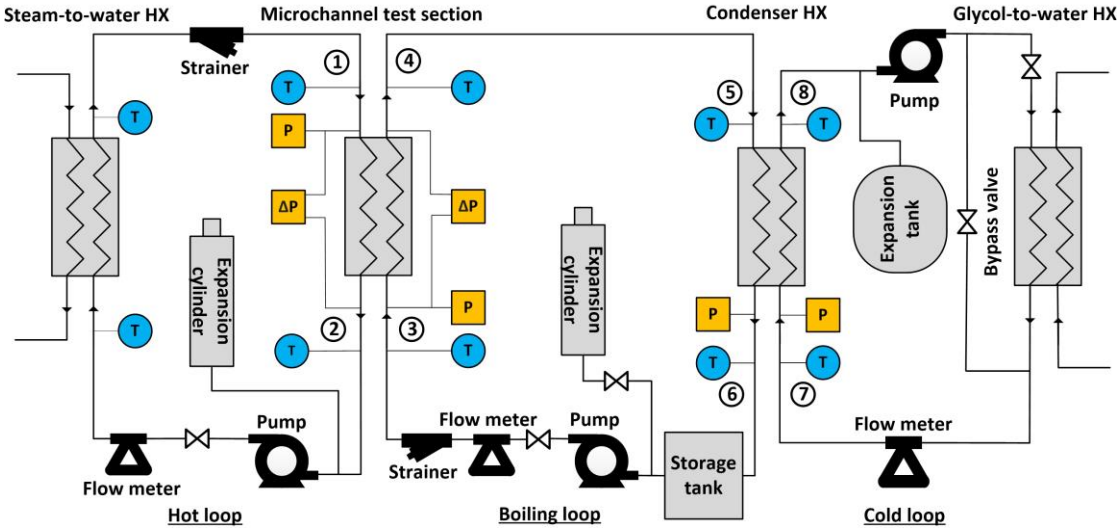

Figure 7.2: Liquid-boiling test facility schematic

type of positive displacement pump) was installed on the boiling loop and is capable of supplying a flow rate of 0.185 kg s^{-1} with a differential pressure of 100 kPa. The gear pump is magnetically coupled to a 1.12 KW Leeson 90 Volt DC motor. The motor/pump speed is

controlled through a variable voltage Leeson DC pump controller. A Parker Hannifin piston-cylinder accumulator is located between the storage tank and pump to account for fluid expansion as vaporization occurs. The accumulator was specifically not placed between the pump and test section in order to avoid the pressure drop oscillations discussed Section 3.5. Strainers are located before the test section on both the hot loop and boiling loop to filter out any material in the loops that could clog MCHX channels.

The cold loop removes heat from the boiling loop through the condenser and rejects heat to the lab chiller loop using a GEA flat-plate heat exchanger (glycol-to-water HX). A Watts bladder expansion tank maintains a constant pressure in the cold loop, ensuring boiling

Table 7.1: Liquid-boiling test facility equipment

Equipment	Manufacturer	Model	Description/Other
Pumps (3)	Liquiflo	Hot / Cold loops: 620FSEE020F08(320)	260°C max temperature
		Boiling loop: H5FS6PEE002000US-8(212)	260°C max temperature
Motors (3)	Baldor	Hot / Cold loops: SuperE VEM3550	1.12 kW Three-phase AC 240V power
	Leeson	Boiling loop: C4D17FK5K	DC 90V power
Pump controller	Baldor (VFD)	Hot / Cold loops: VS1S11PS-0T	Input: Single-phase AC 120V, 20A max Output: Three-phase AC 240V, 5.8A max
	Leeson (variable voltage)	Boiling loop: 174102	Input: Single-phase AC 120V 13A max Output: DC 0 - 90V 10A max
Glycol-to-water heat exchanger	GEA Flat Plate	FP5X12L-10	10 plate 127 mm × 305 mm
Condenser	GEA Flat Plate	FP5X12L-20	20 plate 127 mm × 305 mm
Steam-to-water heat exchanger	Armstrong	WSE-4H-0602-400E-3- 66SSSSS-18	4 pass 4 tube ID 17.8 mm l = 0.705 m
Accumulators (3)	Parker Hannifin (piston-cylinder)	Hot / Boiling loops: A3NW116D1H	116 cm^3 displacement High temperature O-ring (177°C)
	Watts (bladder design)	Cold loop: PLT-5	1035 kPa max pressure 93°C max temperature
Storage tank	Swagelok	304L-HDF8-1000	1 liter volume

does not occur. As in the liquid-liquid test facility, a bypass around the glycol-to-water heat exchanger is used to control the rate of heat transfer from the cold loop. The pump, motor, and VFD on the cold loop are the same as those in the liquid-liquid test facility cold loop. While not directly coupled to the test section, the cold loop serves two important functions in the liquid-boiling test facility. First, it provides a redundant means of measuring the test section heat duty, discussed in Section 7.3.1. Secondly, the cold loop provides a means of controlling the condenser heat duty which is discussed in Section 7.2.2. More details about equipment used in the liquid-boiling test facility are given in Table 7.1.

7.1.2 Data collection and instrumentation

Ten Omega thermocouples are located at the inlet and outlet of all heat exchangers in the facility. J-Type thermocouples are used in the hot loop and boiling loop while cold-loop temperatures are collected using two T-type thermocouples. Thermocouples signals were calibrated between 40°C and 180°C prior to installation in the liquid-boiling facility using a NIST-calibrated thermocouple bath. Rosemount pressure transducers are located at four positions on the three loops required for test section heat duty measurements. Two Rosemount differential pressure transducers measure the pressure drop across the test section in the hot loop and boiling loop. The mass flow rate in each loop is directly measured using Micro Motion Coriolis flow sensors and transmitters. Thermocouple, pressure transducer, and flow transmitter signals are collected using National Instruments measurement modules as discussed in Section 5.2.3. Data are recorded and displayed using a compact DAQ chassis and LabVIEW software produced by National Instruments in the same manner as liquid-liquid experiments. A summary of the liquid-boiling test facility instrumentation and associated measurement uncertainty is shown in Table 7.2

Table 7.2: Liquid-boiling test facility instrumentation

Instrument	Manufacturer	Model	Range (span)	Uncertainty /details
Pressure transducers (4)	Rosemount	3051S2CD4A2E12A1AM5	0 – 4000 kPa	± 0.035% of span (1400 Pa)
Differential pressure transducers (2)		Boiling loop: 3051CD3A22A1AB4M6 Hot loop: 3051S2CD4A2E12A1AM5	0 – 200 kPa	± 0.035% of span (70 Pa)
Flow sensors (2)	Micro Motion	Hot / Cold loops: F100S129CVBAEZZZZ	0 – 1.4 kg s^{-1}	± 0.05% of measurement
		Boiling loop: F050SB77C2BAEZZZZ	0 – 0.6 kg s^{-1}	± 0.03% of measurement
Flow transmitters (3)		1500B3BABMEZZZ	-	-
Thermocouples (10)	Omega	Hot / Boiling loops (8): JMQSS-125U-6	-40 – 750°C	± 0.25°C
		Cold loop (2): TMQSS-125G-6	-250 – 350°C	± 0.25°C
DAQ chassis	National Instruments	NI cDAQ 9174	-	4 card slots
Thermocouple module		NI 9213	± 78.125 mV	16 channel
Current module (loop-powered)		NI 9208	± 20 mA	16 channel
Current module (single-ended measurement)		NI 9203	± 20 mA	8 channel
DC power supply	Sola	SDP 4-24-100LT	-	Input: 120V AC Output: 24V DC

7.2 Experimental Procedures

The procedures for leak checking, charging, and discharging the liquid-boiling test facility loops are the same as the procedures for liquid-liquid facility, discussed in Section 5.3.1. When charging the boiling loop, it is critical to ensure that the piston in the accumulator is at the bottom of the cylinder. This ensures adequate volume is available as liquid is displaced by vaporization in the loop.

7.2.1 Start-up and shutdown

A short, sequential list of steps used to start the liquid-boiling test facility is provided below:

1) The hot-loop expansion cylinder is pressurized to the desired operating pressure using compressed nitrogen. The boiling loop cylinder is not pressurized, allowing for vapor expansion as boiling occurs. The cold-loop pressure is maintained around approximately 500 kPa by the pressurized bladder expansion tank on the loop.

2) The lab chiller loop is started and set to the desired temperature using a Johnson Controls (METASYS©) interface. After a steady flow rate and supply temperature are established in the chiller loop, valves connecting the glycol-to-water heat exchangers to the chiller-loop distribution and return headers are opened.

3) The three loops are started sequentially in the following order: cold loop, boiling loop, hot loop. The flow rate in all three loops is set to the desired flow rate. All three loops are allowed to reach steady-state temperatures.

4) The pressure regulator on the steam distribution line is fully closed. Valves from the high-pressure steam supply and condensate return headers are then opened. A rapid increase in loop temperature may damage components. Therefore, the pressure downstream of the regulator is slowly increased over the course of approximately ten minutes, allowing the facility to slowly heat to the desired temperature. Pressure in the boiling loop is allowed to reach a steady-state value, which is dictated by the vapor generation rate. The pressure and temperature of the loops are then adjusted as described in the following section.

Shutdown of the liquid-boiling test facility is completed by performing the steps listed above in the reverse order. First, the steam pressure is slowly reduced over a ten-minute period to allow the facility to cool. Pressure in the boiling loop drops substantially as less vapor is

generated. The steam distribution and condensate return valves are then closed. After the loops are cooled to steady-state temperatures, the pumps in the three loops are shut down in the opposite order in which they were started. The chiller loop distribution and return header valves are closed and the chiller loop is shut down. The compressed nitrogen in the two expansion cylinders is discharged.

7.2.2 Test facility control

After start-up, the test facility requires manipulation to achieve the desired test conditions. Desired data points are described by the temperature, pressure, and mass flow rate at the inlets of the test section in the hot loop and boiling loop. Hot-loop conditions are controlled with the same methods as the hot loop in the liquid-liquid test facility, discussed in Section 5.3.3. The cold loop is manipulated to help achieve the desired boiling-loop test conditions. The temperature and flow rate in the cold loop are also adjusted in the same manner as the liquid-liquid test facility, with the exception that heat input is from the condenser rather than the test section. The following describes the procedure for setting the conditions in the boiling loop.

- Flow rate

The motor/pump speed (in RPM) is proportional to the voltage supplied by the Leeson DC pump controller. The volume displacement of the gear pump is linearly proportional to the pump speed. Thus, by adjusting the voltage supplied by the DC motor controller, the boiling loop flow rate can be controlled. Unlike centrifugal pumps, the flow rate supplied by the gear pump is not a strong function of the pressure drop through the loop. Therefore, at a

given pump speed, the flow rate stays relatively constant as boiling occurs and the pressure drop throughout the loop increases.

- Temperature

At steady-state, the temperature of the boiling loop at the inlet to the test section is approximately the same as the boiling-loop temperature exiting the condenser. The boiling-loop temperature at the exit of the condenser is a function of the condenser heat duty, which can be adjusted by changing conditions in the cold loop. Decreasing the temperature or increasing the flow rate of the cold loop increases the condenser heat duty, lowering the boiling-loop temperature at the outlet of the condenser (and the temperature at the inlet to the test section). Increasing the temperature or decreasing the flow rate in the cold loop has the opposite effect.

- Pressure

Using a simple manifold, compressed nitrogen can be injected into the top of the piston-cylinder accumulator to increase the boiling-loop pressure or released to decrease the boiling-loop pressure. Pressure control in the boiling loop is more complicated than the liquid hot loop because the pressure and heat transfer rates in the loop are coupled. Pressure changes in the boiling loop affect the saturation temperature, which in turn influences the heat duty of the test section and condenser. Changes in the heat duty of these components affect the temperatures in the loops, including the temperatures at the inlet of the test section. Thus, the boiling-loop pressure and test-section inlet temperatures must be slowly and simultaneously adjusted between data-point measurements. For example, when increasing the boiling-loop pressure, the saturation temperature in the loop increases, decreasing the test-section heat

duty. This results in a higher hot-loop test-section inlet temperature and lower boiling-loop test-section inlet temperature.

7.3 Data Reduction and Test Section Model

Measurements were recorded over a thirty-second period at a rate of five Hertz and stored in LabVIEW. The average and standard deviation of measurement values over the previous thirty seconds were displayed in a LabVIEW interface. After the facility reached the desired steady-state test conditions, measured values were exported to a spreadsheet. The average values of measurements over the thirty-second period were used for data analysis. The pressures at the outlet of the test section in both the boiling and hot loops were calculated from the measured pressure at the inlet and the differential pressure measurement across the test section.

7.3.1 Heat duty measurement

Fluid states at the inlet and outlet of the MCHX test section on the hot loop and boiling loop were required for redundant heat transfer measurements. Single-phase liquid states were determined using temperature/pressure measurements and the specific enthalpy was evaluated using the built-in EES property function. Water in the boiling loop exits the test section as a two-phase mixture and the specific enthalpy cannot be determined from the temperature and pressure. Instead, the test-section outlet enthalpy in the boiling loop was calculated using the condenser heat duty. The condenser heat duty was determined using the enthalpy change in the liquid cold loop, states 1 and 2 in Figure 7.2. The measured inlet pressure was used to evaluate the enthalpy at the inlet and outlet of the condenser in the cold loop, as shown in Eq. (7.1). The outlet of the condenser in the boiling loop is in the subcooled liquid state (state 3),

allowing the two-phase inlet enthalpy (state 4) to be calculated from the condenser heat duty, as shown in Eq. (7.2). Heat losses to the surroundings in the piping between the test section and condenser in the boiling loop were found to be negligible and are discussed in Appendix C. Therefore, the enthalpies at the inlet of the condenser (state 4) and outlet of the test section (state 5) were assumed to be equal: $i_4 = i_5$. The test-section heat duty was then calculated using the enthalpy change in both the hot loop and boiling loop, as shown in Eq. (7.3). The average of the two heat duties was reported as the test-section heat duty for each data point. Uncertainty in the measured heat duty was calculated using the EES uncertainty analysis utility and the measurement uncertainties in Table 7.2.

$$\dot{q}_{\text{cond}} = \dot{m}_{\text{cold}} \left[i\left(T_8, P_8\right) - i\left(T_7, P_7\right) \right] \tag{7.1}$$

$$i_4 = \dot{q}_{\text{cond}} / \dot{m}_{\text{boil}} + i\left(T_3, P_3\right) \tag{7.2}$$

$$\dot{q}_{\text{hot}} = \dot{m}_{\text{hot}} \left[i\left(T_1, P_1\right) - i\left(T_2, P_2\right) \right]$$

$$\dot{q}_{\text{boil}} = \dot{m}_{\text{boil}} \left[i_5 - i\left(T_3, P_3\right) \right] \tag{7.3}$$

$$\dot{q}_{\text{TS}} = \left(\dot{q}_{\text{hot}} + \dot{q}_{\text{boil}} \right) / 2$$

7.3.2 Heat duty model prediction

Heat transfer in the test section was modeled using the same approach and assumptions as the liquid-boiling MCHX model discussed in Section 0, with the following two exceptions: the test section was assumed to be free of fouling build-up and heat transfer in the header regions was accounted for. The two header regions of the test section are shown in Figure 5.8. Ten counterflow segments were added to each end of the heat exchanger model to account for the header heat transfer areas, comprising a length of 22.23 mm at each end. Ten segments were added to account for the changing quality and heat transfer coefficient in the boiling channels, as compared with a single segment in the liquid-liquid test section model. The hot-

loop flow was maintained at a relatively large flow rate of 0.650 kg s^{-1} for all liquid-boiling tests. As a result, the temperature change in the hot-loop fluid in the header regions was small, minimizing the error in treating these regions as in counterflow instead of the more representative cross-flow orientation used to model these regions in liquid-liquid experiments (Section 5.4.2). The resistance network in the headers is the same as the active channel region shown in Figure 4.5, except that the hot-sheet does not include fins due to the absence of microchannel partitions. The heat transfer coefficients in header regions were calculated in the same manner as in the liquid-liquid experiments. One-hundred control volume segments were used to model test section, with eighty segments for the active channel length ($l_{seg,ch}$ = 2.54 mm) and twenty segments for the two header regions ($l_{seg,header}$ = 2.22 mm). The heat transfer correlations used in specific heat transfer regimes were varied and are discussed later in this chapter. Appendix C shows a sample segment calculation where the boiling loop is in the saturated-boiling heat transfer regime.

7.3.3 Pressure drop model prediction

The differential pressure across the test section in the boiling loop was measured with pressure taps directly in test-section headers, as shown in Figure 7.3. This eliminated the need to estimate many of the frictional and minor losses between the pressure taps in the liquid-liquid experiments (Figure 5.9), increasing the percentage of the measured pressure drop occurring in the channels. Because of the relatively large header cross-sectional area and low boiling-loop flow rate, the pressure was assumed to be equal throughout the inlet and outlet headers. In the flow path model used for liquid-liquid test-section data, a uniform flow distribution was observed due to the nearly constant pressures in both headers. Therefore, a uniform flow distribution was assumed between all boiling-loop channels. The predicted

pressure drop was calculated by summing the pressure changes from the contraction into the channels, friction, and acceleration in the channels, and the sudden expansion into the outlet header. The acceleration component of the channel pressure drop was calculated using Eq. (7.4). The boiling-loop quality at the outlet of the test section (state 5) was determined from the measured pressure and enthalpy. By using the experiment outlet quality, the acceleration portion of the pressure drop was decoupled from the heat transfer model. The void fraction was calculated using the correlation of Baroczy (1963), shown in Eq. (7.5). This correlation was selected because the void fraction approaches one as the quality approaches one, unlike the microchannel void faction correlations shown in Figure 3.1. The frictional pressure drop was calculated by summing the frictional pressure drop along each segment in the heat transfer model. Adiabatic lengths of the channels at both ends of the active channel regions were also accounted for (l_{inactive} = 0.0127 m). The pressure changes due to the contraction into the channels and expansion out of channels were calculated using the equations in Table 7.3. The larger area, A_{la}, is the cross-sectional area of the header (2.129×10^{-3} m^2) and the smaller area, A_{sm}, is the total cross-sectional area of the channels (0.266×10^{-3} m^2). The inlet contraction has negligible impact on the pressure due to the low velocity of the liquid (tens of Pa). The sudden expansion results in a pressure gain and has a slightly larger impact due to the higher-velocity, two-phase conditions at the outlet (hundreds of Pa). However, both were small in comparison to acceleration and frictional pressure drop in the channels (tens of kPa).

$$\Delta P_{\text{a}} = G_{\text{ch}}^2 \left(\left[\frac{x^2}{\alpha \rho_{\text{v}}} + \frac{\left(1-x^2\right)}{\left(1-\alpha\right)\rho_{\text{l}}} \right]_{\text{out}} - \left[\frac{1}{\rho_{\text{l}}} \right]_{\text{in}} \right) \tag{7.4}$$

$$\alpha = \frac{1}{1+\left(\frac{1-x}{x}\right)^{0.74}\left(\frac{\rho_{\text{v}}}{\rho_{\text{l}}}\right)^{0.65}\left(\frac{\mu_{\text{l}}}{\mu_{\text{v}}}\right)^{0.13}} \tag{7.5}$$

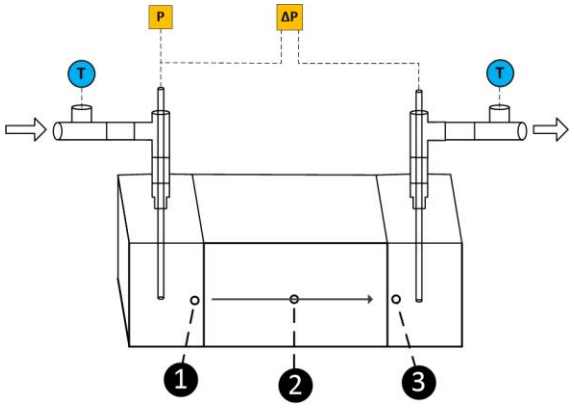

1	Contraction into channels	3	Expansion out of channels
2	Channel friction and acceleration		

Figure 7.3: Boiling-side pressure losses

It is worth noting that the heat transfer and pressure drop models are strongly coupled as the frictional pressure drop is dependent on the quality and the saturation temperature is a function of the pressure. However, the saturation temperature does not vary significantly from inlet to outlet for the experimental conditions in this investigation. As a result, the impact of the predicted heat duty on the predicted pressure drop is greater than the effect of the pressure drop on the heat duty. Therefore, efforts were first made to validate the heat transfer model before analyzing the agreement between the measured and model predicted pressure drop.

Table 7.3: Boiling-loop minor loss calculations

Pressure loss	Equation	Reference
Sudden contraction (single-phase)	$C_c = 1 - \frac{1 - A_{sm}/A_{la}}{2.08\left(1 - A_{sm}/A_{la}\right) + 0.5371}$ $\Delta P_{con} = \frac{G_{ch}^2}{2\rho}\left[\left(\frac{1}{C_c} - 1\right)^2 + \left(1 - \left(\frac{A_{sm}}{A_{la}}\right)^2\right)\right]$ sm = smaller area (channel cross-sections) la = larger area (header cross-section)	Ghiaasiaan (2017)
Sudden expansion (two-phase)	$\phi_{lo,exp} = 1 + x\left(\frac{\rho_l}{\rho_v} - 1\right)\left(0.25x\left(1 - x\right) + x^2\right)$ $\Delta P_{exp} = \frac{G_{ch}^2}{\rho_l}\left(\frac{A_{sm}}{A_{la}}\right)\left[\left(\frac{A_{sm}}{A_{la}}\right) - 1\right]\phi_{lo,exp}$	Hewitt *et al.* (1994)

7.4 Test Matrix

A series of tests was designed to isolate trends in specific heat transfer regimes. These tests were used to compare correlations in specific regimes. A larger general dataset in which multiple heat transfer regimes are present was then used to compare the model predictions with the measured heat transfer and pressure drop. Throughout all liquid-boiling experiments, the hot loop was maintained at a flow rate of 0.650 kg s^{-1} (G_{hot} = 2450 kg m^{-2} s^{-1} and $Re_{hot} \approx$ 12,200) and a test section inlet pressure of approximately 1800 kPa. The boiling-loop inlet pressure, the boiling-loop inlet temperature, the boiling-loop flow rate, and the hot-loop inlet temperature were varied between data points. The boiling-loop flow rate is reported as the evenly distributed mass flux, G_{boil}. The inlet temperatures of both the hot loop and boiling loop are reported in reference to the boiling-loop saturation temperature at the boiling-loop inlet pressure. In the hot loop, the inlet temperature is reported as the degree of superheat above the boiling-loop saturation temperature, $\Delta T_{sup} = T_{hot,in} - T_{sat}\left(P_{boil,in}\right)$, and boiling-loop inlet temperature is reported as the degree of subcooling below the saturation temperature, $\Delta T_{sub} = T_{sat}\left(P_{boil,in}\right) - T_{boil,in}$. As stated in Section 3.2.1, the liquid-boiling tests are performed at lower temperature and pressure than the I^2S-LWR MCHX design, due to the limits of the test facility. A comparison of approximate fluid properties and dimensionless numbers at representative conditions is available in Table 3.1.

7.4.1 Regime specific tests

1) Subcooled boiling:

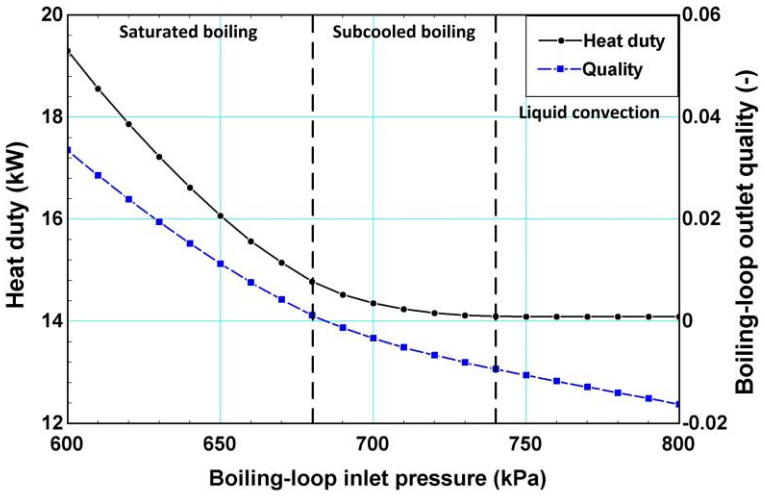

Figure 7.4: Predicted subcooled boiling dataset results

Tests in which the boiling-loop outlet quality was near zero were conducted to provide insights into the heat transfer contribution from subcooled boiling. The flow rates and test-section inlet temperatures of the boiling loop and hot loop were held constant while the boiling-loop inlet pressure was decreased, causing boiling to occur toward the exit of the test section. The subooled-boiling dataset consists of the following conditions: $P_{boil,in}$ = 800 – 600 kPa, G_{boil} = 375 kg s^{-1} ($\dot{m}_{boil}$ = 0.100 kg s^{-1}), ΔT_{sup} = 0 – 11°C ($T_{hot,\,in}$ = 170°C), and ΔT_{sub} = 29 – 40°C ($T_{boil,\,in}$ = 130°C). Figure 7.4 shows the predicted outlet quality and heat duty from the dataset when using the subcooled-boiling heat transfer correlation of Haynes and Fletcher (2003). The predicted heat transfer regime at the outlet of the test section is also displayed. At a higher boiling-loop inlet pressure, the heat duty remains constant because the boiling loop remains a liquid over the entire length of the MCHX. As the pressure is decreased, subcooled boiling and then saturated boiling occur over a portion of the MCHX length, increasing the heat duty.

2) Saturated boiling

Experiments were conducted in which the major portion of the MCHX channel length was in the saturated-boiling heat transfer regime. This was accomplished by limiting the degree of subcooling, ΔT_{sub}, at the inlet of the test section. In addition, the quality at the outlet of the test section was sufficiently low that dryout was not observed. This dataset was used to compare different saturated-boiling heat transfer correlations and two-phase pressure drop correlations. The saturated-boiling dataset consists of the following conditions: $P_{boil,in}$ = 400 kPa, G_{boil} = 185 kg m^{-2} s^{-1} ($\dot{m}_{boil}$ = 0.050 kg s^{-1}), ΔT_{sup} = 10 – 34°C ($T_{hot,\ in}$ = 154 – 178°C), and ΔT_{sub} = 5°C ($T_{boil,\ in}$ = 139°C).

3) Dryout:

It was not possible to analyze the post-dryout heat transfer regime because of the limited length of the test section and preceding subcooled-boiling and saturated-boiling regimes. However, the conditions at which dryout incipience occurred could be investigated. In the dryout dataset, the boiling-loop inlet pressure, inlet temperature, and mass flux were held constant. The hot-loop inlet temperature (ΔT_{sup}) was increased between data points to

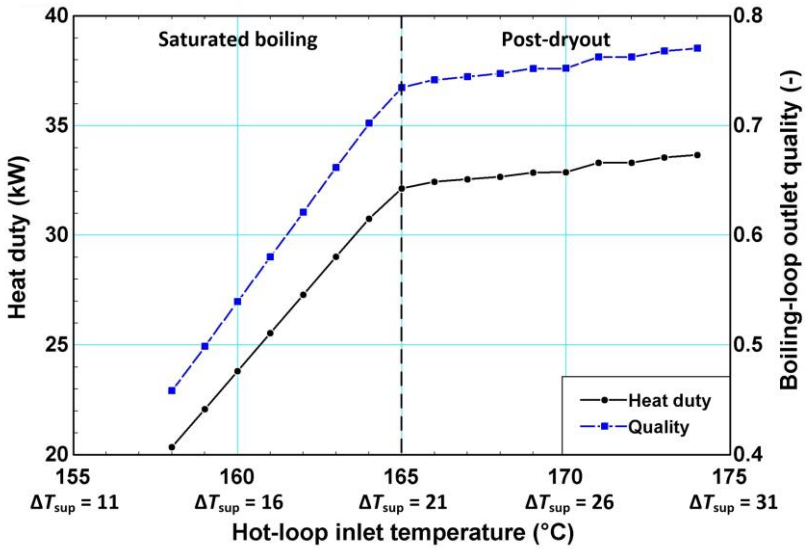

Figure 7.5: Predicted dryout dataset results

increase the heat duty, increase the outlet quality, and produce dryout conditions. A low boiling-side mass flux and low degree of inlet subcooling (ΔT_{sub}) were selected to ensure that a high outlet quality could be achieved in the relatively short test section. The dryout dataset consists of the following conditions: $P_{boil,in}$ = 400 kPa, G_{boil} = 75 kg s^{-1} ($\dot{m}_{boil}$ = 0.020 kg s^{-1}), ΔT_{sup} = 14 – 26°C ($T_{hot,in}$ = 158 – 170°C), and ΔT_{sub} = 10°C ($T_{boil,\ in}$ = 134°C). Figure 7.5 shows the predicted heat duty and outlet quality for this dataset using the dryout incipience correlation of Kim and Mudawar (2013b) and the saturated-boiling correlation of Bertsch *et al.* (2009). After dryout conditions are reached in the test section, further increases in hot-side temperature results in a limited increase in the heat duty due to the inefficient post-dryout heat transfer regime. Thus, this dataset allows the approximate dryout quality to be determined.

7.4.2 Overall dataset

A larger overall dataset of 223 data points was collected to compare the model predicted heat transfer and pressure drop with the experimentally measured values. Eighteen test runs were conducted at one of three boiling-loop inlet pressures: 400 kPa, 500 kPa, and 600 kPa. In each of the test runs, the boiling-loop flow rate (G_{boil}), boiling-loop inlet temperature (ΔT_{sub}), or hot-loop inlet temperature (ΔT_{sup}) were varied while the other two parameters were held constant. A summary of the approximate test conditions is shown in Table 7.4 and actual experimental conditions are shown graphically in Figure 7.6. The lower right-hand graph in Figure 7.6 shows the outlet quality of data points as a function of the mass flux. Larger mass flux data points generally had lower outlet qualities due to the large latent heat capacity of water. In contrast, higher outlet qualities were achieved at lower mass fluxes. The bottom left-hand graph of Figure 7.6 shows the measured heat duty versus the mass flux. It can be observed that the heat duty of low-mass flux data ($G_{boil} \approx$ 75 kg m^{-2} s^{-1}) did not exceed

50 kW due to reduced heat transfer as dryout conditions occurred. The test conditions for the overall dataset were selected to be representative of the multiple heat transfer regimes that would be encountered in the I^{2}S-LWR MCHX. However, due to the shorter length of the test section, no data points included the vapor convection regime and post-dryout heat transfer regime was only predicted to occur in the low mass flux data (20 data points).

Table 7.4: Liquid-boiling overall dataset test conditions

Parameters			**Number of data points**		
G_{boil} (kg m^{-2} s^{-1})	ΔT_{sub} (°C)	ΔT_{sup} (°C)	**Boiling-loop inlet pressure (kPa)**		
			400	**500**	**600**
75 – 375	20	20	22	9	9
265	5 – 30	30	12	11	12
375	20	10 – 30	13	12[*]	10
265	20	10 – 30	13	12	9
150	20	10 – 30	18	11	9
75	10	10 – 30	11	11	9[†]

[*] ΔT_{sub} = 25°C
[†] ΔT_{sub} = 20°C

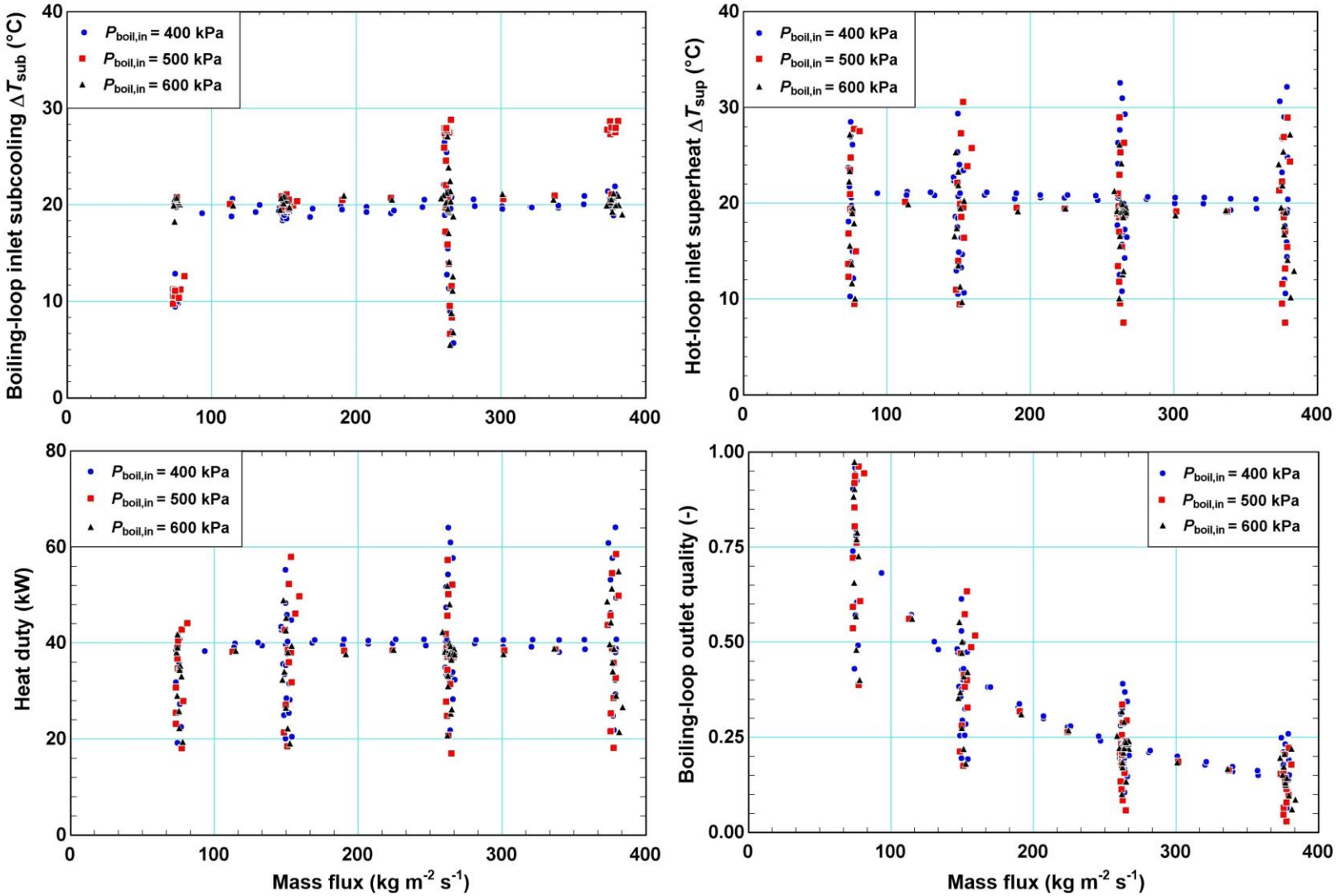

Figure 7.6: Liquid-boiling overall dataset test conditions

7.5 Results and Discussion

Before substantial analysis of the data was conducted, instrument measurements were first verified by comparing the two heat duties calculated from the enthalpy change in the hot loop and the boiling loop. Figure 7.7 shows the agreement between hot loop and boiling loop heat duties for all measured data. The two heat duties have an AAD of 1.493% when the hot-side heat duty is treated as the measured value in Eq. (3.15) and all data points had heat duties within 4.5% of each other. In the remainder of this chapter, the reported test-section heat duty is the average of the hot- and cold-loop heat duties. Heat losses to the surroundings from the test section as well as between the test section and condenser on the boiling loop were ignored. This assumption is supported by the good agreement between the two calculated heat duties. Furthermore, analysis of heat loss between the test section and condenser in the boiling loop showed losses on the order of tens of watts (Appendix C). Losses to the surroundings were therefore considered negligible compared with the test section heat duty, which was measured in the tens of kilowatts. The boiling-loop flow rates were observed to be constant during experimentation and it was therefore concluded that flow oscillations did not influence the overall flow rate. Parallel channel instabilities could not be detected in this experiment, but these do not appear to have had a substantial negatively impact on the heat transfer performance if they were present. Liquid-boiling tests were initially attempted using the liquid-liquid facility discussed in Chapter 5. When boiling started to occur in the cold loop, which contained a centrifugal pump, high-frequency flow rate oscillations were observed.

Regime-specific tests were first analyzed to determine the accuracy of the different correlations. In these tests, the measured heat duties and/or pressure drops were compared

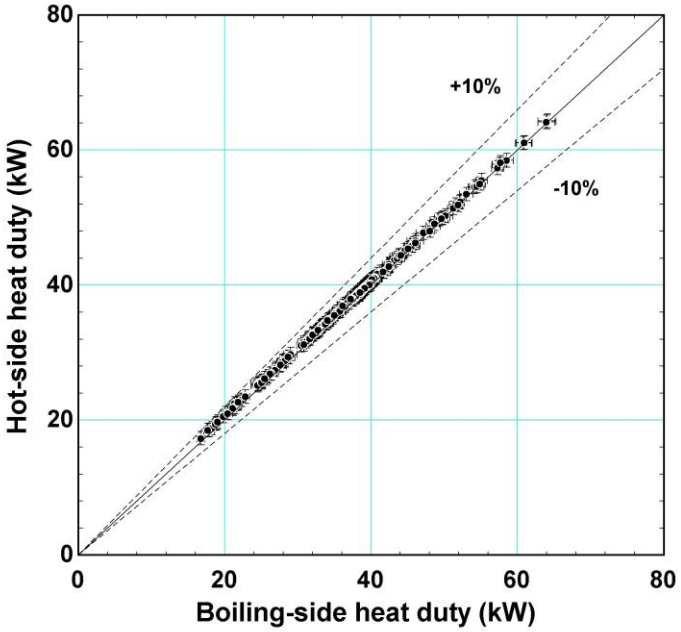

Figure 7.7: Hot-side and boiling-side heat duty

with model predicted values, using several different correlations. While these tests were designed to investigate specific heat transfer regimes, other regimes were inevitably present over some length of the MCHX channel. Correlations and transition criteria presented in Table 6.2 were used in these regimes unless otherwise stated. The most accurate of the tested correlations were selected and used to compare measured values and model predictions using the overall dataset. These were also used to model the I^2S-LWR liquid-boiling MCHX, discussed in Chapter 6.

7.5.1 Subcooled boiling dataset

The measured boiling-loop outlet quality for these tests ranged from $-0.0172 - 0.0603$. A comparison of the measured and predicted heat duties for the subcooled-boiling dataset is shown in Figure 7.8. The average heat flux on the boiling-side of the MCHX is also shown and is calculated by dividing the heat duty by the boiling-side heat transfer area, 0.3055 m^2.

The predicted heat duties were calculated using each of the subcooled boiling correlations presented in Figure 3.6. At high inlet pressures, the boiling loop remained in the liquid-convection regime over the entire length of the MCHX and the predicted and measured heat duties were in good agreement. The boiling-channel Reynolds number for this data set (Re_{lo} ≈ 2000) was in the intermediate Reynolds number range, discussed in Section 5.4, which roughly corresponds to the transition from laminar to turbulent flow. In liquid-liquid experiments, the measured Nusselt number in this range was found to be larger than values predicted by the Churchill (1977a) correlation. As a result, the measured heat duty was slightly larger than the model prediction. As the pressure was decreased, the measured heat duty

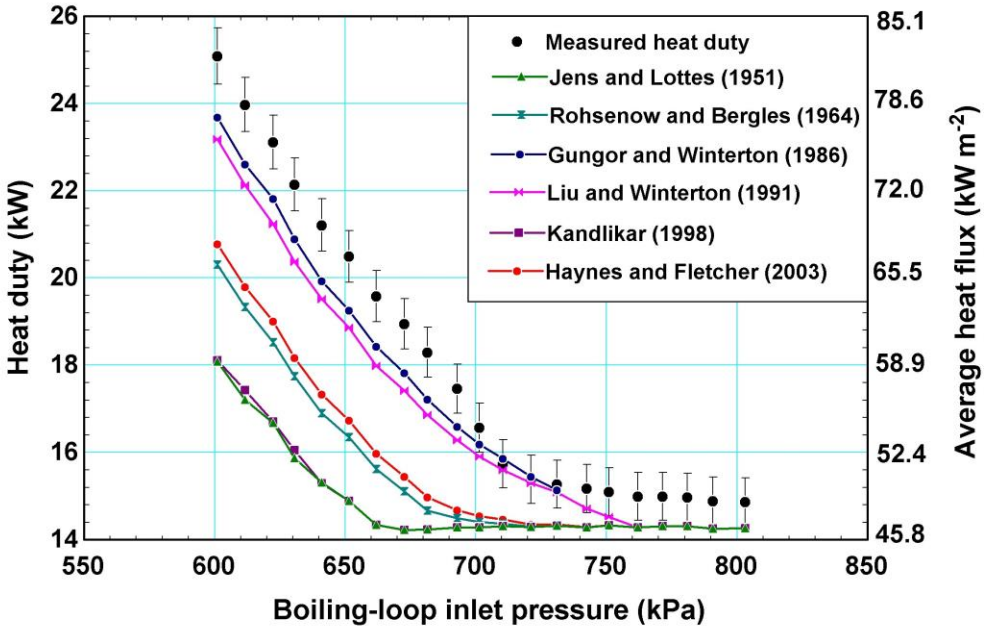

Figure 7.8: Subcooled boiling dataset results

Table 7.5: Subcooled boiling dataset heat duty AAD

Subcooled boiling correlation	Notes	AAD (%)
Jens and Lottes (1951)	fully-developed subcooled boiling	15.66
Rohsenow and Bergles (1964)	partial subcooled boiling	12.58
Gungor and Winterton (1986)	subcooled and saturated boiling	4.314
Liu and Winterton (1991)	subcooled and saturated boiling	5.413
Kandlikar (1998)	fully-developed subcooled boiling	15.57
Haynes and Fletcher (2003)	subcooled and saturated boiling	11.63

increased significantly as subcooled boiling and then saturated boiling occurred along the boiling channel length. The correlations developed by Jens and Lottes (1951) and Kandlikar (1998) both significantly underpredicted the heat duty. These fully-developed subcooled-boiling correlations did not include contributions from liquid convection and both predicted heat transfer coefficients were lower than the single-phase Churchill (1977a) correlation over much of the subcooled boiling length. The onset of significant void (OSV) was predicted by the correlation of Saha and Zuber (1974) and was found to occur at a quality of approximately zero for conditions in this study. The OSV has been used to separate partial boiling from fully-developed nucleate boiling, where forced convection no longer contributes significantly to heat transfer. Therefore, it appears that both forced liquid convection and nucleate boiling are significant, and partial boiling occurs until saturation for the conditions in this study. The correlations of Haynes and Fletcher (2003) and Rohsenow and Bergles (1964) included contributions from both forced liquid convection and nucleate boiling but also underpredicted the heat duty, although to a lesser extent than the two fully-developed subcooled-boiling correlations. The correlations of Liu and Winterton (1991) and Gungor and Winterton (1986) provided the best agreement with AADs of 5.41% and 4.31%, respectively. This is in part due to the turbulent Dittus and Boelter (1930) correlation used by these authors to calculate the forced convection heat transfer coefficient. As a result, theses correlations predicted a larger forced-convection contribution than the other correlations investigated, as can be seen in the highly subcooled region of Figure 3.6. Rohsenow and Bergles (1964) suggested that the onset of nucleate boiling (ONB) may disrupt laminar and transition flows, increasing turbulence and heat transfer. This phenomenon may account for the large increase in the measured heat transfer duty of this dataset following ONB and contribute to the success of these two

correlations. Table 7.5 shows the AAD for the different correlations applied to the subcooled-boiling dataset.

7.5.2 Saturated boiling dataset

Measured boiling-loop outlet qualities for these tests were between $0.161 - 0.548$, and the mass flux was similar to that of the liquid-boiling MCHX design (G_{boil} = 230.9 kg m^{-2} s^{-1}). A comparison of the measured and predicted heat duties for the saturated-boiling dataset is shown in Figure 7.9. The predicted heat duty was calculated using each of the saturated-boiling correlations shown in Table 3.5. The measured heat duty was generally higher than model predictions. At higher hot-loop inlet temperatures and larger heat duties, better agreement was achieved with several of the correlations. There are several possible causes for the underprediction of the heat duty. At lower values of ΔT_{sup}, the heat flux in the test section is substantially lower, increasing the importance of convective boiling. This suggests that these correlations underpredicted the convective-boiling contribution to the heat transfer coefficient at low quality. This would also explain the improved accuracy of several of the correlations at higher heat fluxes (higher ΔT_{sup}), where nucleate boiling becomes more prominent. Harirchian and Garimella (2010) suggested that low-quality confined flows may have enhanced heat transfer due to convective boiling in the thin liquid layer surrounding the bubble. However, the conditions in this study did not meet the criteria for bubble confinement stated by them, Eq. (3.18). The semi-circular shape of the channels in this investigation may also influence heat transfer characteristics in the channels. Finally, the correlation of Gungor and Winterton (1986), used in the subcooled-boiling regime, was shown to underpredict heat transfer in the previous section. However, the boiling-loop test-section inlet temperature was five degrees Celsius below the saturation temperature in this dataset, which led to a relatively

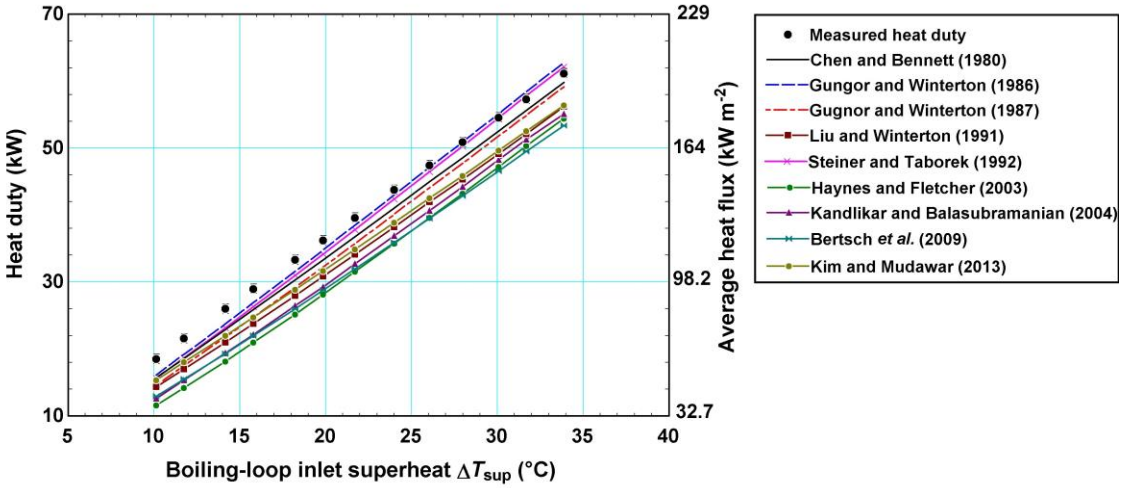

Figure 7.9: Saturated boiling dataset heat transfer results

Table 7.6: Saturated boiling dataset heat duty AAD

Saturated boiling correlation	Notes	AAD (%)
Chen and Bennett (1980)	macrochannel	7.776
Gungor and Winterton (1986)	macrochannel	4.578
Gungor and Winterton (1987)	macrochannel	10.59
Liu and Winterton (1991)	macrochannel	14.58
Steiner and Taborek (1992)	macrochannel	5.813
Haynes and Fletcher (2003)	microchannel	21.82
Kandlikar and Balasubramanian (2004)	microchannel	18.16
Bertsch *et al.* (2009)	microchannel	20.18
Kim and Mudawar (2013d)	microchannel	12.18

short distance before the fluid reached saturation (roughly accounting for between 6% and 12% of the active channel length). Therefore, the underestimation of heat transfer in the subcooled-boiling regime had minimal effects on the overall predicted heat duty. Determining a specific cause for this trend is not possible with the data collected in this investigation. Experiments specifically designed to measure the heat transfer coefficient over a small quality change and with known heat flux would provide more clarity. The generally larger-than-predicted heat duties suggest that there are no significant negative heat transfer effects from maldistribution, flow instabilities, and/or localized dryout due to bubble confinement. Table 7.6 shows the AAD for the different saturated boiling correlations applied to the saturated

boiling dataset. It is worth noting that the correlations developed using datasets from larger channels generally performed better that those developed specifically for mini/microchannels. The correlation of Gungor and Winterton (1986) gave the best agreement with an AAD of 4.58%. This Chen-type correlation uses the the Cooper (1984) correlation as a basis for the nucleate boiling contribution and Dittus and Boelter (1930) for the convective boiling contribution. A large database from 30 sources was used by Gungor and Winterton (1986) to develop the correlations, although no channels with hydraulic diameters less than 2.95 mm were included in the database.

A comparison of the measured and predicted pressure drop for the saturated boiling dataset is shown in Figure 7.9. The uncertainty in the measured pressure drop is small (70 Pa) and error bars cannot be shown on the graph. The predicted pressure drop was calculated using each of the two-phase correlations shown in Table 3.4. The pressure drop model includes contributions from friction and acceleration in the channels as well as the contraction and expansion in and out of the headers. The relative proportions of these pressure changes varied between data points. However, the frictional pressure drop accounted for approximately 80% of the pressure drop while acceleration accounted for nearly 20%. The combined effects of the expansion and contraction resulted in a slight pressure gain in the range of 200 Pa. The best agreement between the measured and predicted pressure drop occurred when using the homogeneous equilibrium model (HEM) and the two-phase viscosity of McAdams *et al.* (1942), resulting in an AAD of 6.19%. When using the HEM, the two-phase viscosity allows a two-phase Reynolds number to be calculated. A single-phase friction factor correlation and the homogenous density are then used to calculate the two-phase pressure gradient, as shown in Table 3.4. The Churchill (1977b) correlation was used to

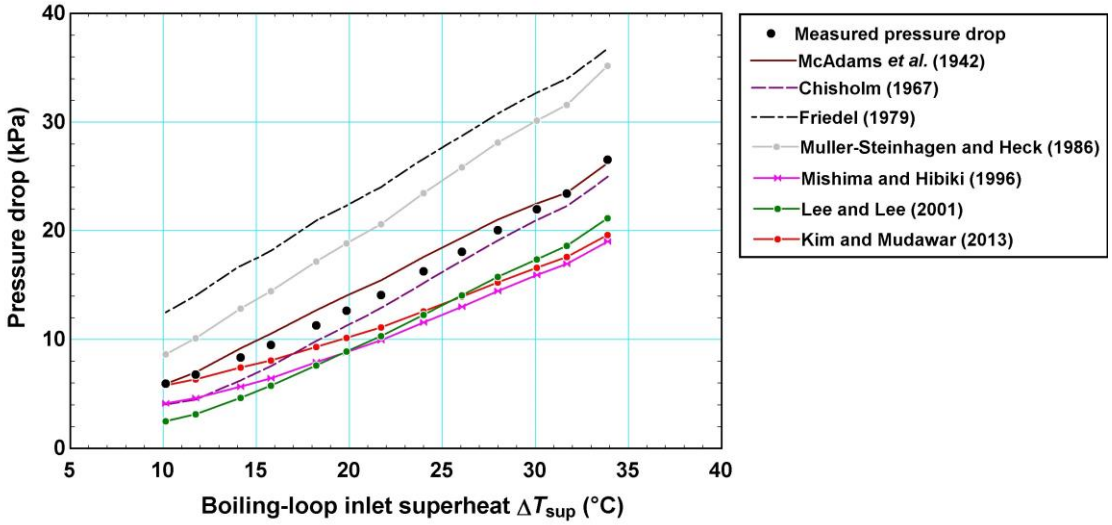

Figure 7.10: Saturated boiling dataset pressure drop results

Table 7.7: Saturated boiling dataset pressure drop AAD

Saturated boiling correlation	Notes	AAD
McAdams *et al.* (1942)	homogeneous equilibrium model	6.194
Chisholm (1967)	macrochannel	13.54
Friedel (1979)	macrochannel	72.84
Müller-Steinhagen and Heck (1986)	macrochannel	44.39
Mishima and Hibiki (1996)	microchannel	29.63
Lee and Lee (2001)	rectangular microchannel	31.86
Kim and Mudawar (2013)	boiling microchannel	18.36

calculate the two-phase friction factor because of its accuracy in single-phase experiments. Ghiaasiaan (2017) noted that several experimental studies have supported the use of the HEM for microchannel frictional pressure drop calculations (Lin *et al.*, 1991; Ungar and Cornwell, 1992; Bao *et al.*, 1994; Triplett *et al.*, 1999). Ungar and Cornwell (1992) and Triplett *et al.* (1999) both recommend using the McAdams *et al.* (1942) two-phase viscosity and Lin *et al.* (1991) used the Churchill (1977b) correlation to calculate the two-phase friction factor. Table 7.7 shows the AAD for the different pressure drop correlations applied to the saturated boiling dataset. The three correlations developed specifically for mini/microchannel underpredicted

the pressure drop. This includes the correlation of Kim and Mudawar (2013d), which was developed using a microchannel boiling database.

7.5.3 Dryout dataset

Dryout testing resulted in experimental outlet qualities between $0.582 - 0.945$. The correlation of Dougall and Rohsenow (1963) was used to determine the heat transfer coefficient in the post-dryout heat transfer regime. Because of the low mass flux in this dataset, the predicted post-dryout and vapor convection heat transfer coefficients were relatively low (~ 700 W m^{-2} K^{-1}). Therefore, little heat transfer was predicted to occur following dryout. Predicted heat duties for this dataset using the dryout incipience correlations of Mastrullo *et al.* (2012) and Kim and Mudawar (2013b) are shown in Figure 7.11. The Mastrullo *et al.* (2012) correlation ($x_{di} \approx 0.98$) predicted dryout to start at a much higher quality than Kim and Mudawar (2013b) ($x_{di} \approx 0.70$). As a result, the predicted heat duty when using the Kim and Mudawar (2013b) correlation stopped increasing around 34 kW, while the heat duty predicted by Mastrullo *et al.* (2012) increased until the boiling-loop outlet was in the saturated vapor state. The measured heat duty, shown in Figure 7.11, continued to increase as the hot-loop inlet temperature increased but was lower than the model predicted heat-duty had dryout not occurred, as shown by the Mastrullo *et al.* (2012). A partial-dryout heat transfer regime may be present in which only a portion of the tube remains wetted. Wojtan *et al.* (2005) suggests using a linear interpolation between the saturated boiling and liquid-deficeint (post-dryout) heat transfer coefficient in this regime. However, this method requires accurate estimates for when dryout is intiated, $x_{di,}$ and when total dryout occurs, x_{de}. Another possible explanation is that the heat transfer coefficient at high quality is significantly lower than that predicted by Gungor and Winterton (1986). Roach *et al.* (1999) performed CHF experiments

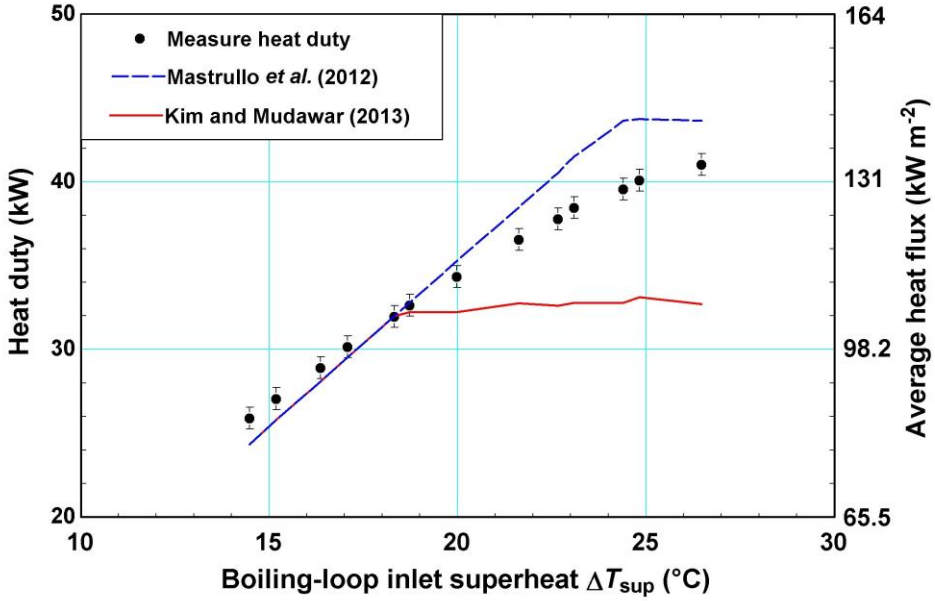

Figure 7.11: Dryout dataset results

Table 7.8: Dryout dataset heat duty AAD

Dryout incipience correlation	Notes	AAD
Mastrullo *et al.* (2012)	microchannel, R410A/Carbon dioxide	5.189
Kim and Mudawar (2013b)	microchannel, many fluids	11.17

using a single, heated microchannel and water at pressures similar to those in this investigation. In some of their data, the wall temperature was found to slowly increase following CHC/dryout conditions, indicating a smooth transition between the saturated boiling and liquid-deficient (post-dryout) heat transfer coefficient. However, it should be noted that this phenomenon was only observed at high mass flux (> 502 kg m^{-2} s^{-1}) where the liquid-deficient heat transfer coefficient was relatively large. Because both the location of dryout incipience and the post-dryout heat tranfer coefficient are unclear, a conservative estimate was used for the liquid-boiling I^2S-LWR MCHX model. Dryout incipience was estimated using the Kim and Mudawar (2013b) correlation and the post-dryout heat transfer coefficient was calcauted using the correlation of Dougall and Rohsenow (1963). The

measured boiling-loop outlet temperature was within 0.25°C of the saturation temperature at the outlet pressure for all data points in this dataset. The uncertainty of the calibrated thermocouples in the test facility was ±0.25°C, indicating that non-equilibrium in the post-dryout regime was not significant. The predicted post-dryout length of the I^2S-LWR liquid-boiling MCHX did not have a large negative impact on the design, accounting for 0.11 m or 22% of the active channel length. Improved heat transfer in this regime, as suggested by this dataset, would allow an increase in the secondary coolant pressure, increasing the thermal efficiency of the coupled power cycle.

7.5.4 Overall dataset

The overall dataset was analyzed using the correlations and transition criteria in Table 6.2. These heat transfer/pressure drop correlations and transition criteria were selected based

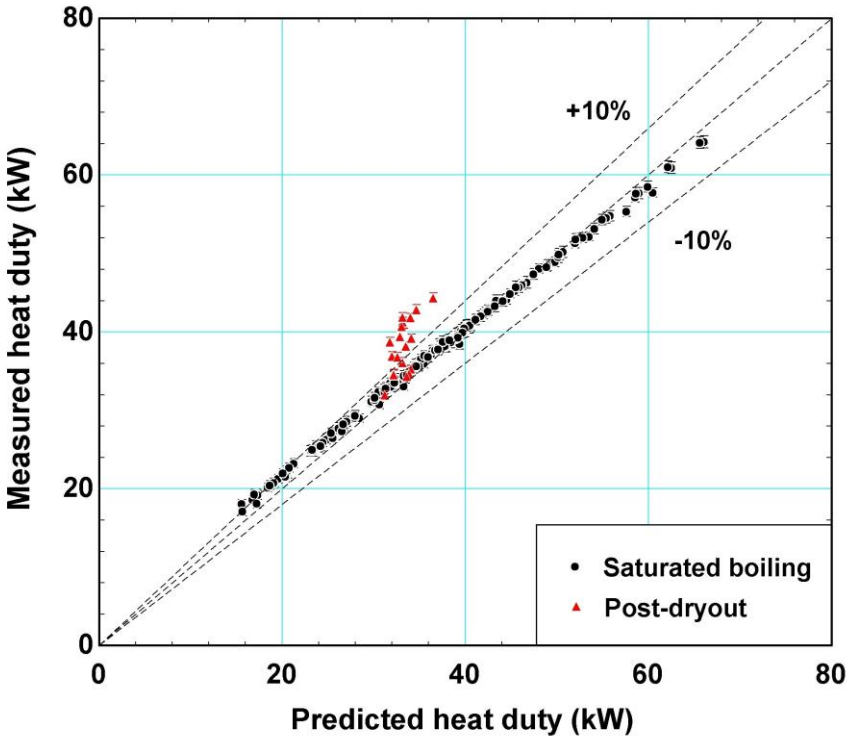

Figure 7.12: Overall data set measured versus predicted heat duty

on the measurements and discussion of the regime-specific datasets above. Figure 7.12 shows the measured versus predicted heat duty for the general dataset. The data are sorted by predicted boiling-side outlet heat transfer regime: saturated boiling or post-dryout. Saturated boiling data had excellent agreement between the measured and predicted heat duty with an AAD of 2.980%. All saturated data points were within 14% of model predictions. This suggests that the heat transfer model is accurate in the subcooled boiling and saturated boiling regimes. Post-dryout data had measured heat duties larger than the model predictions with an AD and AAD of 12.38%. This is a result of the conservative dryout incipience quality and post-dryout heat tranfer coefficient used in the model. The same trend was observed in the dryout dataset when using these correlations.

Figure 7.13 shows the measured versus predicted pressure drop for the overall dataset. The measured pressure drop showed good agreement with the predicted pressure drop, with

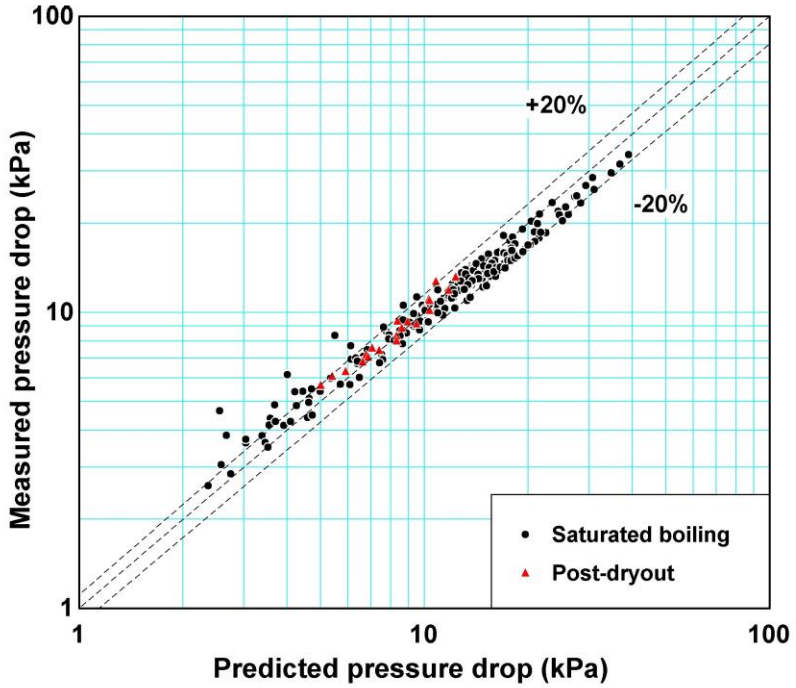

Figure 7.13: Overall data set measured versus predicted pressure drop

an AAD of 9.596%. Somewhat surprisingly, the post-dryout pressure drop data (AAD 5.58%) had better agreement than the saturated boiling data (AAD 9.99%). Due to the conservative heat transfer calculations in the post-dryout heat transfer regime, the predicted quality in this model was reduced in the post-dryout regime. This should lead to an underprediction of the pressure drop in this range because the frictional pressure gradient increases with quality. The frictional pressure-drop correlations of Chisholm (1967) and Kim and Mudawar (2013d) were also used to predict the frictional pressure gradient in the general dataset. However, these did not provide better agreement with the measured pressure drops and had AADs of 21.59% and 20.91%, respectively. The channel pressure drop in the liquid-boiling I^2S-LWR MCHX only constitutes a small fraction of the total pressure drop and is significantly smaller than that in the liquid-liquid MCHX design. Therefore, uncertainty in the secondary coolant channel pressure drop on the order observed here will not significantly influence the liquid-boiling I^2S-LWR MCHX design.

CHAPTER 8. CONCLUSIONS AND RECOMMENDATIONS

8.1 Summary and Conclusions

Steam generators represent the largest components in the reactor cooling system (RCS) of a pressurized water reactor (PWR) and are each individually larger than the reactor pressure vessel (RPV). This study investigated the use of a set of compact microchannel heat exchangers (MCHXs) placed inside the RPV in the downcomer region of a PWR to replace the much larger, external steam generators currently used in PWR designs. In the I^2S-LWR design, the entire RCS (primary coolant loop), which also includes coolant pumps and the pressurizer, is placed within the RPV. In this configuration, there are no large diameter pipes between the external steam generators and RPV, eliminating several loss of coolant accident (LOCA) scenarios. Additionally, the reduced primary coolant inventory allows for a smaller containment structure around the reactor, reducing costs, and enabling passive emergency cooling systems. The I^2S-LWR therefore offers both safety and economic advantages over other large PWR designs, while maintaining the economies of scale that exist in the nuclear industry.

Two MCHX design were analyzed in the study. In the liquid-liquid MCHX design, both the primary and secondary coolant remain subcooled over the length of the heat exchanger. A novel Flash Rankine cycle in which steam is generated in a flashing drum is coupled with the liquid-liquid MCHX for power generation. In the liquid-boiling design, the secondary coolant exits the MCHX as superheated steam, eliminating the need for a flashing drum. Modeling results showed that both the liquid-liquid and liquid-boiling MCHX designs could meet the unique design requirements of the I^2S-LWR. These included size restrictions

in the downcomer, heat duty requirements (2850 MW_{th}), pressure drop limitations (less than 500 kPa for the primary coolant), mechanical integrity (15 MPa pressure), and thermal efficiency of the accompanying power cycle (greater than 33%). The liquid-boiling MCHX and accompanying Rankine power cycle offer both increased thermal efficiency (η_{th} = 39.03%) and potential economic benefits from the removal of flashing drums and elimination of large secondary coolant pumps. An alternative tube-bundle heat exchanger (TBHX), similar to the tubular steam generators used in existing PWRs, was analyzed as an alternative primary-to-secondary heat exchanger of the I^2S-LWR (Appendix A). The liquid-liquid and liquid-boiling TBHX were also able to meet the unique design requirements of the I^2S-LWR. However, both TBHX designs required a larger temperature differences between coolant streams to meet the 2850 MW_{th} heat duty requirement as compared to the MCHX design. This resulted in lower thermal efficiency and electrical output in the associated power cycles.

Heat transfer in the MCHX was modeled using a 1D resistance network and segmenting the channel length into a finite number of equal-length control volumes. A segmented approach was used to account for changing fluid properties, heat fluxes, and heat transfer regimes along the channel. Partitions between microchannels were treated as adiabatically-tipped fins and an overall fin efficiency was applied to channel surfaces. The pressure drop and flow distribution within the MCHX and accompanying headers was modeled using a parallel flow path technique.

Experiments were performed using a representative MCHX test section to validate modeling methods and assumptions. The test section consists of twenty sheets, each containing thirty channels with dimensions similar to those of the I^2S-LWR MCHX (D_h = 0.8608 mm). Tests in which both fluids remained single-phase liquids were first performed to

simulate the liquid-liquid I^2S-LWR MCHX design. Temperature and pressure limitations of the experimental facility prevented testing at reactor conditions. However, tests were conducted at Reynolds numbers similar to those expected in the liquid-liquid I^2S-LWR MCHX design. Excellent agreement was found between measured and model-predicted heat duty (AAD 1.28%) and pressure drop (AAD 5.57%) for channel Reynolds numbers greater than 4000 (representative of the liquid-liquid I^2S-LWR MCHX operating conditions). Additionally, specific tests were performed to measure the Nusselt number and friction factor within channels. These data were compared with the friction factor and Nusselt number correlations developed by Churchill (1977a,b), which were developed for circular macrochannels. Excellent agreement between the measured and correlation-predicted Nusselt number (AAD 4.29%) and friction factor (AAD 8.53%) was found for Reynolds numbers greater than 4000. Furthermore, it was found that single-phase circular-channel correlations can be accurately be applied to the semi-circular cross-sections of microchannels in the I^2S-LWR MCHX design.

Boiling experiments were performed to assess the accuracy of the liquid-boiling MCHX model. Tests designed to isolate specific heat transfer regimes to determine the most accurate heat transfer and pressure drop correlations were also conducted. In the subcooled boiling tests, the best agreement between the measured and predicted heat duty was found when using the correlation of Gungor and Winterton (1986). The same correlation yielded the best agreement between the measured and predicted duty in saturated boiling tests. In general, macroscale correlations provided better agreement with the data than those developed for microchannels. The potentially adverse effects of flow instabilities, partial dryout due to bubble confinement, and maldistribution did not appear to have significant impact on the test

section heat duty. The measured pressure drop in the saturated boiling dataset was compared with predictions of different two-phase frictional pressure gradient correlations. The homogenous equilibrium model correlation develop by McAdams *et al.* (1942) was found to be the most accurate. A final regime-specific test was used to determine conditions at the onset of dryout. These tests showed that heat transfer rates decreased following the predicted dryout incipience quality of Kim and Mudawar (2013b) but complete dryout did not occur until higher quality. After determining the most accurate correlations in the different heat transfer regimes, predicted heat duties and pressure drops were compared with a larger overall dataset. This dataset contained 223 data points with a range of boiling-side mass fluxes (G_{boil} = 75 – 375 kg s^{-1}), boiling-side inlet pressures ($P_{boil,in}$ = 400 – 600 kPa), boiling-side inlet temperatures (ΔT_{sub} = 10 – 30°C), and hot-side inlet temperatures (ΔT_{sup} = 5 – 30°C). The measured and predicted heat duties showed good agreement, with an AAD of 2.980% for the pre-dryout data. The pressure drop through the test section was also in good agreement with model predictions (AAD 9.596%).

This investigation focused specifically on an MCHX design for the unique requirements of the I^2S-LWR. However, MCHX are already in use in non-nuclear industries. The size, strength, and thermal efficiency of MCHX steam generators may make them attractive for other reactor designs or in other applications were steam is needed. The methods and conclusions of this investigation can therefore be used as a starting point to assess MCHXs for other applications.

8.2 Recommendations for Future Work

The following section contains suggestions for additional analyses and investigation to further develop the MCHX concept for the I^2S-LWR.

8.2.1 Further thermal-hydraulic testing

Temperature and pressure limitations of the test facility and heat source used in this study prevented testing at I^2S-LWR primary- and secondary-coolant conditions. Liquid-liquid tests were conducted over a range of Reynolds numbers similar to dimensionless conditions expected in liquid-liquid I^2S-LWR MCHX operation. However, the dimensionless numbers that govern two-phase flow and boiling cannot be easily matched at lower temperature and pressure. Differences in dimensionless quantities and two-phase transport properties are shown in Chapter 3. The experiments in this study provide an estimate of the accuracy of the different correlations investigated. Therefore, liquid-boiling tests, similar to those conducted in this study, should be conducted at reactor primary- and secondary-coolant conditions to provide a more conclusive determination of their accuracy for the I^2S-LWR. A longer test section would allow superheated steam at the outlet and provide a more comprehensive view of liquid-boiling MCHX performance. Single-channel tests in which the quality change across the test section is small and the heat flux is known should also be conducted. This would allow the heat transfer and pressure gradient to be measured and provide further clarity into the accuracy of specific correlations.

8.2.2 Maldistribution and flow instabilities

The experimentally measured heat duties were in good agreement with model predictions. It was therefore assumed that maldistribution and/or flow instabilities did not have a significant negative impact on test section performance. However, the compact design

requirements of the I^{2}S-LWR MCHX result in large pressure drops in the headers compared to the pressure drops in the channels, which can lead to maldistribution. The flow path method used in this analysis showed that a uniform flow distribution could likely be achieved, although a more in-depth analysis should be performed. This could be accomplished with a computational fluid dynamics study. However, flow boiling and the large number of channels in MCHX sheets may require significant assumptions and/or simplifications. A test section consisting of a small number of liquid-boiling I^{2}S-LWR MCHX sheets could also be tested to see if maldistribution or flow instability affects performance. Additionally, a cross-flow orientation could be considered for the MCHX sheets in order to limit secondary coolant maldistribution, as discussed in Section 2.2.

8.2.3 Mechanical design

Significant mechanical design work for the I^{2}S-LWR MCHX remains to be completed. The MCHX stack should be designed such that it can be easily removed from the RPV for inspection, maintenance, or replacement. Ideally, the stack itself could be disassembled into individual MCHX blocks and the associated headers. This would allow the inspection and/or replacement of individual MCHX blocks within the stack. The large number of bonded sheets in the MCHX represent possible leak points between the primary and secondary coolants. Extensive quality control and testing should to be performed in order to ensure the quality and consistency of the diffusion bonding process. The ASME boiler and pressure vessel code was used to determine the required sheet and channel dimensions for the MCHX to operate at reactor temperatures and pressures. Pressure vessel analysis of triangular secondary-coolant headers within sheets and secondary-coolant headers in the MCHX stack is still required. Thermal and cycling stresses on the MCHX blocks have also not yet been

considered. However, manufacturers such as Heatric claim robust performance records for their operating MCHXs.

8.2.4 Fouling and channel blockage

Limited fouling and clogging of MCHX were both shown to have a minor effect on the performance of the I^2S-LWR MCHX. Fouling assumptions were based on a brief review of the literature and channel blockage was assumed to be minimal. Fouling can likely be limited by controlling water chemistry, but an in-depth study of particulate matter in PWR primary and secondary coolants should be conducted to assess the likelihood of channel blockage. If a larger number of channels were to be quickly clogged due to particulate matter in either of the fluid streams, the MCHX concept for integral reactor designs would be compromised. If the potential for channel blockage is found to be significant, filtering screens may need to be incorporated in the design of the MCHX stack and/or feedwater system. This could be accomplished adding filtering screens above the MCHX stack in the downcomer and/or before the secondary coolant enters the RPV.

8.2.5 Economic analysis

A cost estimate for a prototype I^2S-LWR MCHX is presented in Appendix B. This shows that the cost of a series of MCHX may be significantly lower than that of the much larger tubular steam generators currently in use. Transportation and replacement of MCHXs would also be much simpler and cheaper. However, these estimates do not include regulatory and quality assurance costs or the cost of building the headers/structural components of the MCHX stack. Therefore, a more detailed economic assessment should be performed to determine the cost benefits of MCHXs.

Appendix A. TUBE-BUNDLE HEAT EXCHANGER

An alternative design for the I^{2}S-LWR primary-to-secondary heat exchanger was investigated to compare the performance of the novel MCHX design with a conventional tubular steam generator used in the nuclear industry. Liquid-liquid and liquid-boiling TBHX designs are outlined in this Appendix. The geometry and flow pattern of the TBHX is discussed in Section 2.4. Heat transfer was modeled in the same manner as discussed in Chapters 4 and 6 and is only discussed briefly here. The same assumptions were made unless otherwise noted.

A.1. Liquid-liquid Tube-Bundle Heat Exchanger

Dimensions of the tube-bundle heat exchanger used for both liquid-liquid and liquid-boiling designs are shown in Table A.1. The shells of the eight TBHXs occupy the same rectangular cross-sectional areas in the downcomer as the MCHX stacks shown in Figure 2.1. These regions are filled with 316 stainless steel tubes arranged in a square lattice. Tubes span the same axial height as the MCHX stack, 6.6 m. A small tube diameter (OD = 8 mm) and pitch-to-diameter ratio (PDR = 1.25) were required to meet heat transfer requirements within the limited volume of the I^{2}S-LWR downcomer. As a result, the TBHX tubes are significantly smaller than those used in other once-through nuclear steam generators. For example, Babcock and Wilcox steam generators tubes have an outer dimeter of 15.875 mm and are distributed at a pitch of 22.225 mm (Steam, 2005). IRIS helical-coil steam generator tubes have an outside dimeter of 17.24 mm and inside dimeter of 14.24 (Cioncolini *et al.*, 2003). The tube thickness is based on the collapsing pressure applied on the outside of the tube by

Table A.1: Tube-bundle heat exchanger dimensions

Parameter	Value
Radial length of shell	0.85 m
Azimuthal width of shell	1.00 m
Tube pitch (square)	10.0 mm
Number of tubes	8500
Tube outside diameter (*OD*)	8.0 mm
Tube inner diameter (*ID*)	6.0 mm
Tube thickness (t_{tube})	1.0 mm
Tube length (active length)	6.6 m
Number of space grids	6
Spacer grid thickness	0.5 mm

the primary coolant and an appropriate safety factor. The heat transfer performance of the TBHX improves as the diameter of the tubes decreases. Similar to the MCHX, smaller tubes result in larger heat transfer coefficients. Additionally, a larger number of tubes can be fit within the shell, increasing the heat transfer area. The thickness required is also lower for smaller dimeter tubes, decreasing conduction resistance. Therefore, heat transfer performance can be further improved in the TBHX by decreasing the tube diameter, although fabrication may become increasingly difficult. The spacer grids are placed roughly 1 m apart in the axial direction and have a thickness equal to half of the distance between tubes (0.5 mm), consistent with spacer grids in Babcock and Wilcox once-through steam generators (Steam, 2005). The six spacer grids provide structural support to the tube array and protect against flow-induced vibrations.

The liquid-liquid TBHX is capable of meeting the design requirements of the I^2S-LWR primary-to-secondary heat exchanger. Important fluid properties and operating parameters of a liquid-liquid TBHX are shown in Table A.2, while values for all eight TBHXs are listed in parenthesis. The temperature profile along the length of the TBHX tubes is shown in Figure A.1. Comparison with the liquid-liquid MCHX in Table 4.1 and Figure 4.3 shows that the TBHX requires a larger temperature difference between the primary and secondary

coolant to achieve the required heat duty (2850 MW_{th}). The log-mean temperature difference in the liquid-liquid MCHX is 15.3°C compared with 28.0°C in the TBHX. This is primarily the result of the significantly smaller heat transfer area of the TBHX (8,456 m^2 compared to 20,064 m^2). It should be noted that the average heat transfer coefficients in the TBHX are larger than those in the MCHX design. This is due to the geometry and orientation of the TBHX, leading to a higher mass flux and average Reynolds numbers than the MCHX design. Examining the secondary coolant, the MCHXs have a cross-sectional heat-transfer flow area of 7.41 m^2 compared with 1.92 m^2 for the TBHXs. This results in a significantly higher mass flux (6,770 kg m^{-2} s^{-1} compared with 1,757 kg m^{-2} s^{-1}), average Reynolds number (436,626 compared with 16,411), and average Nusselt number (793.4 compared with 46.5) for the same overall mass flow rate (13,016 kg s^{-1}). The MCHX channels have a significantly smaller hydraulic diameter (D_h = 0.812 mm) than the TBHX tubes (ID = 6.0 mm), but the heat transfer coefficient of the TBHX is larger due to the larger Nusselt number (76.88 kW m^{-2} K^{-1} compared with 32.18 kW m^{-2} K^{-1}). The secondary coolant outlet temperature is 11.4°C lower than that of the MCHX design for the same secondary-coolant flow rate (13,016 kg s^{-1}), resulting in a lower cycle thermodynamic efficiency of the Flash Rankine cycle. The TBHX design does not require the relatively long and compact headers of the MCHX stack. Much of the pressure drop in the MCHX design is the result of high velocity flow in these regions and the TBHX therefore has significantly lower pressure drop for both coolants. Furthermore, the large pressure gradients within MCHX headers introduce the possibility of maldistribution between channels, although the analysis in this investigation suggests that a uniform flow distribution can be achieved. The relatively short secondary-coolant distribution headers in

the TBHX design (Figure 2.9) ensure that a uniform pressure differential will exist between the inlet and outlet of all tubes, providing a uniform flow distribution. The primary coolant frictional pressure drop was only 287.1 kPa in the TBHX design compared with 472.9 kPa in the MCHX design. The secondary coolant pressure drop through the liquid-liquid TBHX was also much lower than that for the MCHX design, although only the frictional and gravitational pressure changes in the tubes were calculated for the secondary coolant.

Table A.2: Liquid-liquid TBHX operating parameters

Parameter	**Primary coolant**	**Secondary coolant**
$\dot{q}$(MW)	356.25 (2850)	
A (m^2)	1057 (8456) [secondary coolant]	
$\dot{m}$ (kg s^{-1})	1937 (15,498)	1627 (13,016)
G (kg m^{-2} s^{-1})	4583	6770
T_{in} (°C)	330.0	265.4
T_{out} (°C)	298.8	306.8
P_{in} (MPa)	16.30	12.88
P_{out} (MPa)	16.06	12.23
ΔP_{total} (kPa)	242.1	623.4 (tube only)
ΔP_{fr} (kPa)	287.1	568.5 (tube only)
Re_{avg} (-)	436,534	436,626
h_{avg} (kW m^{-2} K^{-1})	61.14	76.88
f_{avg} (-)	0.01452	0.01678

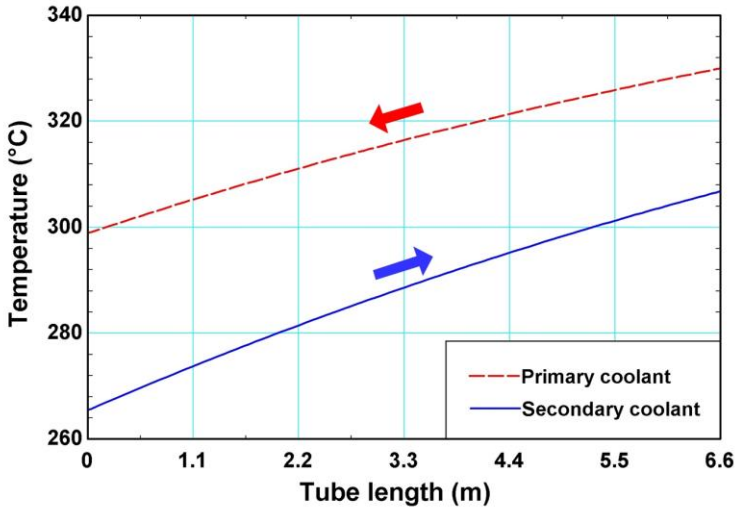

Figure A.1: Liquid-liquid TBHX temperature profile

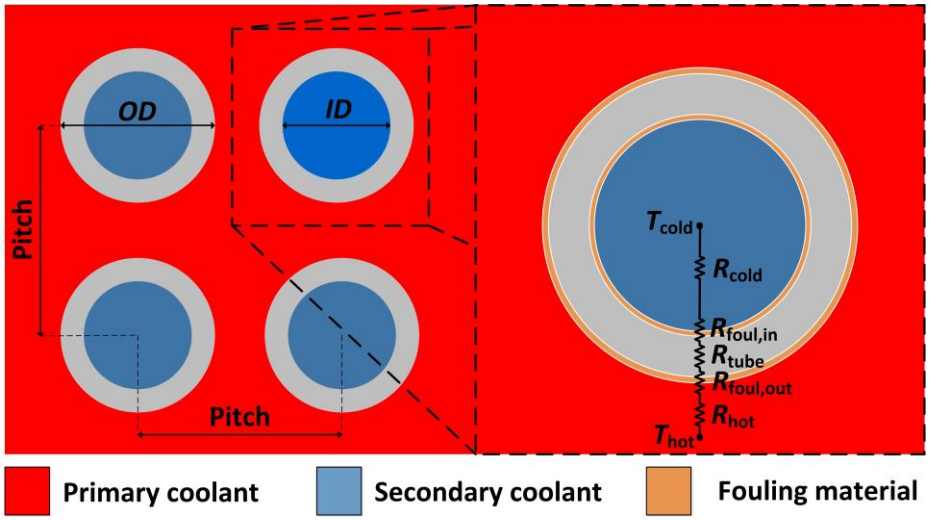

Figure A.2: Tube-bundle heat exchanger resistance network

Heat transfer in the TBHX was modeled using the same one-dimensional, segmented strategy discussed in Section 4.4. The flow rates of the two coolants were assumed to be evenly distributed between the eight TBHXs and all tubes within the heat exchangers were assumed to have the same secondary coolant flow rate. A fouling thickness of 10 μm with a thermal conductivity of 1.3 W m^{-2} K^{-1} was again assumed on both primary and secondary heat transfer surfaces. Figure A.2 shows the geometry and resistance network used to model the TBHX. Thermal resistances in the figure were calculated using Eq. (A.1). The total resistance of a segment, R_{seg}, was calculated by summing the five thermal resistances in the circuit and dividing by the number of tubes in the TBHX (n_{tubes} = 8500). The heat transfer coefficient and friction factor on the inside tubes (secondary coolant) were evaluated using the correlations developed by Churchill (1977a, b), shown in Eqs. (4.5) and (4.6). The Weisman (1959) correlation, shown in Eq. (A.2), was used to determine the primary-coolant heat transfer coefficient. This correlation was developed for turbulent, parallel flow through a square tube array with a PDR between 1.1 and 1.3.

Table A.3: TBHX primary-coolant frictional pressure losses

Pressure loss	k_L **(-)**	ΔP **(kPa)**
Inlet	0.5	7.543
Friction along tube bundle	f_{avg} = 0.0147	183.7
Spacer grids (six total)	0.875	79.26
Outlet	1.1	16.59

$$R_{hot} = \frac{1}{\left(\pi\, OD\, l_{seg}\right) h_{hot}} \quad R_{tube} = \frac{\ln(OD/ID)}{2\pi\, k_{tube}\, l_{seg}} \quad R_{cold} = \frac{1}{\left(\pi\, ID\, l_{seg}\right) h_{cold}}$$
$$R_{foul,in} = \frac{\ln\left[\left(ID - 2t_{foul}\right)/ID\right]}{2\pi\, k_{foul}\, l_{seg}} \quad R_{foul,out} = \frac{\ln\left[\left(OD + 2t_{foul}\right)/OD\right]}{2\pi\, k_{foul}\, l_{seg}} \tag{A.1}$$

$$\mathrm{Nu} = 0.023\mathrm{Re}^{0.8}\,\mathrm{Pr}^{1/3}\left(1.826\,PDR - 1.043\right) \tag{A.2}$$

The primary coolant pressure drop was evaluated for a stream line passing through a TBHX using the method described in Section 4.5. The four frictional and minor pressure losses considered shown in Table A.3. Eq. (A.3), as presented in Todreas and Kazimi (2011), were used to determine the friction factor and frictional pressure drop through the tube bundle. This correlation can be applied to turbulent, parallel flow along a square tube bank with PDR between 1.1 and 1.5. Pressure losses at the inlet and outlet of the TBHX as well as losses associated with flow past the six spacer grids were evaluated as minor losses using a loss coefficient, k_L. Eq. (A.4), developed by Rehme (1973), was used to determine the spacer grid loss coefficient. A_s is the cross-sectional area of the spacer grid and A_v is the unrestricted flow area away from the grid. C_v is a drag coefficient and a function of the Reynolds number, equal to six for the conditions in the TBHX.

$$C = 0.1399 + 0.09059\left(PDR - 1\right) - 0.09926(PDR - 1)^2$$
$$f = C/\mathrm{Re}^{0.18} \tag{A.3}$$

$$k_L = C_v\left(\frac{A_s}{A_v}\right)^2 \tag{A.4}$$

The theoretical pressure required to collapse a thick-walled tube is given by Eq. (A.5) (Luzzi and Di Marcello, 2011a). σ_{yield} is the yield strength of 316 stainless steel at 400°C and equal to 196 MPa. The tube thickness of the TBHX was calculated by multiplying the primary coolant inlet pressure by a safety factor of three ($P_{collapse}$ = 45.9 MPa) and solving for the required tube thickness (t_{tube} = 0.947 mm, rounded up to 1 mm). This method provides a tube thickness similar to that of the ASME boiler and pressure vessel codes (Luzzi and Di Marcello, 2011a). The buckling pressure and burst pressure of the tube were also considered, but the collapsing pressure imposed the largest tube-thickness requirement.

$$P_{collapse} = 2\sigma_{yield}\left(\frac{t_{tube}}{OD}\right)\left[1+\frac{1}{2}\left(\frac{t_{tube}}{OD}\right)\right] \quad \text{(A.5)}$$

A.2. Liquid-boiling Tube-Bundle Heat Exchanger

The liquid-boiling TBHX design has the same geometry as that of the liquid-liquid TBHX. Therefore, the primary-coolant pressure drop analysis performed for the liquid-liquid TBHX also applies to the liquid-boiling design. The secondary coolant was modeled using the same correlations and heat transfer regimes as the liquid-boiling MCHX. The correlations used for different secondary-coolant heat transfer regimes and the transition criteria between regimes are shown in Table 6.2. One hundred control-volume segments were used to model the TBHX and the "opposite side" solution method described in Section 6.3.2 was used to solve the segment heat transfer and conservation equations. The same assumptions used to model the liquid-boiling MCHX were used, including an equal flow distribution between all tubes.

The TBHX was able to meet I^2S-LWR primary-to-secondary heat exchanger requirements. Important fluid properties and operation parameters of a liquid-boiling TBHX

Table A.4: Liquid-boiling TBHX operating parameters

Parameter	Primary coolant	Secondary coolant
$\dot{q}$ (MW)	356.25 (2850)	
A (m^2)	1057 (8456) [secondary coolant]	
$\dot{m}$ (kg s^{-1})	1937 (15,498)	204.4 (1,635)
G (kg m^{-2} s^{-1})	4583	850.4
T_{in} (°C)	330.0	258.0
T_{out} (°C)	298.8	296.0
P_{in} (MPa)	16.30	6.271
P_{out} (MPa)	16.06	6.113
ΔP_{total} (kPa)	242.1	157.4 (tube)
ΔP_{fr} (kPa)	287.1	118.8 (tube)
h_{avg} (kW m^{-2} K^{-1})	61.39	44.08

are shown in Table A.4. The secondary coolant inlet temperature was required to be 20°C below the saturation temperature at the inlet pressure and the outlet temperature was required to be 20°C above the situation temperature. These conditions were achieved by adjusting the secondary coolant inlet pressure and flow rate as described in Section 6.5.2. The secondary-coolant operating conditions were used as input to the Rankine cycle model (described in Section 6.5.2). The maximum thermal efficiency of the cycle was found to be 37.85% compared to 39.03% for the liquid-boiling MCHX. This is explained by the lower secondary-coolant outlet temperature and pressure of the liquid-boiling TBHX as compared to those of the MCHX, shown in Table 6.1.

Figure A.3 shows the temperature profile and heat transfer regimes along the tube length of the TBHX. The relative thermal resistances are shown in Figure A.4. A major difference between the MCHX and the TBHX is the large thermal resistance of the metal tubes. This is most prominent in the saturated-boiling heat transfer regime, where the resistance of the stainless steel tube accounts for roughly 50% of the total resistance compared to roughly 28% in the liquid-boiling MCHX. Tubes in the IRIS steam generator also account for a large fraction of the total thermal resistance (Figure 3.9). This is the result of the

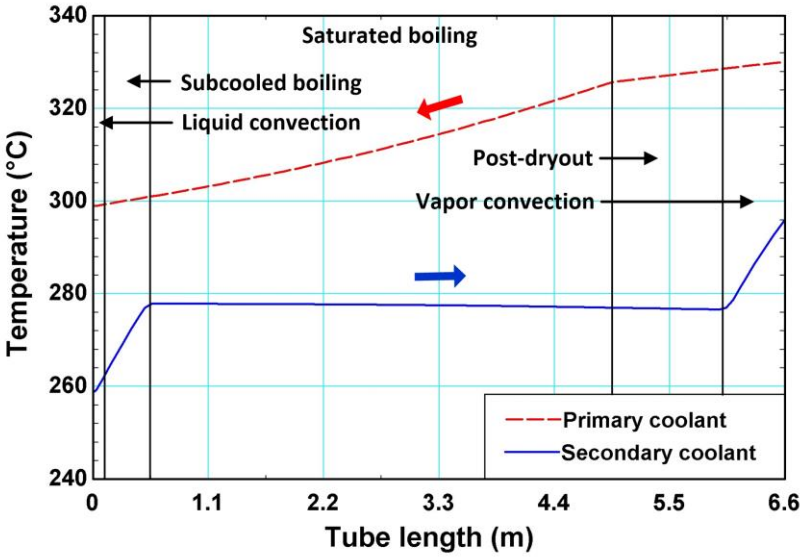

Figure A.3: Liquid-boiling TBHX temperature profile

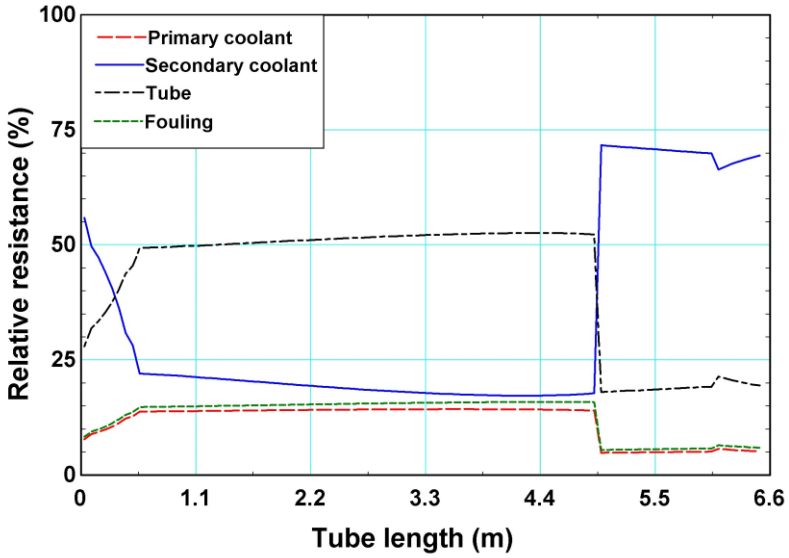

Figure A.4: Liquid-boiling TBHX relative resistance

relatively thick walls required by the ASME boiler and pressure vessel code based on the primary coolant pressure on the outside of the tubes (Luzzi and Di Marcello, 2011a).

The TBHX design represents a practical alternative to the MCHX in the I^2S-LWR. The TBHX design is similar to the once-through steam generators already employed in third-generation nuclear plants and therefore has the advantage of both regulatory and operational

familiarity. Additionally, relatively short secondary coolant headers and primary coolant flow on the shell side of the TBHX promote a uniform flow distribution. Pressure drop through the TBHX is also less than that in the MCHX. However, the TBHX results in decreased thermal efficiency both in the liquid-liquid and liquid-boiling options as compared to the MCHX. This is largely due to the significantly higher area-to-volume ratio of the MCHX. The TBHX requires a larger number of tubes with approximately half the diameter of existing steam generator designs. This may lead to both manufacturing and inspection difficulties.

Appendix B. ADDITIONAL CONSIDERATIONS

B.1. Effect of Heat Transfer Model Boundary Conditions

Several different heat transfer regimes can be encountered in a boiling channel. The heat transfer coefficient and pressure gradient may also vary significantly within the same heat transfer regime as functions of the heat flux, quality, and fluid properties. Therefore, modeling boiling channels often involves subdividing the channel length into smaller control volumes or segments. Boundary conditions are required for both fluids and often the inlet state and the flow rate of both fluid streams are specified. In a counterflow heat exchanger, specifying the inlet conditions for both fluids results in boundary conditions on opposite ends of the heat exchanger. In this case, the equations describing all segments must be solved simultaneously because the temperatures of both coolants are dependent on the heat duties in upstream segments. An iterative "opposite side" solutions method was developed in this study in which the inlet conditions for both fluid streams are specified on opposite ends of a counterflow heat exchanger (Section 6.3.2). Alternatively, the conditions on one end of the heat exchanger can be fully defined if inlet conditions for one fluid and outlet conditions for the other fluid are specified. In this case, segments can be solved one at a time starting from the fully defined end of the heat exchanger. While this approach offers a simpler solution method, it exacerbates overpredictions or underpredictions of the heat duty. An example of this phenomenon is shown in Figure B.1. The boiling fluid is assumed to be a two-phase mixture across the entire channel length. The channel length is split into four segments and inlet/outlet temperatures are shown as points in the figure. The outlet state of the hot fluid (segment one hot-side outlet) and inlet state of the boiling fluid (segment one boiling-side

inlet) are given as boundary conditions. Solving for the segment heat duty determines the inlet temperature of the hot fluid and outlet temperature (and enthalpy) of the boiling fluid. The hot-side inlet temperature for segment one then becomes the hot-side outlet temperature for segment two and the boiling-side outlet temperature (and enthalpy) for segment one becomes boiling-side inlet temperature for segment two. This process is repeated "side-to-side" until all segments have been solved. The left-hand graph shows the temperature profile if the heat duty is accurately captured. The center graph shows the temperature profile if segment heat duties are underpredicted. This may be a result of a correlation that underpredicts heat transfer coefficient in the channel. A lower segment heat duty results in a lower hot-side inlet temperature for the segment and a lower hot-side outlet temperature used as a boundary condition for the neighboring segment. This in turn causes a lower temperature difference between the two coolant streams in the neighboring segment, further reducing the predicted heat duty. This error is propagated over each segment and results in a significant underprediction of the total heat duty. The overprediction of segment heat duties results in a similar compounding effect. An overpredicted segment heat duty causes a higher hot-side inlet temperature in the segment and higher hot-side outlet temperature in the neighboring segment as shown in the right-hand image of Figure B.1. This in turn causes a larger temperature gradient in the neighboring segment, further increasing the predicted heat duty. By specifying the inlet conditions of both fluids at opposite ends of the heat exchanger, the highest and lowest possible temperatures are set. Furthermore, the underprediction of segment heat duties results in a larger temperature difference in downstream segments, increasing the heat duty instead of compounding the underprediction. Therefore, more accurate results can

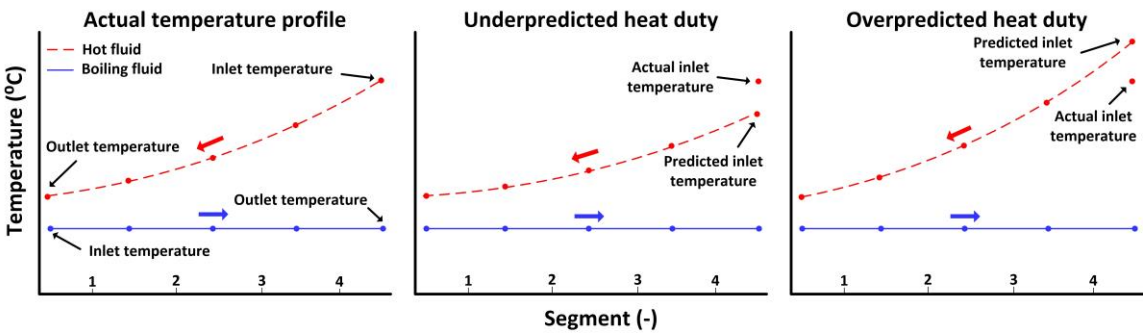

Figure B.1: Side-to-side solution method temperature profiles

be obtained when inlet boundary conditions for both fluids are specified for a segmented counterflow heat exchanger model.

B.2. MCHX Costs

Little information was available in the literature on the costs of MCHXs. Therefore, the vendors used to fabricate the MCHX test section in this study were contacted to obtain approximate pricing information. Although the size of the I^{2}S-LWR MCHX is significantly larger than the test section, these relatively small companies have the capability to fabricate a full-sized prototype of the I^{2}S-LWR MCHX. Vacuum Process Engineering Inc. (VPEI) provided a quote for both the construction of sheets and diffusion bonding. Advanced Metal Etching Inc. (AME) provided an estimate for sheet costs. These costs are summarized in Table B.1. These estimates are for a single unit (88 total in the I^{2}S-LWR design) and do not include required headers/piping. Additional costs would result from the testing and certification required for use in the nuclear industry. However, significant economies of production would be achieved when multiple such heat exchangers are fabricated. It is particularly interesting that the diffusion bonding costs for a MCHX unit are low in comparison with the cost of the etched stainless-steel sheets. The diffusion bonding cost for the MCHX test section in this

Table B.1: I^2S-LWR MCHX prototype costs

Component / Process	Company	Number	Unit Cost	Total Cost
316 SS sheet and etching	AME	530	$286.82	$152,013
316 SS sheet and etching	VPEI	530	$165.00	$87,450
Diffusion bonding	VPEI	1	$16,833	$16,833

study was $4,900. This shows that there is not a significant increase in bonding cost with MCHX size if the required infrastructure is available.

These estimates correspond to a cost of $104,846 to $168,846 per heat exchanger and $9.18 to $14.9 million for the 88 required for the I^2S-LWR design. For comparison, Wade (1995) stated that a single PWR replacement steam generator costs between $12 and $20 million in 1991, although this is only a portion of the total replacement costs. He found that the replacement of the large steam generators in a three-loop PWR plants costs between $125 and $153 million dollars and requires more than a month of downtime. It is expected that the transportation, installation, and potential replacement costs would be significantly lower for the MCHX stacks than those for much larger conventional steam generators.

A more detailed analysis is still required to determine if any significant economic advantages can be achieved with MCHX concepts analyzed in this study. This analysis would also have to include the flashing drum and any other additional components for the liquid-liquid MCHX design. However, this initial prototyping cost shows that there is the potential for significant savings using MCHX heat exchangers compared to larger steam generator designs.

B.3. Rankine Cycle State Properties

Fluid properties for the Rankine cycle associated with the liquid-boiling MCHX are shown in Table B.2. A diagram with labeled state points is shown in Figure 6.12.

Table B.2: Rankine cycle state properties

State	$\dot{m}$ (kg s^{-1})	T (°C)	P (kPa)	i (kJ kg^{-1})	s (J kg^{-1} K^{-1})	x (-)
1	1711	310.1	7472	2860	5946	1.064
2	127.1	310.1	7472	2860	5946	1.064
3	1584	310.1	7472	2860	5946	1.064
4	231.3	257.8	4525	2768	5962	0.9824
5	1353	211.4	1962	2625	5989	0.9087
6	1077	211.4	1962	2798	6346	1.000
7	275.3	211.4	1962	1948	4593	0.5514
8	1077	247.8	1962	2899	6548	1.053
9	231.3	257.8	4525	2296	5073	0.7005
10	1077	280.3	1962	2979	6697	1.096
11	127.1	290.3	7472	2183	4747	0.6048
12	109.1	150.7	485.4	2715	6755	0.9847
13	968.2	95.58	86.42	2452	6821	0.9045
14	798.1	95.58	86.42	2669	7408	1.000
15	170.1	95.58	86.42	1436	4066	0.4567
16	798.1	42.89	8.600	2357	7500	0.9075
17	798.1	42.89	8.600	179.6	610.8	0.000
18	798.1	42.89	86.42	179.7	610.8	-0.09737
19	968.2	95.58	86.42	400.5	1257	0.000
20	968.2	95.62	485.4	401.0	1257	-0.1109
21	1077	150.7	485.4	635.3	1849	0.000
22	1077	150.9	1962	637.2	1850	-0.1409
23	1353	211.4	1962	904.0	2438	0.000
24	1353	212	4525	907.6	2439	-0.1292
25	1711	257.8	4525	1124	2864	0.000
26	1711	258.8	7666	1128	2866	-0.1179
27	1711	272	7666	1195	2989	-0.07258
28	127.1	290.3	7472	1291	3163	0.000
29	127.1	257.8	4525	1291	3180	0.1001

B.4. MCHX Comparison with Existing Steam Generator

The liquid-boiling MCHX design was compared with a Babcock and Wilcox (B&W) once-through steam generator presented in Steam (2005). An image of the B&W steam

generator and the associated primary-coolant loop (RCS) is also shown in Figure B2. The steam generator is 22.25 m tall and has an outside diameter of 3.96 m. It contains 15,531 Inconel® 600 tubes with an OD of 15.88 mm and ID of 14.15 mm. The tubes are arranged in a 22.23 mm triangular pitch and are surrounded by a shroud inside the vessel. The primary coolant enters the top of the vessel and flows through the inside of the tubes to the bottom of the steam generator. The secondary coolant enters as a liquid on the sides of the steam generator. It then flows downward between the shroud and the inside wall of the steam generator vessel. Higher enthalpy (two-phase) secondary coolant from inside the shroud is mixed with the incoming feedwater in this region, bring the mixture to the saturated liquid state. The secondary coolant is then directed upward through the shroud, in counterflow to the primary coolant. At the top of the shroud, the secondary coolant is in the superheated

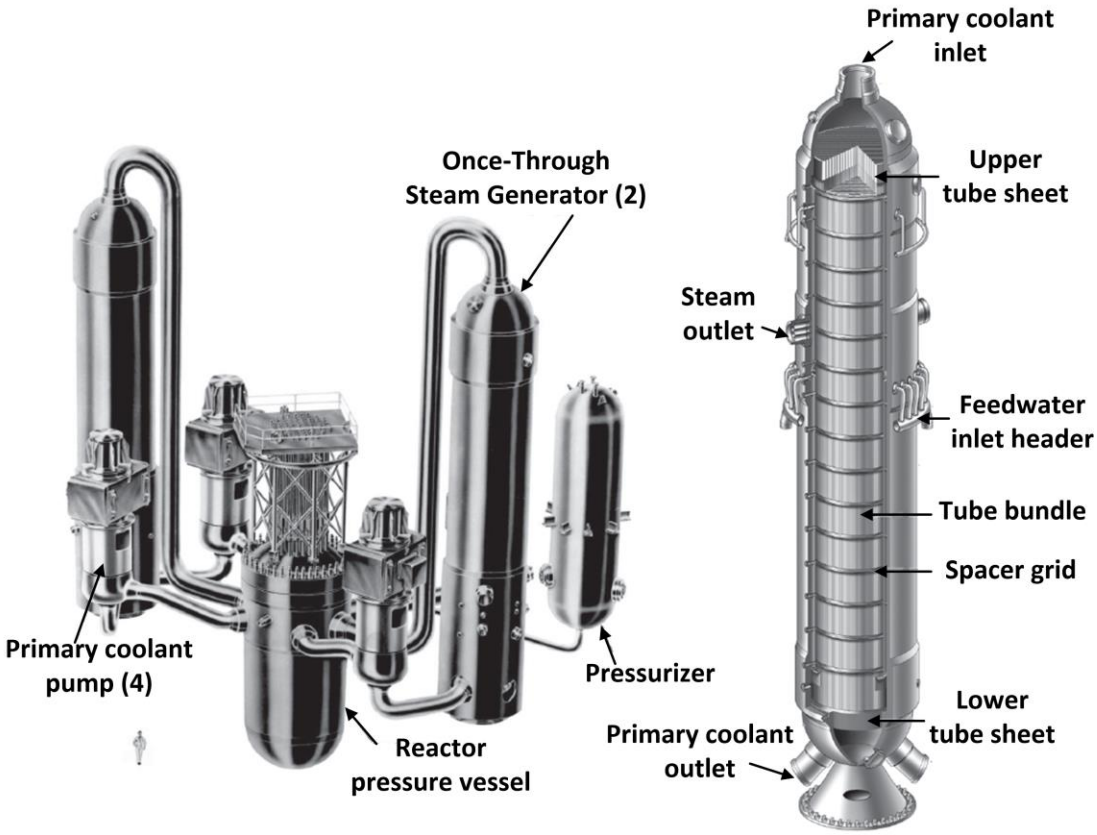

Figure B.2: Babcock and Wilcox once-through steam generator (Steam, 2005)

vapor state. It then flows downward in the annulus between the shroud and inside wall of the steam generator, exiting on the sides of the vessel.

The steam generator data presented in Steam (2005) are for a 2568 MW_{th} reactor at the Oconee nuclear station. The coolant flow rates and reported steam generator heat transfer area (12,356 m^2 for one of two steam generators) were multiplied by a factor of 1.102 (2850 MW_{th} / 2568 MW_{th}) in order to provide a direct comparison with the liquid-boiling I^2S-LWR MCHX design. Parameters for the 2850 MWth reactor comparison are shown in Table B3. The volume of the MCHX was calculated using the rectangular regions in the downcomer occupied by the eight MCHX stacks ($8 \times 1.00\,m \times 0.85\,m \times 6.6\,m$). The volume of the B&W steam generator was calculated using the reported heat transfer area (scaled for a 2850 MWth reactor) and geometry. The number of tubes and tube OD were used to calculate the height of the heat transfer region (18.05 m for one steam generator, 36.10 m total). This was multiplied by the cross-sectional area of the steam generator to obtain the volume (outside diameter of 3.96 m). Exergy analysis shows that the MCHX, $\dot{E}_d$ = 69.6 MW, and the B&W Steam generator, $\dot{E}_d$ = 68.9 MW, have similar exergy destruction rates. However, the B&W Steam generator requires an order of magnitude more volume than does the MCHX. This can be seen

Table B.3: MCHX and B&W steam generator comparison

Full Reactor Parameter	**MCHX**	**B&W**
$\dot{q}$ (MW_{th})	2850	
$\dot{m}_{hot}$ (kg s^{-1})	15,498	18,235
$\dot{m}_{boil}$ (kg s^{-1})	1711	1,499
$T_{hot,in}$ (°C)	330.0	317.7
$T_{hot,out}$ (°C)	298.8	290.0
$T_{boil,in}$ (°C)	272.0	237.8
$T_{boil,out}$ (°C)	310.1	312.8
P_{in} (MPa)	16.30	6.38
A (m^2)	18,260	27,325
Volume	44.88	444.5

in Figure B3 in which each of the steam generators is in fact larger than the RPV. The B&W steam generator has power density of 6.41 MW m^{-3} while the MCHX has a power density of 63.5 MW m^{-3}. The efficiency and power density of the MCHX design allows the I^2S-LWR to be adopted without sacrificing thermal efficiency as the result of larger differential temperature requirements (causing exergy destruction and lost work).

Appendix C. SELECTED SAMPLE CALCULATIONS

Selected sample calculations are presented in this Appendix. Most of the calculations shown in this Appendix were solved iteratively. However, for simplicity, the equations are presented in a linear format, with inputs in the left-hand column and outputs in the right-hand column. The equations used to calculate the outputs are shown in the central column. Notes are used to show the input values obtained through iteration.

C.1. Boiling-loop Ambient Heat Losses

The following calculations show the estimated rate of heat loss to the ambient in the piping between the outlet of the test section and inlet of the condenser on the boiling loop. These heat losses were considered to be negligible compared to the heat duty of the test section, as discussed in Section 7.3.1. Figure C.1 shows a cross-section of the pipe and the resistances included in the calculation. Here "boil" refers to the two-phase fluid in the boiling loop, which condenses as heat is lost to the ambient.

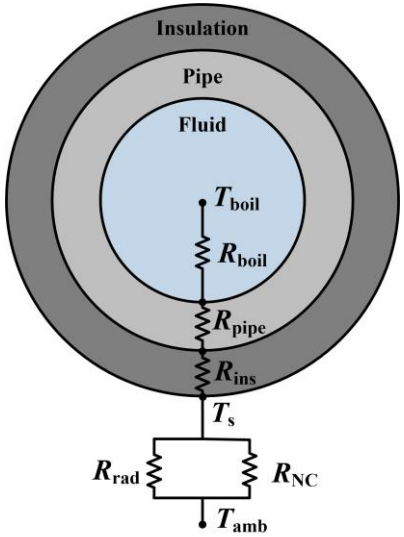

Figure C.1: Piping and insulation cross-section

Table C.1: Ambient heat loss calculations

AMBIENT HEAT LOSSES		
INPUT	**EQUATIONS**	**OUTPUT**
Properties and geometry		
T_{boil} = 143.9°C P_{boil} = 410348 Pa T_s †= 42.60°C T_{amb} = 22.20°C (assumed) P_{amb} = 101325 Pa ID_{pipe} = 0.02118 m OD_{pipe} = 0.0254 m $\dot{m}_{boil}$ = 0.06937 kg s^{-1} t_{ins} = 0.0127 m	Saturated liquid and vapor properties evaluated using P_{boil} and a quality of 0 or 1.	μ_l = 1.899×10^{-4} kg m^{-1} s^{-1} k_l = 0.6905 W m^{-1} K^{-1} Pr_l = 1.181 P_c = 2.206×10^7 Pa
	$P_r = P / P_c$	$P_{r,boil}$ = 0.1860
	$T_{air} = (T_{amb} + T_s)/2$	T_{air} = 32.40°C
	k_{pipe} evaluated using EES built-in function for 316 SS with T_{boil} as an input.	k_{pipe} = 15.43 W m^{-1} K^{-1}
	Air properties evaluated using built-in EES functions with P_{amb} and T_{air} as inputs.	β_{air} = 3.281×10^{-3} K^{-1} k_{air} = 0.02680 W m^{-1} K^{-1} ν_{air} = 1.627×10^{-5} m^2 s^{-1} Pr_{air} = 0.7064
	$A_{cx,pipe} = \pi (ID_{pipe}/2)^2$	$A_{cx,pipe}$ = 3.524×10^{-4} m^2
	$G = \dot{m}_{boil} / A_{cx,pipe}$	G = 196.8 kg m^{-2} s^{-1}
†Insulation surface temperature determined through iterative process.	$OD_{ins} = OD_{pipe} + 2t_{ins}$	OD_{ins} = 0.0508 m

Table C.1: Ambient heat loss calculations (continued)

Resistances		
G = 196.8 kg m^{-2} s^{-1} x_{boil} = 0.2396 ID_{pipe} = 0.02118 m μ_l = 1.899×10^{-4} kg m^{-1} s^{-1} k_l = 0.6905 W m^{-1} K^{-1} Pr_l = 1.181 $P_{r,boil}$ = 0.1860 l_{pipe} = 0.9144 m OD_{pipe} = 0.0254 m OD_{ins} = 0.0508 m k_{pipe} = 15.43 W m^{-1} K^{-1} k_{ins} = 0.03606 W m^{-1} K^{-1} $\alpha_{V,air}$ = 3.281×10^{-3} K^{-1} k_{air} = 0.02680 W m^{-1} K^{-1} ν_{air} = 1.627×10^{-5} m^2 s-^{1} Pr_{air} = 0.7064 T_s †= 42.60°C T_{air} = 32.40°C σ_{sb} = 5.670×10^{-8} W m^{-2} K^{-4} ε_m = 0.85 (assumed) †Insulation surface temperature determined through iterative process.	$Re_l = \frac{GID_{pipe}(1-x)}{\mu_l}$	Re_l = 16694
	$h = 0.023 Re_l^{0.8} Pr_l^{0.4} \left[(1-x)^{0.8} + \frac{3.8x^{0.76}(1-x)^{0.04}}{P_r^{0.38}} \right] \left(\frac{k_l}{ID_{pipe}} \right)$ Shah (1979) correlation.	h_{boil} = 12574 W m^{-2} K^{-1} Note that fluid in the boiling loop is condensing.
	$R_{boil} = \left[\pi ID_{pipe} l_{pipe} h_{boil} \right]^{-1}$	R_{boil} = 1.307×10^{-3} K W^{-1}
	$R_{pipe} = \frac{\ln(OD_{pipe}/ID_{pipe})}{2\pi l_{pipe} k_{pipe}}$	R_{pipe} = 2.047×10^{-3} K W^{-1}
	$R_{ins} = \frac{\ln(OD_{ins}/OD_{pipe})}{2\pi l_{pipe} k_{ins}}$	R_{ins} = 3.346 K W^{-1}
	$Ra = \frac{g(T_s - T_{amb}) Pr \alpha_V OD_{ins}^3}{\nu^2}$	Ra_{air} = 162095
	$h = \left(0.6 + \frac{0.387 Ra^{1/6}}{\left(1 + [0.559/Pr]^{9/16}\right)^{8/27}} \right)^2 \frac{k}{OD_{ins}}$ Churchill and Chu (1975) correlation.	h_{air} = 4.658
	$R_{NC} = \left[\pi OD_{ins} l_{pipe} h_{air} \right]^{-1}$	R_{NC} = 1.471 K W^{-1}
	$T_K = T_{°C} + 273.15 K$	$T_{s,K}$ = 315.7 K $T_{amb,K}$ = 295.4 K
	$h_{rad} = \sigma_{sb} \varepsilon_m \left(T_{s,K}^2 + T_{amb,K}^2 \right) \left(T_{s,K} + T_{amb,K} \right)$	h_{rad} = 5.505 W m^{-2} K^{-1}
	$R_{rad} = \left[\pi OD_{ins} l_{pipe} h_{rad} \right]^{-1}$	R_{rad} = 1.245 K W^{-1}

Table C.1: Ambient heat loss calculations (continued)

Heat transfer and surface temperature		
R_{boil} = 1.307×10^{-3} K W^{-1} R_{pipe} = 2.047×10^{-3} K W^{-1} R_{ins} = 3.346 K W^{-1} R_{NC} = 1.471 K W^{-1} R_{rad} = 1.245 K W^{-1} T_{boil} = 143.9°C T_{amb} = 22.22°C	$R_{amb} = \frac{R_{NC} R_{rad}}{R_{NC} + R_{rad}}$	R_{amb} = 0.6743 K W^{-1}
	$R_{total} = R_{boil} + R_{pipe} + R_{ins} + R_{amb}$	R_{total} = 4.024 K W^{-1}
	$\dot{q} = \frac{T_{boil} - T_{amb}}{R_{total}}$	$\dot{q}$ = 30.25 W
	$T_s = T_{amb} + \dot{q} R_{amb}$	T_s = 42.60°C

C.2. Test Section Liquid-boiling Segment

The following shows the calculations performed for a saturated-boiling control volume segment in the liquid-boiling test section model. These calculation are similar to those performed in the liquid-boiling I^{2}S-LWR MCHX model. These calculations are also similar to those for the liquid-liquid MCHX model used in this investigation, with the exception that both fluid were in the liquid state.

Table C.2: Liquid-boiling segment calculations

LIQUID-BOLING SEGMENT CALCUATIONS		
INPUT	**EQUATIONS**	**OUTPUT**
Channel geometry		
h_{ch} = 0.615×10^{-3} m l_{flat} = 0.475×10^{-3} m t_{fin} = 0.234×10^{-3} m l_{seg} = 2.540×10^{-3} m $n_{ch,ps}$ = 30 n_{sheet} = 10	$l_{fin} = h_{ch} / 2$	l_{fin} = 0.3075×10^{-3} m
	$p_{wall} = 2\left[\pi(2h_{ch})/4\right] + (2h_{ch} + l_{flat}) + l_{flat}$	p_{wall} = 4.112×10^{-3} m
	$A_{cx} = 2(\pi h_{ch}^2 / 4) + h_{ch} l_{flat}$	A_{cx} = 8.862×10^{-7} m^2
	$D_h = 4A_{cx} / p_{wall}$	D_h = 0.8621×10^{-3} m
	$A_{flat} = \left(2h_{ch} + l_{flat} + t_{fin}\right) l_{seg}$	A_{flat} = 4.925×10^{-6} m^2
	$A_{ch,top} = \left(2h_{ch} + l_{flat} + 2\left[2h_{ch}\pi\left(30/360\right)\right]\right) l_{seg}$	$A_{ch,top}$ = 5.967×10^{-6} m^2
	$A_{ch,bottom} = \left(2\left[2h_{ch}\pi\left(60/360\right)\right] + l_{flat}\right) l_{seg}$	$A_{ch,bottom}$ = 4.478×10^{-6} m^2
	$A_{fin} = 2 l_{fin}\, l_{seg}$	A_{fin} = 1.562×10^{-6} m^2
	$A_{total} = 2\left(l_{fin} + h_{ch} + l_{flat}/2\right) l_{seg}$	A_{total} = 5.893×10^{-6} m^2
	$A_{seg} = p_{wall} l_{seg} n_{ch,ps} \left(n_{sheet} - 1/2\right)$	A_{seg} = 2.977×10^{-3} m^2

Table C.2: Liquid-boiling segment calculation (continued)

Hot-side and boiling-side fluid properties		
$P_{hot,in}$ = 1690428 Pa $P_{hot,out}$ † = 1690105 Pa $P_{boil,in}$ = 414548 Pa $P_{boil,out}$ † = 414116 Pa $i_{hot,in}$ = 695553 J kg^{-1} $i_{hot,out}$ †= 694449 J kg^{-1} $i_{boil,in}$ = 1005151 J kg^{-1} $i_{boil,out}$ †= 1015494 J kg^{-1}	$P_{avg} = (P_{in} + P_{out})/2$	$P_{hot,avg}$ = 1690267 Pa $P_{boil,avg}$ = 414332 Pa
	$i_{avg} = (i_{in} + i_{out})/2$	$i_{boil,avg}$ = 1010332 J Kg^{-1}
	Boiling fluid quality evaluated using EES built-in functions with $P_{boil,avg}$ and $i_{boil,avg}$ as inputs. Saturated liquid and vapor properties evaluated using EES built-in functions with $P_{boil,avg}$ and a quality of 0 or 1 as inputs.	$x_{boil,in}$ = 0.1855 $x_{boil,out}$ = 0.1904 $k_{l,boil}$ = 0.6904 W m^{-1} K^{-1} $\rho_{l,boil}$ = 921.7 kg m^{-3} $\rho_{v,boil}$ = 2.235 kg m^{-3} $\mu_{l,boil}$ = 1.894×10^{-4} m kg^{-1} s^{-1} $\mu_{v,boil}$ = 1.3815×10^{-5} m kg^{-1} s^{-1} i_{fg} = 2.130×10^{6} J kg^{-1} P_c = 2.206×10^{7} Pa $Pr_{l,boil}$ = 1.178
	$x_{avg} = (x_{in} + x_{out})/2$	$x_{boil,avg}$ = 0.1879
	$P_r = P_{avg}/P_c$	$P_{r,boil}$ = 0.01878
	Temperatures evaluated using built-in EES functions with P and i as inputs.	$T_{hot,in}$ = 164.45°C $T_{hot,out}$ = 164.23°C $T_{boil,in}$ = 144.90°C $T_{boil,out}$ = 144.86°C
	$T_{avg} = (T_{in} + T_{out})/2$	$T_{hot,avg}$ = 164.36°C $T_{boil,avg}$ = 144.86°C

Table C.2: Liquid-boiling segment calculation (continued)

†Outlet values determined through iterative process.	Hot-side fluid properties evaluated using built-in EES functions with $P_{\text{hot,avg}}$ and $T_{\text{hot,avg}}$ as inputs.	$k_{\text{hot}} = 0.6782$ W m^{-1} K^{-1} $\rho_{\text{hot}} = 903.8$ kg m^{-3} $\mu_{\text{hot}} = 1.657\times10^{-4}$ kg m^{-1} s^{-1} $\text{Pr}_{\text{hot}} = 1.061$
Hot-side dimensionless numbers and correlations		
$\dot{m}_{\text{hot}} = 0.6498$ kg s^{-1} $n_{\text{ch,ps}} = 30$ $n_{\text{sheet}} = 10$ $D_{\text{h}} = 0.8621\times10^{-3}$ m $A_{\text{cx}} = 8.862\times10^{-7}$ m^2 $\mu_{\text{hot}} = 1.657\times10^{-4}$ kg m^{-1} s^{-1} $\varepsilon = 2\times10^{-6}$ m $\text{Pr}_{\text{hot}} = 1.061$ $k_{\text{hot}} = 0.6782$ W m^{-1} K^{-1} $l_{\text{seg}} = 2.54\times10^{-3}$ m $\rho_{\text{hot}} = 903.8$ kg m^{-3}	$\dot{m}_{\text{ch}} = \dot{m} / \left(n_{\text{ch,ps}} n_{\text{sheet}} \right)$	$\dot{m}_{\text{ch,hot}} = 2.166\times10^{-3}$ kg s^{-1}
	$G = \dot{m}_{\text{ch}} / A_{\text{cx}}$	$G_{\text{hot}} = 2444$ kg m^{-2} s^{-1}
	$\text{Re} = GD_{\text{h}} / \mu$	$\text{Re}_{\text{hot}} = 12719$
	$f = 8\left[\left(\frac{8}{\text{Re}}\right)^{12} + \left(\left\{2.457\ln\left(\left[\left(\frac{7}{\text{Re}}\right)^{0.9} + 0.27\frac{\varepsilon}{D_{\text{h}}}\right]^{-1}\right)\right\}^{16} + \left\{\frac{37530}{\text{Re}}\right\}^{16}\right)^{-1.5}\right]^{\frac{1}{12}}$ Churchill (1977b) correlation.	$f_{\text{hot}} = 0.03313$
	$\Delta P = \frac{G^2}{2\rho}\left(\frac{f\, l_{\text{seg}}}{D_{\text{h}}}\right)$	$\Delta P_{\text{hot}} = 322.6$ Pa
	$\text{Nu}^{10} = 4.364^{10} + \left[\frac{\exp\left(\frac{2200-\text{Re}}{365}\right)}{4.364^2} + \left(6.3 + \frac{0.079\left(\frac{f}{8}\right)^{0.5}\text{Re}\cdot\text{Pr}}{\left(1+\text{Pr}^{0.8}\right)^{5/6}}\right)^{-2}\right]^{-5}$ Churchill (1977a) correlation.	$\text{Nu}_{\text{hot}} = 44.05$
	$h = \text{Nu}\, k / D_{\text{h}}$	$h_{\text{hot}} = 34654$ W m^{-2} K^{-1}

Table C.2: Liquid-boiling segment calculation (continued)

Boiling-side dimensionless numbers and correlations		
	$G = \dot{m}_{ch} / A_{cx}$	G_{boil} = 260.9 kg m^{-2} s^{-1}
	$\mu_{tp} = \left(\frac{x}{\mu_v} + \frac{1-x}{\mu_l} \right)^{-1}$ McAdams *et al.* (1942) correlations.	μ_{tp} = 5.590×10^{-5} kg m^{-1} s^{-1}
	$\rho_{tp} = \left(\frac{x}{\rho_v} + \frac{1-x}{\rho_l} \right)^{-1}$	ρ_{tp} = 11.77 kg m^{-3}
	$\mathrm{Re}_{tp} = GD_h / \mu_{tp}$	Re_{tp} = 4024
	$f = 8\left[\left(\frac{8}{\mathrm{Re}} \right)^{12} + \left(\left\{ 2.457 \ln\left(\left[\left(\frac{7}{\mathrm{Re}} \right)^{0.9} + 0.27 \frac{\varepsilon}{D_h} \right]^{-1} \right) \right\}^{16} + \left\{ \frac{37530}{\mathrm{Re}} \right\}^{16} \right)^{-1.5} \right]^{\frac{1}{12}}$ Churchill (1977b) correlation.	f_{tp} = 0.04310
	$\Delta P_{fr} = \frac{G^2}{2\rho_{tp}} \left(\frac{f_{tp}\, l_{seg}}{D_h} \right)$	$\Delta P_{fr,boil}$ = 367.2 Pa
	$\alpha = \left[1 + \left(\frac{1-x}{x} \right)^{0.74} \left(\frac{\rho_v}{\rho_l} \right)^{0.65} \left(\frac{\mu_l}{\mu_v} \right)^{0.13} \right]^{-1}$ Baroczy (1965) correlation.	$\alpha_{boil,in}$ = 0.9226 $\alpha_{boil,out}$ = 0.9243
	$\Delta P_a = G^2 \left[\left(\frac{x^2}{\alpha\rho_v} + \frac{(1-x)^2}{(1-\alpha)\rho_l} \right)_{out} - \left(\frac{x^2}{\alpha\rho_v} + \frac{(1-x)^2}{(1-\alpha)\rho_l} \right)_{in} \right]$	$\Delta P_{a,boil}$ = 65.21 Pa
	$\Delta P = \Delta P_{fr} + \Delta P_a$	ΔP_{boil} = 432.4 Pa

Table C.2: Liquid-boiling segment calculation (continued)

	$h_{NB} = 55P_r^{0.12}\left(-\log_{10} P_r\right)^{-0.55} M^{-0.5} q^{"2/3}$ Cooper (1984) correlations.	h_{NB} = 23068 W m^{-2} K^{-1}
	$\mathrm{Re}_l = GD_h(1-x)/\mu_{tp}$	Re_l = 694.4
	$h_l = 0.023\mathrm{Re}_l^{0.8}\mathrm{Pr}_l^{0.4}\left(k_l / D_h\right)$ Dittus and Boelter (1930) correlation.	h_l = 4799 W m^{-2} K^{-1}
	$X_{tt} = \left((1-x)/x\right)^{0.9}\left(\rho_v/\rho_l\right)^{0.5}\left(\mu_l/\mu_v\right)^{0.1}$	X_{tt} = 0.2388
	$E_1 = 1 + 24000\mathrm{Bo}^{1.16} + 1.37\left(1/X_{tt}\right)^{0.86}$	E_1 = 8.710
	$S_1 = \left(1 + 1.15\times10^{-6} E_1^2 \mathrm{Re}_l^{1.17}\right)^{-1}$	S_1 = 0.7870
	$\mathrm{Fr}_{lo} = G^2/\left(\rho_l^2 g D_h\right)$	Fr_{lo} = 9.484
	IF $\mathrm{Fr}_{lo} < 0.05 \rightarrow E_2 = \mathrm{Fr}_{lo}^{(0.1-2\mathrm{Fr}_{lo})}$ $S_2 = \mathrm{Fr}_{lo}^{1/2}$ ELSE $\rightarrow E_2 = 1$ $S_2 = 1$	$E_2 = 1$ $S_2 = 1$
†Heat flux determined through iterative process.	$h = h_l E_1 E_2 + h_{NB} S_1 S_2$	h_{boil} = 59955 W m^{-2} K^{-1}

Table C.2: Liquid-boiling segment calculation (continued)

Fin efficiency		
$T_{hot,avg}$ = 164.36°C $T_{boil,avg}$ = 144.86°C t_{fin} = 0.234×10^{-3} m l_{fin} = 0.3075×10^{-3} m h_{hot} = 34654 W m^{-2} K^{-1} h_{boil} = 59955 W m^{-2} K^{-1} A_{fin} = 1.562×10^{-6} m^2 A_{total} = 5.893×10^{-6} m^2	$T_{sheet} = \left(T_{hot,avg} + T_{boil,avg}\right)/2$ Thermal conductivity of 304 SS evaluated using built-in EES function with T_{sheet} as an input.	T_{sheet} = 154.62°C k_{sheet} = 17.04 W m^{-1} K^{-1}
	$m = \left(\frac{2h}{k_{sheet}t_{fin}}\right)^{1/2}$	m_{hot} = 4169 m^{-1} m_{boil} = 5483 m^{-1}
	$\eta_{fin} = \frac{\tanh\left(ml_{fin}\right)}{ml_{fin}}$	$\eta_{fin,hot}$ = 0.6685 $\eta_{fin,boil}$ = 0.5537
	$\eta_o = 1 - \frac{A_{fin}}{A_{total}}(1-\eta_{fin})$	$\eta_{o,hot}$ = 0.9121 $\eta_{o,boil}$ = 0.8817

Table C.2: Liquid-boiling segment calculation (continued)

Resistances and wall temperature		
$t_{wall} = 0.470\times10^{-3}$ m $k_{sheet} = 16.66$ W m^{-1} K^{-1} $n_{ch,ps} = 30$ $n_{sheet} = 10$ $h_{hot} = 34654$ W m^{-2} K^{-1} $h_{boil} = 59955$ W m^{-2} K^{-} $A_{flat} = 4.925\times10^{-6}$ m^2 $A_{ch,top} = 5.967\times10^{-6}$ m^2 $A_{ch,bottom} = 4.478\times10^{-6}$ m^2 $\eta_{o,hot} = 0.9121$ $\eta_{o,boil} = 0.8817$	$R_{wall} = \frac{t_{wall}}{k_{sheet} A_{flat}}$	$R_{wall} = 5.599$ K W^{-1}
	$R_{top,hot} = \left[\eta_{o,hot} h_{hot} A_{ch,top}\right]^{-1}$	$R_{top,hot} = 5.302$ K W^{-1}
	$R_{bottom,hot} = \left[\eta_{o,hot} h_{hot} A_{ch,bottom}\right]^{-1}$	$R_{bottom,hot} = 7.065$ K W^{-1}
	$R_{top,boil} = \left[\eta_{o,boil} h_{boil} A_{ch,top}\right]^{-1}$	$R_{top,boil} = 3.171$ K W^{-1}
	$R_{bottom,boil} = \left[\eta_{o,boil} h_{boil} A_{ch,bottom}\right]^{-1}$	$R_{bottom,boil} = 4.224$ K W^{-1}
	$R_{top} = R_{top,hot} + R_{wall} + R_{bottom,boil}$	$R_{top} = 15.13$ K W^{-1}
	$R_{bottom} = R_{bottom,hot} + R_{wall} + R_{top,boil}$	$R_{bottom} = 15.83$ K W^{-1}
	$R_{parrellel} = \frac{R_{top} R_{bottom}}{R_{top} + R_{bottom}}$	$R_{parrellel} = 7.736$ K W^{-1}
	$R_{seg} = \frac{R_{parrellel}}{n_{ch,ps}\left(n_{sheet} - 1/2\right)}$	$R_{seg} = 0.2714$ K W^{-1}
	$UA_{seg} = R_{seg}^{-1}$	$UA_{seg} = 36.84$ W K^{-1}

Table C.2: Liquid-boiling segment calculation (continued)

Heat transfer and pressure drop		
$T_{hot,in}$ = 164.45°C $T_{hot,out}$ = 164.23°C $T_{boil,in}$ = 144.90°C $T_{boil,out}$ = 144.86°C UA_{seg} = 36.84 W K^{-1} $i_{hot,in}$ = 695553 J kg^{-1} $i_{hot,out}$ = 694449 J kg^{-1} $i_{boil,in}$ = 1005151 J kg^{-1} $i_{boil,out}$ = 1015494 J kg^{-1} $\dot{m}_{hot}$ = 0.662 kg s^{-1} $\dot{m}_{boil}$ = 0.0510 kg s^{-1} A_{seg} = 2.977×10^{-3} m^2 $P_{hot,in}$ = 1690428 Pa $P_{boil,in}$ = 414548 Pa ΔP_{hot} = 322.6Pa ΔP_{boil} = 432.4 Pa	$\Delta T_{lm} = \frac{(T_{hot,in} - T_{boil,out}) - (T_{hot,out} - T_{boil,in})}{\ln\left(\frac{T_{hot,in} - T_{boil,out}}{T_{hot,out} - T_{boil,in}}\right)}$	ΔT_{lm} = 19.47°C
	$\dot{q} = UA_{seg}\Delta T_{lm}$ $\dot{q} = \dot{m}_{hot}(i_{hot,in} - i_{hot,out})$ $\dot{q} = \dot{m}_{boil}(i_{boil,out} - i_{boil,in})$ Above three equations solved simultaneously through iterative process.	$\dot{q}$ = 717.5 W
	$q'' = \dot{q} / A_{seg}$	q'' = 241025 W m^{-2}
	$P_{out} = P_{in} - \Delta P$	$P_{hot,out}$ = 1690105 Pa $P_{boil,out}$ = 414116 Pa

C.3. Liquid-boiling Heat Duty Measurement

The following calculations show the calculation of the heat duty using the enthalpy change in both the hot loop and boiling loop. Figure 7.2 shows the different states in the test facility used in the calculations.

Table C.3: Experimental heat duty calculation

EXPERIMENTAL HEAT DUTY CALCULATION		
INPUT	**EQUATIONS**	**OUTPUT**
Fluid properties		
T_1 = 167.01°C T_2 = 152.10°C T_3 = 124.97°C T_6 = 126.50°C T_7 = 121.38°C T_8 = 138.40°C P_1 = 1692771 Pa P_3 = 425367 Pa P_6 = 394131 Pa P_7 = 896336 Pa $\Delta P_{TS,hot}$ = 88524 Pa $\Delta P_{TS,boil}$ = 15019 Pa	$P_2 = P_1 - \Delta P_{TS,hot}$	P_2 = 1604247 Pa
	$P_4 = P_3 - \Delta P_{TS,boil}$	P_4 = 410348 Pa
	Single-phase enthalpy evaluated using EES built-in functions with *T* and *P* as inputs. Cold-side condenser inlet enthalpy (i_7) and outlet enthalpy (i_8) evaluated with P_7 and the measure temperature as inputs.	i_1 = 706542 J kg^{-1} i_2 = 642048 J kg^{-1} i_3 = 525080 J kg^{-1} i_6 = 531565 J kg^{-1} i_7 = 510157 J kg^{-1} i_8 = 582662 J kg^{-1}

Table C.3: Experimental heat duty calculation (continued)

Experimental heat duty		
$\dot{m}_{hot}$ = 0.6498 kg s^{-1} $\dot{m}_{boil}$ = 0.06937 kg s^{-1} $\dot{m}_{cold}$ = 0.5622 kg s^{-1} i_1 = 706542 J kg^{-1} i_2 = 642048 J kg^{-1} i_3 = 525080 J kg^{-1} i_6 = 531565 J kg^{-1} i_7 = 510157 J kg^{-1} i_8 = 582662 J kg^{-1} P_4 = 410348 Pa	$\dot{q}_{TS,hot} = \dot{m}_{hot}(i_1 - i_2)$	$\dot{q}_{TS,hot}$ = 41908 W
	$\dot{q}_{cond} = \dot{m}_{cold}(i_8 - i_7)$	$\dot{q}_{cond}$ = 40762 W
	$i_5 = \frac{\dot{q}_{cond}}{\dot{m}_{boil}} + i_6$	i_5 = 1119167 J kg^{-1}
	$i_4 = i_5$ Assume tube adiabatic between test section and condenser. See ambient loss calculations. Outlet quality evaluated using EES built-in function with i_4 and P_4 as inputs.	i_4 = 1119167J kg^{-1} x_4 = 0.2396
	$\dot{q}_{TS,boil} = \dot{m}_{boil}(i_4 - i_3)$	$\dot{q}_{TS,boil}$ = 41212 W
	$\dot{q}_{TS,avg} = (\dot{q}_{TS,boil} + \dot{q}_{TS,hot})/2$	$\dot{q}_{TS,avg}$ = 41560 W

C.4. Experimental Liquid-boiling Pressure Drop Model

The following shows the calculation of the predicted pressure drop for the boiling loop. The frictional pressure drop in the channels was determined by summing the predicted frictional pressure drop in the segmented channel model discussed above. Here "in" refers to the test section liquid inlet state and "out" refers to the two-phase outlet state.

Table C.4: Boiling-side pressure drop model

BOILING-SIDE PRESSURE DROP MODEL		
INPUT	**EQUATIONS**	**OUTPUT**
Properties		
T_{in} = 124.97°C P_{in} = 425367 Pa i_{out} = 1118479 J kg^{-1} P_{out} = 410348 Pa	Inlet properties evaluated using built-in EES functions with T_{in} and P_{in} as inputs.	μ_{in} = 2.221×10^{-4} kg m^{-1} s^{-1} ρ_{in} = 939.1 kg m^{-3}
	Outlet quality evaluated using built-in EES functions with i_{out} and P_{out} as inputs. Saturated liquid and vapor properties evaluated using P_{out} and a quality of 0 or 1 as inputs.	x_{out} = 0.2393 $\mu_{l,out}$ = 1.899×10^{-4} kg m^{-1} s^{-1} $\mu_{v,out}$ = 1.380×10^{-5} kg m^{-1} s^{-1} $\rho_{l,out}$ = 922.1 kg m^{-3} $\rho_{v,out}$ = 2.215 kg m^{-3}
Geometry and mass flux		
$A_{cx,ch}$ † = 8.862×10^{-7} m^2 $n_{ch,ps}$ = 30 n_{sheet} = 10 l_{header} = 0.0381 m w_{header} = 0.05588 m $\dot{m}$ = 0.06937 kg s^{-1} † Calculated in previous sample calculations.	$A_{cx,ch,total} = A_{cx,ch} n_{sheet} n_{ch,ps}$	$A_{cx,ch,total}$ = 2.659×10^{-4} m^2
	$A_{cx,header} = l_{header} w_{header}$	$A_{cx,header}$ = 2.129×10^{-3} m^2
	$\dot{m}_{ch} = \dot{m} / \left(n_{ch,ps} n_{sheet} \right)$	$\dot{m}_{ch}$ = 2.312×10^{-4} kg s^{-1}
	$G = \dot{m}_{ch} / A_{cx,ch}$	G_{ch} = 260.9 kg m^{-2} s^{-1}

Table C.4: Boiling-side pressure drop model (continued)

Inlet pressure drop (single-phase)		
$A_{cx,ch,total}$ = 2.659×10^{-4} m^2 $A_{cx,header}$ = 2.129×10^{-3} m^2 G_{ch} = 260.9 kg m^{-2} s^{-1} ρ_{in} = 939.1 kg m^{-3} D_h †= 8.621×10^{-4} m μ_{in} = 2.221×10^{-4} kg m^{-1} s^{-1} $l_{inactive}$ = 0.0127 m	$C_c = 1 - \frac{1 - A_{cx,ch,total} / A_{cx,header}}{2.08\left(1 - A_{cx,ch,total} / A_{cx,header}\right) + 0.5371}$	C_c = 0.6288
	$\Delta P_{con} = \frac{G^2}{2\rho}\left[\left(\frac{1}{C_c} - 1\right)^2 + \left(1 - \left(\frac{A_{cx,ch,total}}{A_{cx,header}}\right)^2\right)\right]$	ΔP_{con} = 48.31 Pa
	$\mathrm{Re} = GD_h / \mu$	Re_{in} = 1013
	$f = 8\left[\left(\frac{8}{\mathrm{Re}}\right)^{12} + \left(\left\{2.457 \ln\left(\left[\left(\frac{7}{\mathrm{Re}}\right)^{0.9} + 0.27\frac{\varepsilon}{D_h}\right]^{-1}\right)\right\}^{16} + \left\{\frac{37530}{\mathrm{Re}}\right\}^{16}\right)^{-1.5}\right]^{\frac{1}{12}}$ Churchill (1977b) correlation.	f_{in} = 0.0632
	$\Delta P_{fr} = \frac{G^2}{2\rho}\left(\frac{f\, l_{inactive}}{D_h}\right)$	$\Delta P_{fr,in}$ = 33.75 Pa
† Calculated in previous sample calculations.	$\Delta P_{in} = \Delta P_{con} + \Delta P_{fr,in}$	ΔP_{in} = 82.06 Pa

Table C.4: Boiling-side pressure drop model (continued)

Outlet pressure drop (two-phase)		
x_{out} = 0.2393 $A_{cx,ch,total}$ = 2.659×10^{-4} m^2 $A_{cx,header}$ = 2.129×10^{-3} m^2 G_{ch} = 260.9 kg m^{-2} s^{-1} $\mu_{l,out}$ = 1.899×10^{-4} kg m^{-1} s^{-1} $\mu_{v,out}$ = 1.380×10^{-5} kg m^{-1} s^{-1} $\rho_{l,out}$ = 922.1 kg m^{-3} $\rho_{v,out}$ = 2.215 kg m^{-3} D_h †= 8.621×10^{-4} m ε = 2×10^{-6} m $l_{inactive}$ = 0.01588 m	$\phi_{lo,exp} = 1 + x\left(\frac{\rho_l}{\rho_v} - 1\right)\left(0.25x(1-x) + x^2\right)$	$\phi_{lo,exp}$ = 43.68
	$\Delta P_{exp} = \frac{G^2}{\rho_l}\left(\frac{A_{cx,ch,total}}{A_{cx,header}}\right)\left[1 - \left(\frac{A_{cx,ch,total}}{A_{cx,header}}\right)\right]\phi_{lo,exp}$	ΔP_{exp} = -352.4 Pa
	$\mu_{tp} = \left(\frac{x}{\mu_v} + \frac{1-x}{\mu_l}\right)^{-1}$ McAdams *et al.* (1942) correlations.	μ_{tp} = 4.686×10^{-5} kg m^{-1} s^{-1}
	$\rho_{tp} = \left(\frac{x}{\rho_v} + \frac{1-x}{\rho_l}\right)^{-1}$	ρ_{tp} = 9.186 kg m^{-3}
	$\mathrm{Re}_{tp} = GD_h / \mu_{tp}$	Re_{tp} = 4801
	$f = 8\left[\left(\frac{8}{\mathrm{Re}}\right)^{12} + \left(\left\{2.457\ln\left(\left[\left(\frac{7}{\mathrm{Re}}\right)^{0.9} + 0.27\cdot\frac{\varepsilon}{D_h}\right]^{-1}\right)\right\}^{16} + \left\{\frac{37530}{\mathrm{Re}}\right\}^{16}\right)^{-1.5}\right]^{\frac{1}{12}}$ Churchill (1977b) correlation.	f_{tp} = 0.04114
	$\Delta P_{fr} = \frac{G^2}{2\rho_{tp}}\left(\frac{f_{tp}\, l_{inactive}}{D_h}\right)$	$\Delta P_{fr,out}$ = 2245 Pa
†Calculated in segmented model sample calculations above	$\Delta P_{out} = \Delta P_{exp} + \Delta P_{fr,out}$	ΔP_{out} = 1893 Pa

Table C.4: Boiling-side pressure drop model (continued)

Acceleration, friction, and total pressure drop		
x_{out} = 0.2393 ρ_{in} = 939.1 kg m^{-3} $\mu_{l,out}$ = 1.899×10^{-4} kg m^{-1} s^{-1} $\mu_{v,out}$ = 1.380×10^{-5} kg m^{-1} s^{-1} $\rho_{l,out}$ = 922.1 kg m^{-3} $\rho_{v,out}$ = 2.215 kg m^{-3} G_{ch} = 260.9 kg m^{-2} s^{-1} ΔP_{in} = 82.06 Pa ΔP_{out} = 1893 Pa	$\alpha = \left[1+\left(\frac{1-x}{x}\right)^{0.74}\left(\frac{\rho_v}{\rho_l}\right)^{0.65}\left(\frac{\mu_l}{\mu_v}\right)^{0.13}\right]^{-1}$ Baroczy (1965) correlation.	α_{out} = 0.9384
	$\Delta P_a = G^2\left[\left(\frac{x^2}{\alpha\rho_v}+\frac{(1-x)^2}{(1-\alpha)\rho_l}\right)_{out}-\left(\frac{1}{\rho}\right)_{in}\right]$	ΔP_a = 2497 Pa
	$\Delta P_{fr} = \sum_{i=1}^{n_{seg}} \Delta P_{fr}[i]$ Active channel frictional pressure drop calculated from segmented model.	ΔP_{fr} = 12991 Pa
	$\Delta P_{boil} = \Delta P_{fr} + \Delta P_a + \Delta P_{in} + \Delta P_{out}$	ΔP_{boil} = 17463 Pa

REFERENCES

Adams, T., S. Abdel-Khalik, S. Jeter and Z. Qureshi (1998), "An Experimental Investigation of Single-Phase Forced Convection in Microchannels," *International Journal of Heat and Mass Transfer* Vol. 41(6) pp. 851-857. DOI: 10.1016/S0017-9310(97)00180-4.

Adams, T., M. Dowling, S. Abdel-Khalik and S. Jeter (1999), "Applicability of Traditional Turbulent Single-Phase Forced Convection Correlations to Non-Circular Microchannels," *International Journal of Heat and Mass Transfer* Vol. 42(23) pp. 4411-4415. DOI: 10.1016/S0017-9310(99)00102-7.

Ahmad, S. (1970), "Axial Distribution of Bulk Temperature and Void Fraction in a Heated Channel with Inlet Subcooling," *Journal of Heat Transfer* Vol. 92(4) pp. 595-609. DOI: 10.1115/1.3449729.

Armand, A. (1946), "Resistance to Two-Phase Flow in Horizontal Tubes," *Izv. VTI* Vol. 15(1) pp. 16-23.

ASME (2019). *ASME Boiler and Pressure Vessel Code. Section VIII, Rules for Construction of Pressure Vessels. Division I*, American Society of Mechanical Engineers.

Bajura, R. and E. Jones (1976), "Flow Distribution Manifolds," *Journal of Fluids Engineering* Vol. 98(4) pp. 654-665.

Bao, Z., M. Bosnich and B. Haynes (1994), "Estimation of Void Fraction and Pressure-Drop for 2-Phase Flow in Fine Passages," *Chemical Engineering Research and Design* Vol. 72(5) pp. 625-632.

Baroczy, C. (1963). *Correlation of Liquid Fraction in Two-Phase Flow with Application to Liquid Metals*. Atomics International. Washington D.C.

Behar, C. (2014). *Technology Roadmap Update for Generation IV Nuclear Energy Systems*. OECD Nuclear Energy Agency for the Generation IV International Forum

Bennett, D. L. and J. C. Chen (1980), "Forced Convective Boiling in Vertical Tubes for Saturated Pure Components and Binary Mixtures," *AIChE Journal* Vol. 26(3) pp. 454-461. DOI: 10.1002/aic.690260317.

Benzinger, W., J. Brandner, U. Schygulla and K. Schubert (2007), "Influence of Different Surface Materials on the Fouling Process in a Microstructured Heat Exchanger under Laminar Regime," *Proceedings of 7th International Conference on Heat Exchanger Fouling and Cleaning - Challenges and Opportunities*, Tomar, Portugal, pp. 395-402.

Bergles, A. and W. Rohsenow (1964), "The Determination of Forced-Convection Surface-Boiling Heat Transfer," *Journal of Heat Transfer* Vol. 86(3) pp. 365-372.

Bertsch, S. S., E. A. Groll and S. V. Garimella (2008), "Review and Comparative Analysis of Studies on Saturated Flow Boiling in Small Channels," *Nanoscale and Microscale Thermophysical Engineering* Vol. 12(3) pp. 187-227. DOI: 10.1080/15567260802317357.

Bertsch, S. S., E. A. Groll and S. V. Garimella (2009), "A Composite Heat Transfer Correlation for Saturated Flow Boiling in Small Channels," *International Journal of Heat and Mass Transfer* Vol. 52(7) pp. 2110-2118. DOI: 10.1016/j.ijheatmasstransfer.2008.10.022.

Bowdery, T. (2006), "LNG Applications of Diffusion Bonded Heat Exchangers," *Proceedings of AlChE Spring Meeting 6th Topical Conference on Natural Gas Utilization*, Orlando, FL.

Carelli, M. D., P. Garrone, G. Locatelli, M. Mancini, C. Mycoff, P. Trucco and M. Ricotti (2010), "Economic Features of Integral, Modular, Small-to-Medium Size Reactors," *Progress in Nuclear Energy* Vol. 52(4) pp. 403-414. DOI: 10.1016/j.pnucene.2009.09.003.

Cengel, Y. A. and J. M. Cimbala (2006). *Fluid Mechanics: Fundmentals and Applications*. New York, New York, McGraw-Hill.

Chen, J. C. (1966), "Correlation for Boiling Heat Transfer to Saturated Fluids in Convective Flow," *Industrial and Engineering Chemistry Process Design and Development* Vol. 5(3) pp. 322-329.

Chen, J. C., F. T. Ozkaynak and R. K. Sundaram (1979), "Vapor Heat Transfer in Post-CHF Region Including the Effect of Thermodynamic Non-Equilibrium," *Nuclear Engineering and Design* Vol. 51(2) pp. 143-155. DOI: 10.1016/0029-5493(79)90086-4.

Chisholm, D. (1967), "A Theoretical Basis for the Lockhart-Martinelli Correlation for Two-Phase Flow," *International Journal of Heat and Mass Transfer* Vol. 10(12) pp. 1767-1778. DOI: 10.1016/0017-9310(67)90047-6.

Churchill, S. W. (1977a), "Comprehensive Correlating Equations for Heat, Mass and Momentum Transfer in Fully Developed Flow in Smooth Tubes," *Industrial and Engineering Chemistry Fundamentals* Vol. 16(1) pp. 109-116.

Churchill, S. W. (1977b), "Friction-Factor Equation Spans All Fluid-Flow Regimes," *Chemical Engineering* Vol. 84(24) pp. 91-92.

Churchill, S. W. and R. Usagi (1972), "A General Expression for the Correlation of Rates of Transfer and Other Phenomena," *AIChE Journal* Vol. 18(6) pp. 1121-1128. DOI: 10.1002/aic.690180606.

Cioncolini, A., A. Cammi, C. Lombardi, L. Luzzi, M. Ricotti, L. Cinotti and G. Castelli (2003), "Thermal Hydraulic Analysis of IRIS Reactor Coiled Tube Steam Generator," *Proceedings of American Nuclear Society Topical Meeting in Mathematics and Computations.*

Colburn, A. P. (1933), "Mean Temperature Difference and Heat Transfer Coefficient in Liquid Heat Exchangers," *Industrial and Engineering Chemistry*(8) pp. 873-876.

Collier, J. G. and J. R. Thome (1994). *Convective Boiling and Condensation*. 3rd Ed. Oxford, New York, Oxford University Press.

Cooper, M. (1984), "Heat Flow Rates in Saturated Nucleate Pool Boiling - a Wide-Ranging Examination Using Reduced Properties," *Advances in Heat Transfer* Vol. 16 pp. 157-239. DOI: 10.1016/S0065-2717(08)70205-3.

Dengler, C. and J. Addoms (1956), "Heat Transfer - Louisville," *CEP Simposium Series* Vol. 52(18) p. 95.

Determan, M. D. and S. Garimella (2012), "Design, Fabrication, and Experimental Demonstration of a Microscale Monolithic Modular Absorption Heat Pump," *Applied Thermal Engineering* Vol. 47 pp. 119-125. DOI: 10.1016/j.applthermaleng.2011.10.043.

Dittus, F. and L. Boelter (1930), "Where Did the Dittus and Boelter Equation Come From?," *International Journal of Heat and Mass Transfer* Vol. 41(4-5) pp. 809-810.

Dougall, R. S. and W. M. Rohsenow (1963). *Film Boiling on the inside of Vertical Tubes with Upward Flow of the Fluid at Low Qualities*. Massachusets Insitute of Technology Technical Report 9079-26.

EIA, U. S. (2018a). *Annual Energy Outlook 2018 with Projections to 2050*. U.S. Energy Information Administration. Washington D.C. AEO2018.

EIA, U. S. (2018b). *Levelized Cost and Levelized Avoided Cost of New Generation Resources in the Annual Energy Outlook*. U.S. Energy Information Administration. Washington D.C. AEO2018.

Forster, H. and N. Zuber (1955), "Dynamics of Vapor Bubbles and Boiling Heat Transfer," *AIChE Journal* Vol. 1(4) pp. 531-535. DOI: doi.org/10.1002/aic.690010425.

Friedel, L. (1979), "Improved Friction Pressure Drop Correlations for Horizontal and Vertical Two-Phase Pipe Flow," *Proceedings of European Two-Phase Flow Group Meeting.*

Gad-El-Hak, M. (2006), "Gas and Liquid Transport at the Microscale," *Heat Transfer Engineering* Vol. 27(4) pp. 13-29. DOI: 10.1080/01457630500522305.

Ghiaasiaan, S. M. (2017). *Two-Phase Flow, Boiling, and Condensation: In Conventional and Miniature Systems* Cambridge University Press.

Ghiaasiaan, S. M. (2018). *Convective Heat and Mass Transfer*, CRC Press.

Gnielinski, V. (1976), "New Equations for Heat and Mass-Transfer in Turbulent Pipe and Channel Flow," *International Chemical Engineering* Vol. 16(2) pp. 359-368.

Gorenflo, D. (1993). *Pool Boiling in VDI Heat Atlas (English Version)*. Dusseldorf, Germany.

Groeneveld, D. and G. Delorme (1976), "Prediction of Thermal Non-Equilibrium in the Post-Dryout Regime," *Nuclear Engineering and Design* Vol. 36(1) pp. 17-26. DOI: 10.1016/0029-5493(76)90138-2.

Gungor, K. and R. Winterton (1987), "Simplified General Correlation for Saturated Flow Boiling and Comparisons of Correlations with Data," *Chemical Engineering Research and Design* Vol. 65(2) pp. 148-156.

Gungor, K. E. and R. Winterton (1986), "A General Correlation for Flow Boiling in Tubes and Annuli," *International Journal of Heat and Mass Transfer* Vol. 29(3) pp. 351-358. DOI: 10.1016/0017-9310(86)90205-X.

Haratyk, G. (2017), "Early Nuclear Retirements in Deregulated U.S. Markets: Causes, Implications and Policy Options," *Energy Policy* Vol. 110 pp. 150-166. DOI: 10.1016/j.enpol.2017.08.023.

Harirchian, T. and S. V. Garimella (2010), "A Comprehensive Flow Regime Map for Microchannel Flow Boiling with Quantitative Transition Criteria," *International Journal of Heat and Mass Transfer* Vol. 53(13) pp. 2694-2702. DOI: doi.org/10.1016/j.ijheatmasstransfer.2010.02.039.

Harrod, D., R. Gold and R. Jacko (2001), "Alloy Optimization for PWR Steam Generator Heat-Transfer Tubing," *The Journal of the Minerals, Metals, and Materials Society* Vol. 53(7) pp. 14-17.

Hausen, H. (1943), "Darstellung Des Warmeuberganges in Rohren Durch Verallgemeinerte Potenzbeziehungen," *Z. VDI Beih. Verfahrenstech* Vol. 4 pp. 91-98.

Haynes, B. and D. Fletcher (2003), "Subcooled Flow Boiling Heat Transfer in Narrow Passages," *International Journal of Heat and Mass Transfer* Vol. 46(19) pp. 3673-3682. DOI: 10.1016/S0017-9310(03)00172-8.

Heatric (2015). *Heatric Celebartes Its 25th Anniversary*, Heatric division of Meggitt UK Ltd, Accessed*:* 5/12/2015, http://www.heatric.com/Heatric_celebrates_its_25th_anniversary.html.

Hewitt, G. F., G. L. Shires and T. R. Bott (1994). *Process Heat Transfer*, CRC Press: London, UK.

Ho, C. Y. and T. Chu (1977). *Electrical Resistivity and Thermal Conductivity of Nine Selected AISI Stainless Steels*. Thermopysical and Electronic Properties Information Analysis Center. Lafayette, In. ADA129160.

Huber, M. L., R. A. Perkins, D. G. Friend, J. V. Sengers, M. J. Assael, I. N. Metaxa, K. Miyagawa, R. Hellmann and E. Vogel (2012), "New International Formulation for the Thermal Conductivity of H2O," *Journal of Physical and Chemical Reference Data* Vol. 41(3) p. 033102. DOI: 10.1063/1.4738955.

Incropera, F. P., D. P. Dewitt, T. L. Bergman and A. S. Lavine (2007). *Fundamentals of Heat and Mass Transfer*, John Wiley & Sons Inc.

IPCC (2018). *Global Warming of 1.5°C*. United Nations Intergovernmental Panel on Climate Change. Incheon, Korea.

Jens, W. H. and P. Lottes (1951). *Analysis of Heat Transfer, Burnout, Pressure Drop and Density Data for High-Pressure Water*. Argonne National Lab. ANL-4627.

Kakac, S. and B. Bon (2008), "A Review of Two-Phase Flow Dynamic Instabilities in Tube Boiling Systems," *International Journal of Heat and Mass Transfer* Vol. 51(3) pp. 399-433. DOI: 10.1016/j.ijheatmasstransfer.2007.09.026.

Kandlikar, S. G. (1998), "Heat Transfer Characteristics in Partial Boiling, Fully Developed Boiling, and Significant Void Flow Regions of Subcooled Flow Boiling," *Journal of Heat Transfer* Vol. 120 pp. 395-401.

Kandlikar, S. G. (2002), "Fundamental Issues Related to Flow Boiling in Minichannels and Microchannels," *Experimental Thermal and Fluid Science* Vol. 26(2) pp. 389-407. DOI: 10.1016/S0894-1777(02)00150-4.

Kandlikar, S. G. and P. Balasubramanian (2004), "An Extension of the Flow Boiling Correlation to Transition, Laminar, and Deep Laminar Flows in Minichannels and Microchannels," *Heat Transfer Engineering* Vol. 25(3) pp. 86-93. DOI: 10.1080/01457630490280425.

Kestin, J., J. Sengers, B. Kamgar-Parsi and J. L. Sengers (1984), "Thermophysical Properties of Fluid H2O," *Journal of Physical and Chemical Reference Data* Vol. 13(1) pp. 175-183. DOI: 10.1063/1.555707.

Kew, P. A. and K. Cornwell (1997), "Correlations for the Prediction of Boiling Heat Transfer in Small-Diameter Channels," *Applied Thermal Engineering* Vol. 17(8-10) pp. 705-715. DOI: 10.1016/S1359-4311(96)00071-3.

Kim, S.-M. and I. Mudawar (2013a), "Universal Approach to Predicting Heat Transfer Coefficient for Condensing Mini/Micro-Channel Flow," *International Journal of Heat and Mass Transfer* Vol. 56(1) pp. 238-250. DOI: 10.1016/j.ijheatmasstransfer.2012.09.032.

Kim, S.-M. and I. Mudawar (2013b), "Universal Approach to Predicting Saturated Flow Boiling Heat Transfer in Mini/Micro-Channels – Part I. Dryout Incipience Quality," *International Journal of Heat and Mass Transfer* Vol. 64 pp. 1226-1238. DOI: 10.1016/j.ijheatmasstransfer.2013.04.016.

Kim, S.-M. and I. Mudawar (2013c), "Universal Approach to Predicting Saturated Flow Boiling Heat Transfer in Mini/Micro-Channels – Part II. Two-Phase Heat Transfer Coefficient," *International Journal of Heat and Mass Transfer* Vol. 64 pp. 1239-1256. DOI: 10.1016/j.ijheatmasstransfer.2013.04.014.

Kim, S.-M. and I. Mudawar (2013d), "Universal Approach to Predicting Two-Phase Frictional Pressure Drop for Mini/Micro-Channel Saturated Flow Boiling," *International Journal of Heat and Mass Transfer* Vol. 58(1) pp. 718-734. DOI: 10.1016/j.ijheatmasstransfer.2012.11.045.

Klein, S. A. (2017). *Engineering Equation Solver*, F-Chart Software.

Kumaran, R. M., G. Kumaraguruparan and T. Sornakumar (2013), "Experimental and Numerical Studies of Header Design and Inlet/Outlet Configurations on Flow Mal-Distribution in Parallel Micro-Channels," *Applied Thermal Engineering* Vol. 58(1-2) pp. 205-216. DOI: 10.1016/j.applthermaleng.2013.04.026.

Kuridan, R. and T. Beynon (1997), "Analysis of the Steam Generator for the Safe Integral Reactor Concept: I. Steady State," *Progress in Nuclear Energy* Vol. 31(3) pp. 273-287. DOI: 10.1016/0149-1970(95)00099-2.

Le Pierres, R., D. Southall and S. Osborne (2011). *Impact of Mechanical Design Issues on Printed Circuit Heat Exchagers*. SCO2 Power Cycle Symposium University of Colorado Bolder.

Lee, H. J. and S. Y. Lee (2001), "Pressure Drop Correlations for Two-Phase Flow within Horizontal Rectangular Channels with Small Heights," *International Journal of Multiphase Flow* Vol. 27(5) pp. 783-796. DOI: 10.1016/S0301-9322(00)00050-1.

Li, X., T. Smith, D. Kininmont and S. J. Dewson (2009), "Materials for Nuclear Diffusion-Bonded Compact Heat Exchangers," *Proceedings of ICAPP*, Tokyo, Japan, pp. 1-9.

Lin, S., C. Kwok, R.-Y. Li, Z.-H. Chen and Z.-Y. Chen (1991), "Local Frictional Pressure Drop During Vaporization of R-12 through Capillary Tubes," *International Journal of Multiphase Flow* Vol. 17(1) pp. 95-102. DOI: 10.1016/0301-9322(91)90072-B.

Liu, Z. and R. Winterton (1991), "A General Correlation for Saturated and Subcooled Flow Boiling in Tubes and Annuli, Based on a Nucleate Pool Boiling Equation," *International Journal of Heat and Mass Transfer* Vol. 34(11) pp. 2759-2766. DOI: 10.1016/0017-9310(91)90234-6.

Lockhart, R. and R. Martinelli (1949), "Proposed Correlation of Data for Isothermal Two-Phase, Two-Component Flow in Pipes," *Chemical Engineering Progress* Vol. 45(1) pp. 39-48.

Luzzi, L. and V. Di Marcello (2011a), "Collapse of Nuclear Reactor SG Tubes Pressurized from Outside: The Influence of Imperfections," *Journal of Pressure Vessel Technology* Vol. 133(1). DOI: 10.1115/1.4002769.

Luzzi, L. and V. Di Marcello (2011b), "Collapse of Nuclear Reactor SG Tubes Pressurized from Outside: The Influence of Imperfections," *Journal of Pressure Vessel Technology* Vol. 133(1) p. 011206.

Maranzana, G., I. Perry and D. Maillet (2004), "Mini- and Micro-Channels: Influence of Axial Conduction in the Walls," *International Journal of Heat and Mass Transfer* Vol. 47(17–18) pp. 3993-4004. DOI: 10.1016/j.ijheatmasstransfer.2004.04.016.

Mastrullo, R., A. Mauro, J. Thome, D. Toto and G. Vanoli (2012), "Flow Pattern Maps for Convective Boiling of CO2 and R410a in a Horizontal Smooth Tube: Experiments and New Correlations Analyzing the Effect of the Reduced Pressure," *International Journal of Heat and Mass Transfer* Vol. 55(5-6) pp. 1519-1528. DOI: 10.1016/j.ijheatmasstransfer.2011.11.003.

Matijević, M., D. Pevec and R. Ječmenica (2017), "I2S-LWR Activation Analysis of Heat Exchangers Using Hybrid Shielding Methodology with SCALE6.1," *Energy* Vol. 65(1) pp. 138-150.

McAdams, W., W. Woods and L. Heroman (1942), "Vaporization inside Horizontal Tubes-II, Benzene-Oil Mixtures," *Trans. ASME* Vol. 64(3) pp. 193-200.

McGillis, W. R., V. P. Carey, J. S. Fitch and W. R. Hamburgen (1991), "Pool Boiling Enhancement Techniques for Water at Low Pressure," *Proceedings of 7th Annual IEEE Semiconductor Thermal Measurement and Management Symposium*, IEEE, pp. 64-72.

Memmott, M. J., A. Manera, J. Boyack, S. Pacheco, M. Wang and B. Petrovic (2017a), "The Primary Reactor Coolant System Concept of the Integral, Inherently-Safe Light Water Reactor," *Annals of Nuclear Energy* Vol. 100, Part 1 pp. 53-67. DOI: 10.1016/j.anucene.2016.08.016.

Memmott, M. J., P. R. Wilding and B. Petrovic (2017b), "An Optimized Power Conversion System Concept of the Integral, Inherently-Safe Light Water Reactor," *Annals of Nuclear Energy* Vol. 100, Part 1 pp. 42-52. DOI: 10.1016/j.anucene.2016.08.015.

Mishima, K. and T. Hibiki (1996), "Some Characteristics of Air-Water Two-Phase Flow in Small Diameter Vertical Tubes," *International Journal of Multiphase Flow* Vol. 22(4) pp. 703-712. DOI: 10.1016/0301-9322(96)00010-9.

Morini, G. L. (2006), "Scaling Effects for Liquid Flows in Microchannels," *Heat Transfer Engineering* Vol. 27(4) pp. 64-73. DOI: 10.1080/01457630500523865.

Mukherjee, A. and S. G. Kandlikar (2005), "Numerical Study of the Effect of Inlet Constriction on Bubble Growth During Flow Boiling in Microchannels," *Proceedings of ASME 3rd International Conference on Microchannels and Minichannels*, Toronto, Ontario, ASME, pp. 73-80.

Müller-Steinhagen, H. and K. Heck (1986), "A Simple Friction Pressure Drop Correlation for Two-Phase Flow in Pipes," *Chemical Engineering and Processing: Process Intensification* Vol. 20(6) pp. 297-308. DOI: 10.1016/0255-2701(86)80008-3.

Nageswara, R. and K. Deepak (2007), "Fabrication of Microchannels on Stainless Steel by Wet Chemical Etching," *Journal of Micromechanics and Microengineering* Vol. 17(12) pp. N99-106. DOI: 10.1088/0960-1317/17/12/N01.

Namgung, I. and N. H. Giang (2016), "Investigation of Burst Pressures in PWR Primary Pressure Boundary Components," *Nuclear Engineering and Technology* Vol. 48(1) pp. 236-245. DOI: 10.1016/j.net.2015.11.001.

Ong, C. and J. Thome (2011a), "Macro-to-Microchannel Transition in Two-Phase Flow: Part 2–Flow Boiling Heat Transfer and Critical Heat Flux," *Experimental Thermal and Fluid Science* Vol. 35(6) pp. 873-886. DOI: 10.1016/j.expthermflusci.2010.12.003.

Ong, C. L. and J. Thome (2011b), "Macro-to-Microchannel Transition in Two-Phase Flow: Part 1–Two-Phase Flow Patterns and Film Thickness Measurements," *Experimental Thermal and Fluid Science* Vol. 35(1) pp. 37-47. DOI: 10.1016/j.expthermflusci.2010.08.004.

Perry, J. L. and S. G. Kandlikar (2008), "Investigation of Fouling and Its Mitigation in Silicon Microchannels," *Proceedings of ASME 6th International Conference on Nanochannels, Microchannels, and Minichannels*, American Society of Mechanical Engineers, pp. 1741-1758.

Petrovic, B. (2014), "Integral Inherently Safe Light Water Reactor (I2S-LWR) Concept: Extending SMR Safety Features to Large Power Output," *Proceedings of ICAPP*, Charlotte, North Carolina, pp. 78-85.

Petrovic, B., M. Memmott, G. Boy, I. Charit, A. Manera, T. Downar, J. Lee, L. Muldrow, B. Upadhyaya and W. Hines (2017a). *Integral Inherently Safe Light Water Reactor (I2S-LWR)*. Georgia Institute of Technology. Atlanta, GA. DOE/NEUP-12-4733.

Petrovic, B., F. Rahnema, C. Deo, S. Garimella, P. Singh, K. Oh, C. Yi, D. Zhang, A. Manera, J. Lee, T. Downar, A. Ward, P. Ferroni, F. Franceschini, D. Salazar, B. Upadhyaya, M. Lish, I. Charit, A. Haghighat, M. Memmott, G. Boy, A. Ougouag, G. Parks, D. Kotlyar, M. Ricotti, N. Čavlina, D. Grgić, D. Pevec, M. Matijević and N. Irvin (2017b), "I2S-LWR Concept Update," *Proceedings of The 20th Pacific Basin Nuclear Conference*, Singapore, Springer Singapore, pp. 153-167.

Petrovic, B., M. Ricotti, S. Monti, N. Čavlina and H. Ninokata (2012), "Pioneering Role of IRIS in the Resurgence of Small Modular Reactors," *Nuclear Technology* Vol. 178(2) pp. 126-152. DOI: 10.13182/NT12-A13555.

Phillips, R. J. (1988), "Microchannel Heat Sinks," *Lincoln Laboratory Journal* Vol. 1(1) pp. 31-48.

Qu, W. and I. Mudawar (2004), "Measurement and Correlation of Critical Heat Flux in Two-Phase Micro-Channel Heat Sinks," *International Journal of Heat and Mass Transfer* Vol. 47(10) pp. 2045-2059. DOI: 10.1016/j.ijheatmasstransfer.2003.12.006.

Rehme, K. (1973), "Pressure Drop Correlations for Fuel Element Spacers," *Nuclear Technology* Vol. 17(1) pp. 15-23. DOI: 10.13182/NT73-A31250.

Reyes, J. N. and P. Lorenzini (2010), "Nuscale Power: A Modular, Scalable Approach to Commercial Nuclear Power," *Nuclear News* Vol. 53(7) pp. 97-104.

Roach, G. M., S. I. Abdel-Khalik, S. M. Ghiaasiaan, M. F. Dowling and S. M. Jeter (1999), "Low-Flow Critical Heat Flux in Heated Microchannels," *Nuclear Science and Engineering* Vol. 131(3) pp. 411-425. DOI: 10.13182/NSE99-A2043.

Rohsenow, W. and A. Bergles (1964), "The Determination of Forced-Convection Surface-Boiling Heat Transfer," *Journal of Heat Transfer* Vol. 86(3) pp. 365-372.

Rosa, P., T. G. Karayiannis and M. W. Collins (2009), "Single-Phase Heat Transfer in Microchannels: The Importance of Scaling Effects," *Applied Thermal Engineering* Vol. 29(17–18) pp. 3447-3468. DOI: 10.1016/j.applthermaleng.2009.05.015.

Saha, P. and N. Zuber (1974), "Point of Net Vapor Generation and Vapor Void Fraction in Subcooled Boiling," *Proceedings of The International Heat Transfer Conference*, Tokyo, Japan.

Schwarz, T. (2001), "Heat Transfer and Fouling Behaviour of Siemens PWR Steam Generators–Long-Term Operating Experience," *Experimental Thermal and Fluid Science* Vol. 25(5) pp. 319-327.

Shah, M. M. and M. A. Siddiqui (2000), "A General Correlation for Heat Transfer During Dispersed-Flow Film Boiling in Tubes," *Heat Transfer Engineering* Vol. 21(4) pp. 18-32. DOI: 10.1080/01457630050144479.

Sobhan, C. B. and S. V. Garimella (2001), "A Comparative Analysis of Studies on Heat Transfer and Fluid Flow in Microchannels," *Microscale Thermophysical Engineering* Vol. 5(4) pp. 293-311. DOI: 10.1080/10893950152646759.

Steam (2005). *Steam - Its Generation and Use*. 41 Ed. Barberton, Ohio, USA.

Steiner, D. and J. Taborek (1992), "Flow Boiling Heat Transfer in Vertical Tubes Correlated by an Asymptotic Model," *Heat Transfer Engineering* Vol. 13(2) pp. 43-69. DOI: 10.1080/01457639208939774.

Steinke, M. E. and S. G. Kandlikar (2005), "Single-Phase Liquid Friction Factors in Microchannels," *Proceedings of ASME 3rd International Conference on Microchannels and Minichannels*, American Society of Mechanical Engineers, pp. 291-302.

Suo, M. and P. Griffith (1964), "Two-Phase Flow in Capillary Tubes," *Journal of Basic Engineering* Vol. 86(3) pp. 576-582.

Tanaka, Y. and I. Sato (2011), "Development of High Purity Large Forgings for Nuclear Power Plants," *Journal of Nuclear Materials* Vol. 417(1-3) pp. 854-859. DOI: 10.1016/j.jnucmat.2010.12.305.

Techo, R., R. R. Tickner and R. E. James (1965), "An Accurate Equation for the Computation of the Friction Factor for Smooth Pipes from the Reynolds Number," *Applied Mechanics* Vol. 32 p. 443.

Testa, D. and A. Kunkle (1984). *The Westinghouse Pressurized Water Reactor Nuclear Power Plant*. Westinghouse Electric Corporation Water Reactor Division. Pittsburgh, Pennsylvania.

Thom, J., W. Walker, T. Fallon and G. Reising (1965), "Boiling in Sub-Cooled Water During Flow up Heated Tubes or Annuli," *Proceedings of The Institution of Mechanical Engineers*, London, England, Sage Publications, pp. 226-246.

Thome, J., V. Dupont and A. M. Jacobi (2004), "Heat Transfer Model for Evaporation in Microchannels. Part I: Presentation of the Model," *International Journal of Heat and Mass Transfer* Vol. 47(14-16) pp. 3375-3385. DOI: 10.1016/j.ijheatmasstransfer.2004.01.006.

Todreas, N. E. and M. S. Kazimi (2011). *Nuclear Systems Volume I: Thermal Hydraulic Fundamentals*, CRC press.

Triplett, K., S. Ghiaasiaan, S. Abdel-Khalik, A. LeMouel and B. McCord (1999), "Gas–Liquid Two-Phase Flow in Microchannels: Part II: Void Fraction and Pressure Drop," *International Journal of Multiphase Flow* Vol. 25(3) pp. 395-410. DOI: 10.1016/S0301-9322(98)00055-X.

Tuo, H. and P. Hrnjak (2013), "Effect of the Header Pressure Drop Induced Flow Maldistribution on the Microchannel Evaporator Performance," *International Journal of Refrigeration* Vol. 36(8) pp. 2176-2186. DOI: 10.1016/j.ijrefrig.2013.06.002.

Turner, C. W., S. J. Klimas and M. G. Brideau (2000), "Thermal Resistance of Steam-Generator Tube Deposits under Single-Phase Forced Convection and Flow-Boiling

Heat Transfer," *The Canadian Journal of Chemical Engineering* Vol. 78(1) pp. 53-60. DOI: 10.1002/cjce.5450780109.

U.S. NRC (2018). *Design-Basis Accident*, 7/6/2018, https://www.nrc.gov/reading-rm/basic-ref/glossary/design-basis-accident.html.

Ungar, E. and J. Cornwell (1992), "Two-Phase Pressure Drop of Ammonia in Small Diameter Horizontal Tubes," *Proceedings of 28th Joint Propulsion Conference and Exhibit*, pp. 1-10.

Wade, K. C. (1995), "Steam Generator Degradation and Its Impact on Continued Operation of Pressurized Water Reactors in the United States," *Energy Information Administration/Electric Power Monthly* Vol. 66.

Wagner, W. and A. Pruß (2002), "The Iapws Formulation 1995 for the Thermodynamic Properties of Ordinary Water Substance for General and Scientific Use," *Journal of Physical and Chemical Reference Data* Vol. 31(2) pp. 387-535. DOI: 10.1063/1.1461829.

Wang, B. and X. Peng (1994), "Experimental Investigation on Liquid Forced-Convection Heat Transfer through Microchannels," *International Journal of Heat and Mass Transfer* Vol. 37 pp. 73-82. DOI: 10.1016/0017-9310(94)90011-6.

Wang, M., A. Manera, M. Memmott and S. Qiu (2015), "Passive Decay Heat Removal System Design for the Integral Inherent Safety Light Water Reactor (I2S-LWR)," *Annals of Nuclear Energy*.

Wang, M., A. Manera, M. J. Memmott, J. C. Lee, W. Tian, G. Su and S. Qiu (2018), "Preliminary Design of the I2S-LWR Containment System," *Annals of Nuclear Energy*. DOI: 10.1016/j.anucene.2018.03.014.

Webb, R. L. (2003), "Effect of Manifold Design on Flow Distribution in Parallel Micro-Channels," *Proceedings of ASME 2003 International Electronic Packaging Technical Conference and Exhibition*, American Society of Mechanical Engineers, pp. 527-535.

Weisman, J. (1959), "Heat Transfer to Water Flowing Parallel to Tube Bundles," *Nuclear Science and Engineering* Vol. 6(1) pp. 78-79.

Weisman, J. and S. Ying (1985), "A Theoretically Based Critical Heat Flux Prediction for Rod Bundles at PWR Conditions," *Nuclear Engineering and Design* Vol. 85(2) pp. 239-250. DOI: 10.1016/0029-5493(85)90289-4.

Williams, D. K., D. P. Fassett, B. J. Webb, W. J. Bees and A. S. Kruskamp (2014). *Healical Coil Steam Generator*. U. S. P. a. T. Office, NuScale Power, LLC, Vol. 8,752,510 B2.

Wojtan, L., T. Ursenbacher and J. R. Thome (2005), "Investigation of Flow Boiling in Horizontal Tubes: Part II—Development of a New Heat Transfer Model for Stratified-

Wavy, Dryout and Mist Flow Regimes," *International Journal of Heat and Mass Transfer* Vol. 48(14) pp. 2970-2985. DOI: 10.1016/j.ijheatmasstransfer.2004.12.013.

World Nuclear Association (2018a). *Economics of Nuclear Power*, January 4th, 2019, http://www.world-nuclear.org/information-library/economic-aspects/economics-of-nuclear-power.aspx.

World Nuclear Association (2018b). *Heavy Manufacturing of Power Plants*, January 4th, 2019, http://www.world-nuclear.org/information-library/nuclear-fuel-cycle/nuclear-power-reactors/heavy-manufacturing-of-power-plants.aspx.

Xia, G., M. Peng and Y. Guo (2012), "Research of Two-Phase Flow Instability in Parallel Narrow Multi-Channel System," *Annals of Nuclear Energy* Vol. 48 pp. 1-16. DOI: 10.1016/j.anucene.2012.05.014.

Zhang, W., T. Hibiki and K. Mishima (2010), "Correlations of Two-Phase Frictional Pressure Drop and Void Fraction in Mini-Channel," *International Journal of Heat and Mass Transfer* Vol. 53(1) pp. 453-465. DOI: 10.1016/j.ijheatmasstransfer.2009.09.011.

Zhao, T. and Q. Bi (2001), "Pressure Drop Characteristics of Gas–Liquid Two-Phase Flow in Vertical Miniature Triangular Channels," *International Journal of Heat and Mass Transfer* Vol. 44(13) pp. 2523-2534. DOI: 10.1016/S0017-9310(00)00282-9.